Laser Studies of Plasmas

A Thesis Submitted for the Degree of
Doctor of Philosophy

By

Robert Michael James Jacobs

St Catherine's College, Oxford

Michaelmas Term, 2000

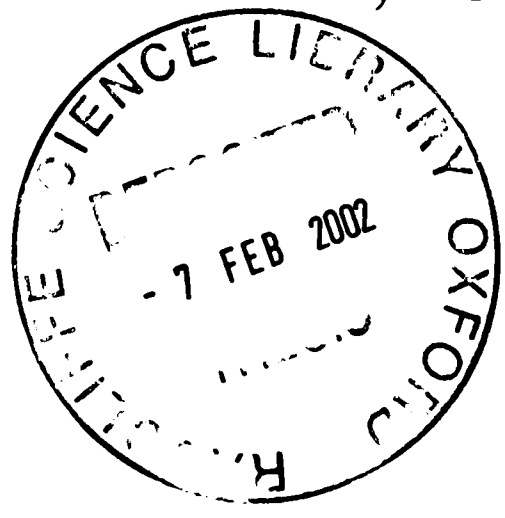

Abstract

Laser Studies of Plasmas

A Thesis Submitted for the Degree of Doctor of Philosophy.

Robert Michael James Jacobs, St Catherine's College, Oxford

Michaelmas Term, 2000

Measurement of the intrinsic properties of processing plasmas is critically important in understanding discharges so that the optimum conditions can be achieved. Several different diagnostic methods have been developed and tested.

A planar probe has been used to measure the ion flux and electron temperature in both inductively coupled and capacitively coupled plasma systems, at various pressures and applied powers, using the assumption that the electron energy distribution is a Maxwellian.

Frequency modulation spectroscopy (FMS) has been used to detect species in a plasma. It has been shown to be very effective, giving a significantly increased S/N ratio compared to both single pass absorption and low frequency mechanical modulation techniques. It has been used to measure excited argon atom concentrations, in both capacitively and inductively produced plasmas. The argon atom $4s[^3/_2]_1$ level concentration was found to be between 2×10^8 and 1×10^{11} atom/cm^3 and to generally increase with increasing applied power and to decrease with increasing total pressure. The temperature of the atoms was also measured and was found to be approximately 323 ± 17 K.

A simple compact laser source at 308 nm has been produced from a frequency doubled cooled commercial diode laser. This has been used to detect the OH radical, by absorption, within the afterglow of a microwave discharge, produced either directly or chemically. Simple kinetic models have provided explanations of the variations in OH concentration with discharge conditions.

A novel method, cavity laser induced fluorescence (CLIF), that combines the advantages of both laser induced fluorescence (LIF) and cavity ring down spectroscopy CRDS, has been shown to increase the sensitivity of a diagnostic system compared to absorption. This method could be used to follow concentration variations of a reaction in a single laser shot. Although such variation can be observed using LIF, it requires a calibration and a many laser shot experiment with a signal recorded at each time point. Whilst CRDS allows temporal information about the absolute concentrations of the species observed to be obtained, it is not as sensitive as LIF. By combining the two in CLIF, it may be possible to retain the sensitivity of LIF with the advantage of CRDS so that absolute and time varying concentrations can be obtained in a single pulsed laser shot.

LIF and CRDS signals have been observed using the A $^2\Pi_u \leftarrow$ X $^2\Sigma_g^+$ transition of the N_2^+ ion. The lifetime of the A $^2\Pi_u$ state in the discharge was found to be sufficiently long for a time of flight experiment to be contemplated (an ion with a velocity of 10 kms^{-1} on average would travel 5 mm before radiating). Although the preliminary tests for the time of flight experiment have shown that this method is not feasible with a pulsed laser, the basic cavity locking procedures required for an analogous continuous wave experiment have been successfully demonstrated.

A frequency doubled diode laser source has been constructed and tested, with the eventual aim of detecting N_2^+ *via* the B $^2\Sigma_u^+ \leftarrow$ X $^2\Sigma_g^+$ electronic transition. This has been found to be insufficiently intense to be used for a proposed two dimensional velocity mapping experiment, but several strategies to improve its performance are suggested.

Acknowledgements

I would like to thank Professor Gus Hancock, my supervisor, for five enjoyable and exciting years. During these years he has not only guided me in a stimulating field but also has generously provided numerous very memorable occasions, including several fantastic group dinners, an excellent 'free' trip to Germany and a great stay at the Prague Hilton. While encouraging me to develop the experiments described in this Thesis, and others, he has given me the opportunity to teach his students and others, hone my technical skills as well as increasing my scientific experience.

I also thank Dr. Nick St. J. Braithwaite and his research group, at the Oxford Research Unit of the Open University, who have generously supplied me the with equipment necessary to complete the experiments described in Chapter 2. He has also provided many excellent ideas and invaluable advice including 'Setting up a plasma matching network is a black art'!

I am very grateful to Dr. Matthew Costen, who, way beyond the call of duty, during my first two years in the Hancock group, taught me about all the instrumentation that I had inherited and then relocated in a new laboratory. He has also been a good friend at times when I needed one the most.

I am indebted to Ben Bakowski a.k.a. The Jazz, his arrival was incredibly well timed. Over the past year, his assistance in the laboratory and with the final stages in the preparation of this thesis has been amazing. I hope soon I can begin to repay you.

I have greatly appreciated the stimulating and constructive discussions I have had with Rob P and his help during the final stages of the preparation of this Thesis. With which Ciara, LawRah, Grant and others assisted.

I have also had the pleasure of sharing experiments and laboratories with Katarina, Ollie, Ray, Torna, Vas, Hugh and Steve and some of the people I have already mentioned. This has always been an enjoyable and interesting experience.

I acknowledge Tim Freegarde for the design work on some of the systems used in this thesis, and thank the mechanical and electrical workshop staff who have tirelessly produced excellent results from his designs and my subsequent redesigns.

My thanks also extends to all those current and previous Hancock group members that I have worked, talked, wined and dinned with but have now failed to mentioned who have generally made life in the group a fantastic experience.

I thank my parents who have provided me with constant understanding, encouragement and support throughout my on going education. Last and certainly not least, long suffering Sally whose love, companionship and support makes my life amazing. It is to her and my parents I dedicate this thesis.

Glossary of Acronyms

a.c.	alternating current
AM	Amplitude Modulation
AOE	Actinometric Optical Emission
AOM	Acousto-Optic modulator
ASE	Amplified Spontaneous Emission
BOC	British Oxygen Corporation
CARS	Coherent Anti-Stokes Raman Scattering
CCD	Charge Coupled Device
CCP	Capacitively Coupled Plasma
CEAS	Cavity Enhanced Absorption Spectroscopy
CFC	ChloroFluoroCarbon
CLIF	Cavity Laser Induced Fluorescence
CRDS	Cavity Ring Down Spectroscopy
d.c.	direct current
EDL	Electrodeless Discharge Lamp
EOM	Electro-Optic Modulator
FFT	Fast Fourier Transform
FM	Frequency Modulation
FMS	Frequency Modulation Spectroscopy
FSR	Free Spectral Range
FWHM	Full Width at Half Maximum
GEC	Gaseous Electronics Conference
IC	Integrated Circuit
ICOS	Integrated Cavity Absorption Spectroscopy

ICP	Inductively Coupled Plasma
IR	InfraRed
LCAO	Linear Combination of Atomic Orbitals
LIF	Laser Induced Fluorescence
LOGS	Laser OptoGalvanic Spectroscopy
MCT	Mercury Cadmium Telluride
MIP	Microwave Induced Plasma
MMS	Mechanical Modulation Spectroscopy
OE	Optical Emission
PC	Personal Computer
PECVD	Plasma Enhanced Chemical Vapour Deposition
PMT	Photomultiplier Tube
PTFE	PolyTetraFluoroEthylene
r.f.	radio frequency
RDT	Ring Down Time
RGA	Residual Gas Analysis
S/N	Signal/Noise
SEERS	Self Excited Electron Resonance Spectroscopy
SFG	Sum Frequency Generation
SHG	Second Harmonic Generation
TEM	Transverse Electromagnetic Mode
UAS	Unmodulated Absorption Spectroscopy
UV	UltraViolet
VUV	Vacuum UltraViolet
XAL	Xenon Arc Lamp

Table of Contents

Chapter 4 – Detection of the Hydroxyl Radical

Chapter 5 – Detection of the N_2^+ Ion

Chapter 1

Introduction

This Thesis describes the application of several diagnostic methods to gas phase plasmas. In this Chapter, plasmas and plasma diagnostics are introduced and diode lasers, one of the radiation sources used in this Thesis, are discussed. Chapter 2 describes the plasma production systems investigated, including some electrical measurements made on these. Chapters 3 to 5 describe the results of other investigations using optical methods including frequency modulation spectroscopy, laser induced fluorescence and cavity ring down spectroscopy.

1.1 Introduction to Plasmas

A plasma consists of a partially ionised gas, which overall is electrically neutral, containing electrons and ions along with neutral species such as atoms, molecules and radicals. A plasma can be distinguished from other partially ionised gas systems (such as the Earth's atmosphere) because the motion of the particles is dominated by electrostatic forces and not simply determined by randomising collisions.

Plasmas occur in nature when there is a naturally occurring ionisation mechanism. For example, during a lightning strike, ions and electrons are produced by a current flowing through the atmosphere. However, when this current ceases they recombine and the ionisation is lost. Plasmas will only naturally exist in a steady state if the rate of ion-electron recombination is low, for instance where electron and ion densities are low. An example of this is the very low density gas system that constitutes the majority of the our solar system. In this interplanetary space, ion-electron pairs are produced by ionisation by high energy radiation. Recombination happens infrequently because the concentration of charged species is very small (≤ 1 cm^{-3})[1].

To produce a plasma it is necessary to ionise a gas system. This requires energy, which is normally supplied by an electrical current flowing across an applied potential difference which is either fixed (d.c.) or varying (a.c.), hence the name electrical gas discharge. The mechanisms of plasma formation are discussed in more detail in Chapter 2. The ionisation products are removed by recombination, either in the gas phase or on the walls of the vessel containing the plasma. Power is primarily lost by heat loss to the surroundings, but also by

optical emission that is produced within the plasma. Therefore, to maintain the plasma, power must be continuously applied. This can be achieved by using the same field that initiated the discharge to induce either direct or alternating currents. If a.c. is used (as found in most laboratory systems), the frequency must be above 1 MHz to maintain near continuous discharge[2], otherwise the charge is neutralised (on the timescale of the period of the applied a.c. potential) and the plasma extinguished while the electrodes exchange polarities.

1.2 Applications of Plasmas

The use of plasmas is very wide spread, the most commonly observed example being the fluorescent lamp. Plasmas are also important in industrial processing systems that have found uses in the aerospace, automotive, steel, biomedical, toxic waste management and, most importantly, the electronics industries. Below, a brief summary of some of the more common and diverse applications is given.

Surface treatment involves the use of chemically reactive plasmas to modify the surface of a material to improve its working properties. Examples include ion-nitriding[3] in a nitrogen plasma to harden vehicle crankshafts, machine tools and titanium alloy[4] which is used for artificial hip joints. This is found to improve the wear resistance of the materials, greatly extending their working lifetimes.

Other surface treatments include deposition and removal of material from the surface. Layer deposition is routinely completed within plasma reactors. This may be one step of many in the production sequence of an integrated circuit (IC), the deposition of artificial diamond onto a tool to harden it or the production of an amorphous silicon film during solar cell manufacture. The deposition process is described as plasma-enhanced chemical vapour deposition (PECVD) and an example regularly used in the semiconductor industry is the $Si(OC_2H_5)_4/O_2$ plasma[1] that deposits SiO_2, which is used as an insulating film (see Figure 1.9; a schematic of the layer structure of a diode laser). A second method of plasma deposition is the sputtering process in which the substrate is placed within a discharge that bombards a target material, sputtering particles from the surface into the plasma and depositing these onto the substrate. An example of this is the coating of stainless steel with TiN for enhanced wear applications[5].

Plasma etching is also an essential part in the IC manufacturing process. Previously, etching was achieved using a wet etch system such as NH_4F/HF. These wet systems are difficult to

handle, leave unetched areas due to bubble formation, form ragged edges and produce an isotropic etch[6] (Figure 1.1).

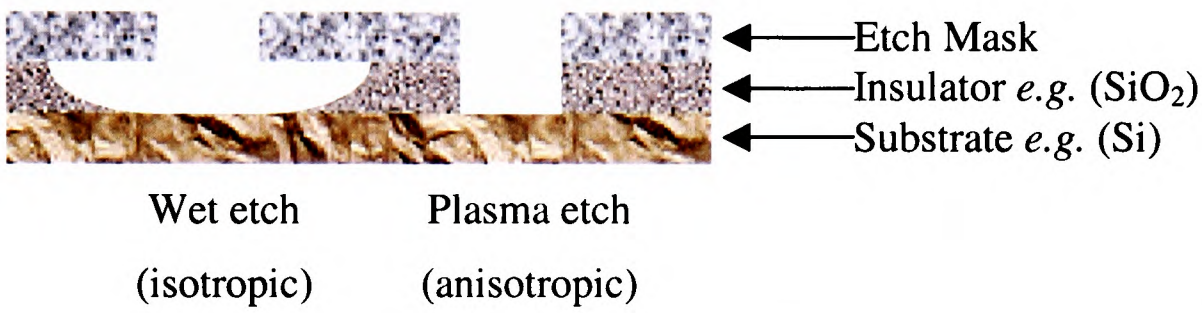

Figure 1.1 Cross section of the features produced by wet chemical etching and reactive ion etching.

The plasma reactive ion etch system produces an anisotropic etch, because the majority of the velocity of the ions responsible for the etching process in the plasma is in the component perpendicular to the surface and therefore the majority of the material that is removed is not from directly under the mask. This process has enabled 200 nm wide, 4 μm deep trenches to be etched into silicon[1]. The anisotropic etch allows components to be closer together on the IC due to negligible lateral etching, creating greater component density and hence enabling smaller and faster semiconductor devices to be produced. The mask can also be removed by plasma etching, for instance a photoresist is generally removed in an oxygen discharge[1].

Because of the temperatures attainable and the reactivity of plasmas, they have been extensively used to destroy toxic and hazardous waste. This method, first patented in 1973[7], is now a common commercial process for destroying materials as diverse as pollutants in exhaust gases, CFCs, medical waste and contaminated soils. Less reactive plasmas have been used to clean surfaces, for example, those of medical instruments[8].

Plasmas are also used for maintaining satellites' positions[9]. The momentum given to an ionised heavy inert gas (*e.g.* xenon) as it is accelerated away from the thrusters by an electric field causes the spacecraft equipped with the plasma thrusters to move in the opposite direction.

1.3 Plasma Parameters

The properties of a plasma depend on the physical conditions under which it is maintained and these are discussed in the following section. However, the intrinsic processing properties are described by parameters such as temperature and charge density. These are essential for understanding the plasma's properties and some examples are given in Sections 1.3.2 to 1.3.6.

1.3.1 Applied Parameters

The properties of a plasma depend on the electrical power dissipated within the plasma, the pressure at which it is generated and the gas from which the plasma is formed (feedgas). The physical size of the discharge is also important in determining the properties of the discharge and for cylindrical systems, an aspect ratio[10] (radius/length) and a volume have been used to describe the geometry of the discharge. The gas flow rate through the discharge has also been shown to have an effect on the processing properties of the plasma[11]. A final significant parameter is the actual method of plasma production; this can have a large effect on the plasma properties. The methods of production of the plasmas investigated in this Thesis are described in Chapter 2.

1.3.2 Plasma Density and Ion Flux

The plasma density (also referred to as the charge density), n, is the concentration of negative charge within the plasma. In a plasma where the only ions present are positive and singly charged, this is equal to the ion density, n_i. This gives directly the fractional ionisation, $x_i = n_i/(n_g + n_i)$, where n_g is the neutral gas density. For the plasmas investigated in this Thesis x_i is of the order of 10^{-6}.

The ion flux within the plasma is the number of ions per unit area per unit time that arrive at a surface in the plasma. This will obviously depend on the potential of that surface and, for an inhomogeneous plasma, the position of the surface within the plasma. By convention, the ion flux is taken to be that observed when the object is biased negatively and therefore no positive ions are repelled from the object. The ion flux is discussed in more detail in Section 2.4.2.

1.3.3 Potentials

If all the components of the plasma are considered to be in thermal equilibrium then the electrons move considerably faster than the heavier ions. If an uncharged and electrically isolated object is placed in the plasma, the electron flux arriving at the object will be greater than the ion flux and hence the object will become negatively charged. This negative charge will increase until the potential difference between itself and the plasma is high enough to repel sufficient electrons, such that the electron and ion fluxes are equal. The object has therefore acquired a negative potential, V_f, with respect to the bulk that is at the plasma potential, V_P, which has been raised (usually slightly) by the loss of negative charge to the object. The

difference between the plasma potential and the objects' 'floating potential', V_f, is given by the following expression[2]:

$$V_P - V_f = \frac{kT_e}{2e} \ln\left(\frac{m_i}{2.3m_e}\right) \tag{1.1}$$

where T_e is the electron temperature (discussed in the following section), e is the electronic charge and m_e and m_i are the electron and mean ion masses respectively. The object will reach V_f independently of its initial charge. The difference in potential between the plasma and the object causes a sheath to form; this is a thin region between the plasma and the object, in which the charged species have rearranged themselves so that the bulk of the plasma is screened from the objects' potential. To achieve this, the sheath is electron deficient in comparison to the bulk (which is neutral overall). In the sheath, the ions are accelerated towards the object because of its negative potential and therefore, as they are moving faster to keep the flux through the sheath constant, their density must decrease. The sheath is observed to produce less optical emission than the bulk, and this can be explained by the lower electron and ion concentrations in the sheath compared to the bulk. This results in fewer collisions and therefore fewer electronically excited species (responsible for the optical emission) are formed. Figure 1.2 shows the variation of potential between the object and the bulk, along with the relative ion and electron densities. The presheath region is discussed further in Section 2.4.2. Sheaths form around the plasma where it comes into contact with any object, including the fabric of the vessel containing it and the electrode or electrodes driving it. The potential difference between a grounded object, such as a metallic wall, and the plasma is given by the plasma potential. The potential difference between the plasma and the driving electrode can be in excess of an order of magnitude higher than this for a.c. coupled reactors, such as the capacitively coupled system described in Chapter 2. In the case of an a.c. coupled reactor, this is due to the ratio of the areas of the driven and grounded material, because the current flowing to the driven electrode must be equal and opposite to that flowing to ground. Because there is generally a larger area in the plasma which is grounded compared to that which is driven, a larger potential difference between the plasma bulk and the driven electrode, compared to the grounded sheath potential difference, is required to equalise the currents at each electrode.

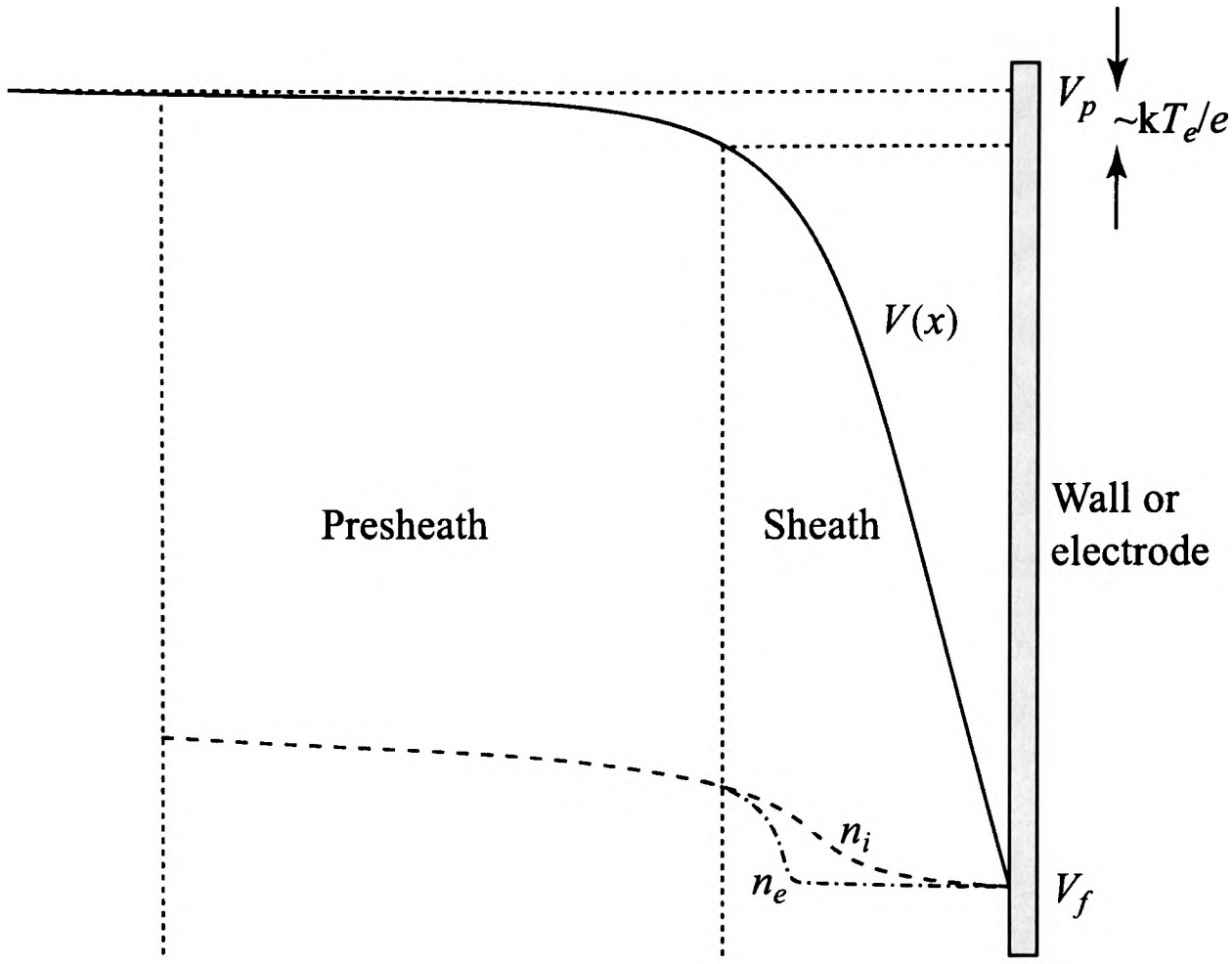

Figure 1.2 A schematic representation of the spatial dependence of the potential $V(x)$, ion density n_i and electron density n_e in the planar sheath and presheath regions adjacent to a disturbing object in the plasma.

1.3.4 Temperature

In electrically generated r.f. plasmas, the electrons, ions and neutrals are almost never in thermal equilibrium[1] *i.e.* their translational temperatures are not equal. This is due to two effects:

- Firstly, the considerably lower mass of electrons compared to ions results in them responding much more swiftly to the changes in potential in the plasma, such as those caused by the r.f. power dissipated into the discharge. It is possible, from the following expressions, to calculate a plasma frequency for both the electrons (ω_e) and the ions (ω_i)[1]:

$$\omega_e = \sqrt{\frac{e^2 n}{\varepsilon_0 m_e}} \tag{1.2}$$

$$\omega_i = \sqrt{\frac{(Ze)^2 n}{\varepsilon_0 m_i}} \tag{1.3}$$

where e is again the electronic charge, ε_0 is the permittivity of free space and Z is the number of units of charge on the ion. These describe the maximum frequency of a

sinusoidally varying electric field which each species will respond to. For the r.f. discharge systems described in Chapter 2, $\omega_e/2\pi$ and $\omega_i/2\pi$ are estimated to be about 1 GHz and 3 MHz respectively. Therefore, only the electrons can efficiently follow the 13.56 MHz modulation of the electric fields supplying the energy to the plasma, and so attain a higher proportion of the applied energy and as a result have a higher average energy.

- Secondly, even if the applied electric fields increase the energy of the electrons and the ions equally, the electron temperature would still be greater than the ion and neutral temperatures because the heavy ions transfer energy efficiently with the similar mass neutrals and ions during collisions. Conversely, much lighter electrons transfer energy inefficiently to these heavier species.

These result in the average energy possessed by electrons in the plasma being greater than that possessed by the more massive species. Although the electrons in a plasma are generally not in complete thermal equilibrium[1], the electron energy distribution is commonly modelled as a Maxwell-Boltzmann distribution[2].

$$f(v) = n\left(\frac{m_e}{2\pi k T_e}\right)^{\frac{3}{2}} \mathrm{e}^{-\left(\frac{m_e v^2}{2kT_e}\right)} \tag{1.4}$$

A graphical example of the distribution is given in Figure 3.21. This model is convenient because the distribution is controlled by one variable parameter, the electron temperature T_e, which is related to the mean speed of the electrons by the following expression[12]:

$$\bar{c} = \sqrt{\frac{8kT_e}{\pi m_e}} \tag{1.5}$$

The plasma is heated by the motion of the electrons in the sheath, caused by the varying electric field applied to the electrode. The two main effects that contribute to the plasma acquiring energy from the applied power are Ohmic and Stochastic heating[1], both of which involve electron 'collisions'. Ohmic heating occurs when the electrons accelerated within the oscillating electric field in the sheath collide with and transfer momentum (and hence energy) to the neutral species in the sheath. Stochastic heating occurs when the electrons 'collide' with, and are reflected by, the large decelerating field of the oscillating high-voltage sheath at the driven electrode and therefore take energy from the moving field and deposit it into the plasma.

1.3.5 Debye Length

The screening of the bulk of the plasma discussed in Section 1.3.3 is known as Debye shielding. This effect is quantified by the Debye length[1], λ_{De}, which is the distance scale over which significant separated charge densities can spontaneously exist.

$$\lambda_{De} = \sqrt{\frac{kT_e\varepsilon_0}{ne^2}} \tag{1.6}$$

Within a single Debye length a perturbation of the potential in the plasma is reduced to $^1/_e$ of its initial value. Therefore, on space scales larger than a Debye length the plasma will tend to remain electrically neutral. The sheaths within the plasma are typically a few Debye lengths wide. A useful way of regarding the Debye length is the approximate radius of a sphere, within which the net interaction of the charged particles is observed to be zero by a particular charged particle at the centre of the sphere.

1.3.6 Mean Free Path and Conductivity

The mean free path λ_{mfp} of a particle is the mean distance the particle travels between successive collisions. It is given by[1]

$$\lambda_{mfp} = \frac{1}{n_{tot}\sigma} \tag{1.7}$$

where n_{tot} is the total number of species, per unit volume, with which the particle can collide and σ is the collision cross section. If the mean speed of the particles is given by v, then the mean time between collisions, τ, is given by λ_{mfp}/v. This is directly related to the conductivity of the plasma, σ_p, for a particular singly charged species of mass m by the following expression.

$$\sigma_p = \frac{ne^2\tau}{m} = \frac{ne^2\lambda_{mfp}}{mv} \tag{1.8}$$

Therefore, a high number density in the plasma results in a short mean free path and hence low conductivity. Both the electrons and the ions contribute to the conductivity, however although the ions have the same number density, their increased mass reduces their contribution and most of the plasma current is therefore carried by the electrons.

1.4 Indirect Plasma Diagnostics by Surface Analysis

A pragmatic approach to plasma diagnostics has involved the use of surface analysis techniques, as most plasma uses involve surface modification. These can be split into two types of measurements; those that can be made during the process and those that are made after the surface modification is completed.

There are several methods regularly used during plasma processing that involve the observation of the optical properties of the material surface. These include spectroscopic reflectivity[13] and ellipsometry[14], both of which give measurements of surface layer thickness allowing information on deposition, etching and modification processes to be obtained in real time. The plasma process can also be followed in real time by using a quartz piezo-electric microbalance[15], which again measures the extent of deposition or etching at the surface.

To obtain more detailed information on the modified surface, the many techniques of the surface scientist's armoury can be applied to the substrate before and after the plasma process. This gives direct information on the surface structure and is a vast field in itself. A discussion of a selection of the techniques available to study the solid surface, and their application, is given by Woodruff and Delchar[16].

1.5 Direct Non-Optical Plasma Diagnostics

Although surface analysis techniques give information on the discharge, it is clear that the performance of the plasmas widely used for industrial processes depends on the intrinsic plasma parameters described in Section 1.3. It is therefore of crucial importance to be able to measure these plasma parameters. Plasma diagnostics are essential to determine the relationships between the applied parameters and the intrinsic plasma parameters. In the following sections, several direct non-optical diagnostics are described.

1.5.1 Electrostatic Probes

This method is the oldest and probably the simplest method of measuring the properties of a plasma. The current-voltage characteristic of a metallic probe was first used as a plasma diagnostic in the 1920s by Langmuir and co-workers[17], a technique now known as the Langmuir probe diagnostic method. The probe is mounted in a given position in the plasma, and the current is then measured as the probe is biased to different voltages relative to a large conducting surface, also in contact with the plasma. The observed current depends on the

probe bias voltage and on the difference in the ion and electron fluxes. An example of a current-voltage characteristic is given in Figure 1.3.

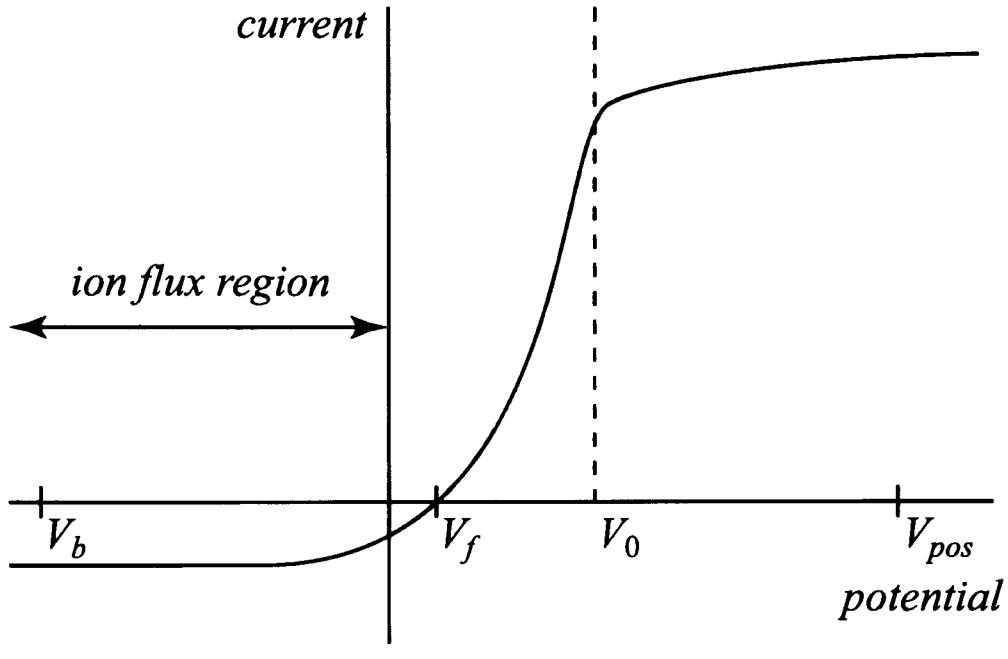

Figure 1.3 Current-voltage characteristic of a plasma probe.

The current-voltage characteristic allows direct measurement of the electron temperature, plasma potential, floating potential and ion and electron fluxes through the probe sheath[6].

In an r.f. plasma, the probe current depends on the applied r.f. potential. This effect can be removed by various methods. One possibility is to record the current using a circuit containing an r.f. blocking filter[18]. A second method is to superimpose an r.f. bias onto the probe d.c. bias at the same frequency as the plasma drive frequency. In some cases, these 'driven' probes have been found to be more effective than those using r.f. filters[19].

Two probe geometries are commonly used, the Langmuir (cylindrical) probe and the planar probe. The Langmuir geometry consists of a metallic small diameter ($\approx$ 1 mm) cylinder with an insulating shield around it almost up to the tip. Around this tip, a sheath forms and therefore the plasma is perturbed. The method of calculation of ion densities from probe characteristics is given in Chapter 2 and involves measuring the electron temperature and ion flux. With a Langmuir probe the flux observed is that crossing the bulk-sheath boundary and therefore to calculate the ion density, the surface area of this boundary is required, making quantitative analysis difficult.

The planar probe[20] is a two-dimensional measurement plate. A guard ring can be incorporated to overcome the disadvantages of the Langmuir geometry. The flux recorded is independent of sheath thickness and hence of the probe potential because the bulk-sheath area that the probe interrogates remains constant as the sheath thickness varies. This ensures consistent analysis

of the plasma's current-voltage characteristic. However, because the probe must be placed on a surface already present in the vessel containing the plasma, spatial measurements are not possible across the bulk of the plasma. If the current flowing into the probe is recorded with time while it is held with a low (50 Ω) impedance to ground, a self excited electron resonance spectroscopy (SEERS) signal can be obtained by comparison of the probe voltage to that applied to the plasma. Analysis yields the mean electron density, mean electron energy and the plasma potential.

With either probe geometry, considerable care must be exercised when interpreting results for plasmas used in material processing, especially those that deposit material onto surfaces. Such deposition can result in an insulating layer forming on the probe, greatly affecting the observed current-voltage characteristic[21].

A more complete discussion of the experimental method, theory and results of an experiment using a planar electrostatic probe are given in Chapter 2.

1.5.2 Mass Spectrometry

A second commonly used non-optical method is mass spectrometry. This technique involves collecting the species that effuse through a small hole in the vessel containing the plasma, (usually in an electrode or chamber wall), and then analysing these species by mass and sometimes also by energy.

This technique generally cannot be used to measure the spatial distribution of species within the plasma because it is difficult to pinpoint the exact volume from which the species entering the spectrometer originated. The standard mass spectrometer allows the identification of the species that are present in the plasma which have a sufficient lifetime to be sampled, including both neutral species and ions. Neutral species that enter the mass spectrometer through the sampling orifice are then ionised, separated by mass and detected. This is called residual gas analysis (RGA) and allows the measurement of the relative concentration of the species present in the plasma[22].

The ions entering the mass spectrometer will have an anisotropic velocity distribution, because a sheath must form between the plasma and sampling orifice. By using an electrostatic ion energy analyser, the kinetic energy distribution of mass-selected plasma ions has been obtained[23]. This information is of considerable interest because if the sampling orifice is in the electrode onto which the substrate would be placed, the ion energy distribution observed is that

impinging on the substrate. It has been shown that the surface processing properties of plasmas depend critically on the ions present[15].

1.6 Direct Optical Plasma Diagnostics

Although a considerable amount of information about plasmas can be obtained from the methods discussed above, these generally involve some perturbation of the plasma. Optical methods involving the absorption and emission of radiation generally perturb the plasma to a much smaller degree. The following section gives a summary of some of the interactions of radiation with species possessing discrete energy levels and in subsequent sections several optical methods are discussed.

1.6.1 Absorption and Emission of Radiation

To understand the interaction of radiation and matter with discrete energy levels, it is necessary to consider two specific energy levels of the system; an upper level L_2, and a lower level L_1 separated by an energy E. These two levels can be linked by a transition involving emission and absorption of radiation. There are three possibilities for a transition between L_2 and L_1; absorption, stimulated emission and spontaneous emission, as shown in Figure 1.4.

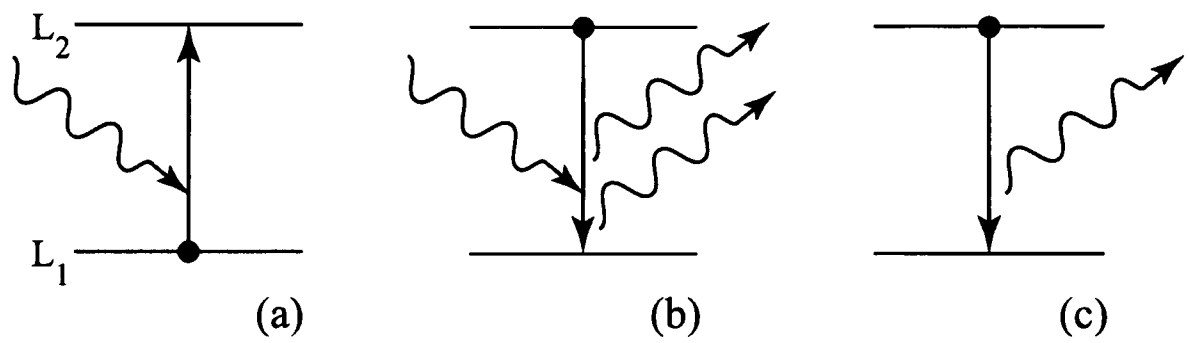

Figure 1.4 Schematic diagram of the interaction of a two level system with a radiation field: (a) absorption, (b) stimulated emission and (c) spontaneous emission.

Absorption occurs when a photon of frequency ν, such that $E = h\nu$, is absorbed by a species in level L_1 promoting the system from L_1 to L_2. This process is described as induced absorption and the probability per second of this occurring, dP_{12}/dt, is proportional to the spectral energy density $\rho(\nu)$ of the radiation field at frequency ν. The rate of absorption is then given by

$$\frac{dP_{12}}{dt} = B_{12}\rho(\nu) \tag{1.9}$$

where the constant of proportionality, B_{12}, is called the Einstein coefficient of induced absorption.

A photon of frequency v can also cause the system initially in L_2 to fall into L_1, simultaneously emitting a photon of frequency v. This process is called stimulated emission and is also proportional to $\rho(v)$; its rate is given by

$$\frac{\mathrm{d}P_{21}}{\mathrm{d}t} = B_{21}\rho(v) \tag{1.10}$$

where B_{21} is the Einstein coefficient of induced emission.

Spontaneous emission is a random event in which the system again relaxes from L_2 into L_1, converting its energy into an emitted photon of frequency v. The rate of spontaneous emission is independent of the radiation field density and is given by

$$\frac{\mathrm{d}P_{21}^{spont}}{\mathrm{d}t} = A_{21} \tag{1.11}$$

where A_{21} is the Einstein coefficient of spontaneous emission.

At thermal equilibrium the population distribution, amongst all i levels each of energy E_i, is given by the Boltzmann distribution

$$N_i = N\frac{g_i}{Z}\mathrm{e}^{-\frac{E_i}{kT}} \tag{1.12}$$

where N is the total number of levels available to the system, g_i is the degeneracy of the i^{th} level and Z is the partition function of the system, which normalises the expression so that $\sum_i N_i = N$. If the radiation field and the medium are in equilibrium, the total radiation field density will not change and therefore the rate of absorption and emission are equal and so

$$(B_{21}\rho(v) + A_{21})N_2 = B_{12}N_1\rho(v) \tag{1.13}$$

Using the Boltzmann distribution for the populations of the two levels, it is possible to obtain an expression for the spectral energy density.

$$\rho(v) = \frac{\frac{A_{12}}{B_{21}}}{\frac{g_1}{g_2}\frac{B_{12}}{B_{21}}\mathrm{e}^{-\frac{E_i}{kT}} - 1} \tag{1.14}$$

This can be compared with Planck's radiation law[24]

$$\rho(\nu)\,\mathrm{d}\nu = \frac{8\pi\nu^2}{c^3}\frac{\mathrm{h}\nu}{\mathrm{e}^{-\frac{h\nu}{kT}}-1}\mathrm{d}\nu \tag{1.15}$$

resulting in

$$B_{12} = \frac{g_1}{g_2}B_{21} \tag{1.16}$$

and

$$A_{21} = \frac{8\pi h\nu^3}{c^3}B_{21} \tag{1.17}$$

Equation (1.16) shows that, in a given radiation field, the Einstein coefficient of stimulated emission is equal to that of induced absorption when $g_1 = g_2$. Equation (1.17) gives the ratio of A_{21}/B_{21} to be proportional to ν^3. Therefore, spontaneous emission rates increase relative to stimulated emission rates at short wavelengths.

1.6.2 Plasma Induced Optical Emission

The direct observation of the intensity and spectral properties of the plasma induced spontaneous optical emission (OE) is a commonly used and completely non-invasive diagnostic. The radiation is produced by excited species, which are formed in the plasma by collisional processes including electron impact and ion-electron recombination, relaxing to a lower energy level, emitting radiation isotropically. The optical emission that has been observed from a plasma ranges from the vacuum ultraviolet[25] to the mid-infrared[26]. By careful use of collection optics, it is possible to obtain information about the spatial variations of the emission within the plasma[27].

By the use of narrow spectral resolution, it is possible to observe the emission signal from a particular transition of a species within the plasma. This enables the end point observation, of an etching process, by detection of a particular product.

The translational temperature of both neutral and ionic excited state species has been deduced from Doppler-resolved spectra obtained using a high-resolution monochromator[28]. Study of the widths of the emission lineshape can give information on the production mechanism of the excited state. In a low temperature plasma, if the line shape of a neutral species is indicative of a thermal velocity distribution, then the species was probably produced by direct excitation of the ground state species. However, if the profile is greatly Doppler broadened, then the excited

state may have been formed by dissociative excitation or recombination. This broadening has been observed in the atomic emission lines of Cl^* and Ar^* in the sheath of a Cl_2/Ar plasma[29].

The rotational and vibrational 'temperatures' can also be obtained for molecular species[30] from the optical emission spectrum because the intensity of emission from a particular energy level is proportional to its population. The rotational temperature of species in the plasma is often assumed to be a good measure of the translational temperature of the ground state neutral species that make up most of the plasma[31].

The excited state 'temperature' one dimensional spatial profile has been obtained by a single measurement using the detection of spectrally dispersed OE with a two dimensional CCD array[32].

A different optical method for measuring the 'temperature' of a plasma is pyrometery. This involves observing the infrared emission from a surface in contact with the plasma, such as the nozzle of a plasma torch, and calculating the temperature assuming the surface is producing a black body emission spectrum[33].

Because the intensity of emission depends on the excitation rate, which in turn depends on the electron energy distribution (electron temperature) and electron concentration, it is possible to obtain estimates of changes in these properties by OE[34]. By comparing the optical emission from two species with significantly different electron energy dependent excitation cross sections (for example Ar^* and He^*, which have well known different electron energy dependent excitation cross sections and thresholds), it is possible to obtain information concerning the electron energy distribution function[35].

Stark splitting of atomic or molecular energy levels can be observed by the consequent shift in observed OE transition frequencies. This enables the electric field strength to be obtained from the magnitude of the shift[36]. The electron density within the plasma can also be obtained by the Stark broadening of optical emission lines[37].

Time resolved optical emission can be used to study the chemical kinetics of many reactive species, by observing the emission as a function of time after igniting or extinguishing the plasma. These measurements enable the production and loss rates of particular species to be obtained, and therefore important reaction scheme information may be elucidated[38]. Fourier transform infrared emission spectroscopy has also been used to detect both feedstock and product molecules and to monitor their kinetics[30].

OE only directly gives information about the excited state properties *e.g.* absolute and relative concentrations and effective vibrational, rotational and translational 'temperatures'. However, actinometric optical emission (AOE) can be used to determine relative ground state concentrations from the optical emission produced by the plasma, normalised for changes in the electrical properties of the discharge. AOE relies on the assumption that the major route for excitation of the emitting species is *via* electron impact excitation from the ground state and that the excited species decay exclusively by emission. If this assumption is valid, then by introducing a known concentration of a suitable 'actinometer' gas (one with a similar excitation threshold and electron energy dependent cross section for electron impact) and comparing its emission to the species of interest, it is possible to remove the effect of changes in the electron energy distribution and concentration in the emission intensity[39]. Therefore, it is possible to obtain the relative concentration of the ground state of the species of interest as the applied discharge parameters are varied. There are, however, several cases in which erroneous results can arise from AOE measurements[40], generally due to the failure of the assumption that the excited state is only formed by direct electron impact. In addition, considerable care must be taken in choosing the 'actinometer' gas to minimise perturbation of the plasma.

Time resolved AOE has been used, in a similar way to OE, to study the chemical kinetics within a plasma. This has been achieved by recording AOE signals as the plasma is ignited at varying time delays after extinction and comparing the concentrations observed to those under the steady state plasma condition[40].

1.6.3 Absorption Spectroscopy

Unlike emission, absorption of radiation directly gives information on the lower state of the transition being interrogated. In principle, the absorption of radiation is the simplest method by which ground state species can be detected. All species that absorb radiation can be studied by this method, which readily provides the line of sight averaged number density, N/V, from quantitative values for the absorbance using the Beer-Lambert Law[24], providing that the absorption cross section, σ, at that particular frequency is known.

$$\frac{I_T}{I_0} = \mathrm{e}^{-\sigma l\left(\frac{N}{V}\right)} \tag{1.18}$$

I_T/I_0 is the ratio of the intensity of the radiation transmitted through the sample to that incident upon it and l is the optical path length over which the measurement is made. This law is only

valid if the number of photons absorbed is small, so that the population produced in the upper state is small. If this is the case, the ratio I_T/I_0 observed is independent of incident intensity. If the population in the upper state becomes significant, then optical saturation is observed (I_T/I_0 increases as the intensity is increased). The intensity at which this optical saturation occurs is dependent on the absorbing species. If the intensity or the cross section is very large, optical pumping occurs as species are cycled between the lower state and the upper state by alternate absorption and stimulated emission and thus the amount of radiation that would be expected to be absorbed is greatly reduced.

From equation (1.18), it can be seen that the measurement is very sensitive to variations in the intensity of the radiation source and therefore the signal to noise ratio observed in absorption experiments is normally significantly lower than the theoretical limit[41]. Therefore, either high densities of absorbing species or very long optical path lengths are required. The long path length can be achieved by the use of multi-pass mirrors within the chamber containing the plasma. It is not generally possible to mount the mirrors outside the chamber because of the optical losses associated with passing through the chamber windows. Hence, the mirrors must be placed inside the plasma chamber, and must be carefully selected so that the mirrors' reflectivities are not reduced by reaction with or deposition of species produced within the plasma. Cavity ring down spectroscopy (discussed in Section 1.6.4) is a modern method of greatly extending the path length in the plasma.

Direct absorption techniques, without the use of multi-pass mirrors, have generally concentrated on the detection of stable species within the plasma, such as constituents of the feedgas or stable reaction products, rather than chemically reactive transient species such as ions or free radicals, which occur in much lower concentrations. There are exceptions to this, either using atomic resonance lamps (which have a spectral output that closely matches the absorption profile) or continuum lamps to monitor ground state atom concentrations (see Section 3.2 for the example of argon). These sources can be extremely stable. Coupled with the generally large atomic absorption cross sections, this results in excellent sensitivity.

A further technique, until now not applied to plasmas, is frequency modulation spectroscopy, the subject of Chapter 3. This enables detection of small absorbances by encryption of the absorption information at radio frequencies greatly reducing the observed noise.

1.6.4 Cavity Ring Down Spectroscopy

Cavity ring down spectroscopy (CRDS) is a modern development in plasma diagnostics in comparison to those discussed previously. A high finesse cavity (see Section 1.7) consisting of two high reflectivity mirrors is constructed around the plasma chamber. A laser pulse is then introduced into the cavity and its time dependent intensity is monitored by the small fraction of light transmitted through one of the cavity mirrors. The advantages of CRDS over absorption spectroscopy are the extremely long effective path lengths that are possible and the fact that CRDS is based on the rate of absorption rather than its magnitude making it relatively insensitive to intensity fluctuations in the radiation source. It is a technique that, like absorption spectroscopy, enables detection of all species that absorb radiation providing high reflectivity mirrors can be obtained in the required wavelength range.

A pulse within an empty cavity, with mirrors of reflectivity R, decays exponentially with time, at a decay rate determined by the mirror reflectivities and any other losses, such as diffraction and scattering from the mirrors. The intensity transmitted through one of the mirrors, $I(t)$ is

$$I(t) = I_0 \mathrm{e}^{\left(\frac{t}{\tau}\right)} \tag{1.19}$$

where I_0 is the intensity at $t = 0$ and τ is the empty cavity ring down time (RDT). The RDT is the time taken for the intensity incident on the detector to fall to $^1/_e$ of I_0 and is given by[42]

$$\tau = \frac{l}{c\left|\ln R\right|} \approx \frac{l}{c(1-R)} \tag{1.20}$$

where l is the separation of the mirrors and c is the speed of light. The average number of round trips that a radiation pulse makes within the cavity is obtained by solving the equation

$$R^{2N} = \frac{1}{\mathrm{e}} \tag{1.21}$$

When the frequency of the laser pulse matches that of an absorption feature of a species in the plasma an additional loss mechanism is introduced and the RDT decreases. Assuming the absorption can be described by the Beer-Lambert Law, the radiation intensity decay will still have an exponential dependence and equation (1.19) is modified to

$$I(t) = I_0 \mathrm{e}^{-\left(\frac{1}{\tau}+\alpha c\right)t} = I_0 \mathrm{e}^{\left(\frac{t}{\tau'}\right)} \tag{1.22}$$

where ct is the path length $L = 2Nl$ over which the absorption is measured and α is the product of the absorption cross section and the concentration. The decay rate is given by $^1/_{\tau'} = {}^1/_{\tau} + \alpha c$. If the empty cavity RDT, τ, is known, measurement of $^1/_{\tau'}$ as the laser frequency is scanned enables a cavity ring down absorption spectrum to be obtained. Over the range of most scans, the reflectivity of the mirrors varies little with laser frequency so that $^1/_{\tau}$ appears as an offset from the baseline level (where $\alpha = 0$ between absorption features).

This analysis relies on the decay of radiation intensity incident upon the detector being exactly exponential, requiring certain conditions to hold. The Beer-Lambert law requires that the width of the absorption feature is significantly greater than the laser linewidth within the cavity so that all the laser frequencies within the cavity are attenuated by the same amount. This only occurs if the pulse duration is greater than the lifetime of the upper state being probed[43]. The cavity mode structure also affects the observed intensity decay (for a discussion of cavity modes see Section 1.7). The frequency spacing of the cavity longitudinal modes must be such that radiation of the appropriate frequency, coincident with the absorption profile of the species of interest, is coupled into the cavity[44]. If the laser bandwidth is narrower than the cavity Free Spectral Range (FSR), then the detector will observe a series of cavity transmission peaks as the laser is scanned. As well as the longitudinal modes, the transverse modes of the cavity can also have an effect on the observed decay. If the radiation is not carefully matched to the lowest order transverse mode, TEM_{00} (achieved by controlling the size and divergence of the input beam and/or placing apertures inside the cavity), or not injected perfectly along the cavity axis, several transverse modes will be excited. The result of exciting several cavity modes, which have different losses within the cavity, is to generate a multiple exponential intensity decay. The result of this is that the observed intensity at the detector is modulated due to the beating between different modes excited in the cavity[45]. Generally, this modulation is much faster than the decay time of the exponential. In practice, the restriction imposed by the longitudinal mode structure of the cavity is relaxed by the transverse mode structure and cavity instabilities so that the frequencies supported by the cavity are essentially continuous.

The limit of the precision to which an RDT can be determined by CRDS corresponds to the time interval of one cavity round trip ($t_r = 2l/c$), the smallest possible detectable change in the RDT. This round trip time can be translated into a minimum detectable absorbance as follows. The fractional loss of intensity per pass through the cavity, δl, is given by

$$\delta I = \frac{I_0 - I}{I_0} \approx \alpha l \approx (1 - R)\frac{\Delta\tau}{\tau} \tag{1.23}$$

for small absorbances in a single pass ($\alpha l << 1$) and where $\Delta\tau$, the change in the RDT when the laser frequency is coincident with an absorption feature, is small.

$$\Delta\tau = \tau' - \tau \tag{1.24}$$

Hence, the minimum detectable fractional absorption per pass, commonly used to quantify the detection limit of CRDS[46], is given by equation (1.25).

$$\delta I_{\min} \approx (1 - R)\frac{t_r}{\tau} = (1 - R)\frac{1}{N} \tag{1.25}$$

From this expression, it is apparent that the greater the number of round trips (the longer the RDT), the greater the sensitivity. However, if the mirror reflectivity is very high, the observed signal on the detector is greatly reduced and therefore uncertainties will be introduced into the RDT measurement by the low signal to noise of the observed decay.

The standard source for CRDS is a high power pulsed laser[44]. The broad frequency bandwidth of such laser sources ensures that some radiation is always coupled into the cavity but limits the spectral resolution of such experiments. The data acquisition rate is limited by the pulse rate and the sensitivity by the inherent trade off between mirror reflectivity and detected intensity. This has been overcome by 'pulse stacking'[47], although this technique has not yet been used as a plasma diagnostic.

Continuous wave lasers have also been used for CRDS[48]. The major difficulty with this method is achieving regular and reproducible overlap between a cavity longitudinal mode and the laser output. If this can be achieved, the noise on the decay trace due to different modes is eliminated, and a large intensity builds up in the cavity; its throughput is only limited by the ratio of the cavity bandwidth to that of the laser. To complete a CRDS experiment, the laser is switched off using an acousto-optic modulator (AOM), allowing high repetition rates. The spectral resolution of this type of experiment is limited only by the bandwidth of the cavity, generally at least three orders of magnitude lower than the bandwidth of a pulsed laser.

Integrated cavity methods using either pulsed or continuous wave lasers have also been developed, such as integrated cavity output spectroscopy (ICOS)[49] and cavity enhanced absorption spectroscopy (CEAS)[50], in which the changes in the continuous wave transmission of the cavity is observed with laser frequency. This can be with or without rapid simultaneous

modulation of the laser frequency or cavity length. However, these methods are still sensitive to variations in the laser intensity as with absorption spectroscopy, but because the path length can be greatly increased this problem is reduced by the increased absorbance. Again, these recent developments have not yet been used for plasma diagnostics.

Although CRDS is a relatively recent addition to plasma diagnostics, this technique has been used to detect CF_x and SiF_x in etching plasmas[51] and negative ions (O^- and H^-) and powder particles in industrial r.f. plasma reactors[52], as well as other radical species in flames[53] and the methyl radical concentration profile in a hot filament (diamond deposition) reactor[54].

1.6.5 Laser Induced Fluorescence

Laser Induced Fluorescence (LIF) involves promoting a species into an excited electronic state by the absorption of laser radiation and then observing its subsequent fluorescence, at either the excitation frequency or some other frequency. Therefore, this technique relies not only on the species absorbing light but also that the excited state has a reasonable fluorescence quantum yield[55]. Thus, although direct absorption of tunable narrow bandwidth laser radiation is generally less sensitive than LIF, it enables detection of all species that absorb radiation. Using LIF, only a subset of these species can be observed. Species that dissociate or are ionised on absorption of radiation cannot be observed by LIF. In addition quenching will compete with fluorescence. Hence the fluorescence may be reduced to below detectable limits in high pressure systems, because of the high collision rates, or if the upper state is very long lived. Very few species with more than three atoms have been successfully studied using LIF because of the many possible fates of the excited state other than fluorescence.

The small bandwidth of the laser and spectrally filtered fluorescence mean that the possibility of ambiguous detection is negligible. If the fluorescence is collected at right angles to the direction of propagation of the laser, LIF is in theory a zero background technique. However the plasma will generally produce species in the upper state of the LIF transition and therefore even with very narrow spectral filtering and careful temporal and spatial filtering, the unwanted emission from this state will give rise to a noisy background and this limits the sensitivity to *ca.* 10^8 cm^{-3} for diatomic species in processing plasmas[41]. LIF has been shown to be sufficiently sensitive to detect the change in products while etching different semiconductor layers and this makes it a useful method of detecting the end-point of an etching process[56].

The detection region from which LIF is collected is defined by the intersection of the collection volume of the imaging optics and the laser beam. Therefore, excellent three-dimensional spatial resolution is possible.

Two or more photon LIF is used to monitor, in particular, atomic radicals such as oxygen[57] and chlorine[58], whose first excited states are inaccessible through conventional LIF without the use of very specialised VUV lasers.

The LIF signal depends on the population of the upper state generated by the laser pulse, the fluorescence quantum yield and the collection efficiency of the detection system. However, similarly to absorption spectroscopy, saturation and optical pumping can occur if high laser intensities are used. Therefore, only at low laser intensities does the LIF signal depend linearly on the laser intensity. A complete discussion of saturation effects in LIF is given in a review of laser induced fluorescence diagnostics in plasmas[55].

If care is taken so that saturation is avoided, LIF enables relative ground state concentrations to be measured, because the signal observed depends on the number of photons absorbed by the species. Unlike absorption methods, the absolute concentration cannot be obtained directly. However, by using the relative fluorescence intensities observed from exciting individual rotational vibrational electronic transitions of a polyatomic species, it is possible to obtain directly the rotation and vibration distributions of that species and therefore its rotational and vibrational 'temperatures'[55].

Tunable lasers with narrow bandwidths have been used to record the velocity distribution of species by sub-Doppler LIF[59]. This method, along with the spatial resolution, allowed the velocity profile of N_2^+ ions to be measured at 2 mm intervals through the sheath of capacitively produced plasma. These profiles directly give information on the electric fields present in the plasma sheath. The spatially resolved electric field strength has also been measured by the observation of Stark mixing, enabling observation of transitions forbidden in the absence of the electric field[60].

Time resolved LIF has been used (in a similar way to OE) to obtain the time dependence of species after extinction of the plasma[30]. This enabled an absolute concentration of N_2^+ to be obtained from a kinetic model. Hence, the LIF signal is then calibrated, enabling direct measurement of this species' absolute concentration within the plasma. Alternatively, it has been possible to calibrate the detection efficiency of LIF by detecting the products of a well-understood photolysis experiment with the same LIF collection apparatus[61], or by using a

stable species which also undergoes LIF: NO has been used to calibrate both CF and CF_2 LIF signals[62].

A related method, amplified spontaneous emission (ASE), has also been used to study plasmas[57]. In this technique, oxygen atoms were excited by the two (226 nm) photon step mentioned previously and the fluorescence at about 845 nm was observed along the laser axis. This technique produces linewidths narrower than the Doppler width of oxygen atoms at room temperature allowing the upper state (^3P) spin orbit splitting, unresolved by LIF, to be clearly observed.

1.6.6 Other Optical Techniques

Laser Optogalvanic Spectroscopy (LOGS) involves measuring the electrical characteristics of the discharge (current, impedance etc.) as a laser is scanned across the absorption spectrum of a species present within the plasma. Unlike absorption methods, only the species which produce a change in the discharge when they absorb radiation can be detected by this method, and clearly this necessarily perturbs the discharge. A review of this diagnostic is given by Reddy[63]. The laser induced changes in the electrical characteristics of the discharge are due to generation of extra ions and electrons by photoionisation, extra free electrons by photodetachment of negative ions[64], excited state neutrals (which have a much larger electron impact ionisation cross section) or ions in excited states with different symmetric charge-exchange cross sections (the process $X + X^+ \rightarrow X^+ + X$) to those of the ground state. These differences in the constituent species of the plasma change its conductivity. The exact changes in the discharge impedance are hard to predict so that LOGS remains mostly a qualitative diagnostic. By observing the Doppler profile of the LOGS signal, the kinetic energy of ions has been measured within the sheath of a d.c. discharge[65], although the information obtained was averaged over the entire sheath thickness. Precise spatial resolution of the LOGS probe region can be achieved with a two laser excitation process[66], however the sensitivity is greatly reduced and the signal obtained is distinctly non-linear with applied laser intensity. The electric field strength in a plasma has also been measured using LOGS by observing the Stark splitting of the energy levels of Rydberg states of helium[67].

Another possibility of the interaction of radiation with matter is that the radiation is scattered from the species present in the plasma. Thompson scattering is the scattering of photons by the free electrons in the plasma. The electron density can be directly measured by this diagnostic,

however the signals are generally very small due to the low cross sections so that photon counting techniques are necessary to achieve a good signal to noise ratio[68].

A further method that allows observation of the electron density is microwave interferometery. Although in practice not a scattering optical diagnostic, it is mentioned here as it gives similar information to that of Thompson scattering. It involves the detection of the changes in phase shift of microwave radiation as it is passed through the plasma due to refractive index variations caused by changes in the electron density. The average electron density along the path can then be calculated directly from the phase shift[69].

Rayleigh scattering is the scattering of the radiation by the electrons bound to atoms or ions and is particularly large in the case of hydrogen atoms. The concentration of species can be obtained *via* combination with other techniques[70].

A final scattering technique is coherent anti-stokes Raman scattering (CARS)[71]. This involves interrogating a molecule with three laser beams, two pump beams and a Stokes beam of frequencies ω_P and ω_S respectively, and observing the radiation produced at $2\omega_P - \omega_S$. This sum frequency generation (SFG) depends on the third order susceptibility. This has two components; a non-resonant component that depends on the number density of the species present and a frequency dependent resonant component depending on the amount of the Stokes beam that is absorbed. This method enables determination of the concentrations of molecular species and their rotational and vibrational distributions[72].

1.7 Lasers and Optical Cavities

In this section, the operation of lasers is described. A laser is simply an instrument that amplifies spontaneously produced radiation. The unique properties of lasers have led to a wide variety of applications. They can produce narrow bandwidth, almost monochromatic radiation, with spatial and temporal coherence that has proven invaluable in spectroscopic applications. Another useful property is the high intensity of radiation that they can produce which has been used for optically pumping systems and multiphoton ionisation.

It is possible to understand the amplification process in a laser using the system of two states discussed in Section 1.6.1. The ratio of A_{21}/B_{21} is proportional to ν^3, hence spontaneous emission rates increase relative to stimulated emission rates at short wavelengths, making it easier to construct an amplifying system for microwave radiation than for visible radiation.

For a system where $g_1 = g_2$, to achieve amplification in the medium there must be a population inversion, *i.e.* the population of L_2 is greater than L_1. This can be achieved in many ways, including optical pumping, electrical discharge or energy transfer between different species. The specific example of semiconductors is discussed in Section 1.8.2.

To ensure that stimulated emission dominates spontaneous emission, a high photon density is required in the laser medium, and this can be achieved by placing the medium between two mirrors to form a resonant cavity (see Appendix 1 for the criteria for a stable optical cavity). This allows a photon spontaneously emitted along the axis of the cavity to be trapped and stimulate emission of other photons, which causes a build up of radiation. For radiation to be resonant with the cavity, it must have nodes in its oscillation at each end of the cavity. As the stimulated radiation has a defined phase, only constructive interference occurs as the radiation travels between the cavity mirrors. To satisfy this condition the length of the cavity must be a whole number of half wavelengths, hence the radiation satisfies the following relationship

$$\frac{m\lambda}{2} = L \tag{1.26}$$

where m is an integer and L is the distance between the mirrors. The frequency separation between adjacent modes, m and m+1, is called the free spectral range (*FSR*). In a cavity of length L, containing a medium of refractive index n, it follows that

$$FSR = \frac{c}{2nL} \tag{1.27}$$

except in the special case of a confocal cavity (see Appendix 1) where the *FSR* is half of this value[73]. A second useful property of a passive cavity (one that has no gain medium within it) is the finesse, which depends only on the reflectivity of the mirrors, and gives a measure of the cavity's ability to trap photons. The finesse, F, is approximately the free spectral range divided by the bandwidth, and is given in terms of the reflectivity, R, of the mirrors by[24].

$$F = \frac{\pi\sqrt{R}}{1-R} \tag{1.28}$$

However, in the case of a laser cavity the bandwidth also depends on the frequency dependence of the gain. Generally, this is a small effect because the gain envelope, the frequency region over which the lasing medium amplifies, is much wider than the cavity free spectral range. Once the laser is operating with a high gain, one mode may be selectively amplified more than all others. Because of the avalanche of photons at that frequency, this mode will become

dominant; all of the radiation given out by the laser will collapse into this mode. The laser is then said to be operating in a single (axial) mode.

As well as the longitudinal modes discussed above, the resonator can also support transverse modes, also know as transverse electromagnetic modes (TEMs). These are resonant oscillations that propagate slightly off axis, and are distinguished by the label TEM_{pq} where p and q take integer values indicating the number of intensity nodes across the cavity in two mutually perpendicular directions. For a laser to have the best coherent properties, all modes except the TEM_{00} mode should be suppressed, because other modes resonate at slightly different frequencies due to their longer path length. This can be achieved by spatially filtering the light within the laser cavity.

1.8 Diode Lasers

Many atomic and molecular systems have been used as the laser medium[24] but in this section the semiconductor diode laser is considered. Recent interest in these devices is mainly due to their wide availability and low cost in comparison to most other laser systems (for instance, the pulsed laser system discussed in Chapters 4 and 5 costs more than an order of magnitude more than a commercial diode laser system[74]).

1.8.1 Semiconductors

The structure and properties of intrinsic semiconductors, for instance silicon and germanium, can be rationalised in terms of atomic orbitals overlapping to form energy level bands. Unlike metals, which form high coordination number structures with a continuous band structure, these semiconductors form tetrahedrally coordinated structures, which leads to a split in the band structure[75]. This separation of bands occurs with an equal number of states above and below the band gap.

This main difference between a metallic material and a semiconductor is that the electrical conductivity of metals decreases with temperature while that of the semiconductor increases. This difference occurs because in metals, the increased temperature causes lattice vibrations that displace the atoms from their lattice sites, thus scattering the electrons more[75]. However in the semiconductor, the current can only be carried by electrons promoted into the conduction band and vacancies (holes) in the valence band. Thus, as the temperature increases so does the number of charge carriers causing the rise in conductivity.

It is also possible to increase the conductivity of a semiconductor by *doping* – the introduction of an impurity into the crystal structure. The material is then described as an extrinsic semiconductor. For example, if silicon is doped with a small quantity of boron, which has one less valence electron than silicon, then for each boron atom a hole is formed in the valence band. An intrinsic material doped with an element with fewer valence electrons is called a *p-type* semiconductor because its conductivity depends on the number of positive holes formed in the valence band. Doping a pure material with an element with more valence electrons introduces a set of energy levels just below the bottom of the conduction band. As these are filled or partially filled, they provide charge carriers that are easily promoted into the conduction band forming an *n-type* semiconductor. This increases the conductivity due to the increase in negative charge carriers *i.e.* electrons.

It is possible to make many devices by combining n-type and p-type materials[76]; here only a single p-n junction is considered. Figure 1.5 shows the energy level diagrams of the junction. At equilibrium, when no current is flowing (Figure 1.5a), a depletion layer forms at the junction due to the electrons in the n-type material filling holes in the p-type material. This depletion layer contains no charge carriers and so if a small potential is applied across the junction no current will flow. However, as the potential difference is increased, the Fermi levels are forced further apart, and the conductivity depends on the magnitude and sign of the voltage difference.

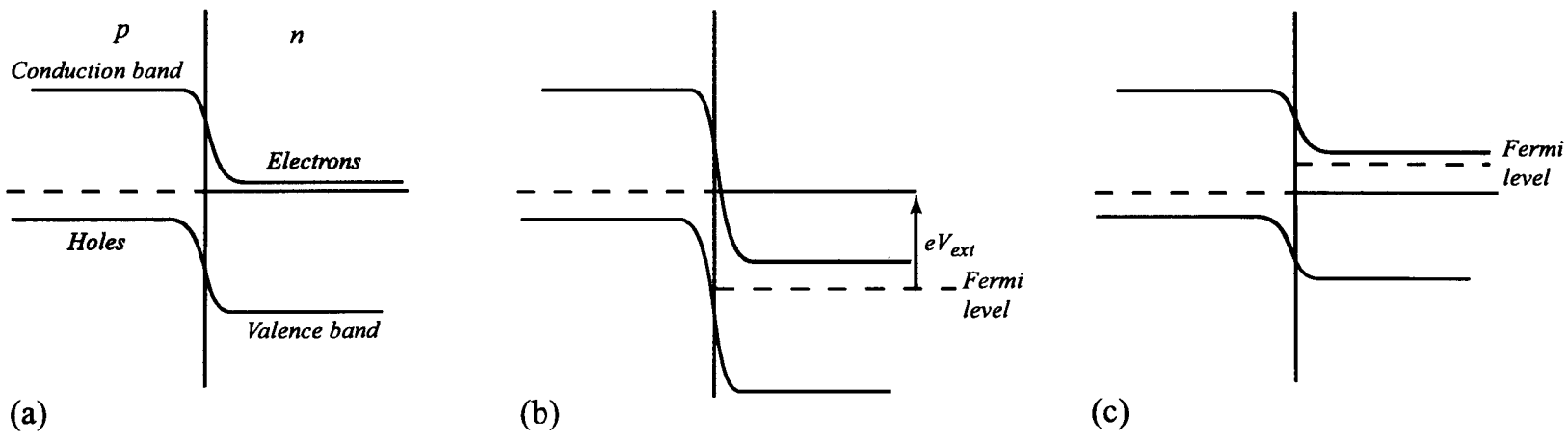

Figure 1.5 Schematic diagram of the energy levels of a junction of n-type and p-type semiconductor materials, (a) in equilibrium, (b) reverse biased and (c) forward biased.

When a potential difference is applied that holds the Fermi level of the n-type material below that of the p-type material the junction is said to be *reverse biased.* At sufficiently large reverse bias, the diode suddenly starts to conduct; this is described as breakdown. This can have two causes: Zener breakdown or avalanche breakdown. Zener breakdown occurs in heavily doped diodes at low voltages and is caused by electrons tunnelling through a potential

barrier. This barrier is due to the band gap and is the width of the depletion zone. This tunnelling occurs more easily as the temperature rises as the energy of the electrons increases. Conversely avalanche breakdown decreases with temperature and is caused when carriers gain energy from the electric field across the junction and make ionising collisions, forming more electron-hole pairs. If the process is uncontrolled, it results in an avalanche. Breakdown can cause damage to the junction by local melting so diodes should generally be operated below their breakdown voltage. If the applied potential is smaller than the breakdown voltage, the depletion layer increases in thickness and no current flows through the junction. This situation is shown in Figure 1.5b.

Alternatively, if the applied potential holds the Fermi level of the n-type material above the Fermi level of the p-type material, the junction is *forward biased*, as shown in Figure 1.5c. In this case, current can flow through the junction as either electrons injected into the conduction band of the p-type material fall into the vacancies in the valence band or holes injected into the valence band of the n-type material accept electrons from the conduction band. The current voltage characteristic of a p-n junction is given in Figure 1.6. For this junction, the current voltage relationship is given by[76]

$$I = I_r\left(e^{\left(\frac{eV_{applied}}{kT}\right)} - 1\right) \tag{1.29}$$

where I_r is the leakage current of the diode when it is reversed biased but not sufficiently to cause an uncontrolled breakdown.

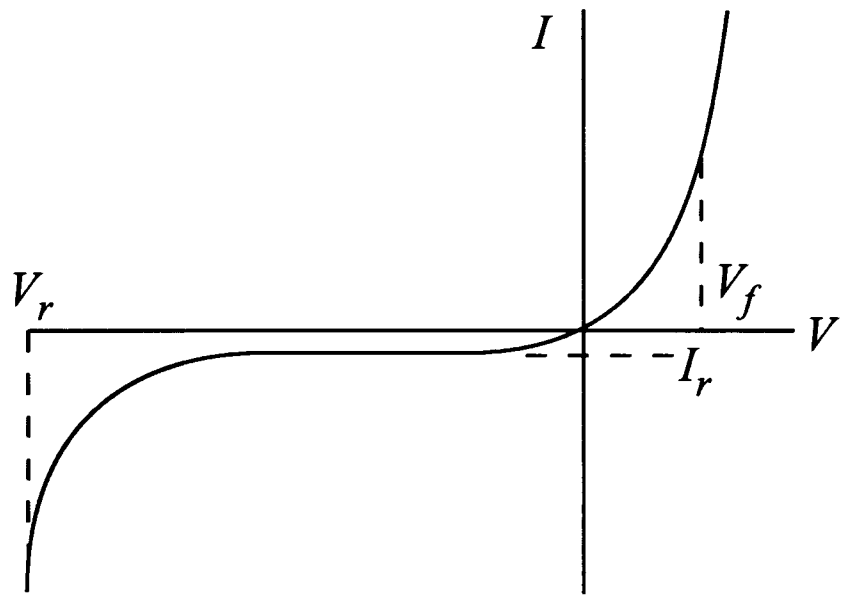

Figure 1.6 The current-voltage characteristic for a p-n junction diode. V_f and V_r are the potentials required to be applied to the diode to cause significant current to flow by forward and reverse biasing respectively. I_r is the leakage current flowing through the diode while it is reverse biased below V_r.

1.8.2 Diode Laser Operation

Bernard and Duraffourg[77] suggested that the number of electrons occupying any state in the conduction band, $E_c(k_j)$, is given by

$$f_c = \left(1 + e^{\left(\frac{E_c(k_j) - F_c}{kT}\right)}\right)^{-1} \tag{1.30}$$

where F_c is the conduction band electron 'quasi Fermi level'. Similarly, it is possible to define F_v, the 'quasi Fermi' level for the holes in the valence band. $F_c = F_v = F_0$ at equilibrium. If a direct radiative transition between a state in the valence band, at energy $E_v(k_i)$, and a state in the conduction band occurs with a probability W per second then the number of photons absorbed per unit time, N_a, in a radiation field of density $\rho(v)$ is given by

$$N_a = AWF_v(k_i)(1 - f_c(k_j))\rho(v) \tag{1.31}$$

If the probability of stimulated absorption is the same as that of stimulated emission, the number of photons emitted per unit time by stimulated emission, N_e, is

$$N_e = AW(1 - f_v(k_i))f_c(k_j)\rho(v) \tag{1.32}$$

where the density of states in the valence and conduction band is included in the probability coefficient A. For amplification to occur, $N_e > N_a$ or

$$f_c(k_j)(1 - f_v(k_i)) > f_v(k_i)(1 - f_c(k_j)) \tag{1.33}$$

which from equation (1.30) is equivalent to

$$e^{\left(\frac{F_c - F_v}{kT}\right)} > e^{\left(\frac{E_c(k_j) - E_v(k_i)}{kT}\right)} \tag{1.34}$$

However, since the photons' energy, hv, is equal to the energy separation of the two states $E_v(k_i)$ and $E_c(k_j)$, the condition in equation (1.34) reduces to

$$F_c - F_v > hv \tag{1.35}$$

In this case, a population inversion is not required for amplification, differing from other laser media due to the continuous distribution of electron levels in a semiconductor compared to the discrete energy levels in atoms of molecules.

Figure 1.7 shows the forward bias energy level diagram for the laser discussed in Section 1.8.3. The two quasi Fermi levels are separated by the bias applied to the diode. If radiation with a

frequency obeying the condition given by equation (1.35) propagates through the active region of the device, conduction band electrons undergo stimulated transitions to empty valence band states, amplifying the radiation. It is not possible for the same frequency of radiation to promote electrons by absorption from the valence band to the conduction band because they would have to originate at or below the quasi Fermi level of the conduction band and would not have sufficient energy to populate the valence band.

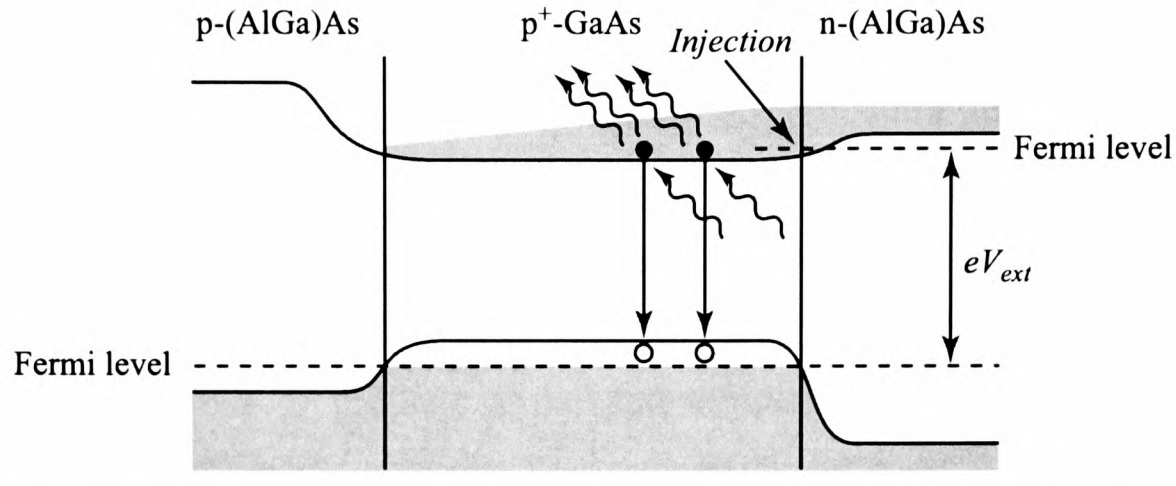

Figure 1.7 A double-heterojunction laser working with a forward bias. Injected electrons are trapped in the p^+-GaAs conduction band.

The power of the radiation output depends on the gain of the semiconductor. The gain depends on the injection current as this increases the number of electrons available in the conduction band (that can emit radiation as they are stimulated) for relaxation into the valence band. The diode needs a minimum current to produce amplified radiation. This is when the number of photons produced by stimulated emission per second is equal to the number of photons lost from the laser medium. Above and below this threshold current, the number of photons produced per second (the radiation intensity) depends linearly on the current applied to the junction. Above the threshold, this quantity is known as the slope efficiency of the laser. Figure 1.8 shows a plot of output power against injection current for a laser diode.

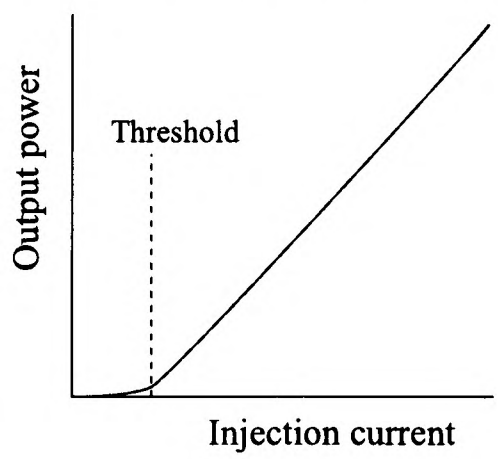

Figure 1.8 The simulated performance of a typical diode laser. The gradient of the plot above threshold gives the slope efficiency.

The optical faces of the crystal are polished perpendicular to the junction to form a resonant cavity. To increase the amplification, the back face of the semiconductor sandwich may be coated with a reflective coating.

1.8.3 Modern Diode Lasers

As early as 1960 a patent[78] describing the 'semiconductor maser' (**m**icrowave **a**mplification by **s**timulated **e**mission of **r**adiation) was filed by Y. Watanabe and J. Nishizawa in Japan. The specific example discussed was a 4 μm tellurium device contained within a microwave resonant cavity.

Previously in 1907, Round observed electroluminesence when current was passed through a silicon carbide detector[79] (which consists of a p-n junction – see Section 1.8.1). A discussion of the conditions required to produce stimulated emission from a transition between the conduction and valence bands is given by Bernard and Duraffourg[77] (see Section 1.8.2), who proposed, amongst others, III-V compounds such as GaAs and GaSb, formed from an element in group three and one in group five of the periodic table. Arsenic has a greater electronegativity than gallium, so the valence band has a larger contribution from arsenic's atomic orbitals than those from gallium. The conduction band shows more gallium orbital character than arsenic orbital character. Shortly after the use of III-V semiconductors had been suggested, Nasledov *et al.*[80] reported that the line width of a GaAs light emitting diode narrowed slightly at high current densities (1.5×10^3 A cm^{-3}), which they attributed to stimulated emission. Later that year, several groups announced lasing from p-n junctions in GaAs[81,82,83,84].

Bond *et al.*[85] were the first to produce a homostructure laser by cleaving parallel to the crystal planes of an intrinsic semiconductor. These homostructure injection lasers had very high threshold current densities at room temperature ($\geq 5 \times 10^4$ A cm^{-2}) and were usually operated with a duty cycle of below one thousandth using very short pulses ($\leq$ 1 μs). Continuous operation of such a device was not achieved until 1967[86] and this was at a temperature of 205 K.

Heterojunction lasers were first produced[87] six years after the first homostructure lasers. These lasers consist of a layer of semiconductor with a relatively narrow band gap sandwiched between two layers of a wider energy-gap semiconductor, reducing the threshold current density by about two orders of magnitude.

Modern commercial diode lasers are double-heterojunction[88] structures that give a further reduction of the threshold current density compared to simple single-heterojunction laser constructs. A schematic of a typical GaAs/GaAlAs narrow stripe double-heterojunction laser diode is shown in Figure 1.9.

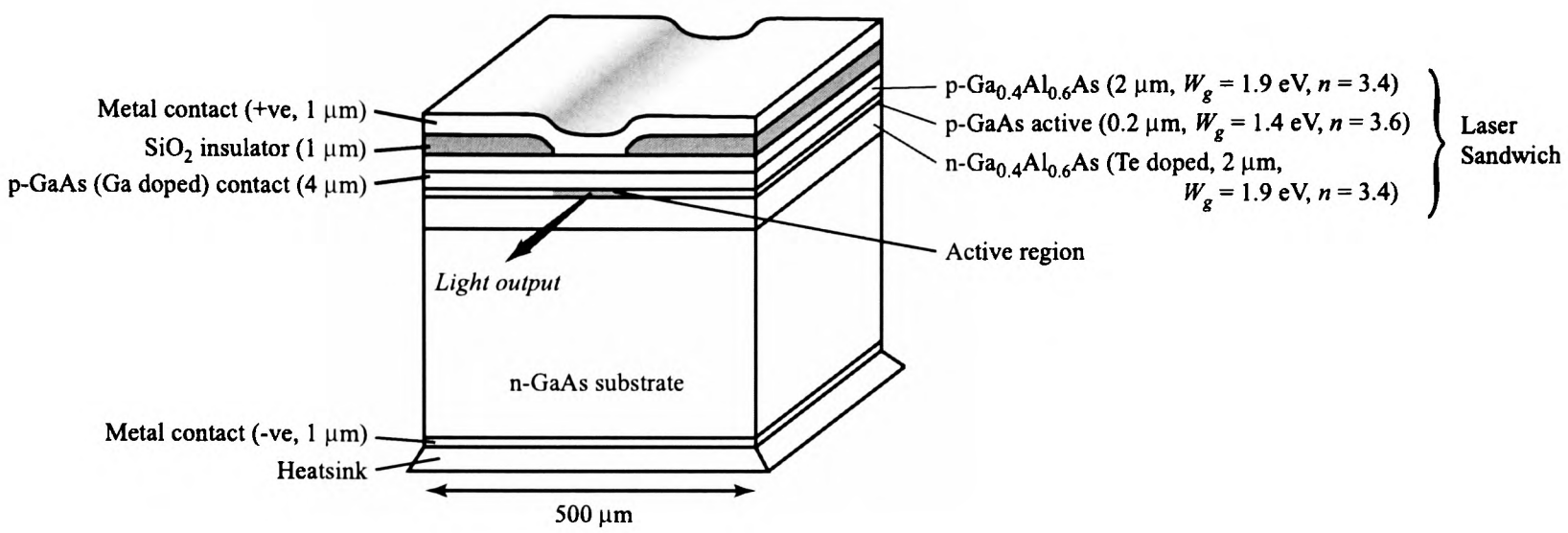

Figure 1.9 A double-heterojunction narrow-stripe laser diode.

The three-layer sandwich structure consists of $Al_xGa_{1-x}As$ which has a band gap of 1.9 eV in comparison to the band gap of 1.4 eV of GaAs. The electrons that are injected into the p-GaAs are confined by the p-$Al_xGa_{1-x}As$, so that sufficient electron density for laser action can build up at low currents. Both the $Al_xGa_{1-x}As$ layers have a lower refractive index than the active region, confining the photons to the p-GaAs. The layers are chosen to have very similar lattice constants so epitaxial growth is possible; in the example given, the whole structure is grown on a n-GaAs substrate, with a top contact of doped GaAs. The active region is confined to a stripe of the layer structure by an etched SiO_2 layer. Due partially to the width of the SiO_2 band gap and the thickness of the active layer and partially to the length of the active region, the beam diverges much less in the plane of the junction than perpendicular to it. Although a collimating lens can be placed within a few millimetres of the laser's front facet, the resultant beam is elliptical. The beam profile of a 810 nm 3 mW diode laser (Sharp LT010MD) is shown in Figure 1.10a. Some commercial devices are available with an integrated beam correcting optic fixed to the front face of the semiconductor[89]. One such device, a Blue Sky Research CircuLaser PS104, is used in Chapter 5 and its beam profile is shown in Figure 1.10b. Another property of modern laser diodes, due to their short cavity length, is the large separation of the cavity modes ($\approx$ 100 GHz $\approx$ 3.3 cm^{-1}). This free spectral range can be obtained from equation (1.27), given that the refractive index of GaAs[90] is approximately 3.6 and the length of the active medium is 500 μm.

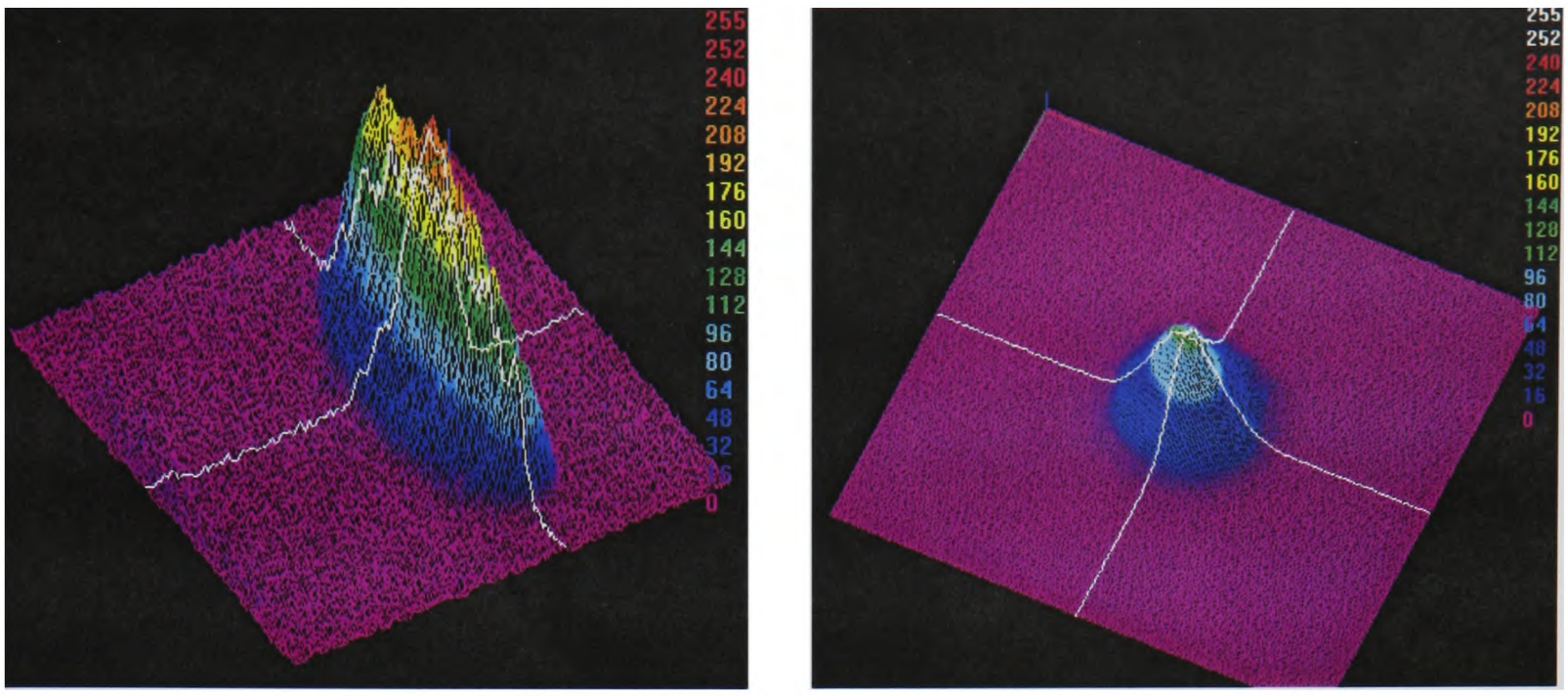

Figure 1.10 Beam profiles of diode lasers, recorded by interfacing a CCD camera with a PC running Spiricon beam profiling software, (a) a standard laser diode, (b) a Blue Sky Research CircuLaser

1.8.4 Diode Laser Modes

The resonant cavity formed by the front and back faces of the semiconductor result in the laser having many longitudinal modes over which it may amplify radiation. Figure 1.11a shows a simulation of frequency transmission spectrum of a cavity with the same mirror reflectivities and dimensions as a diode laser. Also in Figure 1.11a, a simplified laser gain curve has been superimposed on the transmission spectrum. An experimental laser gain curve is given by Thompson[91]. Figure 1.11b shows the expected output from the laser below threshold. In this case, all the cavity modes within the gain curve will give rise to some emission. As the laser goes above its threshold current, the spectrum narrows due to the modes closest to the maximum of the gain curve being amplified in preference to the others. This is shown in Figure 1.11c and with a further increase in gain in Figure 1.11d. In a very high gain medium the mode system collapses to a single axial mode as shown in Figure 1.11e. The gain and the reflectivity of the front and rear facets of most diode lasers results in a bandwidth of less than 100 MHz.

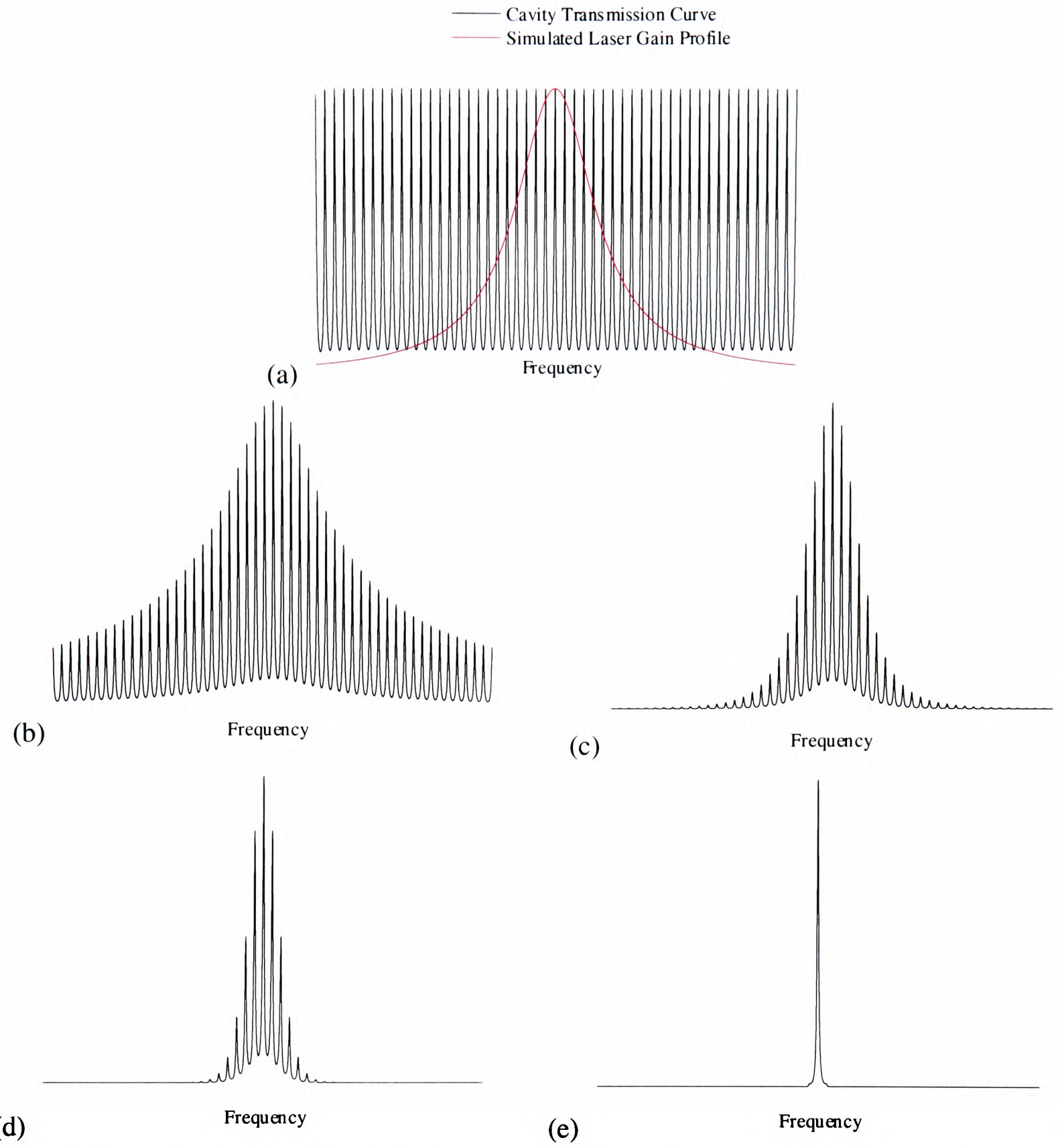

Figure 1.11 Simulated output of a diode laser, (a) the laser cavity transmission spectrum along with a simulated gain profile, (b) output well below the lasing threshold, (c) and (d) sequentially increased gain and (e) laser operating well above threshold on a single mode.

1.8.5 Linewidths

The standard expression for the linewidth of a laser is provided by the Schawlow-Townes theory[90], in which the quantum phase fluctuations produce the linewidth, $\Delta\nu_{ST}$

$$\Delta\nu_{ST} = \left(\frac{\pi h\nu\Delta\nu_{cav}^{2}}{P}\right)\left(1-e^{\left(\frac{h\nu+F_v-F_c}{kT}\right)}\right)^{-1} \tag{1.36}$$

where P is the laser power. This linewidth is the result of spontaneous emission in the medium producing photons with an uncorrelated phase in relation to the photons produced within the medium by stimulated emission. The instantaneous frequency is the differential of phase with respect to time and therefore any change of phase of the radiation causes a change in frequency. The limiting value of $\Delta\nu_{ST}$ for a diode laser is a few MHz, however the measured linewidth is invariably found to be an order of magnitude higher[90]. This increased linewidth has been attributed to the change in the intensity of the electric field of the radiation caused by the spontaneous emission[92]. The carrier density and hence the gain will fluctuate to restore the steady state value. The change in the imaginary part of the optical susceptibility, because of changes in the gain due to carrier density affects, is quantified by $\Delta\chi_i = -(c/2\nu)\Delta G$, where ΔG is the change in gain[93]. The change in the real part of the optical susceptibility can be related to laser wavelength shifts using $\Delta\chi_r = (n/\lambda)\Delta\lambda$. The complex optical susceptibility of a semiconductor is given by $\chi = \chi_r + i\chi_i$. This additional broadening modifies the original Schawlow-Townes linewidth to give

$$\Delta\nu'_{ST} = \left(1+\alpha^2\right)\left(\frac{\pi h\nu\Delta\nu_{cav}^2}{P}\right)\left(1-e^{\left(\frac{h\nu+F_v-F_c}{kT}\right)}\right)^{-1} = \left(1+\alpha^2\right)\Delta\nu_{ST} \qquad (1.37)$$

where α is the ratio of the change in the real part of the refractive index to the change in the imaginary part of the refractive index, due to spontaneous emission events over the same period of time.

1.8.6 Wavelength Tuning

The wavelength output of a single mode diode laser depends on the material it is made from and its operating conditions. Up to now, these lasers have only been produced operating at particular clusters of wavelengths, firstly due to the properties of the semiconductors that have been used to make them and secondly because research has focused on commercial needs, in particular the telecommunications and data storage industries.

A specific laser can be wavelength tuned by changing the temperature of the junction. This affects the physical properties of the material, such as the carrier density, band gap and refractive index. This results in a change to both the gain curve and transmission curve.

The change in the gain curve can be explained in terms of the semiconductor band structure[94]. As the semiconductor's temperature decreases, like most other solids, it contracts. This lattice contraction causes better atomic overlap and therefore the band gap decreases. This effect

alone would cause the wavelength of the radiation that the semiconductor produces to increase because the energy gap has decreased. However, the decrease in temperature also causes an increase in the electron confinement and thus an increase in the charge carrier density. This increase in charge carrier density screens the atomic attractive forces leading to a decrease in the effective atomic orbital overlap and thus a decrease in the widths of the bands. The second effect dominates the change in band gap and therefore the band gap increases and the wavelength decreases as the temperature is decreased.

The changes in the transmission curve, the resonant frequencies of the semiconductor crystal, can be explained in terms of the change in length of the crystal. The cavity contracts as the temperature is reduced and the refractive index of the laser cavity also varies because the optical properties of most materials are temperature dependent[95].

Therefore, the laser modes move around in frequency and thus over a small temperature change, the laser scans smoothly with temperature. However, over a larger temperature change the gain curve shifts sufficiently far to cause the laser to 'hop' into an adjacent cavity mode. This enables coarse wavelength tuning of the laser but does not lead to continuous wavelength coverage. An example of these effects is discussed in Chapter 4.

For fine wavelength tuning, it is possible to vary the current flowing through the junction. This changes both the carrier density and the temperature of the junction by resistive heating. It is reported that the thermal effect is approximately an order of magnitude smaller than that due to the current density variation[90]. The change in carrier density again changes the refractive index and band gap and changes both the gain curve of the semiconductor and the transmission curve of the cavity causing a similar effect to that of temperature (that the laser can be continuously tuned over small ranges but mode hops if the current is varied significantly). This current tuning effect is explained by the same mechanisms as discussed in the previous section on the diode laser linewidths.

It is also possible to tune a diode laser's wavelength by placing it within an external cavity[96]. This involves interaction of the gain and transmission curve of the semiconductor with the transmission curve of the external cavity. If the feedback from the external cavity is sufficiently large then the laser operates on a single external cavity mode rather than its internal mode. If a wavelength-selecting element, such as a grating, is used as part of the cavity, it is possible to use this to vary the wavelength. If the geometry of the cavity is carefully chosen this can enable smooth continuous scanning of the wavelength. The external cavity may also

reduce the laser's bandwidth[97] because of the large reduction in free spectral range but only small changes in cavity reflectivity and gain.

1.9 References

[1]M. A. Liberman and A. J. Lichtenberg, *Principles of Plasma Discharges and Material Processing*, Wiley, (1994)
[2]B. Chapman, *Glow Discharge Processes*, Wiley, (1980)
[3]A. M. Taylor and K. M. Tookey, *Metallurgia*, **48**, 64, (1981)
[4]R. Hutchings and W. C. Oliver, *Wear*, **92**, 143, (1983)
[5]H. J. Ramos, A. G. Mendenilla, C. M. Y. Blanca, I. S. Oconer and A. G. Yap, *Proc. 14th International Symposium on Plasma Chemistry*, **3**, 1481, (1999)
[6]R. A. Morgan, *Plasma Etching in semiconductor Fabrication*, Elsevier, (1985)
[7]S. L. Camacho *U.S. Patent No. 3779182* (1973): Refuse converting method and apparatus utilising arc column plasma torches
[8]K. Takeda, *Proc. 14th International Symposium on Plasma Chemistry*, **3** ,1155, (1999)
[9]H. R. Kaufman and R. S. Robinson, *Journal of Spacecraft and Rockets*, **18**, 470, (1981)
[10]P. N. Wainman, M. A. Lieberman, A. J. Lichtenberg, R. A. Stewart and C. Lee, *J. Vac. Sci. Technol.*, **13**, 3464, (1995)
[11]B. N. Chapman and J. Minkiewicz, *J. Vac. Sci. Technol.*, **15**, 369, (1978)
[12]D. Halliday and R. Resnick, *Fundamentals of Physics*, Wiley, (1988)
[13]T. E. Benson, L. I. Kamlet, P. Klimecky and F. L. Terry, *J. Elec. Materials*, **25**, 655, (1996)
[14]E. Tachibana, T. Shirafuji and S. Muraishi, *Jpn. J. Appl. Phys.*, **35**, 3652, (1996)
[15]H. F. Winters and J. W. Coburn, *Surface Science Reports*, **14**, 161, (1992)
[16]D. P. Woodruff and T. A. Delchar, *Modern Techniques of Surface Science*, CUP, (1986)
[17]H. M. Mott-Smith and I. Langmuir, *Phys. Rev.*, **28**, 727, (1926)
[18]M. J. Kushner, *J. Appl. Phys.*, **20**, 820, (1987)
[19]T. I. Cox, V. G. Deshmuk, D. A. Hope, A. T. Hydes, N. St. J. Braithwaite and M. P. Benjamin, *J. Phys. D: Appl. Phys.*, **20**, 820, (1987)
[20]N. St. J. Braithwaite, J. P. Booth and G. Cunge, *Plasma Sources Sci. Technol.*, **5**, 677, (1996)
[21]M. Šícha. M. Tichý, P. Adámek, J. Kalčik, H. Biederman, L. Soukup and L. Jastrabik, *Proc. 14th International Symposium on Plasma Chemistry*, **2**, 843, (1999)
[22]K. Okada and S. Komatsu, *Proc. 14th International Symposium on Plasma Chemistry*, **2**, 795, (1999)
[23]F. Becker, I. W. Rangelow, K. Maβeli and R. Kassing, *Surface and Coating Technology*, **75**, 485, (1995)
[24]W. Demtröder, *Laser Spectroscopy*, Springer-Verlag, (1981)
[25]J. P. Booth, J. Joubert, J. Petellier and N. Sadeghi, *J. Appl. Phys.*, **69**, 618, (1991)
[26]J. C. Knights, J. P. M. Schmitt, J. Perrin and G. Guelachvili, *J. Chem. Phys.*, **76**, 3414, (1982)
[27]M. J. Buie, J. T. Pender, J. Soniker, M. L. Brake and M. Elta, *J. Vac. Sci. and Tech.: A Vacuum Surfaces and Films*, **13**, 1930, (1995)
[28]J. P. Sucksmith, *D. Phil. Thesis*, Oxford University, (1993)
[29]R. A. Gottscho and V. M. Donnelly, *J. Appl. Phys.*, **56**, 245, (1984)
[30]B. W. Woodcock, *D. Phil. Thesis*, Oxford University, (1995)
[31]Z. Randriamanantenasoa, A.-M. Diamy, N. Turillon and J.-C. Legrand, *Proc. 14th International Symposium on Plasma Chemistry*, **2**, 823, (1999)
[32]A. Chlouah, E. Marode, G. Hartmann and S. Achat, *J. Phys. D*, **27**, 940, (1994)
[33]P. Slavíček, A. Brablec, V. Kapička, F. Štastnỳ and R. Vaculík, *Proc. 14th International Symposium on Plasma Chemistry*, **2**, 1027, (1999)

[34]A. C. Fozza, M. Moisan and M. R. Wertheimer, *Proc. 14th International Symposium on Plasma Chemistry*, **2**, 539, (1999)
[35]R. d'Agostino, F. Cramarossa, S. De Benedicts and G. Ferraro, *J. Appl. Phys.*, **52**, 1259, (1981)
[36]J. P. Booth, J. Derouard, M. Fadlallah and N. Sadeghi, *J. Appl. Phys.*, **74**, 862, (1993)
[37]H. R. Griem, *Spectral Line Broadening by Plasmas*, Acad. Press, (1974)
[38]J. P. Booth and N. Sadeghi, *J. Appl. Phys.*, **70**, 611, (1991)
[39]J. W. Coburn and M. Chen, *J. Appl. Phys.*, **51**, 3134, (1980)
[40]G. Hancock, J. P. Sucksmith and M. J. Toogood, *J. Phys. Chem.*, **94**, 3269, (1990)
[41]R. W. Dreyfus, J. M. Jasinski, R. E. Walkup and G. S. Selwyn, *Pure & Appl. Chem.*, **57**, 1265, (1985)
[42]D. Romanini and K. K. Lehmann, *J. Chem. Phys.*, **99**, 6287, (1993)
[43]P. Zaliki and R. N. Zare, *J. Chem. Phys.*, **102**, 2708, (1995)
[44]D. Romanini and K. K. Lehmann, *J. Chem. Phys.*, **105**, 10263, (1996)
[45]J. Martin, B. A. Paldus, P. Zalicki, E. H. Wahl, T. G. Owano, J. S. Harris Jr., C. H. Krugerm and R. N. Zare, *Chem. Phys. Lett.*, **258**, 63, (1996)
[46]J. J. Scherer, J. B. Paul, A. O'Keefe and R. J. Saykally, *Chem. Rev.*, **97**, 25, (1997)
[47]E. R. Crosseen, P. Haar, G. A. Marcus, H. A. Schwettan, B. A. Paldus, T. G. Spencer and R. N. Zare, *Rev. Sci. Instrum.*, **70**, 1, (1999)
[48]D. Romanini, A. A. Kachanov, N. Sadeghi and F. Stoeckel, *Chem. Phys. Lett.*, **264**, 316, (1997)
[49]A. O'Keefe, J. J. Scherer and J. B. Paul, *Chem. Phys. Lett.*, **307**, 343, (1999)
[50]R. Engeln, G. Berden, P. Peeters and G. Meijer, *Sci. Instrum.*, **69**, 3763, (1998)
[51]J. P. Booth, G. Cunge, D. Romanini, A. Kachanov and L. Biennier, *Proc. 14th International Symposium on Plasma Chemistry*, **2**, 589, (1999)
[52]F. Grangeon, C. Monard, J-L Dorier, A. A. Howling, Ch. Hollenstein, D. Romanini and N. Sadeghi, *Plasma Sources Sci. Technol.*, **8** , 448, (1999)
[53]G. Meijer, M. G. H. Boogaats, R. T. Jongma, D. H. Parker and A. M. Wodtke, *Chem. Phys. Lett.*, **217**, 112, (1994)
[54]P. Zalicki, Y. Ma, R. N. Zare, J. Dadamio, E. H. Wahl, T. G. Owano and C. H. Kruger, *Appl. Phys. Lett.*, **67**, 144, (1995)
[55]T. G. M. Freegarde and G. Hancock, *J. Phys IV France*, **7**, C4-15, (1997)
[56]G. S. Selwyn, *J. Vac. Sci. Tech.*, **A6**, 2041, (1988)
[57]R. M. J. Jacobs, *Part II Thesis*, Oxford University, (1996)
[58]G. S. Selwyn, L. D. Baston and H. H. Sawin, *Appl. Phys. Lett.*, **51**, 898, (1987)
[59]B. K. Woodcock, J. R. Busby, T. G. M Freegarde and G. Hancock, *J. Appl, Phys.*, **81**, 5945, (1997)
[60]C. A. Moore, G. P. Davis and R. A. Grottscho, *Phys. Rev. Letts.*, **52**, 538, (1984)
[61]L. F. DiMauro, R. A. Gottscho and T. A. Miller, *J. Appl. Phys.*, **56**, 2007, (1984)
[62]G. Hancock, *Proc. Int. Symp. Laser-aided Plasma Diagnostics*, **5**, 254, (1991)
[63]M. N. Reddy, *Science Defence Journal*, **44**, 279, (1994)
[64]K. E. Greenberg, G. A. Hebner and J. T. Verdeyen, *Appl. Phys. Lett.*, **44**, 299, (1984)
[65]R. Walkup, R. W. Dreyfus and P. Avouris, *Phys. Rev. Letts.*, **50**, 1846, (1983)
[66]D. K. Doughty, S. Salih and J. E. Lawler, *Phys. Lett. A*, **103**, 41, (1984)
[67]B. N. Ganguly, J. R. Shoemaker, B. L. Preppernau and A. Garcadden, *J. Appl. Phys.*, **61**, 2778, (1987)
[68]C. Busch and H. Soltwisch, *Proc. Frontiers in Low Temperature Plasma Diagnostics II*, 107, (1997)

[69]N. Niemöller, V. Schultz-Von Der Gathen, A. Stampa and H. F. Döbele, *Plasma Sources Sci. Technol.*, **6**, 478, (1997)
[70]W. Biel, M. Bröse, M. David, H. Kempkens and J. Uhlenbusch, *Proc. Frontiers in Low Temperature Plasma Diagnostics II*, 93, (1997)
[71]S. Hädrich, B. Pfelzer, T. Doerk, P. Jauernik and J. Uhlenbusch, *J. Appl. Phys.*, **78**, 1297, (1995)
[72]J. Fincke, S. Snyder, D. Crawford and T. Hyde, *Proc. 14th International Symposium on Plasma Chemistry*, **1**, 203, (1999)
[73]O. Svelto, *Principles of Lasers 4th Edition*, Plenum, (1998)
[74]Sacher Lasertechnik
[75]L. Smart and E. Moore, *Solid State Chemistry*, Chapman and Hall, (1992)
[76]D. A. Fraser, *The Physics of Semiconductor Devices*, Clarenden Press, (1986)
[77]M. G. A. Bernard and G. Duraffoug, *Phys. Status Solidi*, **1**, 669, (1961)
[78]Yansushi Watananabe, Sendai and Jun-ichi Nishizawa, *Japanese Patent no. 273217*, 30 September 1960, Appl. No. 32-9899 filed 22 April 1957: semiconductor laser
[79]T. Round, *Electrical World*, 309, (1907)
[80]D. N. Nasledov, A. A. Rogachev, S. M. Ryvkin and B. V. Tsarenkov, *Sov. Phys. Solid State*, **4**, 782, (1962)
[81]R. N. Hall, G. E. Fenner, J. O. Kingsley, T. J. Soltys and R. O. Carlson, *Phys. Rev. Lett.*, **9**, 362, (1962)
[82]N. I. Nathan, W. P. Dumke, G. Burns F. H. Dill Jr. and G. Lasher, *Appl. Phys. Lett.*, **1**, 62, (1962)
[83]T. M. Quist, R. H. Rediker, R. J. Keyes, W. E. Krag, B. Lax, A. L. McWhorter and H. J. Zeiger, *Appl. Phys. Lett.*, **1**, 91, (1962)
[84]N. Holonyak Jr. and S. F. Bevacqua, *Appl. Phys. Lett.*, **1**, 82, (1962)
[85]W. L. Bond, B. G. Cohen, R. C. C. Leite and A. Yariv, *Appl. Phys. Lett.*, **2**, 57, (1963)
[86]J. C. Dyment and L. A. D'Asaro, *Appl. Phys. Lett.*, **11**, 292, (1967)
[87]I. Hayashi, M. B. Panish and P. W. Foy, *IEEE J. Quanum electron.*, **QE-5**, 211, (1969)
[88]Zh. I. Alverov, V. M. Andreev, E. L. Portnoi and M. K. Trukan, *Sov. Phys.-Semicond.*, **3**, 1107, (1970)
[89]Blue Sky Research
[90]A. Yariv, *Quantum Electronics in Modern Communications*, OUP, (1997)
[91]G. H. B. Thompson, *Physics of Semiconductor Laser Devices*, Wiley, (1980)
[92]C. H. Henry, *IEEE J. Quantum Electron.*, **18**, 259, (1982)
[93]A. Mooradian, *Spectral Properties of semiconductor Diode Lasers, proceedings of the Twenty-third Scottish Universities Summer School in Physics*, edited by W. J. Firth and R. G. Harrison, (1982)
[94]M. Levinshtein, S. Rumyantsev and M. Shur (Eds.), *Handbook, Series on Semiconductor Parameters*, Vol. 2, World Scientific, Singapore, (1999)
[95]V. G. Dmitriev, G. G. Gurzadyan and D. N. Nikogosyan, *Handbook of Nonlinear Optical Crystals*, Spinger-Verlag, (1991)
[96]K. C. Harvey and C. J. Myatt, *Optics Letters*, **16**, 910, (1991)
[97]R. Wyatt and W. J. Devlin, *Electron Lett.*, **19**, 110, (1983)

Chapter 2

The Discharge Systems

2.1 Introduction

In this Chapter, the three discharge systems used in the following Chapters are discussed. Two of these systems are described in detail, both involving a plasma produced using radio frequency (r.f.), firstly in a capacitively coupled system and secondly in an inductively coupled system. The performance of both these systems is compared using a capacitively coupled planar probe to obtain measurements of the ion currents and electron temperatures. The third, a standard microwave discharge (EMS 214L), was used in a flowing gas to produce OH radicals and H atoms (see Chapter 4). The remainder of this Chapter describes the plasma chambers used for spectroscopic investigations of short lived plasma species such as electronically excited argon atoms and N_2^+ ions. In particular the electrical characteristics of the chambers are described.

2.2 The Capacitively Coupled Plasma (CCP) System

Capacitively coupled plasma (CCP) systems have been widely used for materials processing; examples include semiconductor device manufacture and metal surface treatment. The capacitively coupled plasma system used in this Thesis is an extensively modified commercial system. The modifications were required because the system was designed entirely for convenience in processing and not as a research system.

2.2.1 Production of a Capacitively Coupled Discharge

Capacitively driven r.f. discharges are formed between two plates or electrodes; generally one is driven by the r.f. source and the other is grounded and consists of the rest of the chamber. The entire system, plasma and electrodes acts as a non-ideal capacitor; that is, it acts as a charge storage device but, once operating, the charge is carried from one connection to the other (conduction) and so the dielectric is not perfect. The discharge is initiated by a direct electric discharge that causes ionisation of species between the electrodes. The species that are ionised are those with the lowest ionisation potential and are generally contaminants in the

feedgas such as water molecules[1]. The free electrons that are formed are then accelerated by the electric field; if they gain sufficient kinetic energy then in a collision they can ionise other species that in turn cause further ionisation, resulting in an *avalanche process*[1]. A plasma bulk forms, consisting of an overall electrically neutral system containing neutral species, electrons and ions. Around this bulk, sheaths form to the negatively charged surroundings as discussed in Section 1.3.2. The electric field in these sheaths vary with time because of the applied r.f. voltage. Therefore, electrons are accelerated in different directions and by different amounts at different points of the r.f. cycle unlike the ions because the much lighter electrons respond rapidly to the changing potential. The energy lost to the fabric of the chamber is compensated by that supplied to the bulk by electron stochastic heating (in which the electrons 'collide' with the oscillating electric fields present in the sheath) and ohmic heating (electrons losing energy to other species by collision) directly in the bulk[1]. Fast moving electrons produced in the sheath also maintain the ion number density in the bulk by collisional ionisation. This enables the discharge to be maintained between the two electrodes effectively shielded from each other by the plasma bulk.

2.2.2 The Chamber

The modified Plasma Technology RIE 80 chamber is shown schematically in Figure 2.1. It consists of two aluminium electrodes and a glass cylinder; the upper electrode (electrically isolated from an aluminium base plate) is connected to ground while the lower electrode is driven at 13.56 MHz. The 28 cm diameter cylindrical borosilicate glass chamber has been modified by the addition of three QVF sidearms; diametrically opposite ports allow a transverse optical path through the discharge. Mounted on the end of these two side arms were either two quartz windows in anodised aluminium mounts or high reflectivity mirrors, when an optical cavity was required. The high reflectivity mirrors were attached to gimbal mirror mounts by a piezoelectric transducer (Lutz Pickelmann HPSt 150/20-15/12). The piezoelectric transducer allows small ($\approx$ 100 μm) translations of the mirror along the cavity axis. Brewster angle windows were fitted external to the mirrors to minimise reflection losses. This arrangement limited the laser interrogation region between the electrodes to a distance of 0 to 50 mm above the lower driven electrode. The third port was used for the insertion of the planar probe used for the electrical measurements discussed later in this Chapter or to enable the observation of laser induced fluorescence (see Chapter 5).

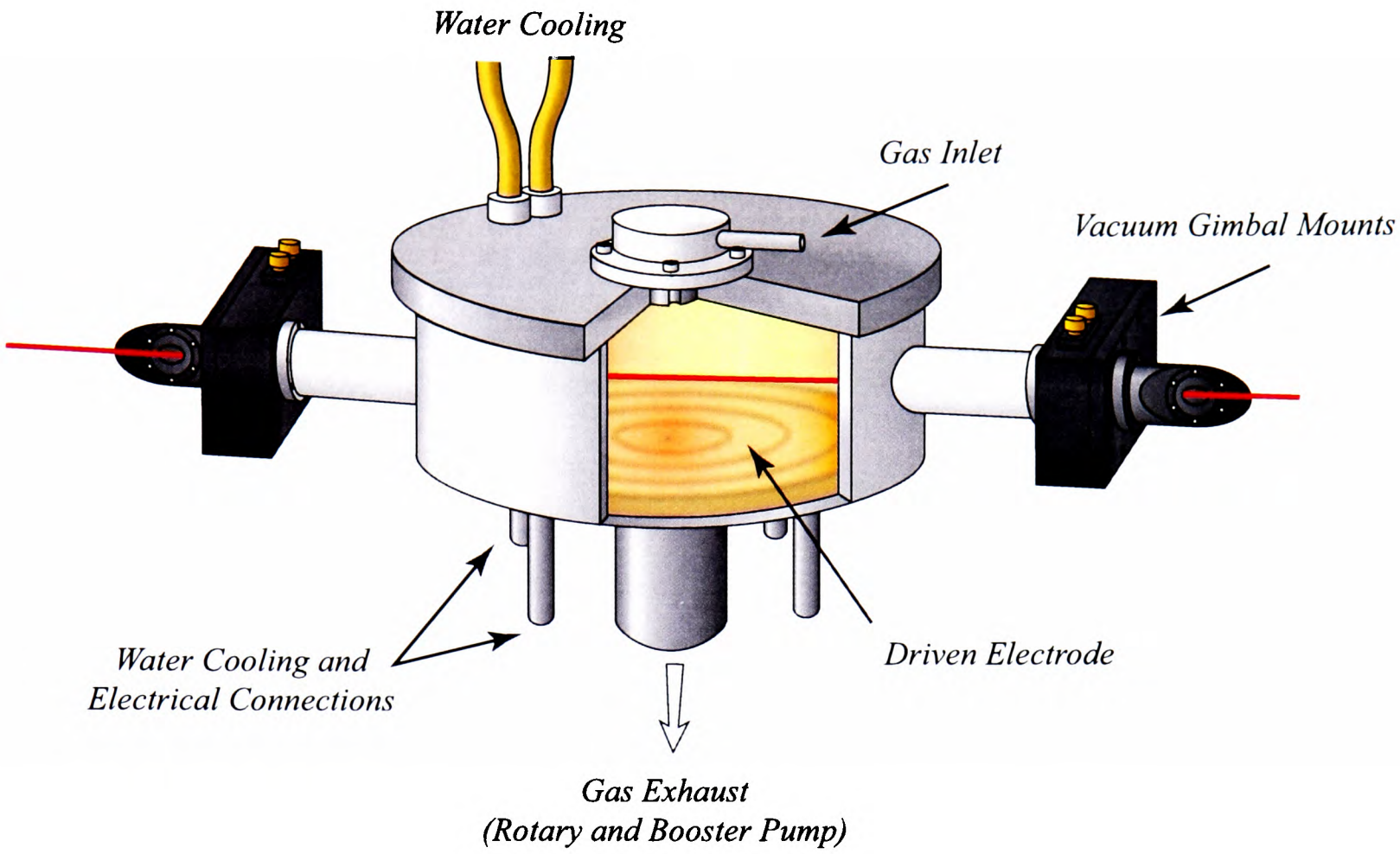

Figure 2.1 Diagrammatic representation of the modified RIE 80 Plasma chamber, showing two of the QVF ports.

The lower driven electrode, separated from the upper electrode by 80 mm, comprised an aluminium 'four legged table' (240 mm diameter) coated in a 50 μm anodised layer and seated in a PTFE cradle. This was fitted with a dark shield mesh to restrict the plasma from extending down the pump outlet under the electrode. The gas was fed into the chamber through a 'showerhead' in the upper grounded electrode. Both electrodes were water cooled and were maintained at approximately 15 °C using a closed loop water cooler.

The energy required to initiate and maintain the plasma was provided by a solid state r.f. power supply (Advanced Energy RFX 600, 13.56 MHz, 600 W maximum power). This power supply functions at 13.56 MHz, a frequency that falls within the region allotted to industrial and research systems which is chosen so as not to interfere with public and government frequencies. This power supply was connected to the chamber *via* a variable capacitive and inductive impedance matching network to minimise the reflected power (measured at the power supply). This was achieved by tuning so that the matching network, chamber and plasma collectively have a real impedance of as close to 50 Ω as possible at the drive frequency.

The net power applied measured at the power supply is not necessarily all coupled into the plasma. In fact, the amount of power transferred from the power supply may be grossly

overestimated[2]. This is because the chamber is behaving like a capacitor and therefore the current flowing is out of phase with the applied voltage[3]. To estimate the minimum true power coupled into the plasma, measurements of the power dissipated into the upper electrode and base plate cooling water were made. It was found by observing the temperature increase in a known flow of cooling water that about 30 % of the power was transferred from the power supply to the water cooling of the fabric of the chamber excluding the lower electrode, although the exact proportion varied significantly with pressure and feedgas.

2.2.3 The Gas Handling System and Pumping System

The gas handing system comprised of a set of mass flow controllers (ASM AFC260 total flow 100 or 200 sccm (standard cubic centimetres per minute) of N_2). Gases were mixed on the low pressure side of the controllers and fed into the chamber *via* the 'showerhead' in the upper electrode. The chamber was pumped by a rotary pump/Roots blower combination (Edwards E2M40 & EH250) *via* the 50 mm diameter aperture under the driven electrode and a 70 mm diameter corrugated flexible tube, which was necessary to isolate the chamber and its mounted optics from the vibrations of the pump.

The chamber pressure was manually controlled by a VAT 70 mm valve on the outlet, and was measured using a capacitance manometer (MKS 220A, 0 - 1 Torr). The base pressure of the chamber was lower than 0.5 mTorr, with a leak rate for the system of lower than 1 mTorr/min, equivalent to less than 0.2% of the total flow in the experiments described in this Thesis. The precise flow patterns inside the chamber were not determined, but the residence time of species was estimated to be approximately 350 msec under conditions of 50 mTorr and 42 sccm. The feed gases used were argon (BOC 99.995 %), nitrogen (BOC 99.998 %) or helium (BOC 99.996 %)

2.2.4 Modifications to Reduce Radiated Noise

Equipment such as personal computers, optical diagnostics and, most critically, diode lasers were found to be adversely affected by the high frequency noise radiating from the plasma system. The relative amount of electrical noise radiated by the system was measured using a length of unshielded cable wrapped around a ferrite ring across the input of a LeCroy 9314 M digital oscilloscope (300 MHz 100 Msamples/s). The WP02 waveform processing firmware includes a fast Fourier transform (FFT) routine that was used to convert the recorded time trace into a frequency spectrum. An example of one of these spectra is shown in Figure 2.2.

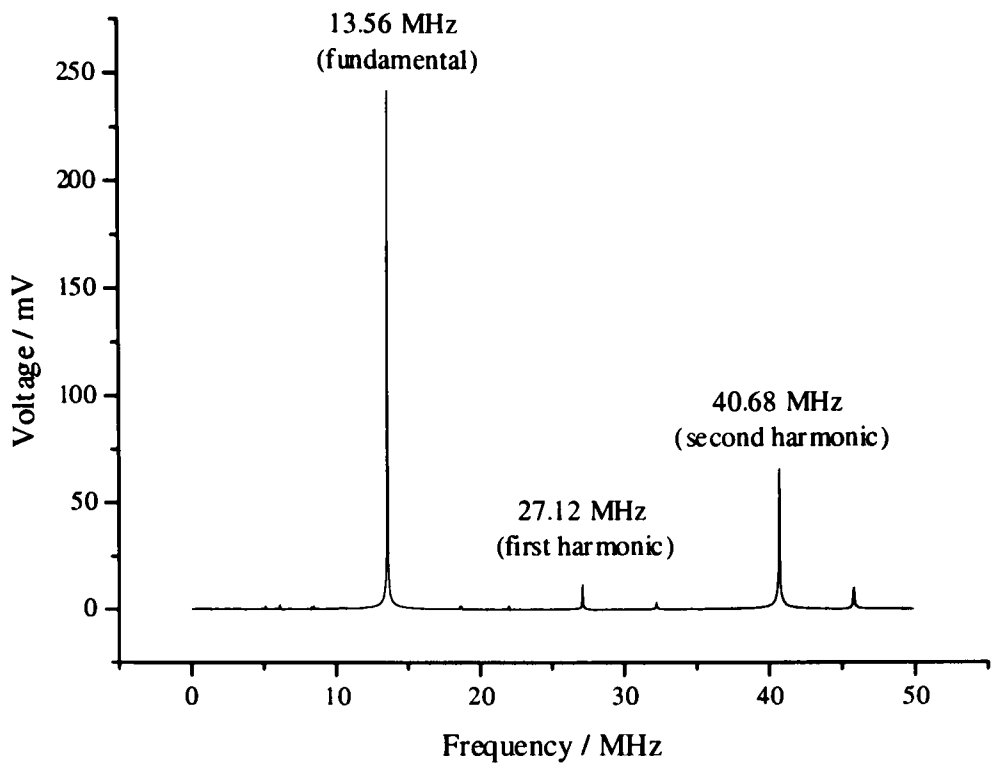

Figure 2.2 Noise spectrum of the RIE 80 plasma chamber, recorded using a simple aerial.

To reduce the radiated noise, several modifications were made to the system. Firstly, the matching network was moved into the Faraday cage containing the base of the chamber, thus removing the requirement for a transmission cable. Secondly, a further aluminium Faraday cage was constructed around the chamber with the only apertures being those necessary to allow optical access and for the input of gas and water. Thirdly, the power return was separated from the Faraday cage earth at all points apart from the power supply, thus reducing the current flowing in the cage and cable screen to a minimum. An electrical schematic of the resulting system is shown in Figure 2.3. Finally, the mains electrical supply to the capacitance manometer and the r.f. power supply was filtered. The signal line from the capacitance manometer was also filtered. These modifications were found to reduce the radiated noise at 13.56 MHz and its low harmonics by more than two orders of magnitude, greatly reducing the effects of the discharge on the surrounding instrumentation. However, some noise effects could still be observed, for instance on the spectral output of diode lasers operating within the laboratory. This interference could be further reduced with the use ferrite rings on all signal and power cables.

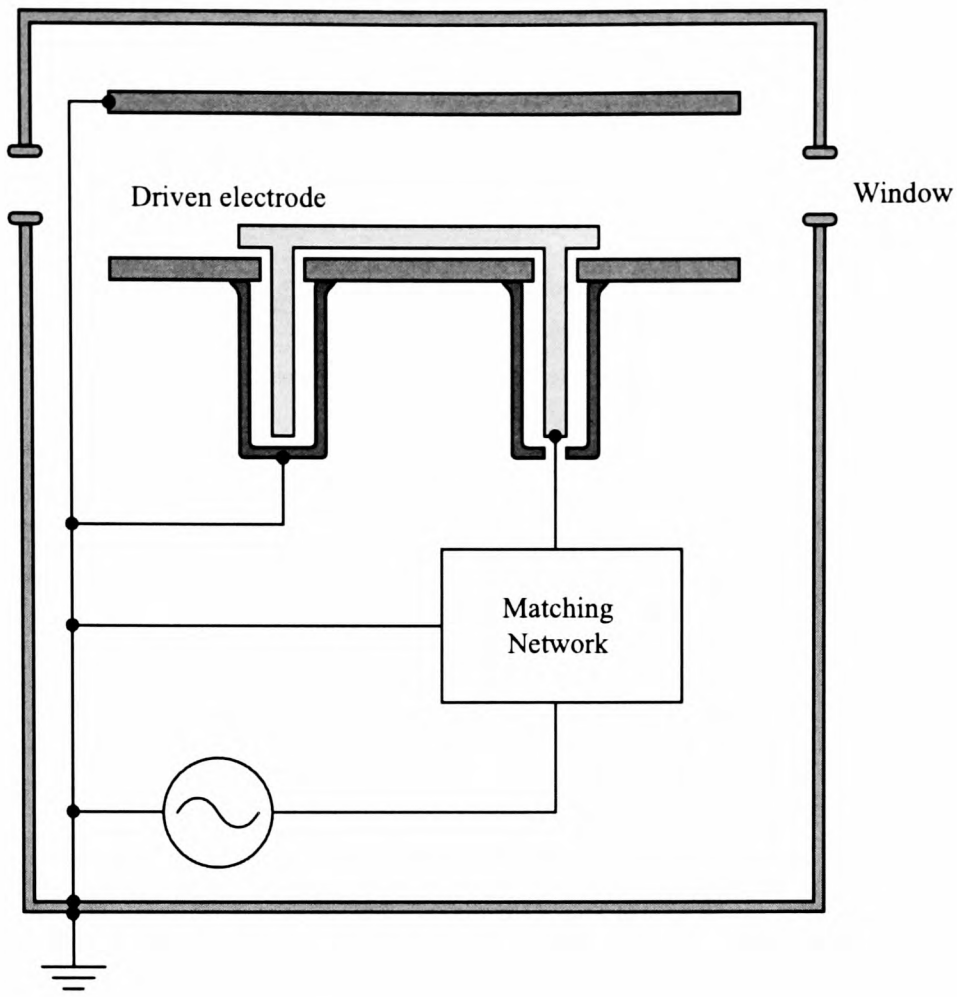

Figure 2.3 Schematic of the electrical connections of the modified RIE 80 capacitively coupled plasma chamber.

2.3 The Inductively Coupled Plasma (ICP) System

A recent advance in industrial discharge technology is the development of low-pressure, high density discharges. An example of this type of system is given in this section. These inductively coupled plasma (ICP) systems have a larger ion density than CCP systems for the same input power density because the power is applied through a dielectric material and therefore sheath voltages are significantly reduced. Ion fluxes and ion impact energies at the work piece can be controlled by placing it on a separately (capacitively) driven electrode within the discharge. Processing can therefore be controlled to a greater degree than in a capacitively driven system.

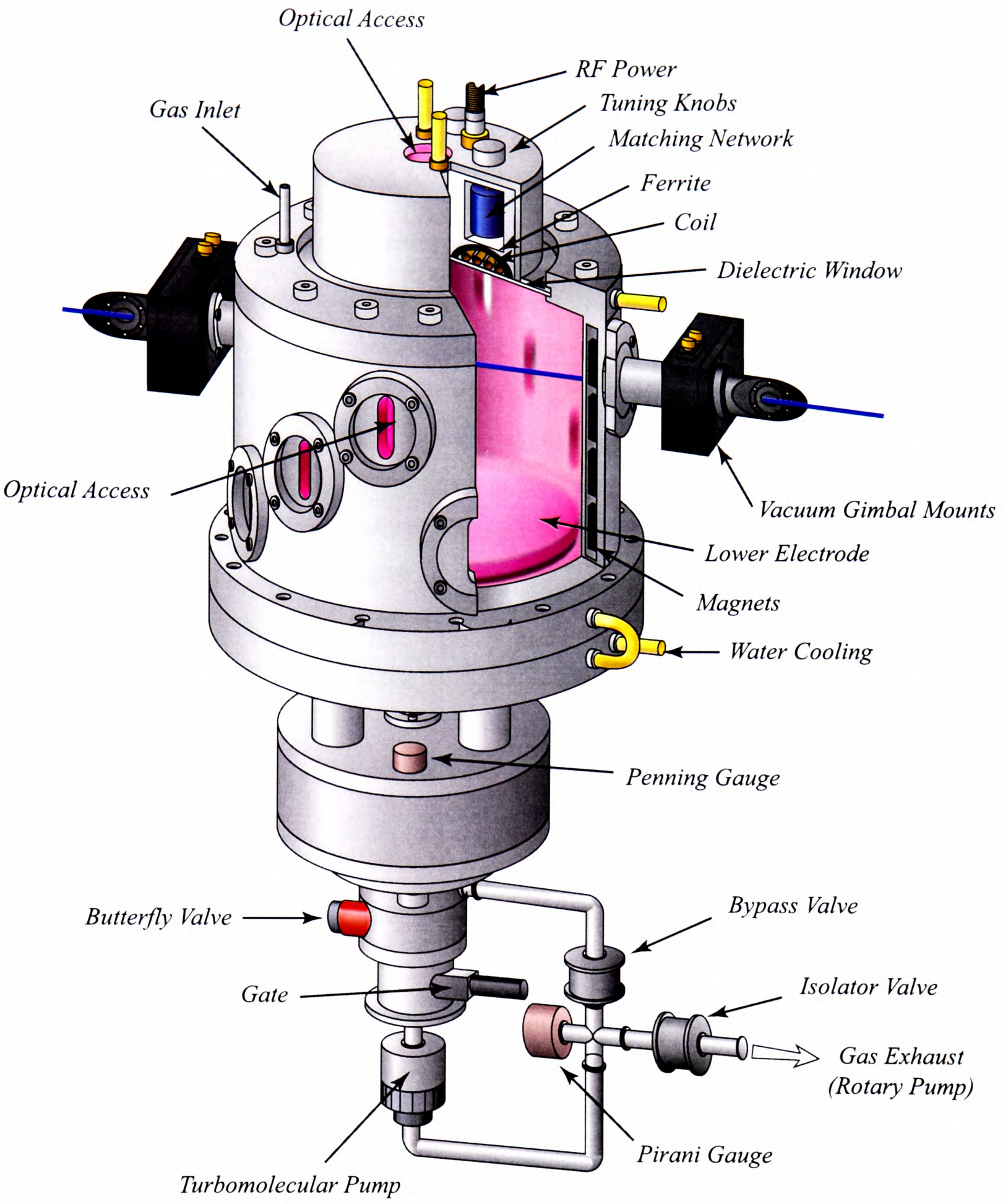

Figure 2.4 Diagrammatic representation of the inductively coupled plasma chamber.

The inductively coupled plasma (ICP) chamber used for experiments described in this Thesis, is shown in Figure 2.4, and was designed primarily for optical investigations. Therefore, unlike the CCP system, the main consideration in the initial design was optical access to all regions of the discharge. The chamber was designed to be compatible with a similar system at

the UKAEA research laboratory in Culham, produced jointly by their beam science and technology department and Nordiko[4]. It is of a similar design to the ICP version of the Gaseous Electronics Conference (GEC) Reference Cell[5], except that optical access is available through the centre of the inductor.

2.3.1 Production of an Inductively Coupled Discharge

The power in an inductively coupled system is transferred into the plasma magnetically, rather than electrostatically, by using a nonresonant inductive coil[1]. The coil is separated from the discharge by a dielectric material (Pyrex glass in the experiments described in this Thesis). The r.f. applied to the coil causes a time varying magnetic field and electric field to be produced within the discharge. The electrons in the discharge are induced to move in a way to oppose this magnetic field (according to Lenz's law[6]). A diagram of how an ICP system functions electrically is given in Figure 2.5.

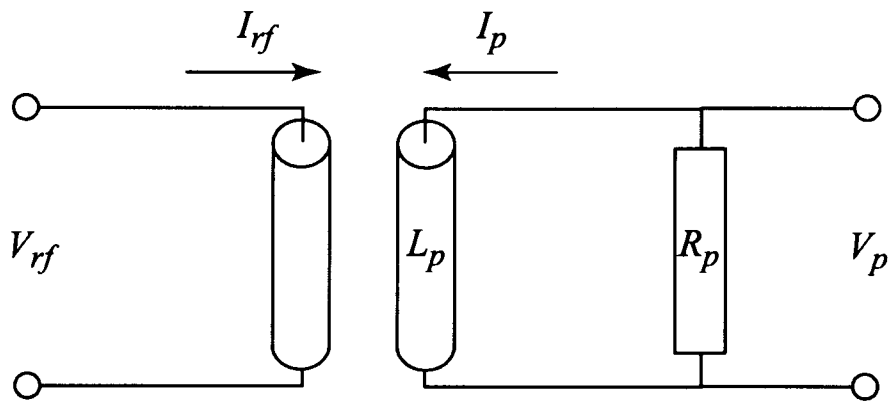

Figure 2.5 Equivalent transformer coupled circuit of an inductive discharge. I_P, V_P, L_P and R_P are the plasma current, potential, inductance and resistance respectively, while I_{rf} and V_{rf} are the applied current and potential.

The plasma resistance, R_p, is inversely proportional[1] to the plasma conductivity and hence inversely proportional to the mean free path λ_{mfp}. This resistance is attributed to the electrons losing energy in collisions (ohmic or collisonal heating), which also further generates ionisation, or by a process similar to stochastic heating, in which the electrons 'collide' with the oscillating electric fields present in the sheath produced by the coil[1].

If the electron density is too low, the current induced by the electron's response to the time-varying magnetic field is insufficient to sustain the discharge. Therefore, to initiate the discharge, *i.e.* create the ionisation, the system must initially be capacitively driven; once the charge reaches a threshold value the system becomes inductively driven, and the power will be coupled into the plasma more efficiently.

2.3.2 The Chamber

The main body of the chamber consists of a 275 mm high aluminium vessel with an internal diameter of 350 mm that was thoroughly cleaned in an ultrasound bath before use. Thirty-two water cooling channels are contained within the walls of the vessel, along with thirty-two slots into which sets of four high-flux magnets (VMX 225 HR) in iron keepers have been inserted. These one hundred and twenty eight magnets provide a field that confines the plasma, reducing recombination losses at the walls and thus increasing the plasma density and uniformity. This type of magnetic confinement has been shown to increase the ion density by about a factor of two in an inductively coupled r.f. argon plasma[7]. Twelve 15×65 mm slots (at three different heights) faced with ISO–63 vacuum flanges, allow optical access to the plasma. For simple optical experiments, these were directly fitted with 12 mm thick quartz windows. For cavity experiments, they were fitted with the aluminium boxes containing high reflectivity mirrors attached to gimbal mirror mounts. The top of the vessel consists of a water cooled stainless steel lid containing a 12 mm thick, 240 mm diameter Pyrex window. The lid also has a ring of small holes around the circumference of the window through which the feed gas flows into the chamber.

A hollow water cooled aluminium electrode of 200 mm diameter was mounted approximately 190 mm below the window in the lid, on an adjustable pedestal controlled by a stepper motor allowing it to be translated vertically by up to 36 mm. An r.f. bias may also be applied to this electrode if required, but for the experiments described here, the potential of this electrode was allowed to float. Around the electrode pedestal, a stainless steel baffle plate acts as a dark space shield to minimise the charge density reaching the pumping system.

The stainless steel chamber base supporting the electrode consists of a 280 mm diameter cylindrical chamber, from which three 78 mm internal diameter 240 mm long tubes connect to a second stainless steel chamber of diameter 225 mm, onto which the pumping system is attached *via* an ISO-63 flange. The space between the three tubes contains the electrode height adjustment mechanism and stepper motor. This base, also water cooled, is mounted directly through a hole cut into the optical table. All the water cooled components were maintained at 15 °C using the closed loop water cooling system.

The pressure in the chamber was measured using a capacitance manometer, and was used as the sensor for a pressure controller, to vary the pressure between 10 and 100 mTorr, with an

accuracy of 1 mTorr, by operating a butterfly valve mounted directly onto the bottom of the chamber base.

2.3.3 The Gas Handling System and Pumping System

If the feed gas consisted of a single component gas (argon, nitrogen or helium) then its flow was controlled by a mass flow controller. If more than one gas was used, a set of mass flow controllers was required, and the gas was again mixed on the low pressure side of the controllers.

The chamber was rough pumped through a bypass valve by an Edwards (E2M2) rotary pump, with the pressure before the pump monitored using a Pirani gauge. After rough pumping, the bypass valve was closed and the chamber was pumped by a Varian Turbo-V70D turbomolecular pump. This was fitted with a fine mesh inlet screen and a vibration damper, designed to reduce the transmission of its intrinsic vibrations onto the optical table. Pressures below 1 mTorr were measured using a Penning gauge. The base pressure of the system, with the turbo-rotary combination, was measured to be less than 10^{-7} Torr, with a leak rate of less than 0.06 mTorr/min. This leak rate is equivalent to less than 0.03 % of the total flow in the experiments described in this Thesis. The residence time of species was estimated to be approximately 10 s under conditions of 50 mTorr and 10 sccm.

The turbomolecular pump could be isolated from the chamber by an ISO-63 electropneumatically operated gate valve (VAT 1203 PA44). The vacuum pumps and valves and their respective controllers, the pressure controller and gauges and the r.f. power supply are automatically sequenced, interlocked and supervised by an in-house designed and constructed programmable controller.

2.3.4 The Source

Above the Pyrex window in the lid is seated a double start 1½ turn planar inductor, constructed from 6 mm diameter copper tubing, through which cooling water flows to maintain its temperature at around 15 °C. The external diameter of the coil is 180 mm and the internal diameter is 120 mm. It is therefore possible to get longitudinal optical access to the plasma through the centre of the inductor through a 75 mm viewport. The coil water cooling is necessary as the r.f. current flowing in the coil can be as high as tens of amps[8], which causes significant resistive heating of the coil. By adding a ferrite material around the coil, it is possible to increase the mutual inductance between the coil and the plasma and so reduce the

coil losses[8]. In this case, a set of 16 ferrite half rings spanned the coil with the aim of enhancing the field inside the plasma chamber, reducing the external field in the viewport and reducing coil power losses.

The coil and matching network consists of two vacuum spaced variable capacitors (Jennings UCSL-5S, one in parallel and the other in series with the coil), contained in an aluminium can to minimise the effects of interference on the plasma diagnostic systems caused by the radiated power from the plasma source. The matching network is used to minimise the reflected power by making itself, the plasma and the coil collectively have a real impedance of as close to 50 Ω as possible at the drive frequency. The power for the source was supplied by either an ENI Power Systems HF300 (capable of delivering up to 400 W) or an Advanced Energy RFX 600 (capable of delivering up to 600 W) power supply.

Preliminary tests showed that the system maintains a stable plasma with a net applied power of below 5 W (at 10 mTorr), although at higher pressures larger powers were required to strike the discharge. Again, in an ICP, just like the CCP, the net applied power (the power applied to the matching network and coil minus the reflected power returning to the power supply, generally less than 5 % of that applied) will not be completely coupled into the plasma[9]. Some of the power is used to heat the cooling water flowing through the inductor and its environment, some will be lost in the matching network and some will be lost in the cabling. In an attempt to measure the power that is transferred from the power supply to the plasma, which is then lost to the surfaces within the chamber by collision of species from within the plasma, the power that was dissipated into the cooling water was determined. This was achieved by isolating the water circuits that cooled the lid body, electrode and base of the chamber. The inlet and outlet temperatures were carefully measured using Pt100 platinum resistance thermometers and the flow rate was also recorded using a pre-calibrated stainless steel ball flow meter. The power dissipated into the fabric of the chamber and then into the water can therefore be calculated from basic thermodynamics[10]. Figure 2.6 shows the results of these measurements; a similar measurement was made of the power dissipated into the water flowing through the inductor. From the figure, it can be seen that at low powers (below 100 W), about two thirds of the net applied power is dissipated into the fabric of the chamber and the rest is lost in the inductor.

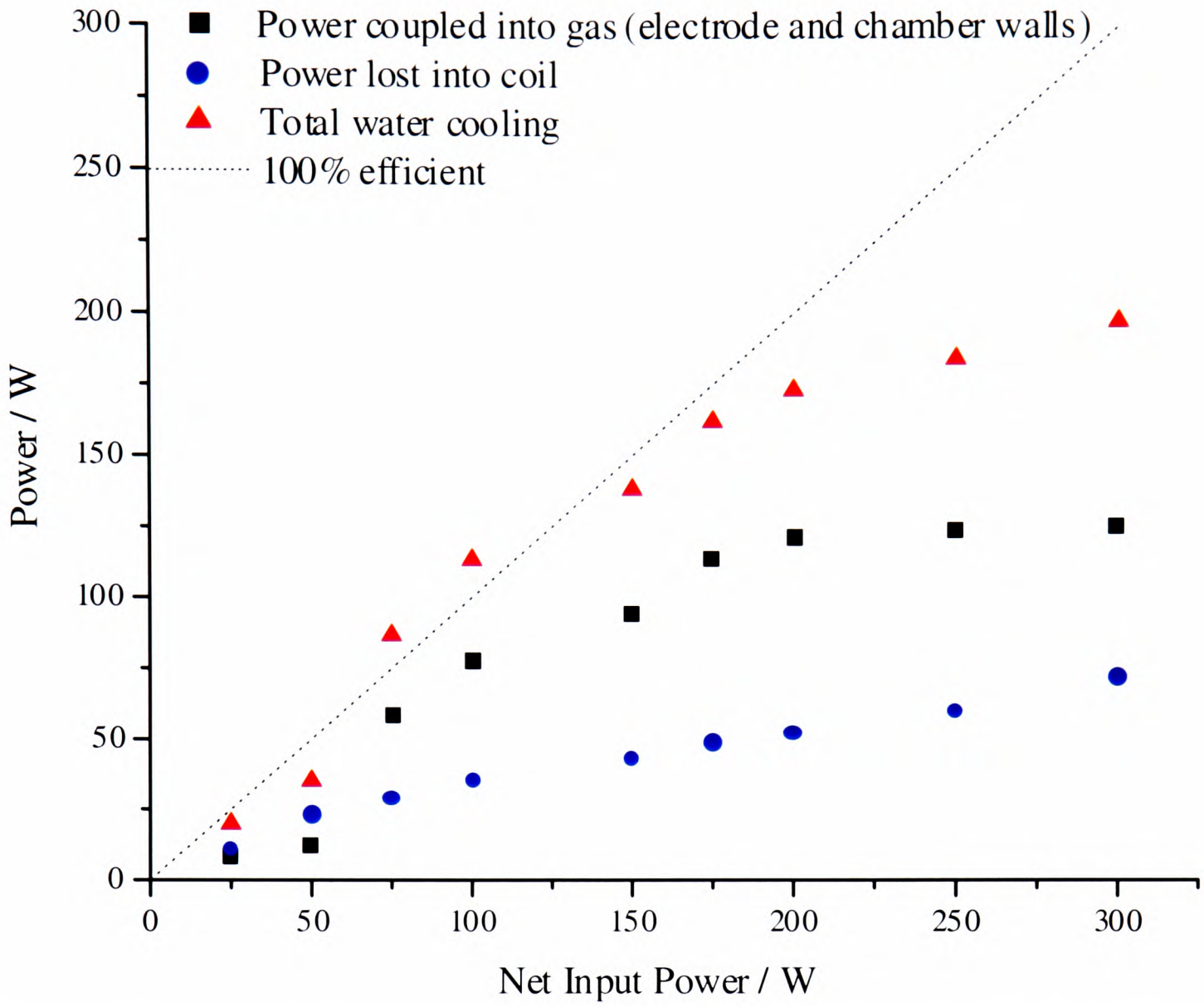

Figure 2.6 A plot showing measurement of the power transferred from the coil to the fabric of the chamber by the plasma in the ICP system.

At higher powers, it is clear that power is lost in other ways. This may well be due to conduction into the optical table and convection losses into the air, because the chamber temperature is significantly above ambient temperature (at a net applied power of 200 W, the temperature difference between the air and the chamber was 7 °C). From the figure, it can be seen that the amount of power lost in the coil is approximately proportional to the net applied power across the whole power range implying that about 25 % of the power applied was lost in this manner. These data suggest that this chamber is more efficient than previously investigated ICP systems[11]. These measurements were made by measuring the power dissipated in the coil at the same current with and without the plasma, on a chamber with a similar matching network, and showed that only 40 % of the power was absorbed into the plasma at 40 mTorr and 32 % at 5 mTorr for an applied power of 400 W.

2.4 Electrical Diagnostics

To compare and characterise the two chambers discussed in Sections 2.2 and 2.3, measurements of plasma properties have been made using a capacitively coupled planar probe. This involves measuring the current flowing into a surface in contact with the plasma when its potential differs from the floating potential of an object in the plasma. In the probe system developed during this project, the probe is biased negatively with respect to the floating potential by application of an r.f. burst. This is analogous to the self-biasing of the driven electrode of a capacitively coupled discharge. A guard ring is placed around the probe to attempt to completely remove the effects of the edge of the probe. The current flowing to the probe can be attributed almost entirely to the positive ions if the probe bias is sufficiently negative, and therefore the positive ion flux from the plasma into the sheath can be obtained. From the dependence of the current with potential is it possible to obtain information on the high energy tail of the electron energy distribution, from which it is possible to estimate the electron temperature. From the combination of the electron temperature and ion flux it is possible to obtain the plasma density.

2.4.1 Experimental Apparatus

The planar probe consisted of a circular aluminium disc (4.5 ± 0.02 mm in diameter) separated from a surrounding guard ring by a thin insulating Makor ring. The area of the guard ring is six times larger than the probe area. The probe is mounted on the end of an aluminium tube from which the guard ring, the probe, and their respective connecting leads are mutually electrically isolated by Makor spacers. Electrical connections from the probe and guard ring were made *via* PTFE covered cables through vacuum compatible BNC sockets. A schematic of the probe is given in Figure 2.7.

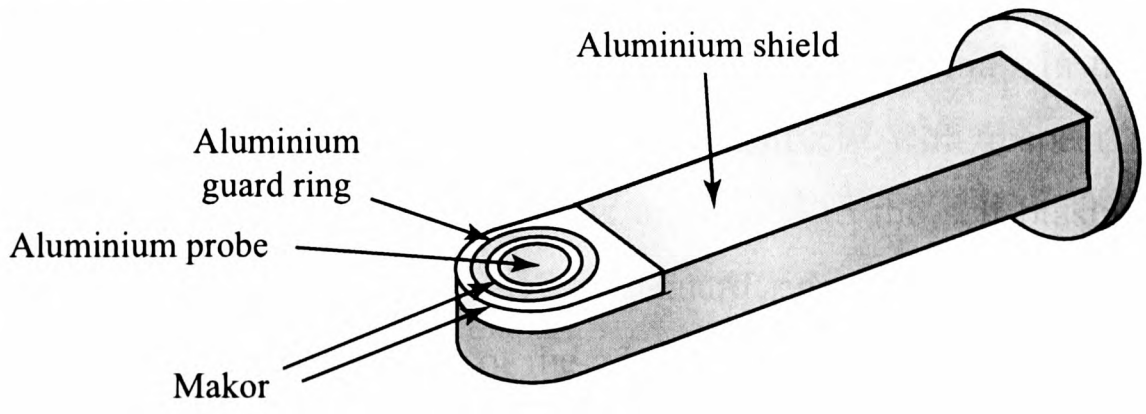

Figure 2.7 Schematic diagram of the probe.

To minimise disruption to the plasma, the probe should be placed flush with a surface within the chamber (an electrode or a wall), thus enabling a direct measurement of the ion flux incident on that surface. The probe was mounted in three configurations in the ICP chamber and one in the CCP system.

Initially the probe was positioned in the ICP chamber flush with the wall through one of the middle row of transverse access slots (position (1)). However, due to the magnetic field produced by the magnets contained within the walls, the probe only gained a very small negative bias. Therefore, a second position (2) was tried involving a lengthening of the probe by 50 mm, while still positioning it in the plasma through the access slot, so as to penetrate the bulk of the plasma. The final probe position (3) pointing vertically upward adjacent to the lower electrode. This position is preferable because firstly, in position (2) the probe will perturb the plasma significantly by its presence in the bulk and secondly, in position (2) it is hard to verify that the effect of the magnets present in the walls has been completely overcome. Within the CCP, the probe was positioned through one of the QVF ports so that it was flush with the chamber walls, with the surface of the probe perpendicular to the electrode surface. In this case, no magnetic confinement was present so that the flux observed by the probe is the same as that striking the walls.

The potential of the probe and the guard ring were recorded using a pair of identical oscilloscope probes with either 10 MΩ impedance or 100 MΩ impedance on a LeCroy digital oscilloscope allowing acquisition of the traces with 11 bit resolution. A diagram of the layout of the measurement circuit is given in Figure 2.8a. The equivalent electrical circuit after the r.f. burst is shown in Figure 2.8b. The parasitic capacitances C_{p1} and C_{p2} are present because of the connecting cables, but were minimised by keeping these cables as short as possible. A pair of similar parasitic capacitances are present in the guard ring circuit but are neglected from the diagram because they do not affect the probe measurements.

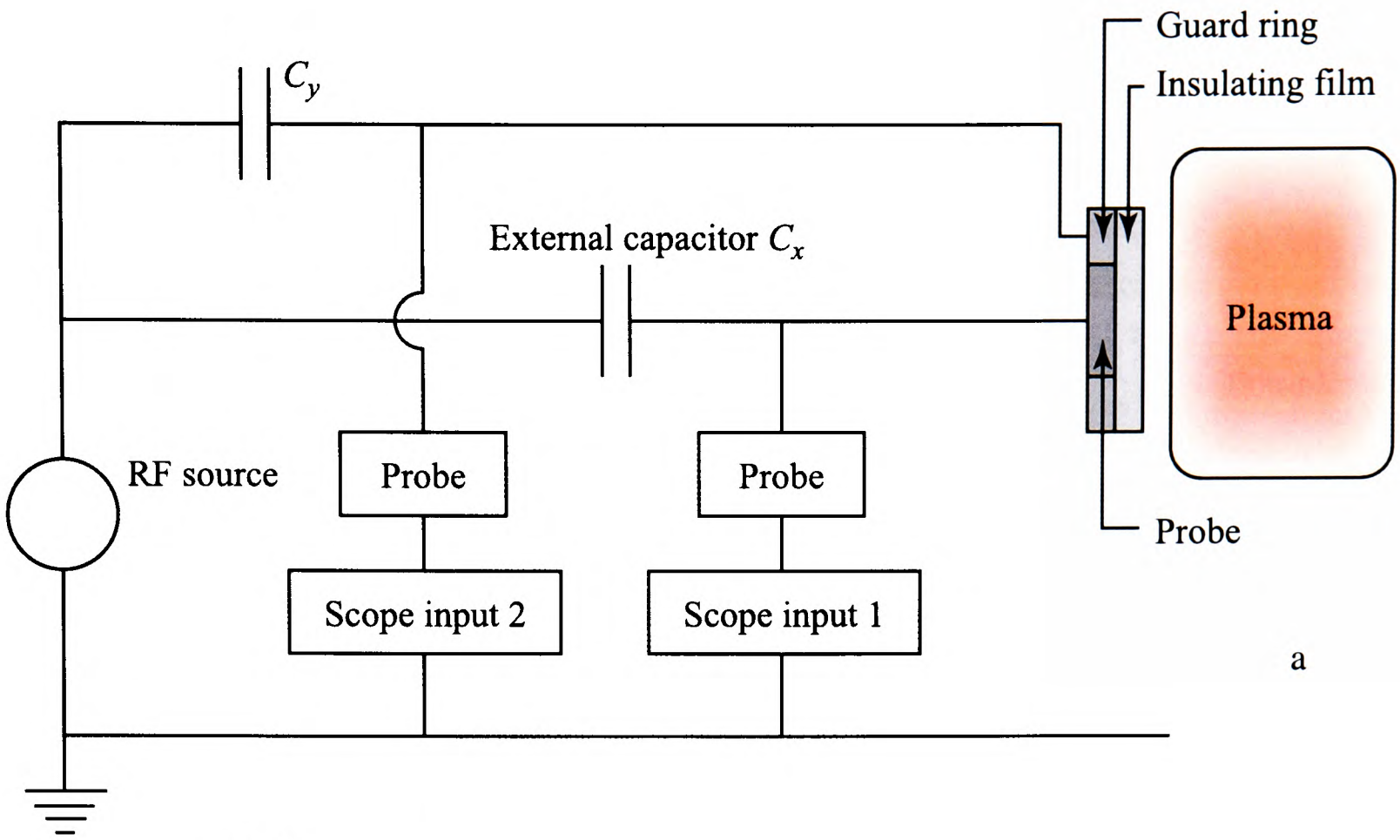

Figure 2.8 Diagram of (a) the measurement circuit and (b) the equivalent circuit at the end of the r.f. burst. The effective capacitance was determined by the external capacitance C_x. C_y is the equivalent variable capacitance for the guard ring. R_p and C_p are the resistance and capacitance of the oscilloscope probe connected to the probe, R_g and C_g are the resistance and capacitance of the oscilloscope probe connected to the guard ring, C_{p1} and C_{p2} are the parasitic capacitances associated with the cables connecting to the probe. Z_{sheath} is the impedance of the plasma sheath and V_{surf} is the potential difference of the probe to ground.

Once recorded on the oscilloscope, the time traces were transferred on to a Pentium PC, *via* a PCI GPIB card (National Instruments), where they were then converted into current voltage characteristics using Microsoft Excel and analysed using Mathsoft MathCad 2000 Professional.

It was necessary, when taking measurements with low ion fluxes, to account for the leakage current through the probe, especially when using the pair of 10 MΩ impedance probes, as it was found to be comparable to the ion current observed. This effect was accounted for simply by correcting the time dependent current observed by adding $V(t)/(10\ \mathrm{M\Omega})$ to it. When using the 100 MΩ probes, the effect is clearly reduced by a factor of 10 and therefore the correction was less important, however it was applied to minimise systematic errors introduced into the measurements.

The r.f. power to bias the probe was provided by a pulsed 13.56 MHz source separate to that maintaining the plasma. An in-house 20 A, 13.8 V power supply was used to power the r.f. source. The high power was required to maximise the negative bias acquired by the probe during the r.f. burst and thus give a long saturation curve (see Section 2.4.2), increasing the accuracy of the ion flux measurement. The pulsed r.f. source was used to bias both the probe and the guard ring through separate variable capacitors and then switched off and the resulting decay trace observed. The guard ring capacitance C_g was varied until the discharge rate was equal to that of the probe. An exact superposition of the two curves of V against t indicates correct tuning. This results in the plasma not being able to distinguish between the probe and guard ring and therefore, for sheath depths less than the difference in radius of the probe and guard ring, edge effects are eliminated. The geometry is therefore two dimensional and fluxes measured at the planar probe should equal those at the interface of the plasma presheath and sheath. For the plasmas discussed in this Thesis, the dominant ions are singly charged, and therefore the mean ion charge is taken to be e.

2.4.2 Theory

The current flowing to the probe can be obtained directly from the gradient of the recorded trace of the time dependence of the potential by

$$I(t) = C_x \frac{\mathrm{d}V_c}{\mathrm{d}t} \tag{2.1}$$

where C_x is the capacitance of the discharging capacitor attached to the probe. If the negative bias acquired by the probe is sufficiently large, the only contribution to the current observed will be due to the positively charged ions present in the discharge; all but the very high energy electrons will be repelled and therefore deflected from the probe. The current flowing into the probe is thus constant (due only to the positive ion flux as the electron current is negligible) and at a maximum. This is called the *saturation current* I_0 and can be obtained from the

asymptote of a plot of current versus potential at large negative potential. The corresponding ion flux incident at the surface of the probe can be found from the area of the probe and the saturation current.

$$Flux_{probe} = \frac{I_0}{eA} \tag{2.2}$$

The flux at the probe can be assumed to be the flux at the plasma-sheath interface using the assumption that all ions that enter the sheath above the probe will be accelerated to it by the electric field existing as a result of the potential difference between the bulk and the probe. The flux will be equal to the product of the ion density and the velocity of the ions in the direction of the probe, v_{0z}, at the interface of the sheath and plasma. A minimum for this velocity can be obtained from the *Bohm sheath criterion*[12].

$$v_{0z} \geq v_B = \sqrt{\frac{kT_e}{m_i}} \tag{2.3}$$

This velocity, v_B (the *Bohm velocity*[12]), is the minimum velocity required for an ion to enter the sheath. This is because the sheath has a higher positive ion density than electron density owing to a positive space charge shielding of the electrically neutral plasma from the wall. All ions with a velocity greater than the Bohm velocity will be accepted into the sheath. The region adjacent to the sheath is called the presheath. The field in the presheath is determined by the electrons and therefore their temperature determines the ion velocity. By equating the kinetic energy attained by the ion across the presheath ($\frac{1}{2}m_i v_B^2$) with the potential energy drop across the presheath (eV_{ps}) it is possible to obtain the result that the energy gained per ion across the presheath is $kT_e/2$. Therefore, to obtain the ion density in the bulk, n_i, it is necessary to apply the Boltzmann relation across the presheath[1]

$$n_s = n_i e^{\frac{-eV_{ps}}{kT_e}} \tag{2.4}$$

where n_s is the ion density at the sheath-presheath interface. This expression, with $eV_{ps} = kT_e/2$, gives $n_i \approx 1.65 n_s$.

The maximum ion density, $n_{i(max)}$, can be obtained from the ion flux by assuming that all the ions that enter the sheath are travelling at the Bohm velocity of ions at the presheath-sheath interface.

$$n_i \leq n_{i(\max)} \approx \frac{1.65 Flux}{v_B} \tag{2.5}$$

To obtain a value of the Bohm velocity it is necessary to evaluate the electron temperature of the discharge, which can be obtained from the probe current voltage characteristic. The shape of this can be explained as follows. Only the ion *saturation current* flows until the potential becomes high enough that the electrons in the high energy tail of the distribution have sufficient energy to reach the probe, reducing the observed rate of discharge of the capacitor, C_x. This reduction of discharge rate increases until eventually the floating potential of the probe is reached, at which point the positive ion current is exactly matched by the electron and negative ion current.

The current due to the electrons can be obtained assuming a Maxwellian electron distribution at a temperature T_e. The total current variation with time is then given by the difference of the ion current, I_0, and the electron current[13].

$$I(t) = I_0\left(1 - e^{\left[\frac{e(V(t)-V_0)}{kT_e}\right]}\right) \tag{2.6}$$

where V_0 is the steady floating potential and V is the potential of the probe surface. The current-voltage characteristics were fitted to this expression to obtain the parameters I_0 and T_e.

The reproducibility of the method was investigated[14]. Twenty measurements were made, over a short time, at a power of 100 W and at a pressure of 10 mTorr in the ICP chamber, and were found to give a standard deviation of less than 1 % in the *saturation current* and less than 2 % in the electron temperature. The reproducibility of these results is unusually high; errors ≥ 20 % in plasma physics are not uncommon[15].

This procedure of measurement of the electron temperature effectively involves fitting to the high energy tail of the distribution and then extrapolating the entire distribution from this tail. This is because even though the floating potential of the probe is still below the plasma potential only the highest energy electrons have sufficient energy to cross the sheath. To measure the entire electron energy distribution, a Langmuir probe could be used but with the disadvantages over the planar probe as discussed in Section 1.5.1.

An example of the raw data trace of probe potential (and guard ring potential) against time is given in Figure 2.9a. This clearly shows the initial straight line (in the saturation region) as the potential rises linearly with time and then the plot curves asymptotically to the floating

potential. Figure 2.9b shows the corresponding current against potential characteristic of the probe, obtained by application of equation (2.1).

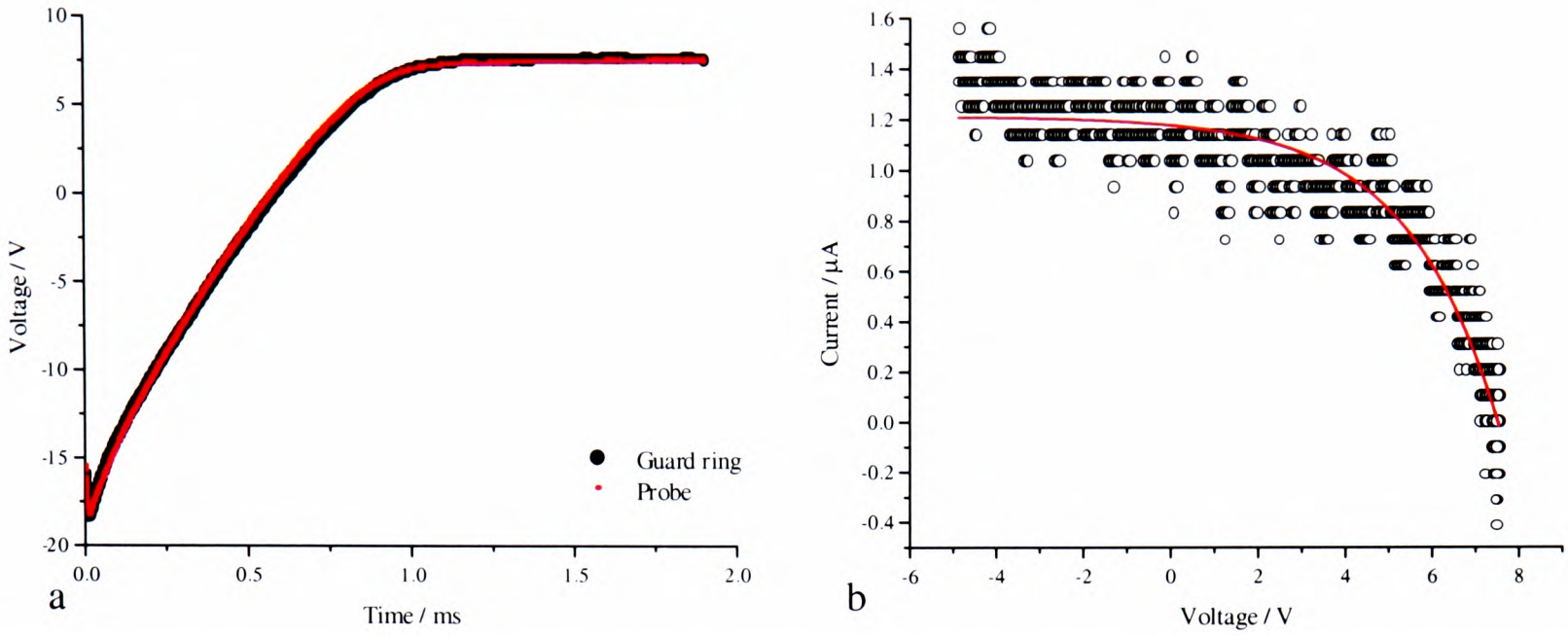

Figure 2.9 An example of the raw data obtained in the ICP system for a 60 W N_2 plasma at 10 mTorr, (a) probe and guard ring potential against time and (b) the corresponding current and voltage characteristic.

2.4.3 Ion Flux Measurements in the CCP System

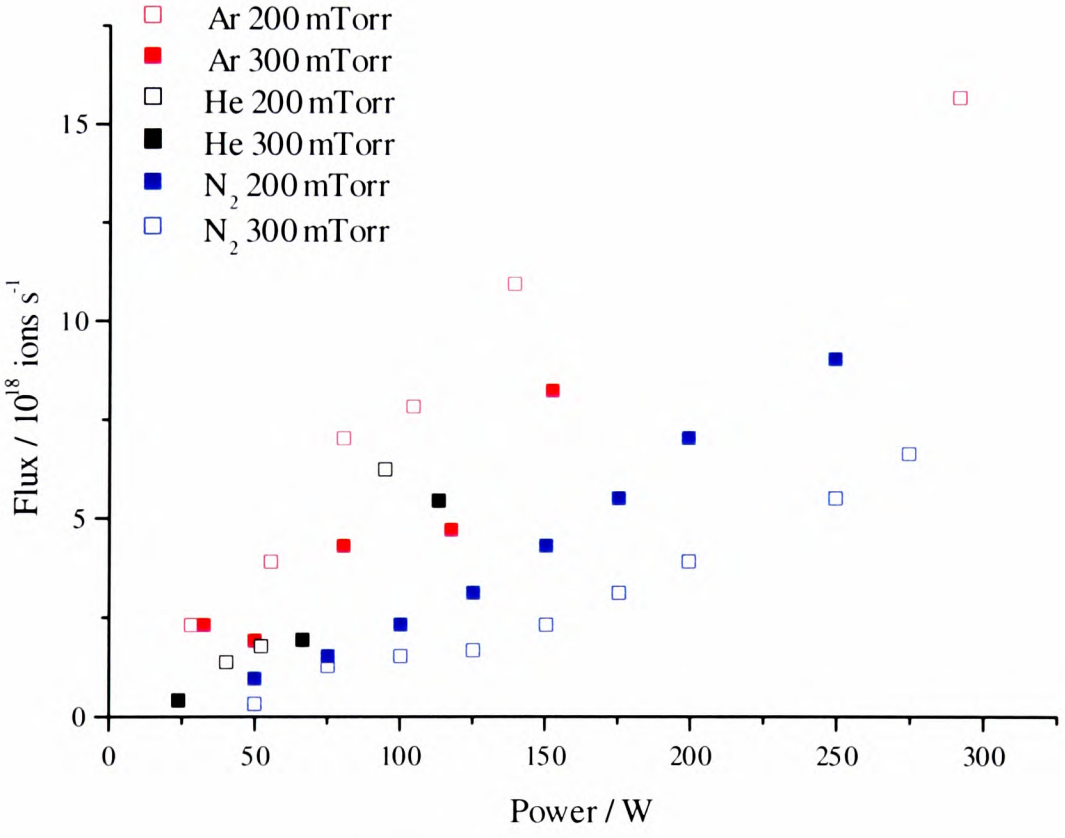

Figure 2.10 The variation of the ion flux in the CCP chamber with power at two different pressures for the three different flow gases (argon, helium and nitrogen).

Figure 2.10 shows the variation of ion flux in the CCP system with power for two different pressures of argon, helium and nitrogen plasmas. These ion fluxes are observed to increase as the power applied is increased, which can be rationalised by the conservation of energy per unit time. The only energy lost from the discharge will be that transferred to the fabric of the

chamber by collisions and that lost by energetically excited (mainly neutral) species leaving the discharge through the flow outlet, ε_n per ion lost to the wall. Therefore, the power lost can be found from the product of the particle flux with the surface, the total surface area available for particle loss and the energy lost per particle[1]. The mean kinetic energy lost per electron is found to be $2kT_e$ for Maxwellian electrons. The mean kinetic energy lost directly *via* collisions with the fabric of the chamber per ion, ε_i, depends largely on the sheath potential due to the acceleration of the ions by the corresponding electric field. The plasma is electrically neutral overall, hence the number of electrons lost is equal to the number of ions. Therefore, the mean energy lost per charged particle pair is the sum of the mean energy lost per ion and per electron. The mean energy lost by neutrals can be directly related to that lost *via* charged species because the energy stored by the neutral species in the plasma is initially obtained by recombination of ions and electrons or collisonal excitation by these charged species. Thus, the mean energy lost by the neutral species can be directly related to the mean energy lost by the ions or electrons from which they were formed. This can therefore be expressed as an energy loss per ion lost to fabric of the chamber. From this it is possible to write an expression for the total mean energy lost per ion, ε_T.

$$\varepsilon_T = \varepsilon_n + 2kT_e + \varepsilon_i \tag{2.7}$$

Thus the energy lost per unit time can be found from the product of ε_T, the total surface area of the chamber, A_{sur}, and the ion flux (the product of the Bohm velocity and ion number density at the sheath edge). This power loss is equal to the power absorbed by the plasma in a steady state of operation, P_{abs}, given by

$$P_{abs} = 0.61 n_i v_B A_{sur} \varepsilon_T \tag{2.8}$$

Therefore, in agreement with that observed in Figure 2.10, the ion density is predicted to increase with increasing power absorbed by the plasma providing that the Bohm velocity and total mean energy lost per ion do not change significantly. Both properties are weakly dependent on the electron temperature, which is observed to change only slightly during these experiments.

The flux in the argon plasma is greater than that observed in either the nitrogen or helium plasma. A significantly greater flux in an argon discharge than the nitrogen discharge was previously observed[15] in a GEC reactor[5]. This is due to the lower electron densities observed in nitrogen plasmas compared to those measured in argon plasmas[16]. The lower flux in the helium plasma than the argon plasma can be explained by its significantly larger ionisation

potential (IP_{He} = 24.6 eV and IP_{Ar} = 15.8 eV)[17] and therefore the energy lost by the plasma for each ion electron pair removed is greater in helium than in argon and thus a lower plasma density will result.

The figure clearly shows that the flux decreases with increasing pressure. This can be explained because the mean free path of the electrons decreases as the pressure increases, resulting in a reduction of the electron temperature and therefore a decrease in the flux due to a lower ionisation rate. This effect was observed previously by an optical method (LIF) under the same conditions in a nitrogen plasma produced in this system[18].

In all three plasmas the electron temperature was found to be between 16 000 K and 39 000 K (corresponding to energies of 1.4 to 3 eV respectively). As mentioned previously electron temperature measurements are much more susceptible to errors than flux measurements. Within the expected errors of the measurements the electron temperature was found to be independent of power. An increase in pressure of 100 mTorr decreased the mean value of the temperature by approximately 10 % (a value well within the expected experimental error). Similar effects were certainly observed in the ICP system (see Section 2.4.4). To understand these electron temperature dependencies, charged particle conservation must be considered; in the steady state plasma the rate of production of ions must be equal to the rate of ion loss. The rate of production of ions in the entire plasma volume, V can be written as a the rate at which the ion electron pairs are created (almost exclusively) by an energetic electron colliding with a neutral gas molecule.

$$\text{Production rate} = k_i(T_e) n_g n_e V \tag{2.9}$$

Here n_g is the neutral gas number density (proportional to the pressure), n_e is the electron number density and $k_i(T_e)$ is the electron temperature dependent rate constant. This is equal to the loss rate, the product of the flux of ions entering the sheath, $0.61 n_i v_B$, and the total surface area for particle loss, A, *i.e.*,

$$0.61 v_B n_i A = k_i(T_e) n_g n_e V \tag{2.10}$$

However, because the plasma is electrically neutral, the number of ions in these electropositive plasmas must be equal to the number of electrons ($n_i = n_e$), thus this expression reduces to

$$\frac{k_i(T_e)}{0.61 v_B} = \frac{1}{n_g d_{eff}} \tag{2.11}$$

where d_{eff} is the effective plasma size (V/A). Equation (2.11) implies that T_e is independent of the plasma density and therefore the input power as observed. The rate constant $k_i(T_e)$ can be approximated by an Arrhenius relationship over a small temperature range with an activation energy corresponding to the ionisation potential of the neutral species.

$$k_i(T_e) = k_0 \, e^{-\left(\frac{IP}{kT_e}\right)} \tag{2.12}$$

Thus for a particular feedgas, the Bohm velocity and the ionisation rate constant depend only on the electron temperature. Also, as the temperature dependence of the ionisation rate constant from equation (2.12) is stronger than the square root dependence of the Bohm velocity, the ratio $v_B/k_i(T_e)$ depends on the pressure (n_g) in the discharge, the electron temperature is predicted to fall as the pressure is increased as observed.

The electron temperature is expected to be different for different feedgases due to different ionisation potentials and electron energy dependent collision cross sections. Because of the substantial variations in the electron temperature measurements it is unfortunately impossible to make sensible comparisons of the three plasmas.

2.4.4 Ion Flux Measurements in the ICP System

Measurements on a nitrogen plasma in this system have been previously recorded[14,19], and are reproduced together with new results on argon and helium plasmas, for comparison with other plasmas in this system and measurements made in the CCP chamber.

The initial measurements were made with the probe in position (1) (flush with the wall). In this position the probe gained insufficient negative bias to allow measurements to be made, implying the charge loss rate to the walls is small.

Lengthening the probe into the bulk of the plasma, position (2), allowed measurements to be taken at the expense of perturbations to the discharge. These measurements[19] show the same trends in the ion flux and electron temperature with plasma parameters in a nitrogen plasma as the measurements[14] made at position (3). However, the ion flux was found to be about an order of magnitude lower at position (3) than position (2) and the electron temperature was found to be about a factor of two lower. The difference in ion flux can be explained in terms of the probe position relative to the source; in position (2) it is much closer to region of plasma generation (closer to the coil), and therefore the charged species in the plasma have less time to recombine before arriving at the presheath-sheath interface of the probe than those impinging

on the sheath of the probe in position (3). The difference in electron temperature can be explained by a similar argument; the electrons will have undergone more collisions due to an extended average lifetime before they are observed at position (3) than those observed at position (2). These collisions, although inefficient[1], reduce the electron velocities and hence their temperature. Although position (2) gives larger fluxes and higher temperatures, because the probe protrudes into the bulk, significant plasma perturbation must result and hence the results discussed in this section were recorded with the probe in position (3) adjacent to the lower electrode.

Figure 2.11 shows how the ion flux incident on the probe varies with power in three different plasmas (argon, helium and nitrogen) at 10 mTorr. From this, it can be seen that in all the plasmas the ion flux increases with increasing power. This can be explained in the same way as the variation observed in the CCP; that the higher flux causes an increased energy loss rate compensating for the increased input power. From the figure it is clear that the ion flux is again higher in the argon plasma in comparison to the other plasmas. This is due to their different ionisation potentials and ionisation cross sections and a more complete explanation for the different fluxes is given in the previous section.

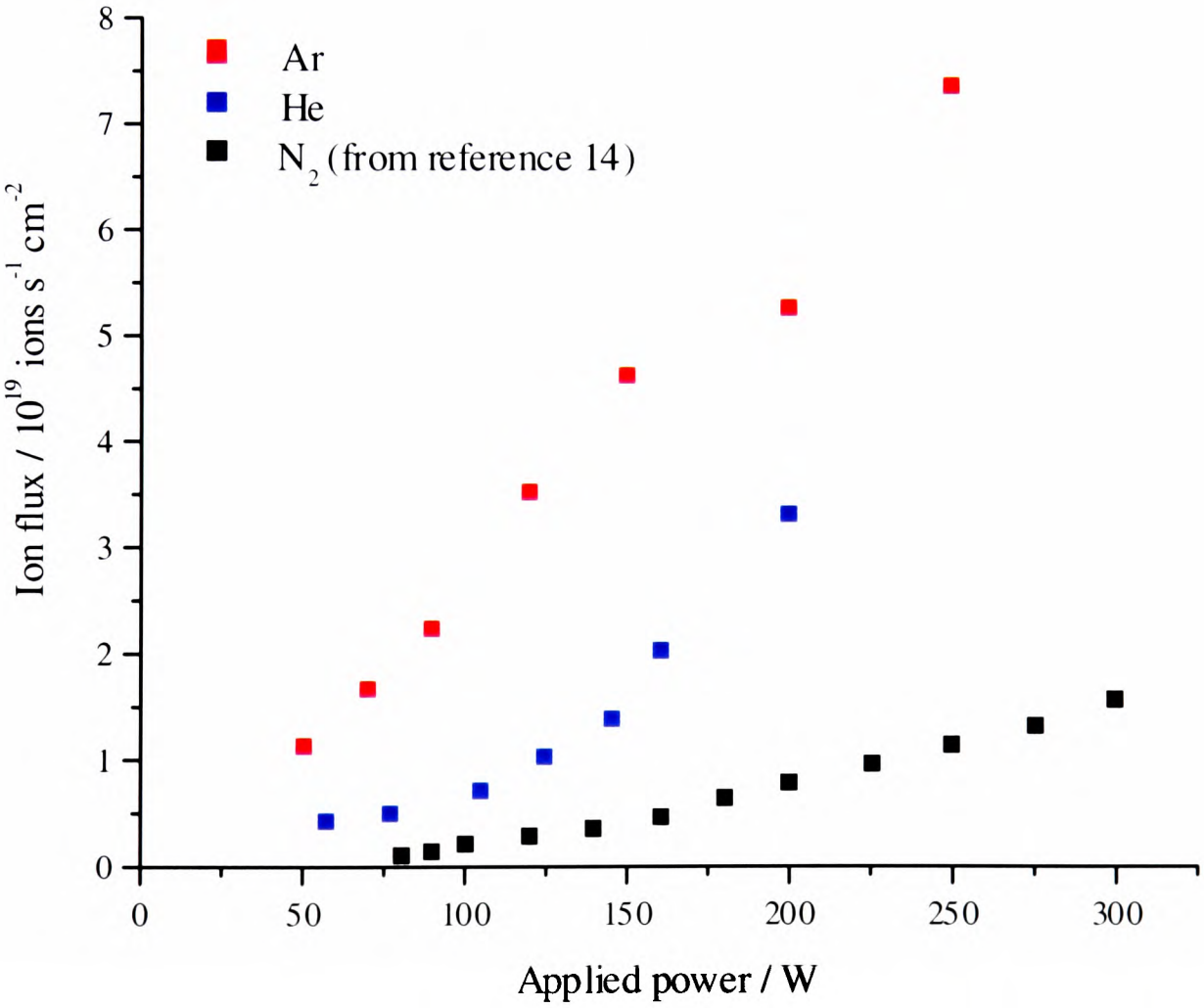

Figure 2.11 The variation of the ion flux in the ICP chamber with power at 10 mTorr for the three different flow gases (argon, helium and nitrogen).

At low pressure in nitrogen plasmas a discontinuity in the gradient of the ion flux curve with power has been observed at low power[14]. To further investigate this effect the measurements were extended to two different pressures in helium/argon plasmas at different applied powers and these measurements are displayed in Figure 2.12. However, only at 10 mTorr in helium was a discontinuity observed, and even this was considerably less obvious than that in the previous measurements. Therefore, as conformation the measurements previously taken in the nitrogen plasma were repeated, and these are shown on Figure 2.13.

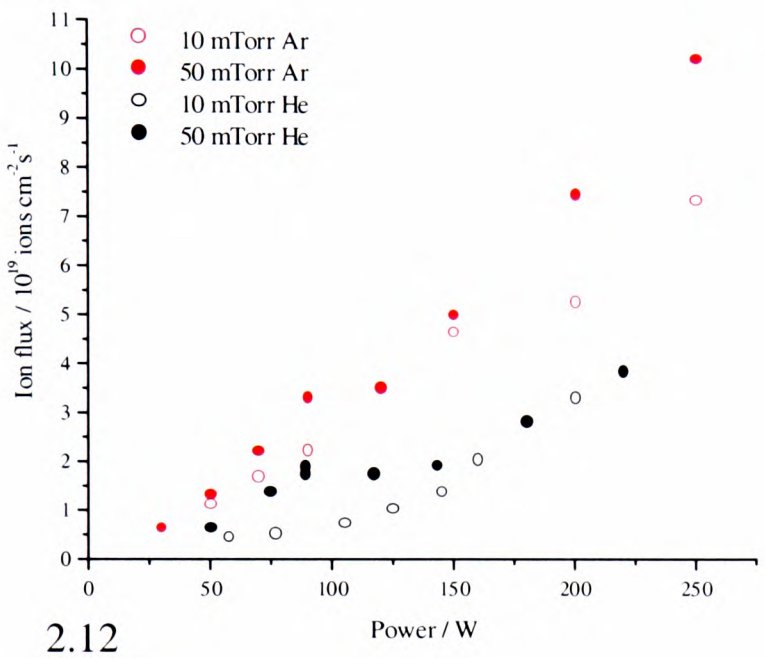

2.12

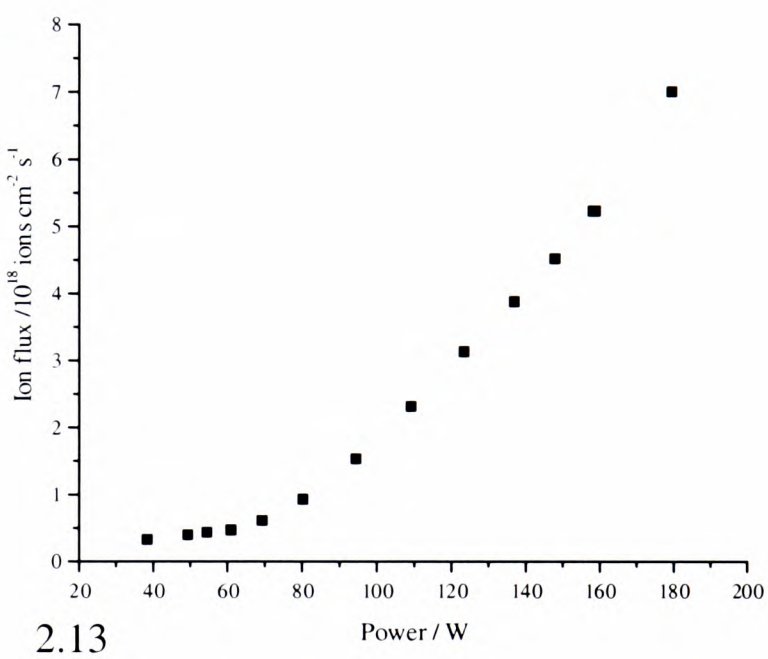

2.13

Figure 2.12 and 2.13 The variation of the ion flux in the ICP chamber with power at (2.12) two different pressures and two different flow gases (argon and helium) and (2.13) 10 mTorr of nitrogen.

Clearly visible in Figure 2.13 is a discontinuity in the gradient above which the rate of change of flux with power is greater than that below it and at this point a significant change in the intensity of the optically induced plasma emission was also observed. This can be explained in terms of the transition between the discharge being produced entirely capacitively, to both inductively and capacitively, as discussed in Section 2.3.1. At this transition, the efficiency of the coupling of the power into the plasma increases and therefore the ion density increases. The point at which this transition occurs is found to increase with pressure. This can be explained by the decrease in mean free path decreasing the plasma conductivity and therefore a higher power is required to generate sufficient conduction for the plasma to couple efficiently to the changing magnetic field produced by the coil. This also accounts for the fact that at lower pressure, the coupling efficiency is higher than at higher pressures (the plots are steeper at low pressure than those at high pressure).

It has been proposed that around the discontinuity point a hysteresis effect may be observed[14], *i.e.* once the charge density required to inductively couple power efficiently into the discharge was reached the applied power could then be reduced and the discharge would continue to

operate inductively. The curve of ion flux against applied power should therefore be dependent on whether the measurements were taken whilst increasing the power applied or decreasing it. To test this hypothesis a set of measurements were recorded firstly by increasing and then decreasing the power applied at a pressure of 10 mTorr and the results are shown in Figure 2.14. Although again the discontinuity is obvious, no detectable hysteresis was observed, implying that it is too small to detect with the present system.

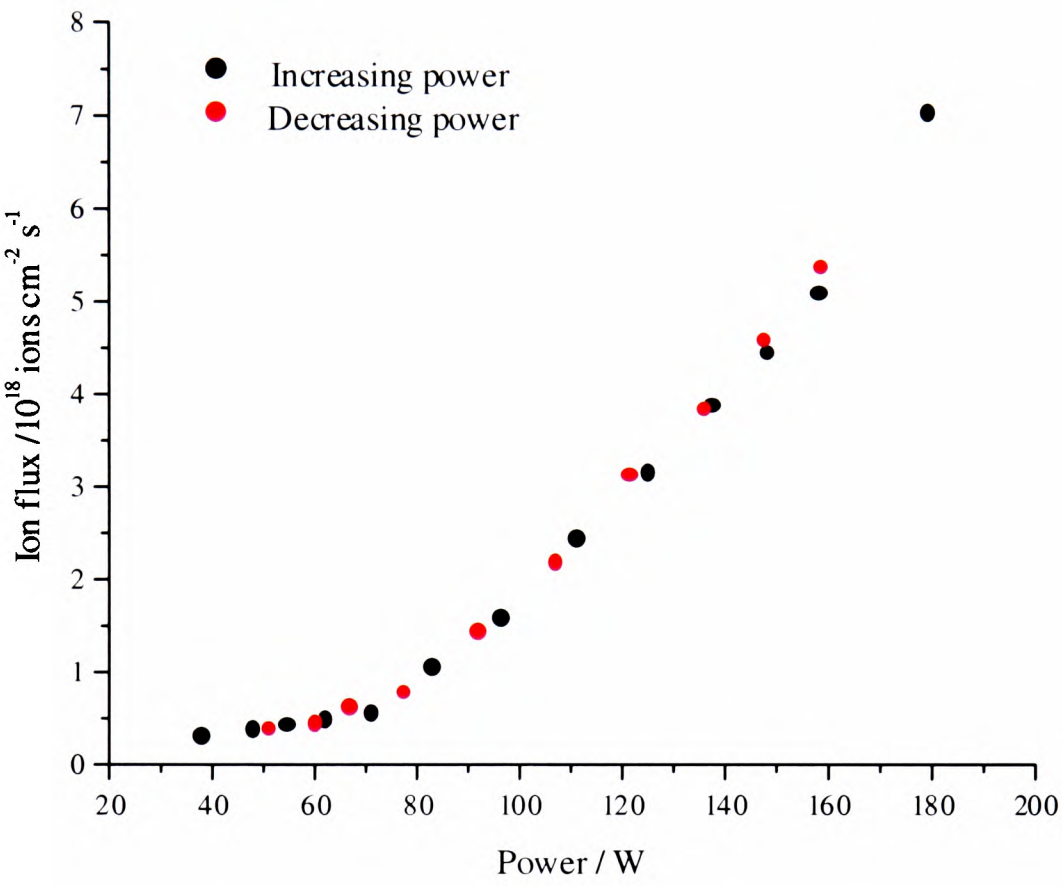

Figure 2.14 Variation in ion flux at 10 mTorr in nitrogen by increasing and then decreasing the applied power.

Figure 2.12 clearly shows that the flux decreases with increasing pressure. As in the CCP system, this can be explained by the decrease in the mean free path of the electrons, as the pressure increases, causing a reduction in the electron temperature. For an entirely inductively produced plasma, this reduction of the mean free path increases the plasma resistance and therefore decreases the current induced in the plasma, reducing the ionisation rate and hence decreasing the ion density and the ion flux.

	kT_e / eV at 10 mTorr	kT_e / eV at 50 mTorr
He	4.4 ± 1.8	2.5 ± 0.3
Ar	2.6 ± 0.9	2.3 ± 0.7
N_2	3.0 ± 0.4	2.1 ± 0.2

The above table gives the average electron energies (above an applied power of 100 W), along with standard deviations of the measurements, at the two different pressures for the three different plasmas. As previously mentioned, the percentage error in the measured values of electron temperature are greater than those of the ion flux. Again within the measurement errors the electron temperature appears almost invariant with power. In the nitrogen plasma an increase in the electron energy (from about 1.3 eV to about 2 eV) is observed at the same power ($\approx$ 75 W) where the gradient discontinuity in the flux curve is observed. Equation (2.12) implies that the electron temperature should be invariant with power, and therefore certainly does not explain the limited power dependence of the electron temperature. This change in electron temperature with power can, however, be again explained by the transition from purely capacitive behaviour discussed above, causing an increase in the electron heating efficiency and thus an increase in the electron temperature.

In this case T_e is certainly found to fall with increasing pressure, which can be explained by the change in pressure reducing the ratio of the ionisation rate constant to the Bohm velocity.

The three different plasmas were found to have different electron temperatures at different pressures which is due to their different ionisation potentials and electron energy dependent collision cross sections. Again because of the large standard deviations found for the measurements it is impossible to make sensible comparisons of the three plasmas.

2.4.5 Ion Densities

From the measurements of I_0 and T_e in both chambers, and using equations (2.3) and (2.5), it is possible to make an estimate of the ion density in the chambers. From these estimates it is possible to directly compare the two chambers.

Measurements in the two chambers at identical powers and pressures are hard to obtain because the CCP system does not operate stably below 200 mTorr and the ICP pressure control system does not work above 100 mTorr. Also, above 50 mTorr in the ICP no obvious capacitive-inductive transition was observed. Despite these difficulties, measurements were made in nitrogen plasmas at 100 mTorr and 250 W in both chambers. The maximum ion density in the CCP system is estimated to be 2×10^9 cm^{-3} ($kT_e \approx 1.5$ eV and $I_0 = 2.2 \times 10^{18}$ ions cm^{-3}s^{-1}) while that for the ICP system is 4×10^8 cm^{-3} ($kT_e = 1.5$ eV and $I_0 = 5.7 \times 10^{17}$ ions cm^{-3}s^{-1}). Thus the plasma density is observed to be higher in the CCP system. This can be explained in terms of the power dissipated into the discharge per unit volume; the capacitive

discharge is about $^1/_5$ the volume of the inductive discharge hence the power density per unit volume in the ICP is lower than that in the CCP. Also the ion density has been measured to fall with increasing pressure[18] and at 100 mTorr the CCP system is operating efficiently, however 100 mTorr is a high pressure for an inductively coupled discharge. The plasma density measured in the CCP is an order of magnitude lower than the density measured ($\approx 2 \times 10^{10}$ cm^{-3}) by an optical method (LIF)[18] (see Chapter 5) in the same system under identical conditions. The discrepancy between these measurements may be partially due to the error in the measurements of the electron temperature but is the most probably due to inhomogeneity in the discharge. The LIF optical method recorded the plasma density in the centre of the bulk of the discharge rather than at the edge, which is where the electrical method observes the density. The plasma density has previously been observed to vary markedly[20] with position in the discharge and it is therefore unsurprising that the density observed by the two methods is significantly different. A set of planar probes on the upper electrode of the CCP system and lower electrode of the ICP system, which would allow spatially resolved measurements across their diameters to be made, is being devised.

2.5 Conclusions

The ion flux in both the ICP and CCP were measured for a variety of plasma conditions. It is found that the flux was generally larger in the ICP system but as this operates at lower pressures higher fluxes are expected. The electron temperature was also recorded in both systems, but due to large variations in its measured value it is difficult to deduce which system shows the higher temperature. The ion density was calculated for both systems under comparable conditions and it was found that the ionisation ratio was greatest in the CCP due to its larger applied power density. The transition between an inductively produced and capacitively produced discharge was observed in the ICP system, however attempts to observe a hysteresis effect were unsuccessful.

2.6 References

[1]M. A. Liberman and A. J. Lichtenberg, *Principles of Plasma Discharges and Materials Processing*, Wiley, (1994)
[2]L. D. B. Kiss, J. P. Nicolai, W. T. Conner and H. H. Sawin, *J. Appl. Phys.*, **71**, 3186, (1992)
[3]P. Horowitz and W. Hill, *The Art of Electronics*, CUP, (1980)
[4]Nordiko Ltd.
[5]P. A. Miller, G. A. Hebner, K. E. Greeberg, P. D. Pochan and B. P. Aragon, *J. Res. Natl. Inst. Stand. Technol.*, **100**, 427, (1995)
[6]D. Halliday and R. Resnick, *Fundamenals of Physics*, Wiley, (1974)
[7]W. Wang, J. Foster, A. E. Wendt, J. H. Booske, T. Onuoha, P. W. Sandsttrom, H. Liu, S. S. Gearhart and N. Hershkowitz, *Appl. Phys. Lett.*, **71**, 1622, (1997)
[8]S. Lloyd, D. M. Shaw, M. Watanabe and G. J. Collins, *Jpn. J. Appl Phys.*, **38**, 4275, (1999)
[9]P. N. Wainman, M. A. Lieberman, A. J. Lichtenberg, R. A. Stewart and C. Lee, *J. Vac. Sci. Technol.*, **4**, 3464, (1995)
[10]E. B. Smith, *Basic Chemical Thermodynamics*, Clarendon Press, (1973)
[11]N. Sadeghi, M. van de Grift, D. Vender, G. M. W. Kroesen and F. J. de Hogg, *Appl. Phys. Lett.*, **70**, 835, (1997)
[12]K-U Riemann, *J. Phys. D: Appl. Phys.*, **24**, 493, (1991)
[13]N. St. J. Braithwaite, J. P. Booth and G. Cunge, *Plasma Sources Sci. Technol.*, **5**, 677, (1996)
[14]K. Rosolankova, *M. Phys. Thesis*, Oxford University, (2000)
[15]Y. Wang and J. K. Olthoff, *J. Appl. Phys.*, **85**, 6359, (1999)
[16]A. Schwabedissen, E. C. Benck, and J. R. Roberts, *Phys. Rev. E*, **55**, 3450, (1997)
[17]P. W. Atkins, *Physical Chemistry*, OUP, (1978)
[18]B. K. Woodcock, *D.Phil. Thesis*, Oxford University, (1995)
[19]K. Rosolankova, *Physics Summer Project*, Oxford University, (1999)
[20]K. Okada, S. Komatsu and S. Matsumoto, *J. Vac. Sci. Technol. A*, **17**, 721, (1999)

Chapter 3

Frequency Modulation Spectroscopy of Atomic Argon

3.1 Introduction

In Chapter 1, several optical plasma diagnostics were discussed. However, until now, frequency modulation spectroscopy (FMS), a technique that has been widely used in many fields[1], has not been used to study low temperature plasmas. In this Chapter, one tone FMS is discussed as a novel plasma diagnostic. To assess its usefulness, it is compared to absorption spectroscopy and a low frequency laser modulation technique.

Argon atoms were chosen as the target species because the absorption cross sections are relatively large in the wavelength range of readily available diode lasers, and the concentrations of the excited states produced in the plasma chambers discussed in Chapter 2 were expected to be sufficiently large to allow detection. In addition, unlike some other species (for example iodine molecules), the absorption line profiles are symmetric and uncongested under these conditions. Furthermore, measurements of argon atoms are useful because of the wide variety of applications for which these atoms are used.

Argon is used as a dilutant gas in semiconductor wafer processing and welding, it has also been used as an inert buffer gas for kinetic studies[2]. Although argon atoms in their ground state are very unreactive, once electronically excited, for example by an electric discharge, argon atoms can become chemically reactive, and the kinetics of reactions of excited argon atoms have been studied. For example, the rate constants of the reaction of argon atoms ($^3P_2$ and $^3P_0$) with F_2, Cl_2, CCl_4, PCl_3 and $SOCl_2$ have been measured[3] by the observation of ArCl* and ArF* excimers.

The excited states of argon can both give and receive energy. Studies of the relaxation of many molecules have been carried out with excited argon atoms as the energy acceptor, for instance, in the vibrational relaxation of N_2[4]. Conversely, the energy transfer from Ar* to ground state N_2 also plays an important role in the electron beam Ar-N_2 laser mechanism[5].

The excitation of other species by Ar atoms has also been widely studied including energy transfer from metastable Ar atoms to metal halides, causing the halide to dissociate[6]. The

quenching rates of the argon metastable atoms, with SF_6, Cl_2, BCl_3 and N_2, in radio-frequency glow discharges, similar to those described in Chapter 2, have also been measured[7]. The energy transfer process occurring between ground state hydrogen atoms and metastable argon atoms has also been investigated and the results compared with those obtained from the calculated potential curves for the reaction[8].

The measurement of the translational temperature of argon metastables in a plasma has enabled indirect measurements of the temperature of heavy particles[9]. This is possible because the metastable levels live for several seconds, considerably longer than it takes for many collisions to occur in the discharge, thus these argon atoms are in thermal equilibrium with their surroundings.

Summarising, it can be seen that there are many uses for measurements on excited Ar atoms. A simple method that enables measurement of their concentration and temperature, in plasmas and other environments, is therefore exceptionally useful.

3.2 Previous Studies of Argon Plasmas

In 1980, a research note[10] was published containing an investigation of various light sources for measurements of absorption of radiation at 811.5 nm by metastable argon atoms in an inductively coupled plasma (ICP). The sources considered were all incoherent; an argon-sealed mercury electrodeless discharge lamp (EDL), a xenon arc lamp (XAL, a continuum source) and an atmospheric pressure argon microwave-induced plasma (MIP). This investigation was completed in a similar manner to the low frequency modulation measurements made in this Chapter. Both the measurements with the EDL and the XAL failed. In the former case, this was due to the emission from the ICP overwhelming the emission from the lamp. The XAL measurements were unsuccessful because the monochromator had insufficient resolution to allow isolation of the atomic line of interest. Although in this publication the relative number density of the metastable level was measured as a function of plasma parameters and even plasma composition, no absolute number density was obtained.

Absorption measurements to obtain absolute number densities of excited argon levels have been completed in various types of plasmas. Measurements on sputtering plasmas were reported in 1979[11] and the following year similar measurements were made in a wall-confined arc plasma[12]. In 1985, Moussouda *et al.*[13] published work containing measurements of

metastable number densities in a microwave plasma and the next year, Hart *et al.*[14] measured the concentrations of the four levels associated with the $(1s^2 2s^2 2p^6 3s^2)3p^5 4s^1$ electronic configuration for the first time in an ICP. In this study, using a Xenon arc lamp as the light source, the concentration measurements were made with and without the presence of water and nebulizing gas. The metastable number densities were found to be between 2.3×10^{10} and 7.4×10^{11} cm^{-3}, depending on the ICP conditions.

The first diode laser (line-of-sight) absorption measurements of Ar* were reported in 1991[15]. These were carried out by current tuning a free running diode laser over two excited argon atom transitions, and although absolute concentrations of the excited argon atoms were not reported, the translational temperatures of the argon atoms were calculated despite observing in excess of 30 % absorption. This method of diode laser line-of-sight absorption has been subsequently used for many measurements. Jonkers *et al.*[16] measured the radial dependence of the absolute number density and temperature of argon Ar* in an inductively coupled argon–mercury plasma in a Philips QL 'light bulb' at different pressures. The concentration was found from the fractional absorption at the peak of the line and the temperature determined from the line shape. Similar sets of measurements have been conducted in a low-density argon plasma produced from DC hot filament discharges within a 40 l vessel[17]. In the same year, the Ar metastable translational temperature was measured to be about 600 K in an ICP[18], while simultaneously the argon ion velocity distribution was recorded by Doppler resolved LIF. In 1999, a much more extreme plasma, the argon arcjet, was also studied by this technique[19] yielding simultaneous velocity and temperature measurements of the plume. This enabled the total enthalpy, thrust efficiency and thermal efficiency of the arcjet, similar to those used as positioners on spacecraft, to be determined. Concurrently, measurements of the spatial distributions of metastable argon atoms were made in a Gaseous Electronics Conference (GEC) reference cell[20]. The number density was found to be approximately 10^{10} cm^{-3} and found to vary significantly across the diameter of the chamber.

From the Doppler widths of the absorption transitions, observed using a diode laser, argon metastable temperatures have been measured in a 100 MHz argon ICP[9] working at atmospheric pressure. As mentioned in Section 3.1, spatial variations of heavy particle temperatures were deduced from these measurements.

3.3 Spectroscopy of Argon Atoms

The ground state electronic configuration of Ar is $1s^2 2s^2 2p^6 3s^2 3p^6$. The first excited states arise from the excitation of an electron from a $3p$ to a $4s$, $4p$, $3d$, $5s$ or $5p$ orbital. The energy level diagram is given in Figure 3.1. In this Chapter, one of the 'red line' transitions between the first, $1s^2 2s^2 2p^6 3s^2 3p^5 4s^1$, and the second, $1s^2 2s^2 2p^6 3s^2 3p^5 4p^1$, excited configurations is used to detect argon atoms in the plasmas. The following sections discuss the terminology required to identify the transition that has been used.

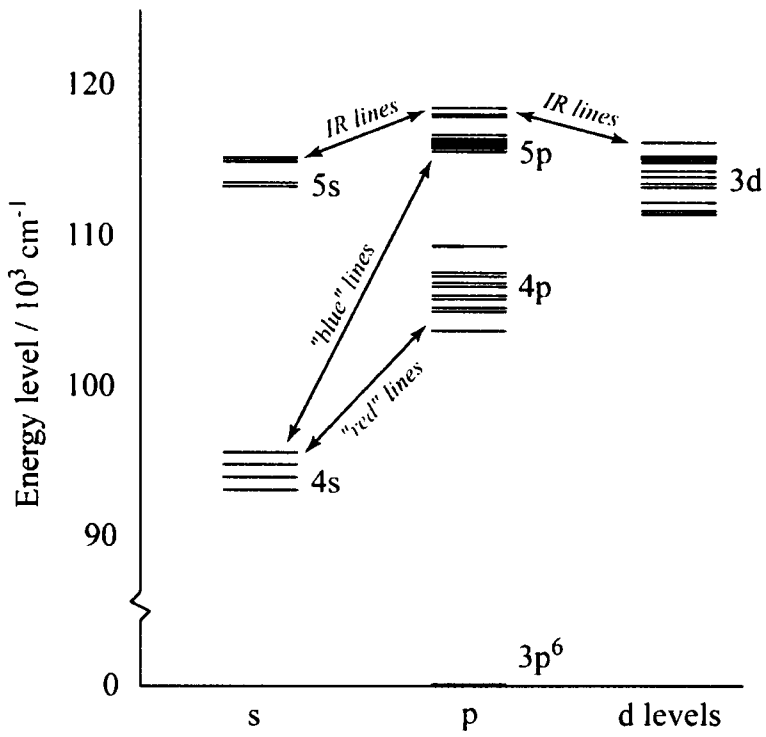

Figure 3.1 A partial energy level diagram for argon.

3.3.1 Atomic Spectroscopy

In many electron atoms, the electrons occupy orbitals similar to those in hydrogen. Unlike hydrogen however, the Schrödinger equation cannot be solved exactly due to electron-electron interactions and so the energy levels and the wavefunctions cannot be obtained exactly. To understand the spectra of many electron atoms, an approximation needs to be made – one possibility is the orbital approximation. This states that the total wavefunction for the atom can be written as the product of single electron wavefunctions, which can be hydrogen like orbitals. These hydrogenic single electron orbitals are described by the same set of four quantum numbers n, l, m_l and m_s that are used in the hydrogen atom.

n is the principal quantum number and gives the number of the shell that the electron is in. In a hydrogen atom, it is directly related to the mean distance of the electron from the nucleus and therefore the energy of the electron.

l, the azimuthal quantum number, is directly related to the amount of orbital angular momentum, $|\mathbf{l}| = [l(l+1)]^{½}\hbar$, the electron possesses in that orbital. In hydrogen atoms, the orbitals with the same value of n but different values of l have the same energy. However, in multi-electron atoms, this degeneracy is removed; the lower the value of l, the lower the energy. l and n together define the radial distribution of the wavefunction and the number of radial nodes (where the wavefunction changes sign) is equal to $n - l - 1$.

m_l is the magnetic quantum number that characterises the angular distribution of the wavefunction. For each value of l there are $2l + 1$ independent wavefunctions, with quantum numbers $m_l = -l, l+1, \ldots, l-1, l$. These define the orientation of the wavefunction with respect to an arbitrary z-axis within the atom.

m_s, the electron spin quantum number, quantifies the amount of intrinsic angular momentum the electron possesses and is given by $m_s = \pm ½$.

The Pauli exclusion principle states that no two electrons in an atom can have the same set of four quantum numbers and together with the Aufbau Principle is used to generate the electronic configurations of atoms. The orbital approximation gives approximate orbitals for the electrons in many electron atoms, but the electrons couple to each other. For light atoms, H, He and those in the first full row of the periodic table, the Russell-Saunders coupling approximation works well. This is discussed below.

3.3.2 Russell-Saunders Coupling Notation

For light atoms there is only a weak interaction between the spin and orbital angular momenta and an *LS* coupling scheme is used (*i.e.* electrostatic coupling dominates magnetic spin orbit coupling). In this scheme, the orbital angular momentum of each of the electrons, l, is summed to give a total orbital angular momentum L. Similarly, the total spin angular momentum, S, is also found by summing the individual spin angular momentum, m_s, of all the electrons. L is then coupled with S to give the total angular momentum, J, of the level. The energy level of the atom can then be described by a term symbol, ${}^{2S+1}L_J$, where the $2S+1$ term is called the multiplicity. The value of the total orbital angular momentum, L, is expressed as a letter: 0=S, 1=P, 2=D, 3=F... . For example, the ground state energy level of Ar can be expressed as ${}^1S_0$. The *LS* coupling term symbols are included in the energy level diagram given in Figure 3.2. However, because in Ar the spin orbit coupling interaction is strong, it is considered a heavy atom and the *LS* coupling scheme is not a good approximation and hence its nomenclature is

not a good description of the system. Therefore, other notation has been introduced to specify the levels.

3.3.3 Paschen Notation

Paschen used a semi-empirical convention that has been widely used in the literature for rare gas electronic states where only one electron is excited[21]. The notation takes the form of $(n\text{-}3)l_i$, where n is the principal quantum number of the orbital which contains the single excited electron and the azimuthal quantum number of this orbital, l, is represented by the letter (*i.e.* *s*, *p*, *d*, ...), corresponding to its type. i is an arbitrary label specific to the level within a particular orbital configuration, and by convention is numbered as an increasing integer from the highest energy level down to the lowest.

3.3.4 Racah Notation

Racah proposed a *jl* notation based on the *jj* coupling scheme. The *jj* coupling scheme is used when the spin-orbit interaction is significant compared to electrostatic effects such as electron-electron repulsion and therefore the Russell-Saunders quantum numbers are not good for describing the energy levels. In the *jj* scheme, each unpaired electron spin angular momentum is coupled directly by spin-orbit coupling to its own orbital angular momentum to produce a total angular momentum, j. The total angular momentum of each of the unpaired electrons is then coupled together to get the total angular momentum quantum number of the atom, J. For two unpaired electrons J takes the values $j_1 + j_2,\ j_1 + j_2 - 1, \ldots, |\ j_1 - j_2\ |$, where j_1 and j_2 are the total angular momenta of the unpaired electrons 1 and 2 respectively. The energy levels are then labelled by $(j_1, j_2)_J$. In Ar*, with a single excited electron, the excited atom is considered as a Rydberg system; a parent ion (the nucleus and core electrons) and an excited electron, because the excited orbitals are at a significantly higher energy than the orbitals occupied in the ground state. The strongest interaction is that of the spin-orbit coupling of the unpaired electron in the core, described by a quantum number j_{core}. The next strongest interaction is the electrostatic interaction between the Rydberg electron and the core, which is stronger than the spin-orbit coupling interaction of the Rydberg electron. Once the parent ion has been assigned a total quantum number, j_{core}, this can be coupled with the orbital angular momentum of the excited electron, l_{ex} to give a resultant energy level denoted by the quantum number K, hence the description as *jl* coupling. K is then coupled to the spin of the excited electron to give a total atomic angular momentum quantum number J. The Racah notation of an energy level is

$nl_{ex}[K]_J$ where again l_{ex} is represented by the letter (*i.e. s*, *p*, *d*, ...), corresponding to the type of orbital the Rydberg electron is in. l_{ex} is primed (l_{ex}') when the ion this level converges to, lies above the lowest ionisation limit.

3.3.5 Systematic Notation

Systematic notation is sometimes used in the literature, which is a modification of the Racah nomenclature. The coupling described by this notation is still the *jl* scheme, however each level is labelled nl_{ex} with two subscripts. The first is K - ½, and the second is J, the total angular momentum of the atom. Again, if the ion this level converges to, lies above the lowest ionisation limit, the l_{ex} is primed.

3.3.6 The Energy Level Diagram for the First and Second Excited States of Argon

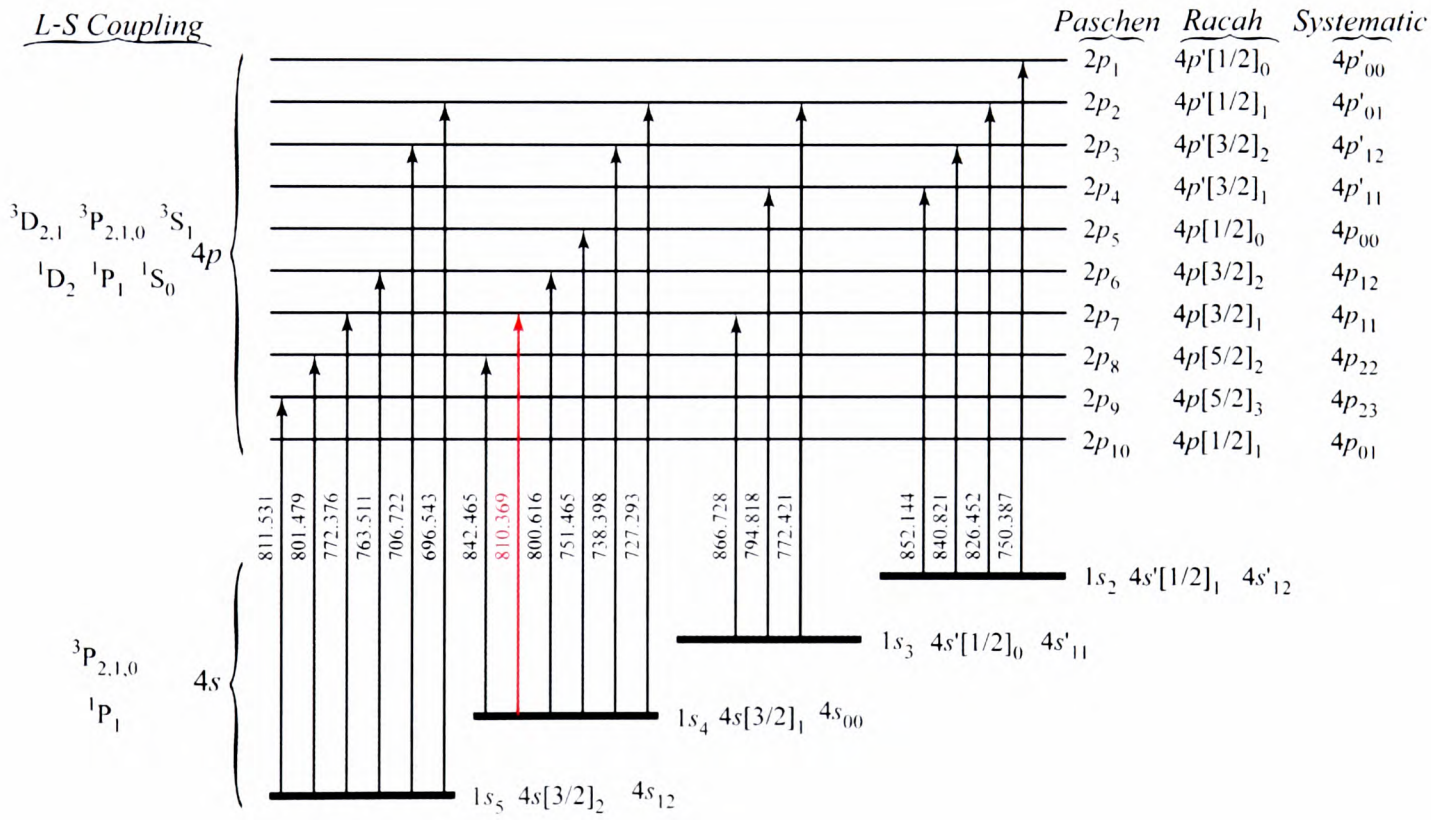

Figure 3.2 Energy level diagram of the first and second excited states of argon.

The spectroscopy of Ar atoms has been extensively studied and documented[21]. Wiese *et al.*[22] gives a unified set of the measured atomic transition probabilities and a critical review of previous studies. Figure 3.2 shows the energy level diagram for the first, $1s^2 2s^2 2p^6 3s^2 3p^5 4s^1$, and the second, $1s^2 2s^2 2p^6 3s^2 3p^5 4p^1$, excited configurations of argon with each level labelled using all four notations explained above. The Racah notation is much more informative about the level it represents and therefore will be used throughout this Chapter. The $4p[^3/_2]_1 \leftarrow 4s[^3/_2]_1$ transition at 810.369 nm used in this study is shown in Figure 3.2. Hart *et al.*[14]

calculated the absorption cross section at the line centre for this transition to be $1.77 \times 10^{-12}\,cm^2$ from the transition probabilities of Borge and Campos[23].

3.3.7 Absorption Linewidths

The temperature of an atomic species can be obtained from its absorption profile (see Section 3.2). This is possible because the absorption line of an atom or molecule is not infinitely narrow but is broadened by several effects, including Doppler and lifetime broadening mechanisms.

Doppler broadening occurs due to a shift of the transition frequency if the species, of mass m, is moving towards or away from the radiation source. For thermal motion, this results in a Gaussian line profile. The full width at half maximum (FWHM) of a line broadened only by the Doppler effect is given by[24]

$$\Delta\nu = \frac{2\nu_0}{c}\left(\frac{2kT}{m}\ln 2\right)^{1/2} \tag{3.1}$$

where ν_0 is the line centre frequency. For the atomic transition observed in this Chapter the Doppler width has a value of 723 MHz at room temperature.

Lifetime broadening occurs because it is impossible to specify the energy levels exactly for a system that is changing with time due to the Heisenberg uncertainly principle and gives a Lorentzian profile, with a FWHM that can be calculated from equation (3.2)[24].

$$\Delta\nu = \frac{1}{\tau} \tag{3.2}$$

If the lifetime, τ, of the state is only controlled by its radiative lifetime, then $\Delta\upsilon$ is called the natural linewidth of the transition. For the $4p[^3/_2]_1$ and $4s[^3/_2]_1$ states in argon, studied in this Chapter, the radiative lifetimes are 29 ns and 10 ns respectively[25]. The lifetime of the lower $4p[^3/_2]_1$ level is very short considering that within the Russell-Saunders coupling scheme this transition ($^1S_0 \leftarrow {}^3P_1$) is forbidden. The lifetimes of the other J levels, $^3P_0$ ($4s[^1/_2]_0$) and $^3P_2$ ($4s[^3/_2]_2$), are 50 s and 60 s respectively, showing that the selection rules for J ($\Delta J = 0, \pm 1$ but not $J = 0 \leftrightarrow J = 0$) are still valid. This is because the system must conserve angular momentum, and when a photon (always possessing one unit of angular momentum) is absorbed or emitted the atom's angular momentum must change by a quantum of angular momentum (if $J = 0$). The linewidth of the $4p[^3/_2]_1 \leftarrow 4s[^3/_2]_1$ transition is dominated by the shorter lived $4s\ [^3/_2]_1$ level's radiative lifetime, which gives a FWHM line width of 100 MHz.

This is almost an order of magnitude less than the Doppler line width and thus can be neglected.

A second lifetime broadening mechanism, collisional broadening, can occur in which collisional deactivation decreases the actual lifetime of the species in the excited state. This also gives rise to a Lorentzian profile with a FWHM also given by equation (3.2) where τ is the average time between collisions. This collisional lifetime depends on pressure and assuming simple collision theory[26], is given by

$$\frac{1}{\tau} = \frac{4p\sigma}{\sqrt{kT\pi m}} \tag{3.3}$$

where σ is the collision cross section (0.36 nm^2 for argon[26]) and p is the pressure. This gives a collisional broadening of about 6.5 MHz/Torr at 300K. In the plasmas investigated in this Chapter, the maximum pressure used was 1 Torr, giving a theoretical maximum collisional broadening of 6.5 MHz. This is two orders of magnitude lower than the Doppler broadening and can therefore also be neglected.

Thus, the line profiles of the argon absorption are expected to be fitted well by a Gaussian function with a FWHM defined by equation (3.1).

3.4 Frequency Modulation Spectroscopy

Frequency modulation spectroscopy (FMS) was introduced into the analytical scientists' tool kit in 1979 by Bjorklund[27]. In his letter, he described how a continuous wave dye laser, externally modulated at 925 MHz, could be used to detect the absorption of a Fabry-Perot resonator. External modulation introduces side bands on the spectral output of the laser, separated from the fundamental frequency by the modulation frequency, and are used to detect the absorption feature. The high sensitivity of this technique is due to the narrow bandwidth detection systems and the encoding of the absorption signal at the modulation frequency, where the laser and mechanical noise is lower compared to lower frequencies[28]. Silver[28] discussed many experimental methods in 1992 and concluded that the minimum detectable absorbance is about 10^{-8} with a 1 Hz detection bandwidth.

In Bjorklund's conclusion, he discusses the use of this technique not just to measure weak absorption features but also time-varying absorptions in the nanosecond regime. Since the introduction of FMS, it has been applied to many diverse situations including measurements on transient species, for example TiS and PtC[29].

Until now, FMS has not been used as a plasma diagnostic, although it has been used to measure the line positions of Na, NaH and Ar ($5p$–$4s$) transitions between 340 and 440 nm[30]. These were produced in a specialist laser-guided plasma, which consists of a low frequency (310 Hz) discharge between two copper cylindrical electrodes in a heat pipe oven (at ≈ 680 K) guided by a continuous wave dye laser and probed by a second continuous wave dye laser.

3.4.1 The Theory of Frequency Modulation Spectroscopy

Frequency modulation spectroscopy involves the generation of two sidebands at $\omega_0 \pm \omega_m$, where ω_m is the modulation frequency, either side of the fundamental laser frequency, ω_0. Typically, this is achieved with an external electro-optic phase modulator, enabling many types of continuous wave laser to be modulated. For instance, the first reported FMS study was completed using a ring dye laser[27]. However, as discussed in Chapter 1, it is possible to tune the frequency of a diode laser by varying the current flowing through the junction, and hence it is possible to produce modulated radiation by directly modulating the laser's injection current. A typical intensity spectrum of the current modulated laser diode used in this study, is shown in Figure 3.3.

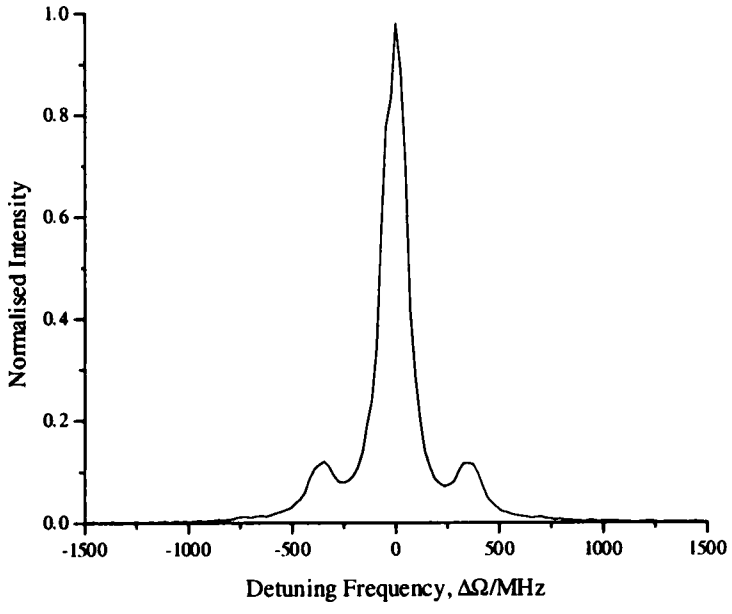

Figure 3.3 Frequency spectrum of a diode laser modulated at 350 MHz.

When the intensity of the laser beam (proportional to $E(t)\cdot E(t)^*$[24], the square modulus of its field strength) is time independent, the optical field, $E(t)$, produced by a laser subject to pure FM, can be expressed as

$$E(t) = E_0\left(-\frac{\beta}{2}e^{i(\omega_0-\omega_m)t} + e^{i\omega_0 t} + \frac{\beta}{2}e^{i(\omega_0+\omega_m)t}\right) \tag{3.4}$$

where E_0 is the electric field amplitude and β is the modulation index and is less than or approximately equal to unity. The modulation index is a measure of the depth of modulation, and can be estimated from the spectral output of the laser because the ratio of intensity in one of the sidebands to the carrier frequency is $\beta^2/4$ from equation (3.4).

When the optical field, given by equation (3.4), is passed through an absorbing medium of length L, refractive index $n(\omega)$, and intensity absorption coefficient $\alpha(\omega)$, each component of the field may experience different amplitude attenuation, due to the frequency dependent absorption, and different phase shifts, because of the frequency dependent refractive index of the medium. It is convenient to define this attenuation, utilising the Beer-Lambert Law, to be $\delta_{0,h,l} = \alpha_{0,h,l}L/2$ and the phase shift to be $\varphi_0 = n_0 L\omega_0/c$, $\varphi_h = n_h L(\omega_0 + \omega_m)/c$ and $\varphi_l = n_l L(\omega_0 - \omega_m)/c$ for the individual components (the subscripts h, l and 0 denote the higher frequency sideband, lower frequency side band and fundamental laser frequency, ω_0, respectively). From these it is possible to define the amplitude attenuation of each component to be

$$T_{0,h,l} = \mathrm{e}^{\left(-\delta_{0,h,l} - i\varphi_{0,h,l}\right)} \tag{3.5}$$

Thus, once the field has passed through the absorbing medium it is modified to

$$E(t) = E_0\left(-T_l\frac{\beta}{2}\mathrm{e}^{i(\omega_0-\omega_m)t} + T_0\,\mathrm{e}^{i\omega_0 t} + T_h\frac{\beta}{2}\mathrm{e}^{i(\omega_0+\omega_m)t}\right) \tag{3.6}$$

Taking the square modulus of this expression to obtain an expression for the intensity of the laser on a detector after the absorbing medium, neglecting terms of order β^2 and assuming that $|\delta_0 - \delta_h|$, $|\delta_0 - \delta_l|$, $|\varphi_0 - \varphi_h|$ and $|\varphi_0 - \varphi_l|$ are all $<< 1$, results in

$$I(t) \approx \frac{cE_0^2}{8\pi}e^{-2\delta_0}\left(1 + (\delta_l - \delta_h)\beta\cos(\omega_m t) + (\varphi_h + \varphi_l - 2\varphi_0)\beta\sin(\omega_m t)\right) \tag{3.7}$$

Therefore, the detector will observe a beat signal at the modulation frequency, ω_m, provided that $(\delta_l - \delta_h) \neq 0$ or that $(\varphi_l + \varphi_h - 2\,\varphi_0) \neq 0$. The first condition occurs when the two sidebands experience different amplitude attenuation (in-phase, absorption) and the second occurs if the average of the phase shifts experienced by the sidebands is different to that experienced by the fundamental laser frequency (quadrature, dispersion). Signals corresponding to the magnitude of the absorption and dispersion can be obtained by demodulating the detector signal with the modulation applied to the laser. The demodulated output is in fact a linear combination of the in-phase, $I_0(\chi) \propto \beta(\delta_l - \delta_h)$, and quadrature, $Q_0(\chi) \propto \beta(\varphi_l + \varphi_h - 2\,\varphi_0)$, signals, where χ is a

parameter defining the position on the spectral feature. Generally, the observed signals $I(\chi)$ and $Q(\chi)$ are given by

$$I(\chi) = I_0(\chi)\cos\theta + Q_0(\chi)\sin\theta \tag{3.8}$$

$$Q(\chi) = I_0(\chi)\cos\left(\theta - \frac{\pi}{2}\right) + Q_0(\chi)\sin\left(\theta - \frac{\pi}{2}\right) \tag{3.9}$$

where θ is the relative phase angle between the detector signal and the laser modulation signal at the point of demodulation. Thus, the absorption and dispersion signals can be separated with careful adjustment of this phase.

The observed signals depend on the ratio of the width of the absorption feature compared to the modulation frequency. In the limit when the modulation frequency is much smaller than the width of the feature being interrogated, the $\cos\omega_m t$ term in equation (3.7) is proportional to the derivative of the absorption feature while the $\sin\omega_m t$ term is proportional to the second derivative of the dispersion. Simulated signals for this condition are shown in Figure 3.4a.

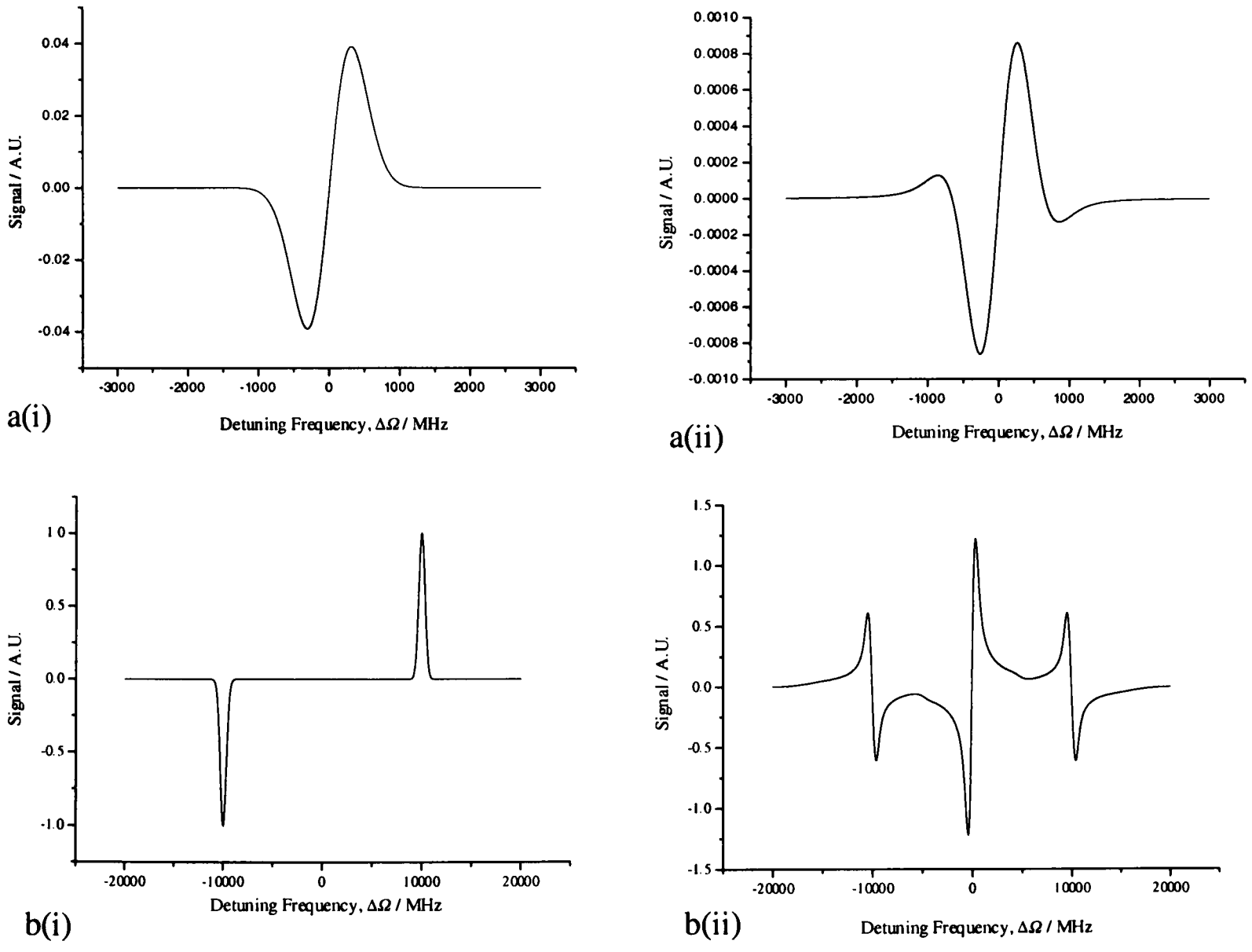

Figure 3.4 Extremes of FM signals ((i) absorption and (ii) dispersion): at a modulation frequency (a) smaller than profile width and (b) greater than profile width.

The other extreme of FMS is when the modulation frequency is much greater than the width of the absorption feature, in which case only one of the three parts of the laser frequency spectrum interrogate the feature at any one time, and therefore the absorption profile is obtained independently and directly by each of the side bands. Simultaneously, the first derivative of the dispersion is obtained directly by all three parts of the laser intensity spectrum. This limit is shown in Figure 3.4b.

The absorption signal ($\delta_l - \delta_h$) can be simulated assuming the expected Gaussian absorption profile.

$$Abs(\omega) = Abs_c \, \mathrm{e}^{-\left[\frac{c}{\omega_c}\left(\frac{m}{2kT}\right)^{1/2}(\omega-\omega_c)\right]^2} = Abs_c \, \mathrm{e}^{-\chi^2} \tag{3.10}$$

where Abs_c is the absorption of the species, of mass m, at the line centre, ω_c. The dimensionless quantity χ is introduced as a reduced detuning or reduced velocity parameter. The dispersion can be obtained from the absorption profile using the Kramers-Kronig relationship[31], and for a Gaussian absorption profile is[32]

$$Dis(\omega) = -\frac{2Abs_c}{\sqrt{\pi}} \mathrm{e}^{-\chi^2} \int_0^{\chi} \mathrm{e}^{u^2} \, du \tag{3.11}$$

The integral can be either calculated using Simpson's rule[32] or alternatively by the sum given in equation (3.12) which was found to require less computational time.

$$\int_0^{\chi} \mathrm{e}^{u^2} \, du = \sum_{s=0}^{\infty} \frac{\chi^{2s+1}}{(2s+1)s!} \tag{3.12}$$

This was obtained by performing a Taylor series expansion of the exponential term in the integral, an exact expansion, and then integrating the sum. For the analysis in this work it was found that truncation of this sum after less than one hundred terms was found to introduce a smaller error than the Simpson's rule method with the same number of terms.

3.4.2 Amplitude Modulation

The asymmetry of the sidebands shown in Figure 3.3 is due to amplitude modulation of the laser. This occurs simultaneously with the frequency modulation because the electrical power dissipated at the diode junction varies with injection current, see Figure 1.8 in Chapter 1, and therefore the intensity of the radiation emitted changes (amplitude modulation, AM). This effect can be quantified in terms of the α factor introduced in Section 1.8.5 which couples

amplitude to phase fluctuations and hence amplitude fluctuations to frequency fluctuations. The radiation produced by directly modulating the current of the laser is therefore both frequency and amplitude modulated. Thus to understand quantitatively the signals produced from passing this radiation through an absorbing medium, both amplitude and frequency modulation must be considered.

The optical electric field of the laser that is simultaneously being frequency and amplitude modulated is given by equation (3.13)[33]

$$E(t) = E_0\left[1 + M\sin\left(\omega_m t + \psi\right)\right]e^{\left[i\left(\omega_0 t + \beta\sin\omega_m t\right)\right]} \tag{3.13}$$

where M is the amplitude modulation index and ψ defines the phase difference between the AM and the FM. From expansion of equation (3.13)[34], the intensities of each of the three frequency components of the modulated laser are given below, again assuming a strong carrier at ω_0 and two weak side bands at $\omega_0 \pm \omega_m$.

$$I(t) \propto E^2(\omega_0) = E_0^2\left(J_o^2(\beta) + M^2 J_1^2(\beta)\cos^2(\psi)\right) \tag{3.14}$$

$$I(t) \propto E^2(\omega_0 + \omega_m) = E_0^2\left\{\begin{array}{l} J_1^2(\beta) + \dfrac{M^2}{4}\left[J_0^2(\beta) + J_2^2(\beta)\right] \\ -\dfrac{M^2}{2}J_0^2(\beta)J_2^2(\beta)\cos(2\psi) \\ + MJ_1(\beta)\left[J_0(\beta) + J_2(\beta)\right]\sin(\psi) \end{array}\right\} \tag{3.15}$$

$$I(t) \propto E^2(\omega_0 - \omega_m) = E_0^2\left\{\begin{array}{l} J_1^2(\beta) + \dfrac{M^2}{4}\left[J_0^2(\beta) + J_2^2(\beta)\right] \\ -\dfrac{M^2}{2}J_0^2(\beta)J_2^2(\beta)\cos(2\psi) \\ - MJ_1(\beta)\left[J_0(\beta) + J_2(\beta)\right]\sin(\psi) \end{array}\right\} \tag{3.16}$$

Here $J_n(M)$ are the n^{th} order Bessel functions. From equations (3.15) and (3.16), it is evident that the laser intensity spectrum is only symmetrical when the FM-AM phase difference is an integral number of π radians. This can be seen not to be the case in Figure 3.3. This phase difference for diode lasers has been found to generally be $-\pi/2$ for modulation frequencies less than 750 MHz[34], but has also been found to vary markedly with laser, laser wavelength, modulation frequency and frequency modulation index[35]. When the diode laser produces both frequency and amplitude modulated light, a beat signal can be observed by the detector even in

the absence of an absorbing sample. This can be seen from the intensity of the current modulated diode laser which is

$$I(t) \propto \left|E(t)\right|^2 = E_0^2\left[1 + 2M\sin\left(\omega_m t + \psi\right)\right] \tag{3.17}$$

To derive the signal that the detector observes, when the laser radiation field has an intensity spectrum given by equations (3.14), (3.15) and (3.16) a similar procedure to that adopted in the previous section must be used. First, by expansion of equation (3.13)[34], the optical field that probes the sample is given by

$$E(t) = E_0\left[1 + M\sin\left(\omega_m t + \psi\right)\right]\left\{\begin{array}{l} J_{-1}(\beta)\mathrm{e}^{\left[i(\omega_0-\omega_m)t\right]} \\ + J_0(\beta)\mathrm{e}^{\left[i\omega_0 t\right]} \\ + J_1(\beta)\mathrm{e}^{\left[i(\omega_0+\omega_m)t\right]} \end{array}\right\} \tag{3.18}$$

The complex transmission function given by equation (3.5) can again be used on each of the three components of the laser intensity spectrum giving

$$E(t) = E_0\left[1 + M\sin\left(\omega_m t + \psi\right)\right]\left\{\begin{array}{l} T_l J_{-1}(\beta)\mathrm{e}^{\left[i(\omega_0-\omega_m)t\right]} \\ + T_0 J_0(\beta)\mathrm{e}^{\left[i\omega_0 t\right]} \\ + T_h J_1(\beta)\mathrm{e}^{\left[i(\omega_0+\omega_m)t\right]} \end{array}\right\} \tag{3.19}$$

Again, assuming small laser modulation (M, $\beta << 1$), higher order terms can be neglected and equation (3.19) simplifies to

$$E(t) \approx E_0\left\{\begin{array}{l} T_l\left[-\frac{\beta}{2} - \frac{M}{2i}\mathrm{e}^{-i\psi}\right]\mathrm{e}^{\left[i(\omega_0-\omega_m)t\right]} \\ + T_0\,\mathrm{e}^{\left[i\omega_0 t\right]} \\ + T_h\left[\frac{\beta}{2} + \frac{M}{2i}\mathrm{e}^{i\psi}\right]\mathrm{e}^{\left[i(\omega_0+\omega_m)t\right]} \end{array}\right\} \tag{3.20}$$

Using the same assumptions as used to derive equation (3.7), namely that the absorption losses and phase shifts experienced by each of the components of the laser intensity spectrum are small, it is possible to obtain

$$I(t) \tilde{\propto} \mathrm{e}^{-2\delta_0}\left(\begin{array}{l} 1 + \left[\begin{array}{l}\beta(\delta_{-1} - \delta_1) + M(2 + 2\delta_0 - \delta_{-1} - \delta_1)\sin\psi \\ + M(\varphi_{-1} - \varphi_1)\cos\psi\end{array}\right]\cos\omega_m t \\ + \left[\begin{array}{l}\beta(\varphi_{-1} + \varphi_1 - 2\varphi_0) + M(2 + 2\delta_0 - \delta_{-1} - \delta_1)\cos\psi \\ - M(\varphi_{-1} - \varphi_1)\sin\psi\end{array}\right]\sin\omega_m t \end{array}\right) \tag{3.21}$$

This detector signal again consists of an in-phase component, I_0 (the $\cos\omega_m t$ term), and a quadrature component, Q_0 (the $\sin\omega_m t$ term), which will be detected by phase sensitive detection as the linear combinations given in equations (3.8) and (3.9).

A simulation produced in Microsoft Excel was used to generate the expected I and Q traces observed when laser radiation, containing both amplitude and frequency modulation, is passed through an absorbing medium. This simulation allowed the variation of T, β, M, ψ and θ. To test the effect of AM several sample I and Q traces, recorded using the experiments outlined later in this Chapter, were fitted assuming no AM on the laser and with the full AM/FM simulation; one of these pairs of traces is shown in Figure 3.5. The best fit to the data considering the signal to be derived purely from FM of the laser, after offsets on the traces had been removed, is shown in Figure 3.5a, and the full AM/FM analysis, is shown in Figure 3.5b.

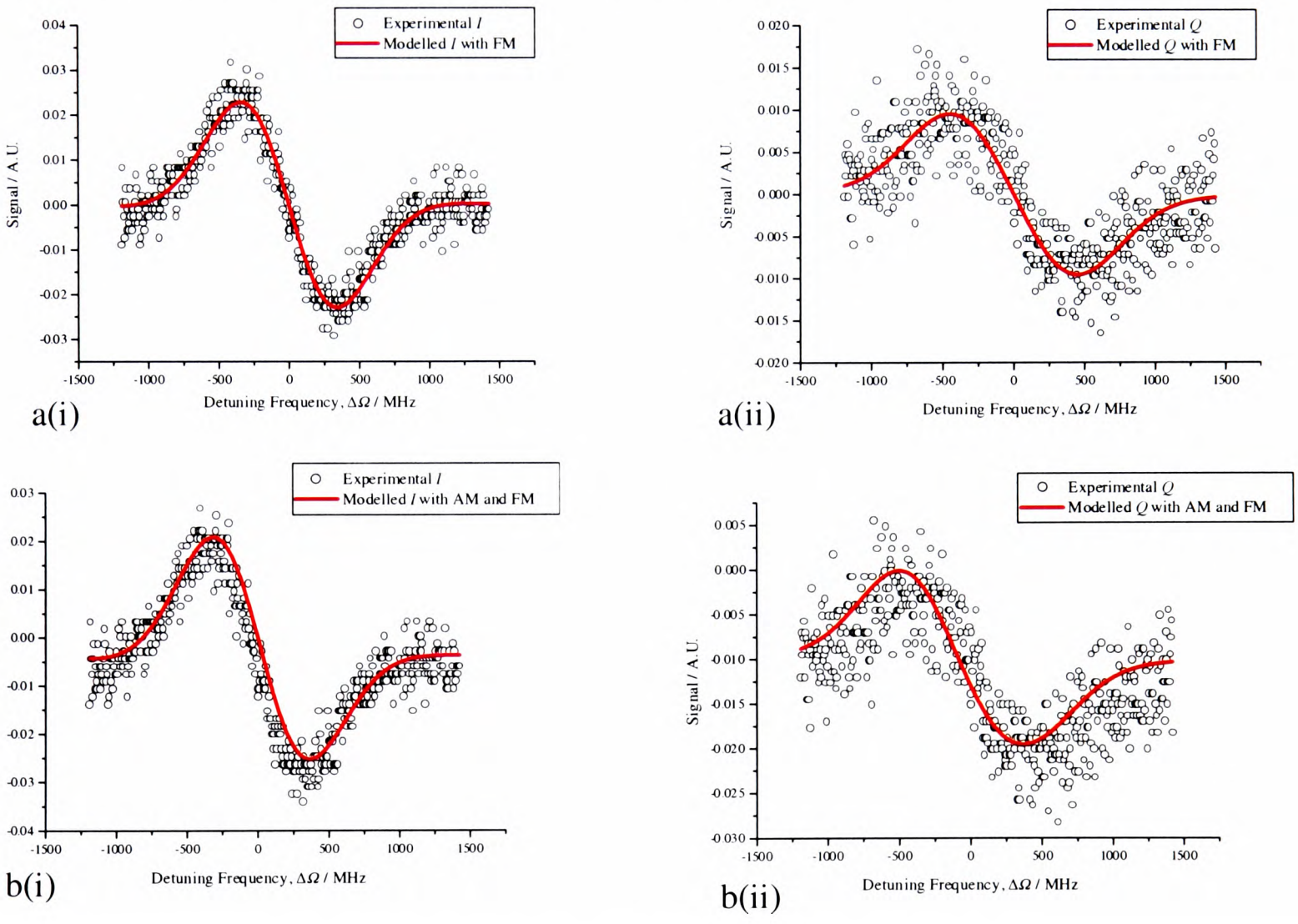

Figure 3.5 Comparison of pure FM and AM/FM simulations for an example data set.

From a comparison of these data it is found that the error in calculating the magnitude of the absorption signal, only considering FM, is less than 10 % and the width of the profile is affected by less than 1 %. Full AM/FM analysis takes several minutes on a modern PC, comparable to a plasma process time, and therefore the duty cycle is very low compared to the processing timescale. For a process diagnostic, this is unacceptable as the process being

monitored would be past its end-point before concentrations and temperatures of the species being detected had been calculated, and therefore the end-point identified. Therefore, as the error introduced by only considering FM is small, all subsequent analysis is completed with this approximation. This is not an unexpected result, as Lenth[34] found that for a current modulated diode laser the frequency modulation index, β, is approximately an order of magnitude larger than the amplitude modulation index M and thus the overall effect of AM, on the spectra taken at various modulation frequencies, is small.

3.4.3 Line Shape Analysis

The ideal situation for FMS is to use one of the two extreme cases discussed in Section 3.4.1 and shown in Figure 3.4. The second limit, when the modulation frequency is much larger than the width of the absorption profile (*i.e.* the ratio of modulation frequency to absorption FWHM is greater than 10), is hard to achieve because of the specialist electronics and detectors required. For example for the case of argon, the absorption profile's FWHM is 723 MHz and therefore to have only one of the three parts of the laser intensity spectrum coincident with the absorption feature at any one time the modulation frequency would have to be over 2 GHz. Although it is certainly possible to modulate diode lasers and detect signals at above 5 GHz[36], the cost of the high bandwidth detectors and electronics makes the price of a complete diagnostic system considerably more expensive than for lower frequency systems.

The other extreme, where the modulation frequency is at least an order of magnitude smaller than the absorption FWHM (*i.e.* the ratio of modulation frequency to absorption FWHM is less than 0.1), is also not possible. There are two reasons for this. Primarily, the I_0 and Q_0 signals depend on the three parts of the laser spectrum experiencing different amplitude attenuations and phase shifts; if these do not change significantly over a $2\omega_m$ region then the observed signals will be very small. Secondly, the diode laser has a bandwidth of a few tens of MHz (see Section 1.8.5), and therefore modulating at any frequency below 100 MHz will not completely separate the three parts of the laser intensity spectrum, decreasing the signal due to the overlapping portions of the spectrum experiencing identical amplitude attenuations and phase shifts.

It is therefore not possible to operate in either of the extremes discussed in Section 3.4.1, complicating the recovery of the absorption and dispersion profiles. In this study we use a modulation frequency of 195 MHz, giving a ratio of modulation frequency to absorption feature FWHM of approximately 0.25. The reasons for this choice are explained in

Section 3.5. The result of this ratio is that the signals resemble the limit of a small modulation frequency relative to the absorption feature FWHM but are broader. Therefore, the I_0 signals observed are not proportional to the derivative of the absorption profile and the Q_0 signals are not proportional to the second derivative of the dispersion.

A method for recovering the absorption profile in this regime, and when the laser linewidth is much smaller than the modulation frequency, has been demonstrated by North *et al.*[32]. Firstly, the detection phase angle needs to be determined and then I_0 and Q_0 signals can be obtained by the inversion of the simultaneous equations (3.8) and (3.9) which leads to

$$I_0(\chi) = I(\chi)\cos\theta + Q(\chi)\sin\theta \tag{3.22}$$

$$Q_0(\chi) = I(\chi)\sin(\theta) - Q(\chi)\cos(\theta) \tag{3.23}$$

The I_0 signal contains all the information that is required to recover the absorption profile.

To complete the reconstruction method[32], the I_0 signal must be considered as an array of measurements at a uniformly spaced set of frequencies corresponding to increments of the laser scan, $I_0(\omega)$. For simplicity, the scan increment, $\Delta\omega$, is chosen to be a factor of the modulation frequency, *i.e.* $N\Delta\omega = \omega_m$, where N is an integer. The observed signal, I_0, measured at the laser carrier frequency, $\omega_{i\text{-}N}$, is given from equation (3.7), by the difference of the absorption at the two sideband frequencies, ω_i and $\omega_{i\text{-}2N}$,

$$I_0(\omega_{i-N}) = \delta(\omega_i) - \delta(\omega_{i-2N}) \tag{3.24}$$

Rearrangement of this expression leads to the following recursion relationship.

$$\delta(\omega_i) = I_0(\omega_{i-N}) + \delta(\omega_{i-2N}) \tag{3.25}$$

If the signal acquisition is started sufficiently far from the absorption feature, the first $2N$ points can be set to zero [$\delta(\omega_i) = 0$ for $i = 1$ to $2N$]. Repeated application of the recursive relation then enables recovery of the underlying absorption line shape, $\delta(\omega_i)$.

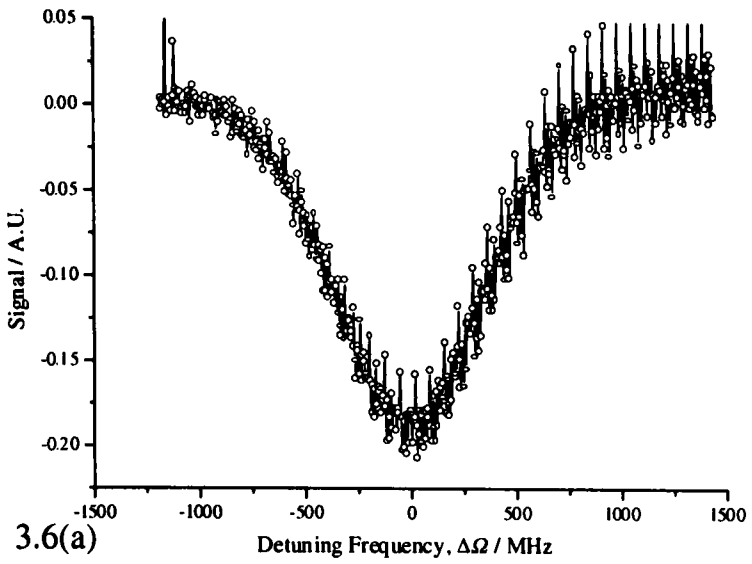

3.6(a)

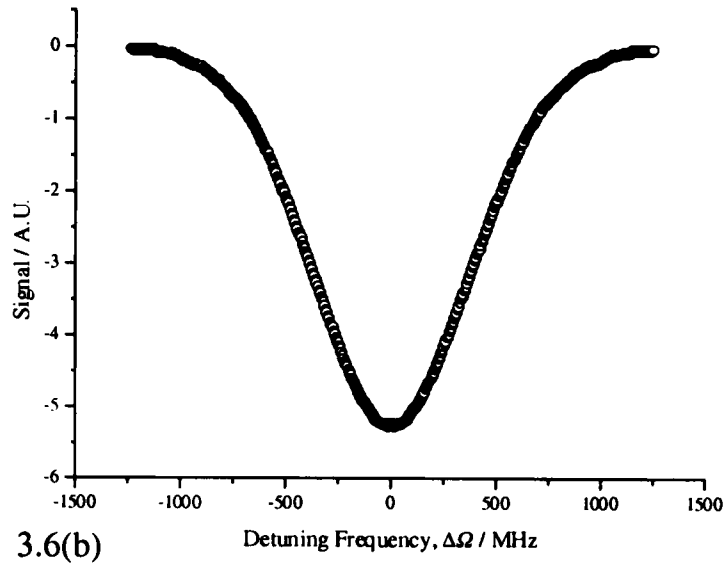

3.6(b)

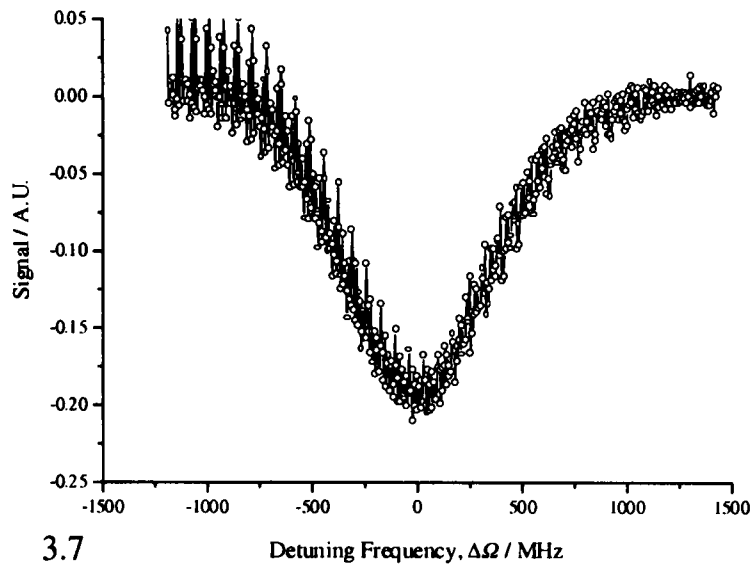

3.7

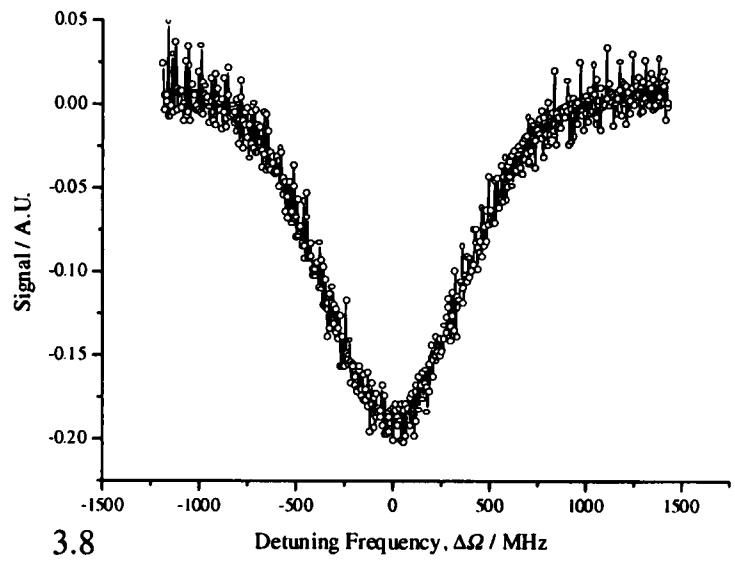

3.8

Figures 3.6-3.8 Recovered absorption signals: 3.6(a) recursive, 3.6(b) integrated, 3.7: Reversed recursive. 3.8: Averaged recursive.

Figure 3.6 shows an absorption trace recovered from signals obtained by the method discussed in Section 3.5, using both the recursive method (a) and simple integration of the I_0 signal (b). The recursive method clearly produces a trace with a lower signal to noise ratio. It was noted by North *et al.*[32] that this method of profile recovery introduces a monotonic increase in noise across the profile. This noise is also periodic because in effect the recursive formula generates $2N$ uncorrelated absorption curves, offset from each other by the scan increment, $\Delta\omega$. Therefore, the error introduced in each curve is due to the cumulative sum of errors in the I_0 signal, the growth of which follows random walk statistics across the profile. North *et al.*[32] proposed a simple method to reduce this noise by exploiting the red-blue symmetry of the inversion. If the recursive procedure is repeated in the opposite direction across the trace, the noise will build in the opposite direction as shown in Figure 3.7. If the two absorption curves, one reconstructed left to right and the other reconstructed right to left, are then averaged the noise becomes evenly distributed across the profile. Figure 3.8 shows the result of this averaging by finding the line centre, ω_c, from the crossing point of the I and Q signals and

taking the average of the point at ω_x with the point at ω_y where $\omega_y = 2\omega_c - \omega_x$. By defining a detuning parameter $\Delta\Omega = \omega - \omega_c$, the points averaged are those at $\Delta\Omega_x$ and $-\Delta\Omega_x$. This symmetrisation procedure is only valid if the absorption profiles are symmetric. In this case, it achieves the same result as repeating the recursive method and averaging.

3.5 The Experiment

To be of use as an industrial diagnostic, a technique has to be inexpensive, simple to construct and easy to use. The electronics used for the high frequency part of the experiments discussed in this Chapter are all available at low cost from standard electronics suppliers.

3.5.1 Experimental Apparatus

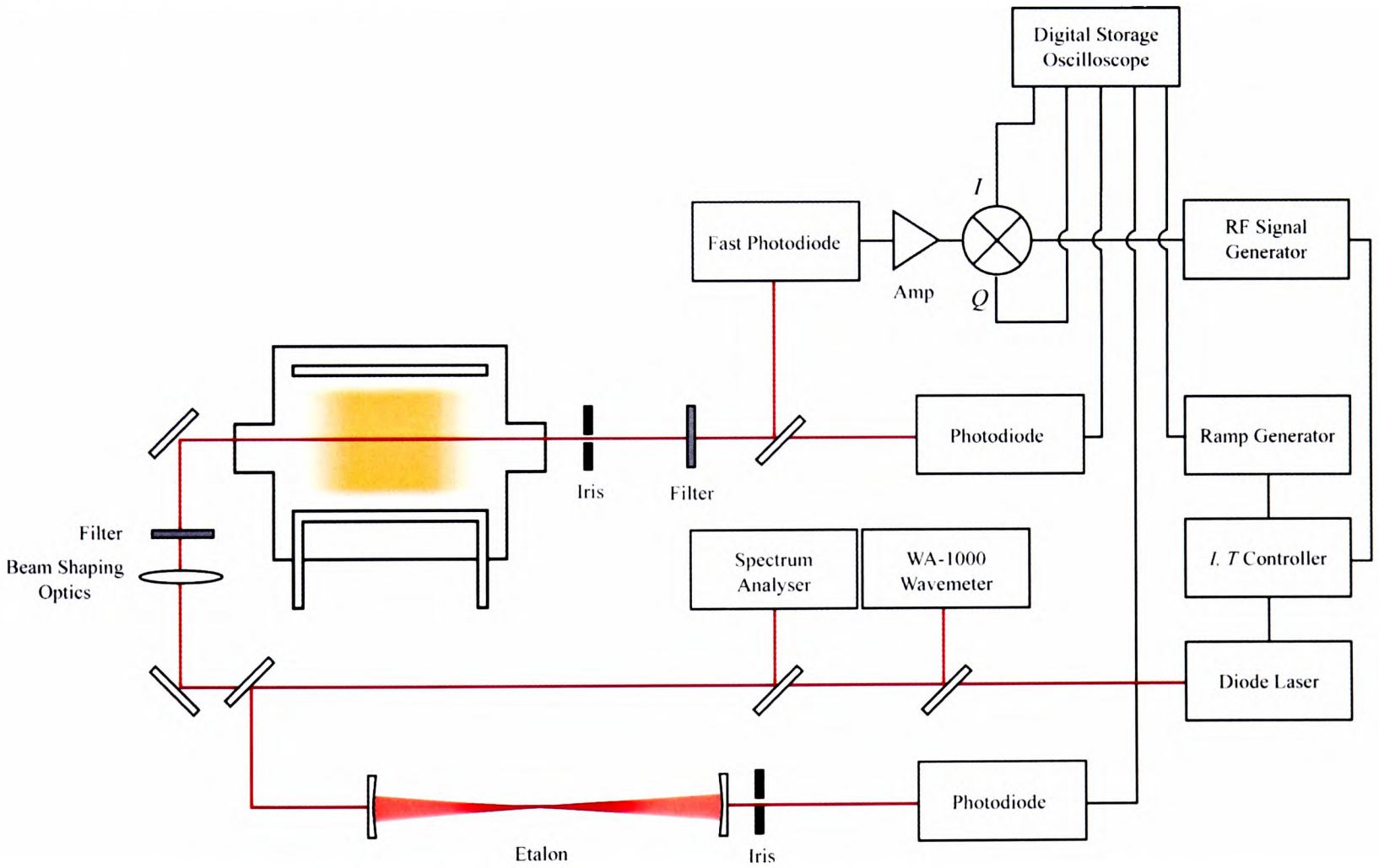

Figure 3.9 FMS experimental apparatus.

Figure 3.9 is a schematic of the FMS experimental apparatus. A Sharp LT010MD 3 mW diode laser was mounted in a compact anodised aluminium block containing a Thorlabs C220TM-B corrective lens to produce an elliptical beam that changed in size by less than 10% over 1 m. Also mounted within the block was an AD590kH (R.S.) temperature sensor IC and a laser protection circuit. The diagram of this protection circuit is given in Figure 3.10. It consists of two current inputs to the laser; a low frequency input for the current to power the laser, with a

low pass filter to protect the laser diode from electrical 'spikes', and a high frequency input enabling direct modulation of the laser current. The laser was protected from damage caused by large forward bias voltages using the three high frequency diodes and from reverse bias voltages using one high frequency diode.

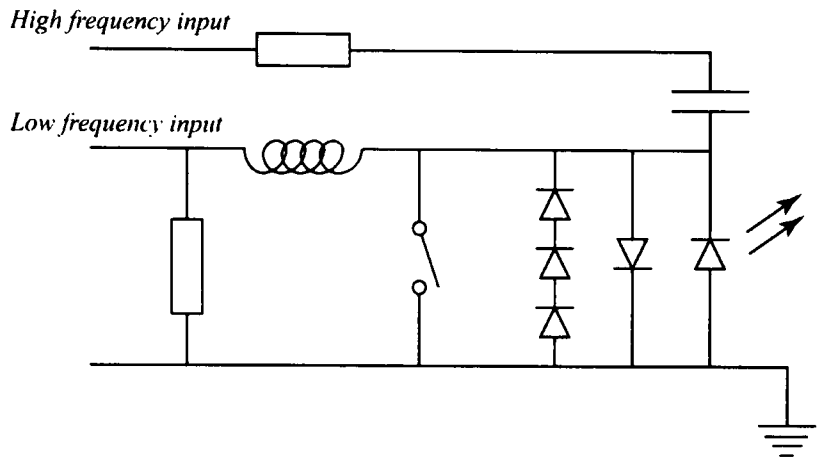

Figure 3.10 Schematic of diode laser protection circuit.

The block containing the laser was thermally isolated from an aluminium base plate by a Delrin block, on to which it was bolted using nylon bolts. The temperature of the laser block was controlled by a home built proportional and integral controller that maintained the laser at a constant temperature of about 310 K to within 1 mK using a Peltier cooler (R.S. 9.2W) and a water cooled heat sink. The protection circuit board also contained a low pass filter across the temperature sensor integrated circuit, which stopped the r.f. noise radiated from the plasma disrupting the temperature controller's input and thus causing variations in the temperature of the laser. The laser block was then protected from changing air temperature, air currents and any r.f. radiation produced from the plasma chamber by placing it in a Perspex box lined with aluminium foil. The main drive current was supplied by a home built stabilised current controller, which even with the plasma chamber discharge in operation kept the frequency of the laser constant to better than 100 MHz. The 10 dBm output from a Marconi Instruments 2022E 10 kHz – 1.01 GHz signal generator was used to drive the demodulator and to modulate the laser. To enable the control of the laser modulation index, the r.f. power used to modulate the laser was passed through a variable attenuator before connection to the laser protection circuit board. The laser was scanned across the absorption profile by varying the main drive current, *via* a modulation input on the diode laser current controller, using a ramp voltage produced from a Thurlby Thandar Instruments sweep/function generator (TG 230).

The 810 nm radiation, invisible to the eye, was observed for alignment purposes by the use of an infrared sensitive card which when exposed to infrared radiation between 0.7 and 1.3 μm visibly fluoresces. For accurate alignment, for instance onto the active surface of photodiodes

or alignment of the reference etalon, the card was not sufficiently precise or sensitive and so it was necessary to use a ½" Charge Coupled Device Camera, (Pulnix TM526A) which responded well to the radiation at 810 nm, with the image displayed on a 10" Sony monitor.

The laser beam first passed through a Leysop type 5/57 Faraday Rotator (tunable between 660 and 860 nm), in order to optically isolate the laser from any reflections from other components used. Unwanted reflections or feedback can cause laser mode selection which affects the frequency tuning of the laser; feedback can be used in a positive manner, and is exploited in external cavity tuning of diode lasers as discussed in Section 1.8.6. The laser mode structure and the modulation index were monitored using a TecOptics V4323 spectrum analyser (10 GHz Free Spectral Range and a finesse of greater than 100). For modulation index measurements, the signals from the spectrum analyser were recorded using a Tektronix TDS380 2 Gsamples/sec 400 MHz digital oscilloscope. A wavemeter (Burleigh WA1000) was used to monitor the absolute wavelength of the laser. However, in order to more precisely record the relative frequency of the laser an etalon with a low FSR needed to be incorporated into the experiment. This consisted of a pair of plane high reflectivity mirrors (> 90%), mounted almost parallel in finely adjustable mirror mounts, rigidly connected by an aluminium bar, separated by 76 cm giving a FSR of 197 MHz. The transmission of the etalon was monitored using a red sensitive photomultiplier tube (Hamamatsu R636-10 biased using a Brandenburg 2475R high voltage power supply). An iris in front of the photomultiplier tube was used to obtain the best resolution from the etalon. Figure 3.11 shows an example of the trace obtained from the etalon along with the *I* and *Q* traces obtained during that scan.

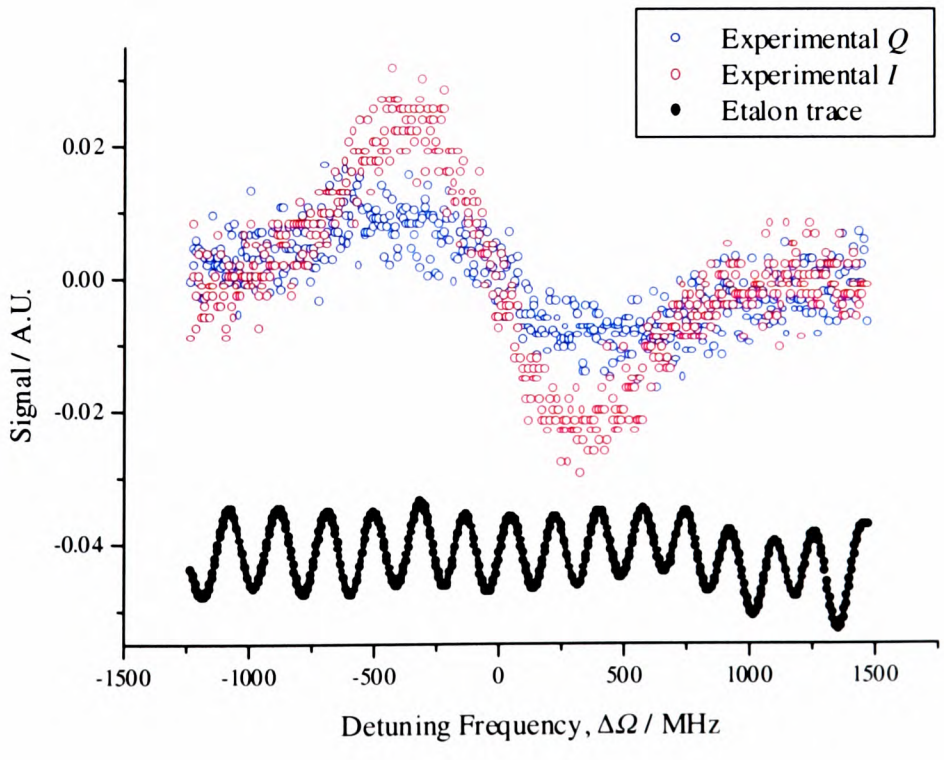

Figure 3.11 Experimental data for *I* and *Q* with a corresponding etalon trace.

In order to avoid saturation and optical pumping of the transition[18] the laser beam was attenuated and expanded, using Schott colour glass filters and a set of quartz lenses, so that its intensity was less than 10 $\mu W/cm^2$ and then passed through the plasma (produced in the chambers discussed in Chapter 2).

After the plasma chamber, the beam was focused through a 500 μm aperture and a CVI F03-810.0-1.00 narrow band interference filter. This filter has a centre wavelength of 810 nm, a FWHM transmission of 3 nm and a peak transmission of greater than 40 % and, together with the aperture, reduced the optical emission from the plasma so that the detectors were not saturated.

To detect the absolute absorption at the higher argon atom concentrations, a significant proportion of the beam was focused on to a BPX 65 Photodiode (R.S. peak response at 850 nm). The current from this photodiode was amplified using a preamplifier powered by a 9 V PP3 battery, which also biased the photodiode. The remainder of the laser radiation was focused onto a second BPX 65 Photodiode, the signal from which was amplified by a homebuilt a.c. coupled high frequency preamplifier that utilised CLC425 integrated circuits. The output from preamplifier was amplified by a Minicircuits ZFL 500 amplifier.

The I and Q signals were obtained by mixing the modulation signal and the output of the ZFL 500 amplifier in a Minicircuits MIQC 195M demodulator, mounted in a brass box to reduce interference from the radiation produced by the plasma. Careful choice of the length of the input cables resulted in the phase angle, θ, being close to 0. The outputs of the demodulator were passed through low pass filters, Minicircuits SLP-30 (the 3 dB cut off frequency was 36 MHz), to remove any noise at the modulation frequency transmitted through the modulator.

The I, Q, absorption photodiode and etalon signals were recorded on a digital oscilloscope (LeCroy 9314 M 300 MHz 100 Msamples/s), which was triggered by the ramp generator. The traces were transferred on to a Pentium PC, *via* a PCI GPIB card (National Instruments), where they were then analysed; see Section 3.5.3.

3.5.2 Variation of Modulation Index with Current

The laser was tuned and simultaneously modulated by using the injection current. The amount of optical power that is introduced into the sidebands at a particular radio frequency is proportional to the r.f. power applied to the injection current of the laser providing the slope efficiency of the laser is linear. This will not change significantly if the laser 'd.c.' injection

current is changed over a small range; in this instance a change of less than 2 mA is required to scan over the atomic transition. However, this small change in 'd.c.' injection current will change the total output power of the laser. Therefore, the ratio of the fundamental intensity to the sideband intensity changes across the profile, and thus the frequency modulation index changes across the scan. This results in asymmetric I and Q traces because the signals are proportional to the modulation index (equation (3.7)).

Over the small scan range, to a good approximation, this change in modulation index was found to be linear and therefore if the profile is assumed to be symmetric the effect of changing the modulation index with current can be removed by the symmetrisation procedure discussed in Section 3.4.3.

3.5.3 Signal Analysis

The concentration and the temperature of the argon atoms were deduced from the observed I and Q signals using the method of Section 3.4.2. The four traces I, Q, reference etalon photomultiplier tube and absorption monitor photodiode were recorded. The offsets were removed from the I and Q signals and the line centre was determined from their crossing point. The scan rate was determined from the separation of the peaks and troughs of the reference etalon signal and this was used to convert the independent variable of the other three signals from time to detuning frequency, $\Delta\omega$. A simulation of the expected I and Q traces was produced for a Gaussian absorption profile using the theory discussed in Section 3.4.1. The line position, ω_c, and the modulation frequency, ω_m, were entered into this simulation. The variables θ (the experimental phase angle between the in-phase and quadrature signals), T and the magnitude of the signal were varied to minimise the sum of the squares of the difference between the modelled I and Q and the experimental I and Q using the Microsoft Excel Solver. This gives a measurement of the temperature of the argon atoms and absorption magnitude. Figure 3.12a shows an example of experimental I and Q traces with the Solver fits.

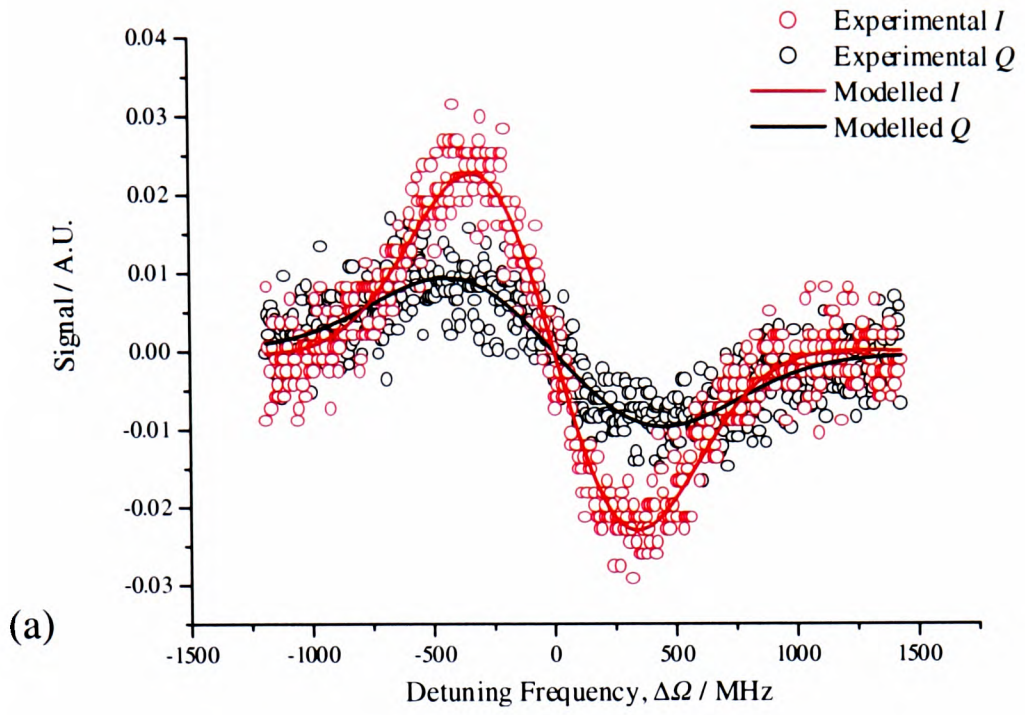

Figure 3.12 Examples of experimental FMS signals: (a) I and Q traces complete with the respective Solver fits and (b) recovered I_0 signal.

Knowledge of the phase angle θ enabled the recovery of the I_0 trace from the I and Q signals using equations (3.22) and (3.23) (see Figure 3.12a and Figure 3.12b). The absorption profile was reconstructed by integration of the I_0 signal. A Gaussian profile was then fitted to this absorption profile by a least squares fitting routine, giving another measurement of the argon atom temperature and the absorption magnitude. Figure 3.13a shows an example of this profile and the fit.

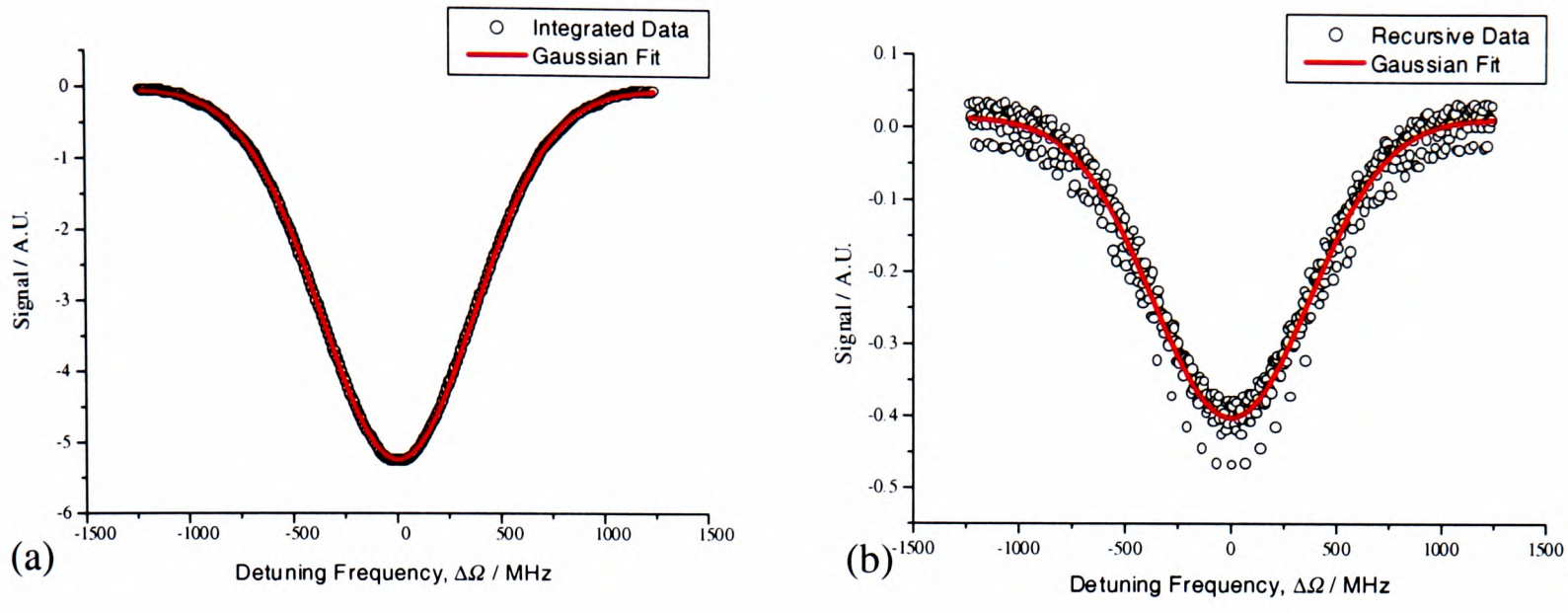

Figure 3.13 Reconstruction of the absorption profile using (a) the integration method and (b) the recursive method.

The recursive method described in Section 3.4.3 was also used to regenerate the absorption profile. The smooth scanning of the laser and recording of the signal against time resulted in $\Delta\omega$ not being a factor of ω_m and therefore N was chosen to be the nearest integer to $\omega_m/\Delta\omega$. N was found to be large, around 100 for the data presented in this Chapter, and so this small change to N resulted in a negligible error in the reconstruction. In addition, instead of recording a long baseline before and after the absorption feature and then setting the first and/or last $2N$ points to zero, as suggested by North *et al.*[32], $2N$ or more points were added to the beginning and/or end of the data and set to zero. This maximised the number of points taken on the absorption feature while minimising the experimental acquisition time. A Gaussian profile was fitted to the symmetrised reconstructed absorption profile by a least squares fitting routine, giving a third measurement of the argon atom temperature and the absorption magnitude. This profile is shown in Figure 3.13b, along with the fit.

It is not possible to obtain the percentage absorption directly from FMS as the signal depends on the frequency response of the detector and electronics. It is therefore necessary to calibrate the FM absorption magnitude with the percentage absorption observed in a standard absorption experiment. To achieve this calibration, the absorption monitor photodiode was used when the absorption signal was sufficiently large to be observed without using FM. A Gaussian profile on a sloping baseline (because of the change in laser intensity with current) was fitted to the signal recorded on the absorption monitor photodiode using Microsoft Excel Solver. One of the signals recorded on the monitor photodiode is shown in Figure 3.14 along with the Solver fit.

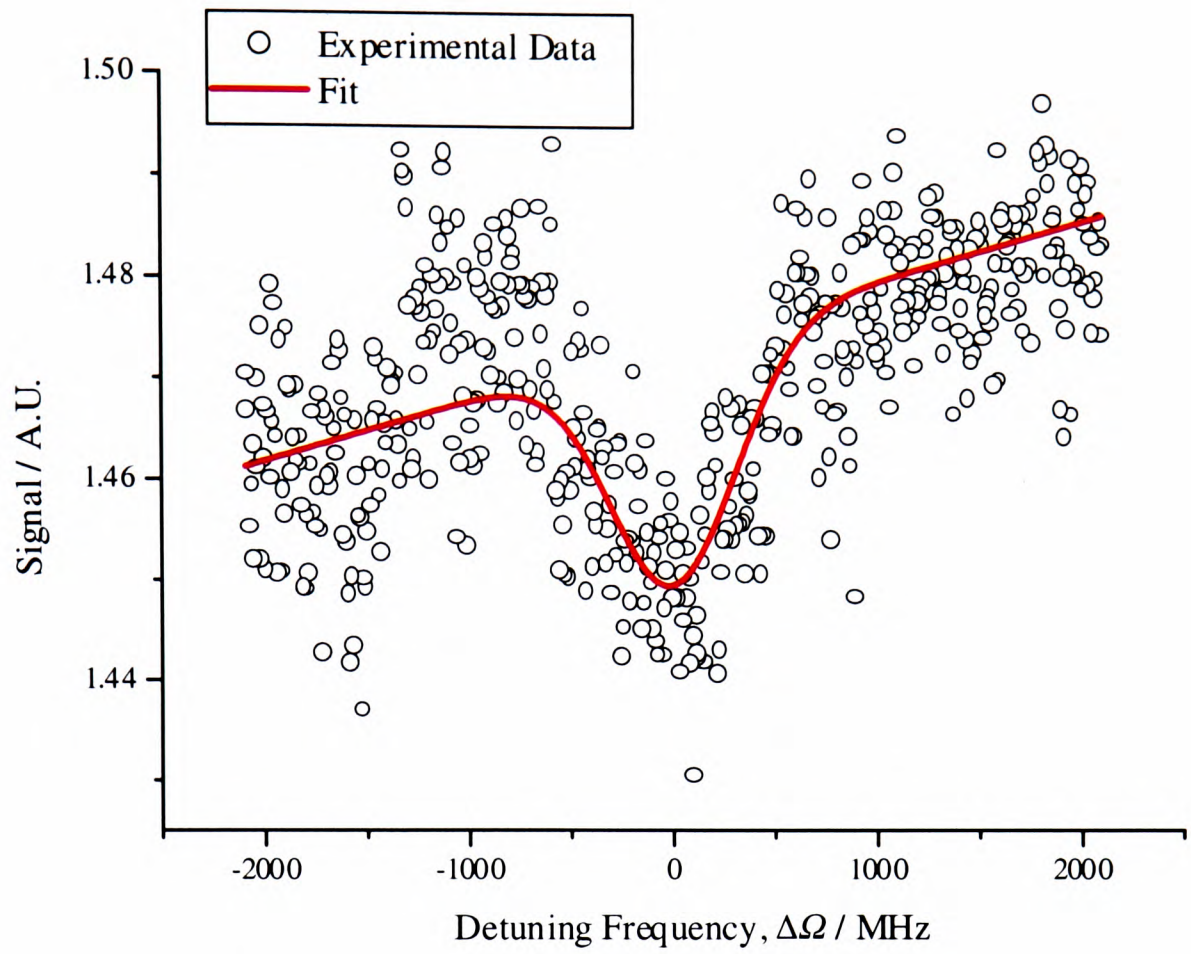

Figure 3.14 An example of an absorption photodiode signal, with Solver fit.

3.5.4 Parameter Selection

From equation (3.7) it can be seen that the I and Q signals obtained by FMS depend linearly on modulation index. Therefore, it would be expected that to obtain the largest signals, the largest possible modulation index should be employed. However, once β is greater than 1, the assumption used to derive equation (3.4) is not valid, and therefore simple FM theory is no longer applicable. This can be observed in the frequency spectrum of the laser. As the modulation index increases, 'harmonic' sidebands start to appear at $\omega_0 \pm 2\omega_m$, $\omega_0 \pm 3\omega_m$, etc, and although these are weak at modulation indices only just greater than 1 they become dominant at high modulation indices. In addition, as the FM index is increased, the AM index will also increase, making the AM is a non-negligible effect. Therefore, to investigate the best FM modulation index and frequency to use for the experiments discussed in this Chapter, a set of I and Q traces were obtained at various modulation frequencies and indices. These were analysed as described in the previous section, to obtain the relative magnitude of the absorption signal. Simultaneously, the modulation index was determined from the spectrum analyser signal. First, the independent variable was converted from time to frequency. The spectrum of the laser without the r.f. modulation was then fitted to a Lorentzian curve. The bandwidth of the spectrum analyser is greater than the laser bandwidth and therefore dominates the width of

the frequency profile, W. To obtain the frequency modulation index, the frequency spectrum of the modulated laser was fitted with a triplet of Lorentzian peaks, with width W, separated by the modulation frequency, ω_m. Figure 3.15 shows an example of this procedure for a modulation frequency of 350 MHz.

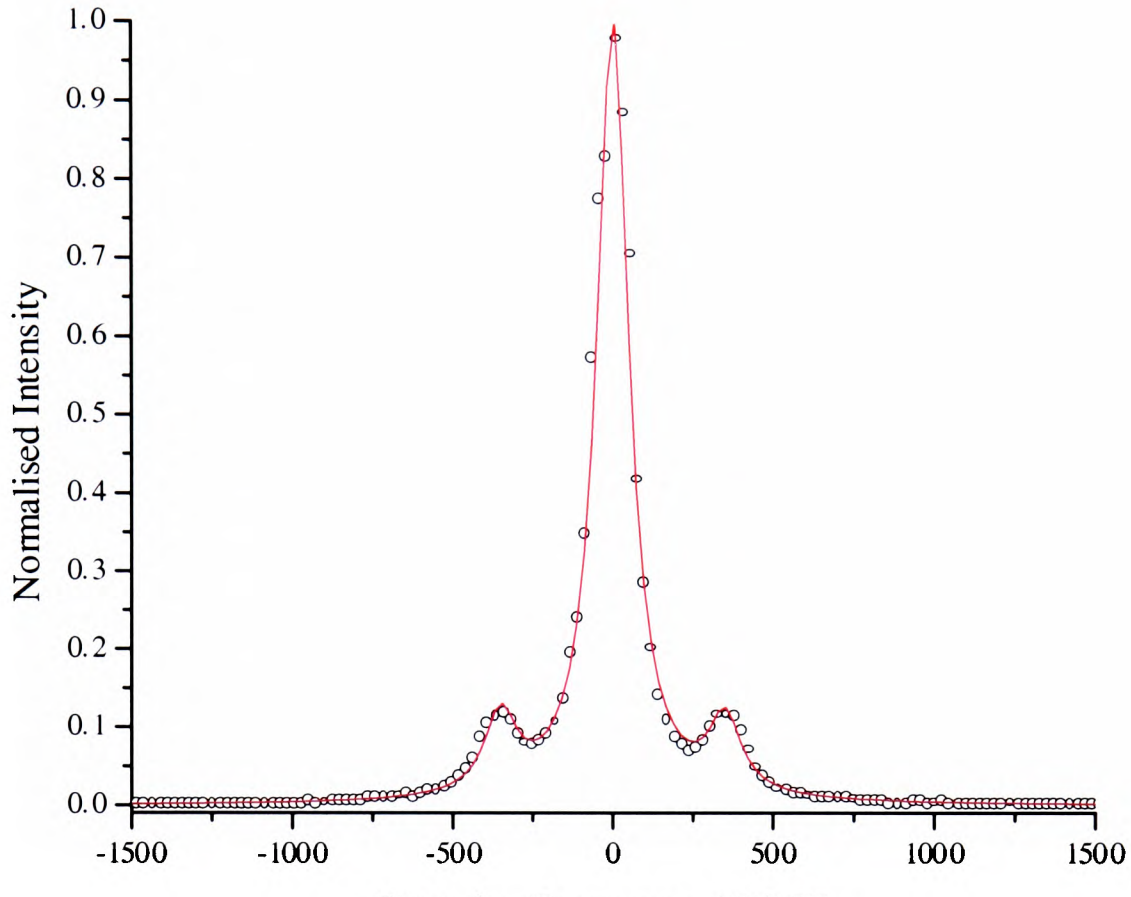

Figure 3.15 Modelling the frequency spectrum of a modulated (350 MHz) diode laser with a triplet of Lorentzian peaks.

The FM modulation index, β, was calculated from the ratio of the carrier intensity to the average intensity in the side bands, $I_0/((I_h+I_l)/2)$, using

$$\frac{1}{\beta} = \sqrt{\frac{8I_0}{I_h + I_l}} \tag{3.26}$$

from equation (3.4)

Figure 3.16 shows the relative FMS signal, the magnitude of the absorption signal, plotted against modulation index, for various modulation frequencies.

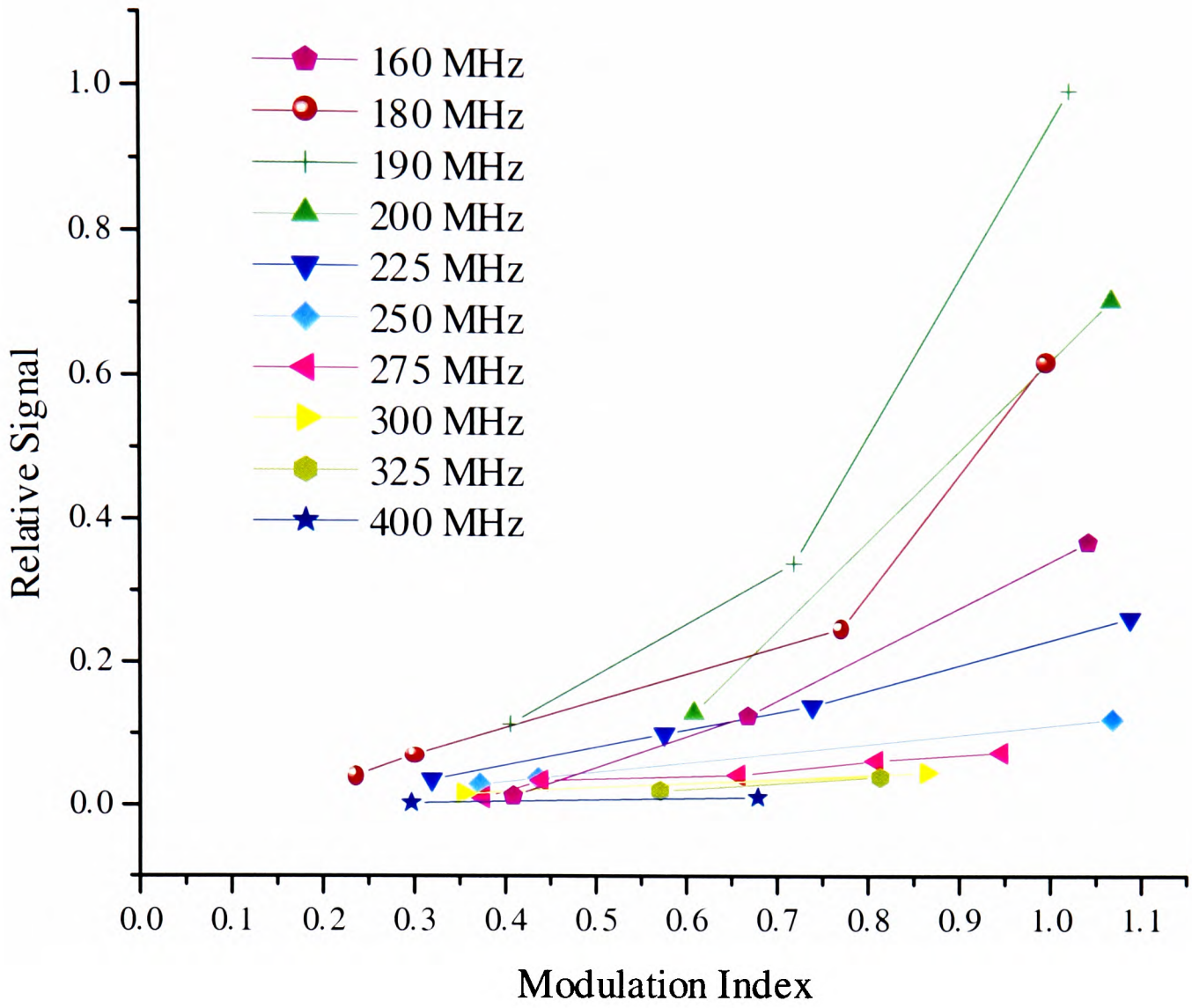

Figure 3.16 Variation in observed FMS signal with frequency and modulation index.

The general trend indicates clearly that the larger the modulation index, the bigger the signal. However, for several frequencies, these plots are not linear; it appears that at modulation indices around or above 1, larger signals than expected are obtained (for the most dramatic example, see the set at 180 MHz). This can be explained qualitatively by the extra signal resulting from interaction of the sets of 'harmonic' sidebands with the absorption feature. In order to determine accurately the modulation index at large β the intensity of these 'harmonic' side bands would need to be considered, and the FM theory outlined in Section 3.4.1 would be greatly complicated. Qualitatively, the measurement of the modulation index is an underestimate of the true index and therefore the points at $\beta \geq 1$ should be shifted to higher β. To ensure that the 'harmonic' sidebands and AM did not affect the measurements reported later in this Chapter, all measurements were completed with a frequency modulation index of less than 0.5.

To determine the frequency response of the electronics for each point on Figure 3.16, for $\beta \leq$ 0.95, the relative FM absorption signal was divided by the modulation index and these were averaged for each particular frequency. The result of this is shown in Figure 3.17.

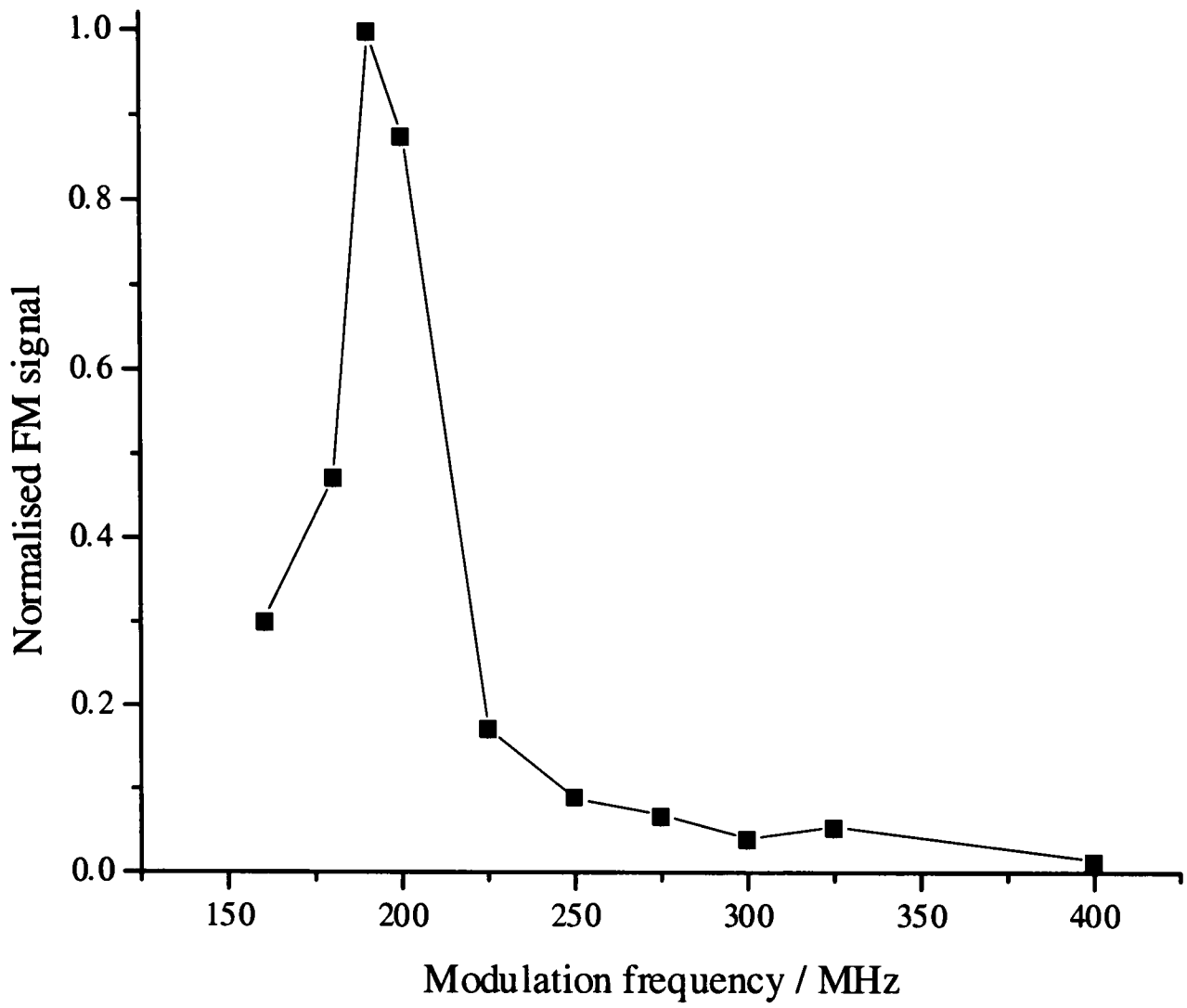

Figure 3.17 A plot of normalised FMS signal, obtained from the gradients of the lines shown in Figure 3.16, against modulation frequency.

It is not unexpected that the largest signal obtained is at the centre frequency of the demodulator, although prior to this experiment the frequency response of the other electronic components, especially the photodiode and the preamplifier, were not known. For the experiments described in the following sections of this Chapter, the modulation frequency was fixed at 195 MHz corresponding to the peak of Figure 3.17. It should be noted that when an FMS experiment is constructed, to generate the largest signal the laser modulation frequency should be carefully chosen to optimise the response of the laser and detection electronics.

3.5.5 Comparison of Unmodulated Absorption Spectroscopy (UAS), Mechanical Modulation Spectroscopy (MMS) and FMS

Absorption signals were recorded by FMS, in a 'd.c.' experiment using a biased BPX 65 photodiode as the detector while the laser is not modulated (UAS) and by a phase sensitive method using a mechanical chopper to modulate the laser (MMS). The data traces presented in this section were acquired over the same time period of approximately 100 ms.

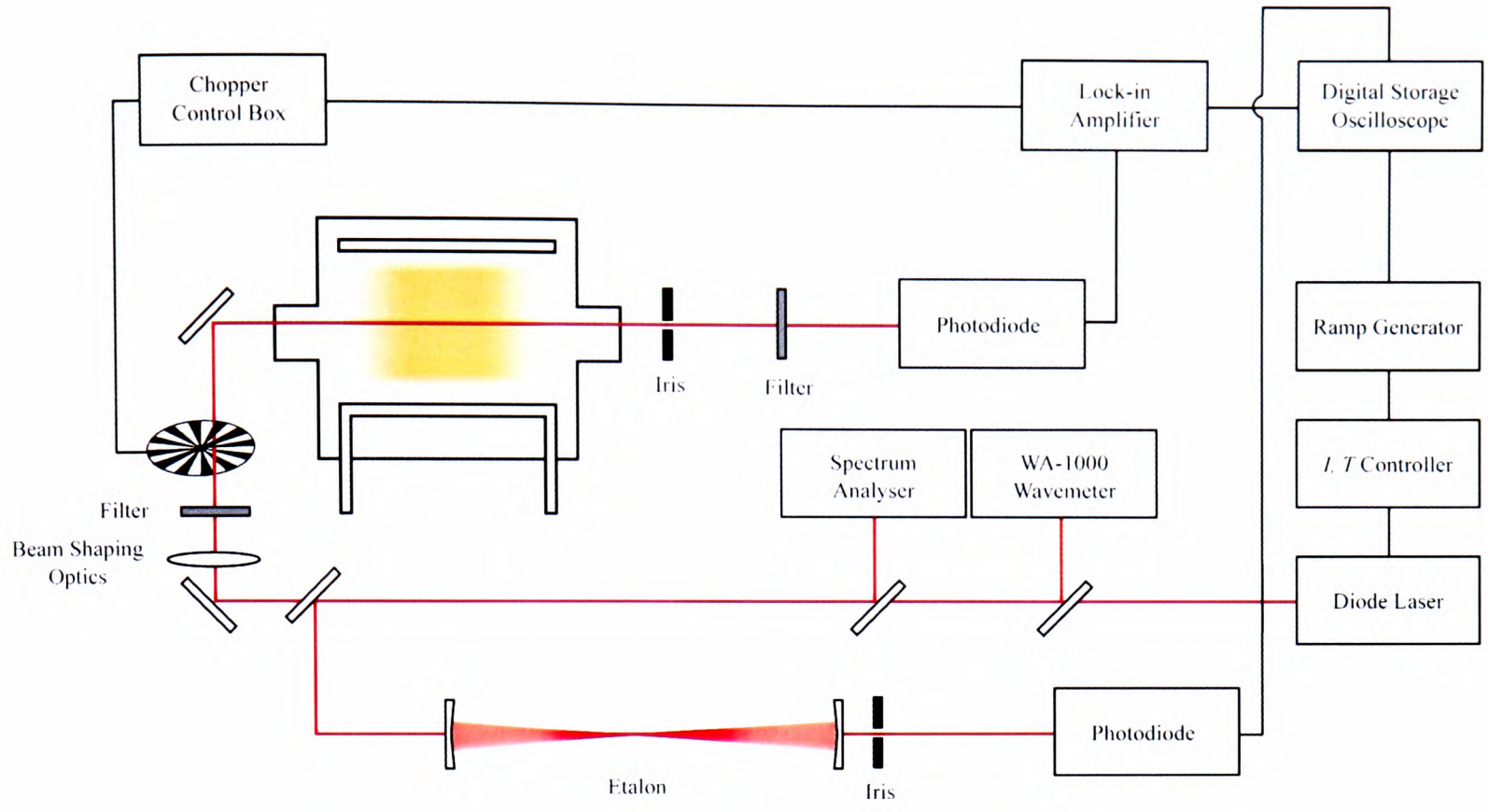

Figure 3.18 Schematic of the MMS experimental layout.

The experimental layout used for the MMS experiment is shown in Figure 3.18. It is the same as the layout for the FMS except that the laser was mechanically amplitude modulated rather than electrically modulated and the signal from a biased BPX 65 photodiode was amplified using a Lock-in Amplifier (Stanford Research Systems SR5-10). This is a phase sensitive detection method similar to FMS, but conducted at lower frequencies. The use of a mechanical chopper and a lock-in scheme to achieve a real time background correction for absorption measurements is common and is used in many commercial spectrometers[37].

Figure 3.19a shows the absorption profile obtained using the UAS method, after a background correction was applied to remove the sloping baseline caused by the change in laser intensity resulting from the current tuning. Figure 3.19b shows an example of the profile obtained under the same conditions using MMS optically chopping at 920 Hz and again with a background correction. The signal to noise ratio has increased by a factor of 10 over the UAS method. This is in part due to the removal of some of the plasma optical emission from the signal by the lock-in method.

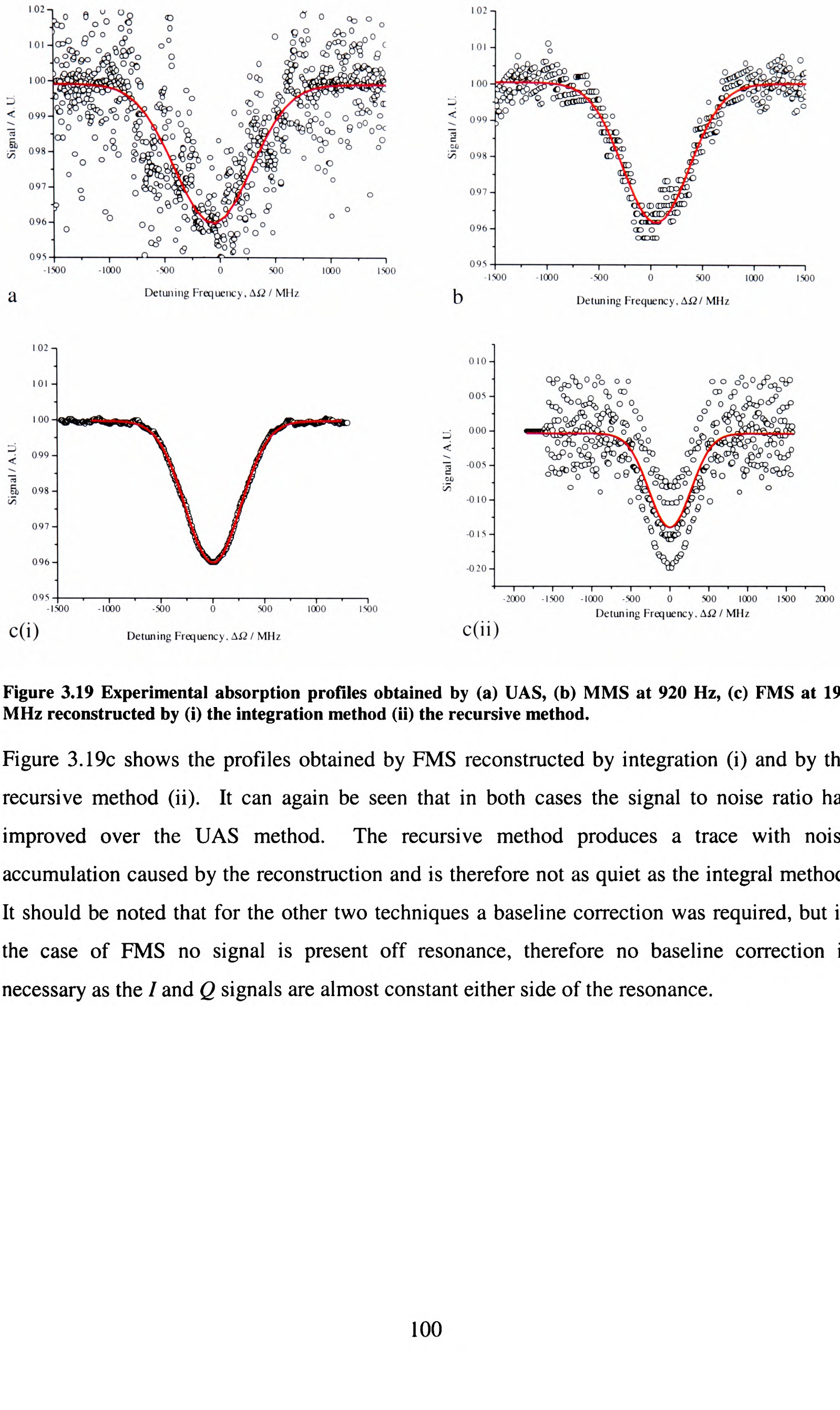

Figure 3.19 Experimental absorption profiles obtained by (a) UAS, (b) MMS at 920 Hz, (c) FMS at 195 MHz reconstructed by (i) the integration method (ii) the recursive method.

Figure 3.19c shows the profiles obtained by FMS reconstructed by integration (i) and by the recursive method (ii). It can again be seen that in both cases the signal to noise ratio has improved over the UAS method. The recursive method produces a trace with noise accumulation caused by the reconstruction and is therefore not as quiet as the integral method. It should be noted that for the other two techniques a baseline correction was required, but in the case of FMS no signal is present off resonance, therefore no baseline correction is necessary as the I and Q signals are almost constant either side of the resonance.

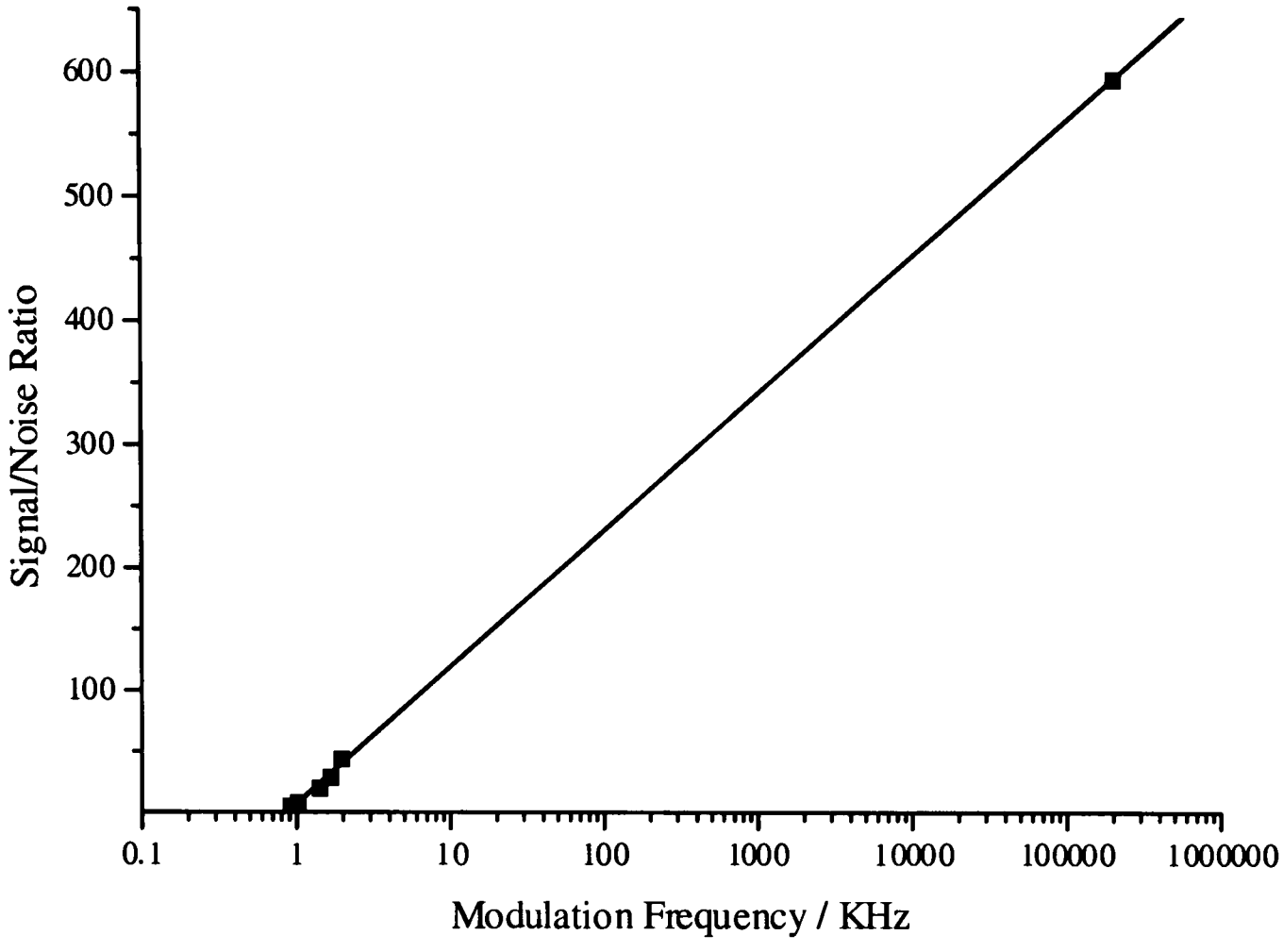

Figure 3.20 A plot of the observed signal to noise ratio for various modulation frequencies for the MMS experiment. Also included is the FMS at 195 MHZ. The corresponding noise to signal ratio of the UAS experiment was unity.

Figure 3.20 shows how the signal to noise ratio varies with the chopping frequency (f) for both the MMS and FMS methods. For the same signal with the unmodulated 'd.c.' absorption method the signal to noise ratio is approximately unity. The signal to noise ratio is smaller at low frequencies than would be expected if all sources of noise in this experiment varied as $1/f$, a commonly observed frequency dependence for which no unifying principle has been found[38]. This is probably because of the plasma induced emission and the effect of the discharge on the laser (see Section 2.2.4). It is clear the best signal to noise ratio is observed at high modulation frequencies, which can only be achieved electrically.

3.6 Results

FMS cannot provide an absolute absorption and hence the absolute concentration of the excited argon atoms cannot be directly obtained, and thus the UAS method has to be used to calibrate the FMS absorption signal. As the signal to noise ratio is low for the UAS signal (Figure 3.19 and 3.20) the accuracy of the FMS derived concentrations are limited, and each will be subject to a systematic error. The calibration was repeated 10 times using a feed gas consisting of 10 % argon in helium at a total pressure of 100 mTorr and an applied power of 50 W in the

CCP chamber, and the concentration of the $4s[^3/_2]_1$ level of argon atoms was found to be 2.9×10^9 atoms/cm^3 with a standard deviation of 1.9×10^8 atoms/cm^3. If this error, taken to be a fixed absolute value on the transmitted radiation, was larger than the FMS fitting percentage uncertainty then it was used to provide error bars on the concentration measurements. For high concentrations of excited argon atoms, the Beer-Lambert law will no longer be applicable, and the absorption profiles become distorted. The maximum absorption under these conditions is less than expected and this limited the conditions over which measurements can be taken. If a wider variety of conditions were required, a set of several absorption lines with different cross sections could be used to extend the parameter space over which absorption methods could be used to study argon atoms in discharges. The lowest concentration of the $4s[^3/_2]_1$ level of argon atoms that could be observed by the integral reconstruction method, with a S/N ratio of greater than or equal to 1 and a 100 ms acquisition time, was calculated to be 3×10^5 atoms/cm^3.

3.6.1 Temperature Determination by Profile Reconstruction

Three methods were used for calculating the translational temperature of the argon atoms from the absorption profiles obtained by FMS, namely:

a) The temperature determined from the detector phase angle fitting routine, T_θ.

b) The temperature determined from the width of the absorption profile obtained by simple integration of I_0, T_{Int}.

c) The temperature deduced from the width of the absorption profile obtained by use of the recursive recovery method discussed in Section 3.4.3, T_{Rec}.

As expected the translational temperatures found using the recursive reconstruction method (c) were lower than those found from simple integration of the FMS derived absorption profile (b) by about 20 % (see Section 3.4.3). The most reliable temperature was found to be that obtained from method (a); the average of the 10 sets of data taken using a feed gas consisting of 10 % argon in helium at a total pressure of 100 mTorr and an applied power of 50 W in the CCP chamber gave a result of 323 K ± 17 K. Method (a) is the most reliable because it does not contain the error introduced by the estimation of the phase angle which produces an error in I_0 (the I and Q traces will not be separated correctly) and hence errors will be introduced into $Abs(\omega)$ reconstructed by either method (b) or (c). The translational temperature observed under these discharge conditions is comparable to that observed in other discharges; in a very low density discharge the temperature was observed to be 376 ± 20 K[17], at pressures comparable to

those used in this Chapter, but in plasmas with a much higher power density, argon atom temperatures of around 600 K have been observed[16,18].

3.6.2 Variations in Argon Atom Concentration with Plasma Conditions

The concentrations of argon atoms produced in the $4s[^3/_2]_1$ level by the two different plasma chambers discussed in Chapter 2 were measured under various discharge conditions. To understand any variation in concentration it is necessary to consider the rate of formation and removal of the $4s[^3/_2]_1$ level, which under the steady state condition of the discharge, will control its concentration.

The rate of formation depends on the rate of excitation/ionisation of the ground state of the argon atoms by electron impact. The $4s[^3/_2]_1$ level can be populated in three ways; firstly by direct electron induced excitation from the ground state, secondly from electron excitation to a higher level which cascades through other levels either by radiative decay or collisional deactivation into the $4s[^3/_2]_1$ level or thirdly by recombination of an argon ion (produced by electron impact ionisation) and an electron, either directly forming the $4s[^3/_2]_1$ level or forming a higher level and again cascading into it. The rate of electron impact excitation of the ground state depends on the electron density and the electron impact excitation cross section, which in turn depends on the electron energy distribution.

The removal rate depends on the natural lifetime of the state, the collision rate (*via* collisional deactivation) and the rate of removal by electron excitation/ionisation. In this case the natural lifetime of the level is very short (10 ns and therefore $k_r = 10^8\ s^{-1}$) and as discussed in Section 3.3.7 within the pressure range considered in this Chapter the collisional quenching of the level can be neglected. Therefore it is possible to obtain a simple relationship for the concentration of the $4s[^3/_2]_1$ level by equating the formation rate to the destruction rate:

$$k_e[e^-][Ar] = k_r[Ar^*] \tag{3.27}$$

where k_e is the total rate constant for electron collisional excitation to the $4s[^3/_2]_1$ level and $[e^-]$, [Ar] and [Ar*] are the electron density, ground state argon atom concentration (which is approximately the argon concentration in the feed gas) and the concentration of the $4s[^3/_2]_1$ level respectively. k_e is not only the rate constant for direct excitation to the $4s[^3/_2]_1$ level but also includes the contributions from cascade formation from other excited states and collisonal formation from the other ^3P levels (namely $4s[^3/_2]_2$ and $4s[^1/_2]_0$)[39].

The electron density at a pressure of 100 mTorr and an applied power of 50 W in the CCP chamber, the conditions used for the calibration described at the beginning of Section 3.6, can be estimated to be 1×10^{10} electrons cm^{-3} from previously measured ion densities in this chamber[40] and extrapolation of measurements made in Chapter 2. The value of k_e can be obtained from the electron energy distribution, $f(E)$, and the electron excitation cross section for the production of the $4s[^3/_2]_1$ level, $\sigma(E)$, *via* equation (3.28)[41].

$$k_e = \left(\frac{2}{m_e}\right)^{1/2} \int_0^\infty E^{1/2} \sigma(E) f(E)\, dE \tag{3.28}$$

Here m_e is the electron mass and, $f(E)$, is the normalised electron energy distribution which is, as in Chapter 2, assumed to be Maxwellian. From Chapter 2 the electron temperature is estimated to be at least 17000K (corresponding to an energy of 1.5 eV).

The value of k_e can be found from the sum of the rate constants for excitation to the $4s[^3/_2]_1$ radiative level and the $4s[^3/_2]_2$ and $4s[^1/_2]_0$ metastable levels, with the assumption that because the metastable levels have long radiative lifetimes they are only removed by collisional conversion into the $4s[^3/_2]_1$ radiative level. Figure 3.21 shows the dependence of these cross sections on electron energy[42]; also shown is the Maxwellian electron energy distribution with T_e = 1.5 eV.

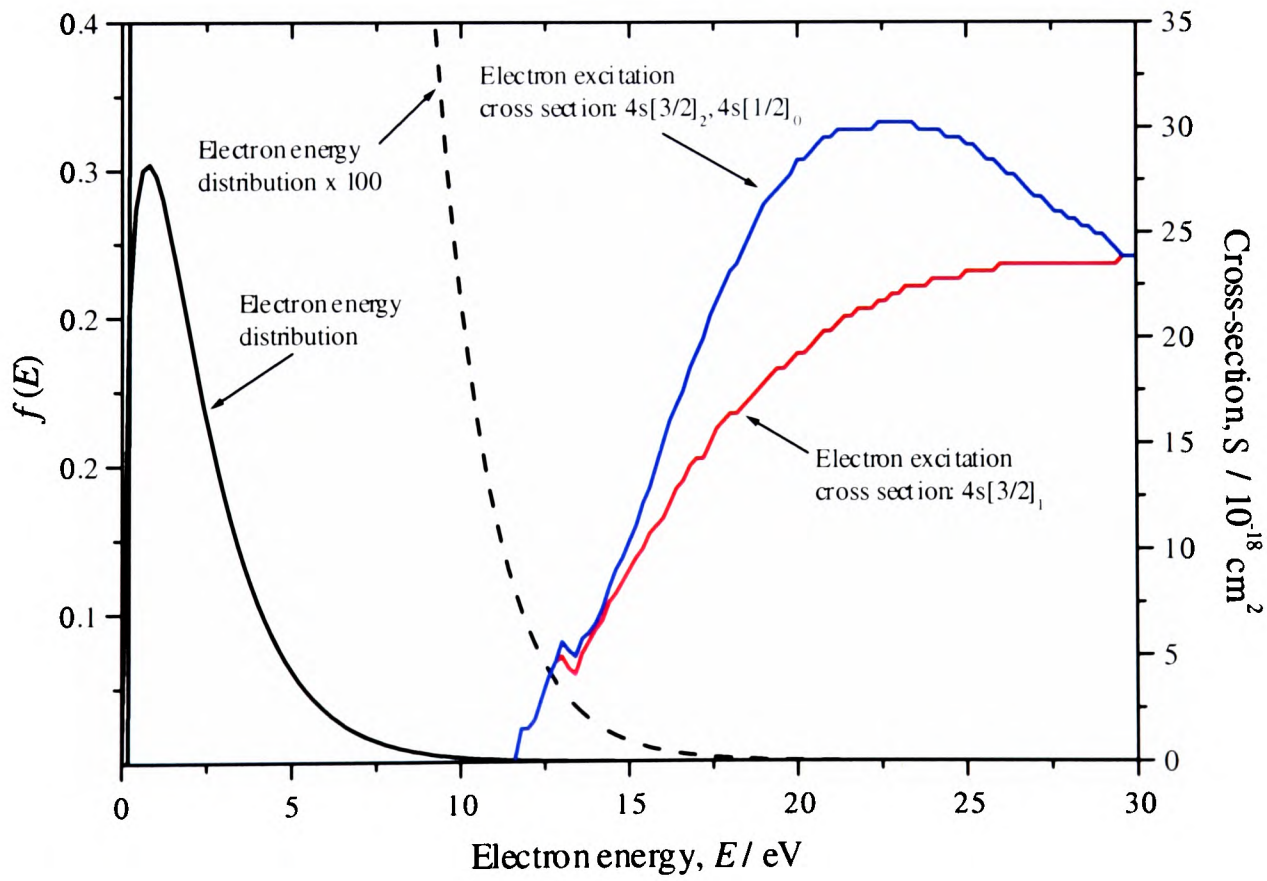

Figure 3.21 A 1.5 eV Maxwellian electron energy distribution along with the electron energy dependent excitation cross sections for formation of the $4s[^3/_2]_1$ radiative level and the $4s[^3/_2]_2$ and $4s[^1/_2]_0$ metastable levels of argon (from C. M. Ferreira and J. Loureiro[42]).

Equation (3.28) yields values of k_e to the $4s[^3/_2]_1$ radiative level and the $4s[^3/_2]_2$ and $4s[^1/_2]_0$ metastable levels of 1.5×10^{-12} cm^3s^{-1} and 1.8×10^{-12} cm^3s^{-1} respectively, giving a total k_e of 3.3×10^{-12} cm^3s^{-1}.

If the radiative rate $k_r = 10^8$ s^{-1} is used in equation (3.27), it results in a concentration of the $4s[^3/_2]_1$ level of 1.1×10^5 atoms/cm^3, more than four orders of magnitude lower than the measured value of 2.9×10^9 atoms/cm^3. This large discrepancy can be explained by radiation trapping. A photon emitted by one argon atom as it returns to the ground state, *via* a strongly allowed transition, has a high probability of being reabsorbed by a surrounding gas atom, leading to the transfer of the excitation from one atom to another. This results in a large number of emissions and absorptions of the quanta of energy before it escapes the boundary of the enclosed gas, and the radiation is said to be 'trapped'. This trapping leads to an increase in apparent lifetime for the radiating level. This extended lifetime ($\tau_{app} = 1/k_{rad(app)}$) can be calculated from equation (3.29)[39] where τ is the radiative lifetime of the transition (in this case 10 ns), and γ is the radiation trapping factor. The trapping gas is considered to be a cylinder, of radius R (equal to 15 cm for the CCP chamber) and infinite height.

$$\frac{\tau}{\tau_{app}} = \gamma = \frac{1.6}{k_0 R(\pi \ln(k_0 R))^{1/2}} \tag{3.29}$$

Here k_0 is the absorption coefficient at the centre of the profile:

$$k_0 = \frac{\lambda^3 [Ar] g_2 A_{21}}{8\pi g_1 c^* \sqrt{\pi}} \tag{3.30}$$

and λ is the wavelength of radiation being trapped (106.666 nm)[43], A_{21} is the probability of the downward transition (1×10^8 s^{-1}), g_1 (= 1) and g_2 (= 3) are the degeneracies of the lower and excited levels of the transition, respectively, and c^* is the most probable speed of atoms in the ground state (≈ 350 ms^{-1}). From this analysis the apparent radiative lifetime, τ_{app}, is found to be 40 μs.

Equation (3.27) modified to account for the radiation trapping yields

$$[Ar^*] = \tau_{app} k_e [e^-][Ar] \tag{3.31}$$

and results in a concentration of 4.2×10^8 atoms/cm^3, less than an order of magnitude lower than was measured. It was found that by increasing the electron temperature to 1.9 eV the calculated concentration agreed exactly with the measured value. This slightly increased

electron temperature may be explained by the breakdown of the approximation that the electron distribution is Maxwellian. In a similar system the electron distribution has been observed to be better modelled by a two temperature distribution[44] in which the second temperature describes a higher energy electron distribution, generally containing fewer electrons than the first lower energy distribution. If this is a good description of the electron distribution in the system used here then the extra higher energy electrons, which are not predicted by the single Maxwellian distribution, would increase k_e. A small increase in the proportion of the electrons in the high energy tail of the distribution will affect this rate constant significantly as can be seen from Figure 3.21 and equation (3.28). Furthermore, using equation (3.31) it is possible to understand the trends observed in the concentration of the $4s[^3/_2]_1$ level of argon atoms as the plasma parameters are varied.

3.6.2.1 Variation of Argon Atom Concentration with Discharge Power

As discussed in Section 2.2.2, the net power applied to the plasma chamber coupling networks is not necessarily the power that is coupled into the plasma. In this section, the powers quoted are the net powers applied to the matching networks. Despite the underestimate of the applied power, the general trends of the excited argon atom concentration can be observed.

Figure 3.22 shows the variation, at three different pressures, of the concentration of the $4s[^3/_2]_1$ level of argon atoms with applied power for a plasma produced in the CCP chamber from a 1:1 flow gas mixture of argon and nitrogen. Measurements with more than 60 % argon in the flow gas were subject to a large error because the amount of absorption became sufficiently large to distort the line profile. The figure clearly shows that as the power applied to the discharge is increased the argon atom $4s[^3/_2]_1$ level concentration increases. This can be explain qualitatively from equations (3.30) and (3.31): an increase in power causes an increase in the concentration of the electrons above the 11.4 eV threshold because of an increase in both the total electron concentration and temperature as shown in Chapter 2.

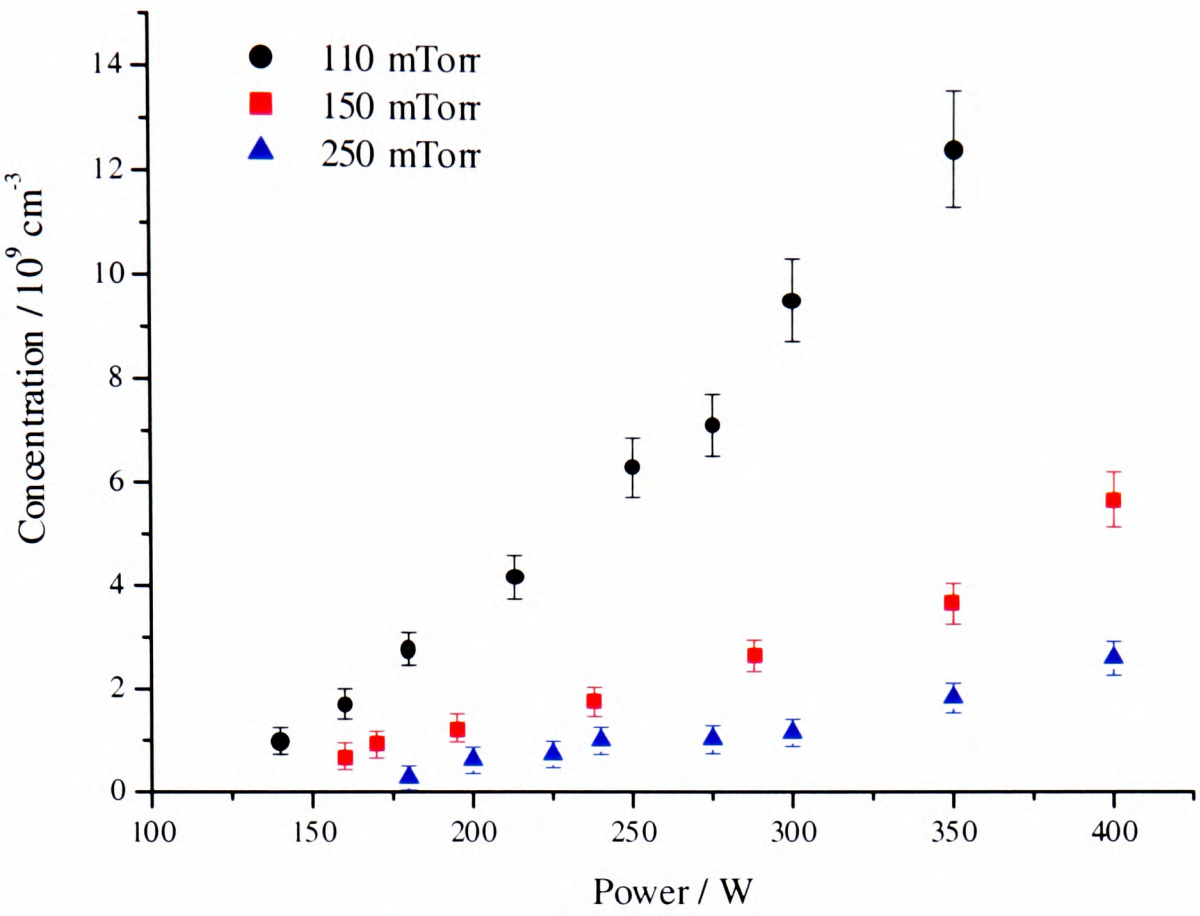

Figure 3.22 The absolute concentration of the $4s[^3/_2]_1$ level of argon atoms in a plasma produced in the CCP chamber from a 1:1 flow gas mixture of argon and nitrogen at three pressures for various applied powers.

The net applied power dependence of the argon atom $4s[^3/_2]_1$ level concentration in a plasma produced in the CCP from a flow of helium containing 10 % argon, at three different pressures is shown in Figure 3.23. This again follows the trend that the concentration increases with increasing net applied power; the dependence on pressure is discussed in Section 3.6.2.2.

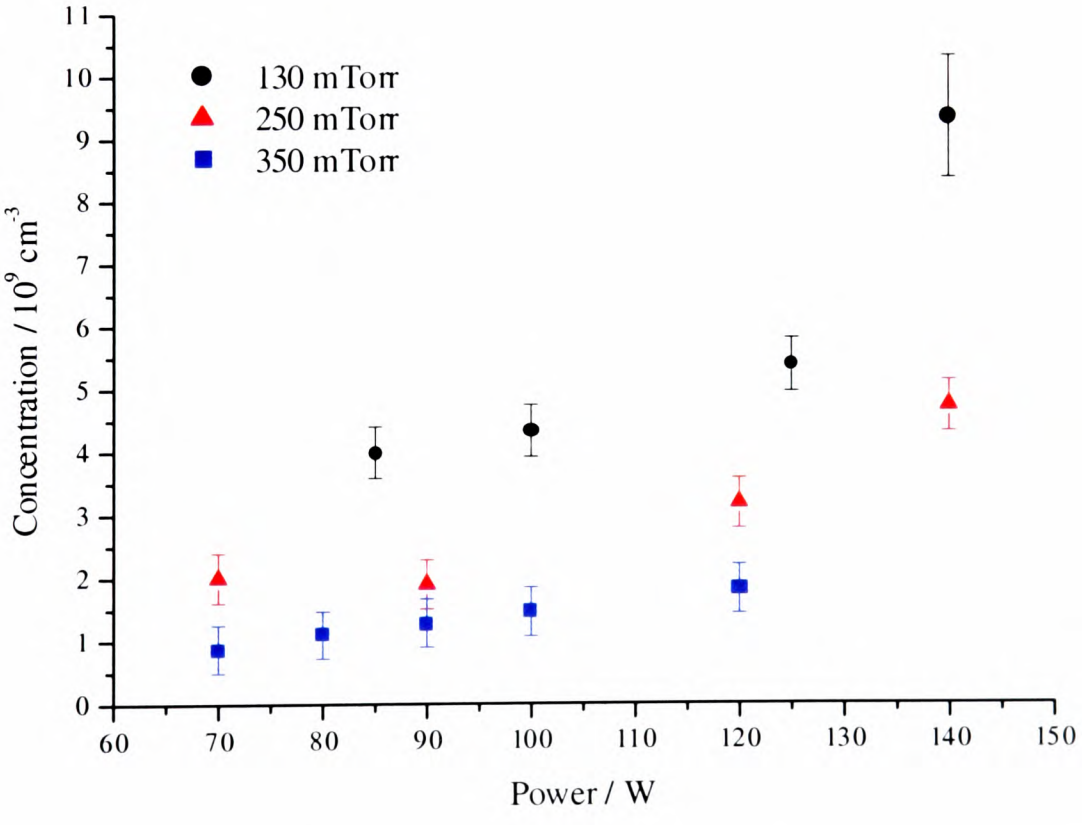

Figure 3.23 The absolute concentration of the $4s[^3/_2]_1$ level of argon atoms in a plasma produced in the CCP chamber from a 1:9 flow gas mixture of argon and helium at three pressures for various applied powers.

A similar set of experiments were completed in the ICP chamber. Figure 3.24 shows the applied net power dependence of the argon atom $4s[^3/_2]_1$ level concentration in a plasma, produced from a feed gas consisting of 60 % nitrogen and 40 % argon, at three different total pressures. As expected the concentration increases with applied power. Measurements above 100 W, or at pressures below 25 mTorr, gave distorted profiles, again caused by the significant amount of absorption occurring.

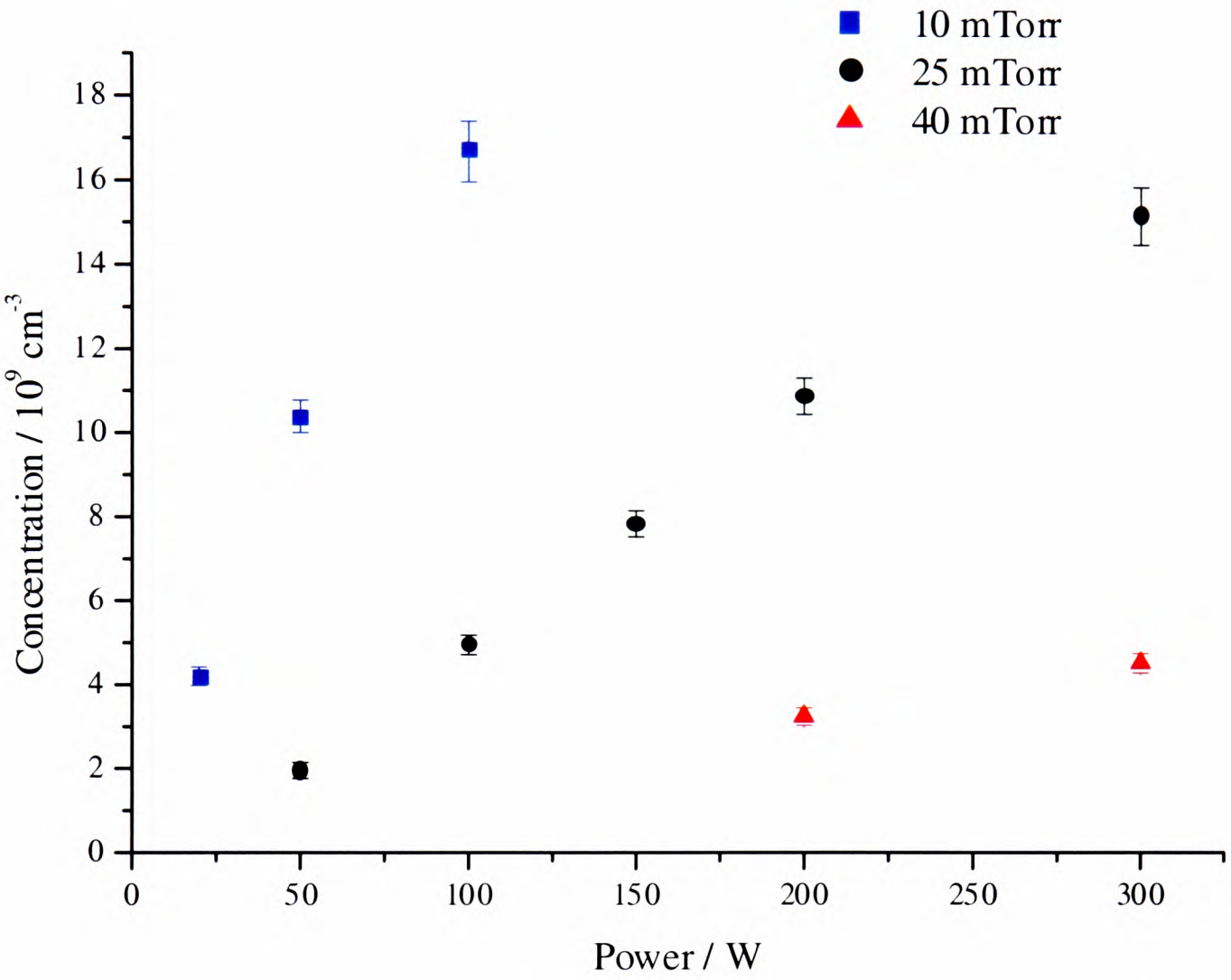

Figure 3.24 The absolute concentration of the $4s[^3/_2]_1$ level of argon atoms in a plasma produced in the ICP chamber from a 2:3 flow gas mixture of argon and nitrogen at three pressures for various applied powers.

3.6.2.2 Variation of Argon Atom Concentration with Discharge Pressure

The concentration of argon atoms in the $4s[^3/_2]_1$ level can also be observed to change with total pressure. Figure 3.22 in the previous section shows measurements made in the CCP chamber where the feed gas was a 1:1 argon and nitrogen mixture. This shows a very clear decrease in excited argon atom concentration with increasing pressure. Equation (3.31) implies that as the pressure increases the excited level concentration should also increase not only because [Ar] increases but also because τ_{app} increases; see equations (3.29) and (3.30). The decrease in the concentration of the argon atom $4s[^3/_2]_1$ level can be explained by a reduction of the electron

concentration and temperature as the pressure is increased, an effect observed in the measurements described in Chapter 2. The same trend is observed in a plasma produced from a feed gas consisting of 10 % argon in helium as shown in Figure 3.25, and from Figure 3.24 it can also be seen that the ICP system shows the same effect.

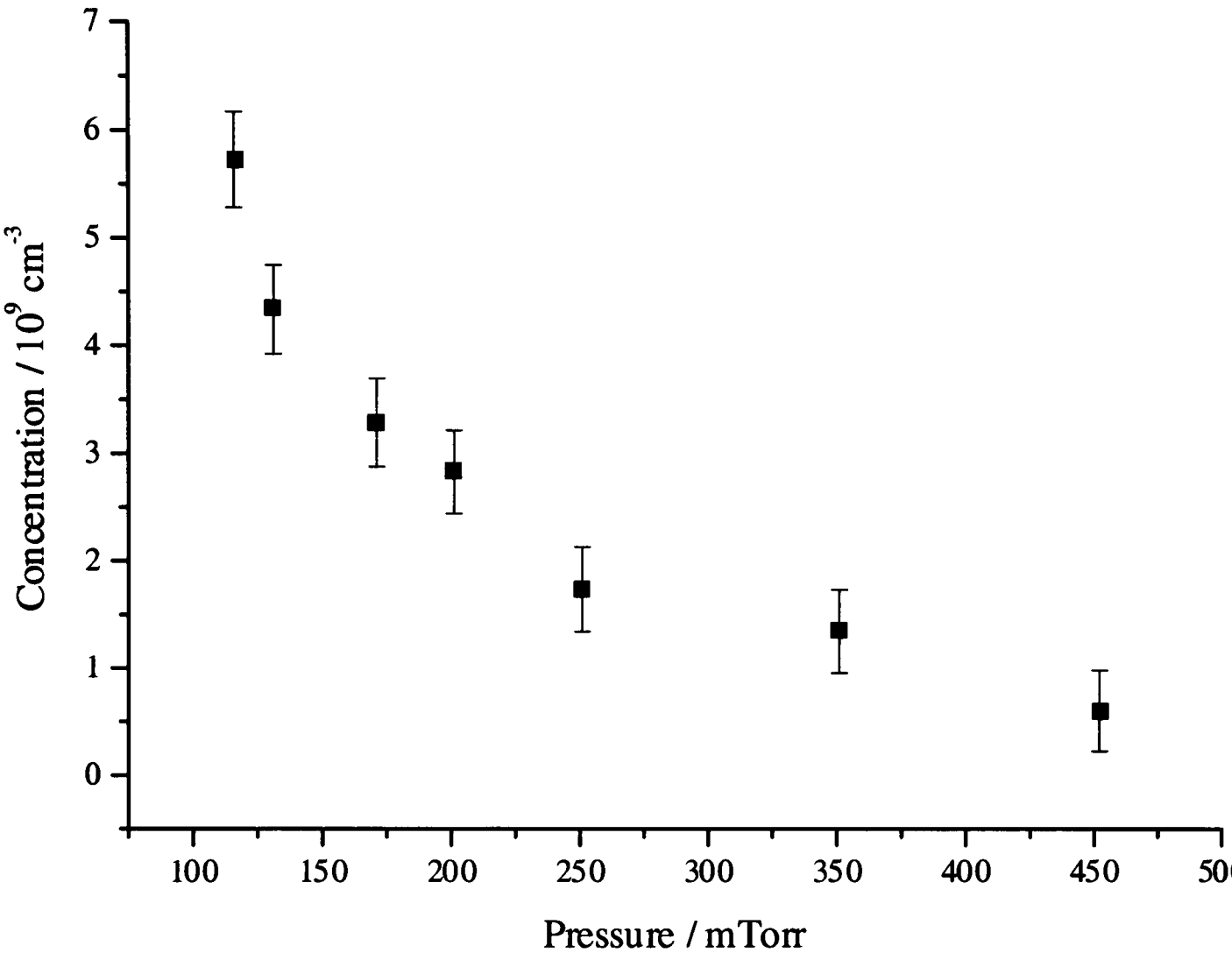

Figure 3.25 The absolute concentration of the $4s[^3/_2]_1$ level of argon atoms in a plasma produced at an applied power of 100 W in the CCP chamber from a 1:10 flow gas mixture of argon and helium at various pressures.

3.6.2.3 Variation of Argon Atom Concentration with Plasma Composition

Figure 3.26 shows the variation of the concentration of argon atoms in the $4s[^3/_2]_1$ level as the percentage of argon diluted in nitrogen is increased in the flow gas, at a total pressure of 115 mTorr and an applied power of 200 W in the CCP reactor. The excited level concentration can be seen to increase with argon concentration in the flow gas. Measurements at and above 40 % argon in the flow gas also showed distortion due to the large absorption occurring and above 60 % it was not possible to obtain a reasonable fit to the *I* and *Q* traces obtained. The slope of the line, below 40 % argon, suggests that under these conditions in the plasma about one argon atom in 2×10^6 is in the $4s[^3/_2]_1$ level.

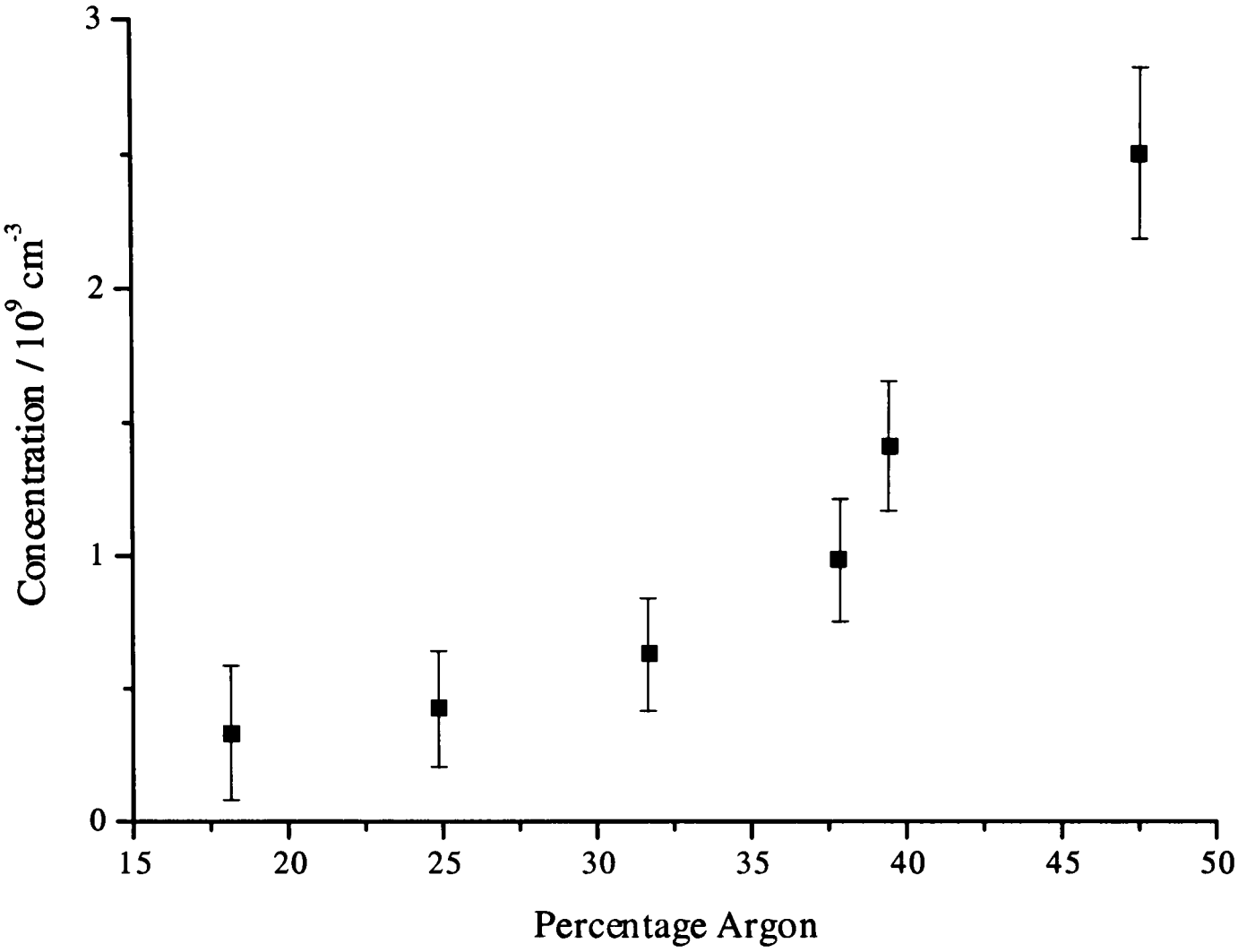

Figure 3.26 The absolute concentration of the $4s[^3/_2]_1$ level of argon atoms in a plasma produced at an applied power of 200 W in the CCP chamber at a pressure of 115 mTorr at various flow gas mixtures constituting argon and nitrogen.

The concentration of argon atoms in the $4s[^3/_2]_1$ level in the nitrogen plasma is much lower than in the helium plasma under the same conditions. An explanation for this is that the electron temperatures and concentrations are lower in the nitrogen plasma than the helium plasma (see Chapter 2), reducing the $[e^-]$ and k_e terms in equation (3.31), thus reducing the concentration of the argon $4s[^3/_2]_1$ level. The lower concentration of the argon atom $4s[^3/_2]_1$ level in the nitrogen plasma compared to the helium plasma could also be due to the larger probability of deactivation of the metastable $4s[^1/_2]_0$ and $4s[^3/_2]_2$ excited levels of argon atoms by the molecular nitrogen[5] compared to helium. This is due to the near continuum of molecular energy levels in nitrogen compared to the isolated levels present in the helium atoms. Although these metastable levels were not observed directly, collisions with other species will convert them in to the observed level, therefore if the metastable concentrations are lower the concentration of the $4s[^3/_2]_1$ level will also be lower.

3.6.3 Comparison of the Two Plasma Chambers

It can be observed from the figures in the previous sections that under similar conditions the argon atom concentration is larger in the ICP than the CCP. This can be observed in the extreme case where the flow gas used was 'pure' helium (Grade A BOC). In the CCP system no FMS absorption signal was observed, but an FMS absorption signal corresponding to a concentration of the $4s[^3/_2]_1$ level in argon atoms of approximately 1.5×10^9 atoms/cm^3, was observed in the ICP chamber for an applied net power of 200 W and a pressure of 90 mTorr. The detectivity of the experimental system used in this Chapter, calculated at the beginning of Section 3.6, suggests that the concentration of the $4s[^3/_2]_1$ level of argon atoms in the CCP chamber (under the same conditions) was less than 3×10^5 atoms/cm^3. This implies that under these conditions the ICP system is at least 5×10^3 times more efficient at producing the $4s[^3/_2]_1$ level argon atoms compared to the CCP system, a consequence of the higher electron temperatures and concentrations in the ICP system than the CCP.

3.7 Conclusion

In this Chapter, the possibility of using FMS to detect species in the electrically noisy environment of a plasma has been investigated. It has been shown to be very effective, giving an increased S/N ratio compared to single pass absorption and low frequency mechanical modulation techniques, by three orders of magnitude and at least an order of magnitude respectively. Argon is already used for kinetic studies and chemical diagnostics and therefore the use of FMS in this field may be exceptionally useful. The implementation of this technique in industry would be relatively inexpensive; the complete diagnostic system would cost less than £12 000 including a commercial diode laser system[45]. If a home built laser control system was used, the entire system would cost an order of magnitude less.

The analysis of the FM signal can be rapidly completed using readily available software, for example Microsoft Excel. The complete process, including acquisition, could easily be automated using Visual Basic, enabling the quick determination, on the timescale of an industrial plasma process, of species temperature and concentration.

This technique could be used to give information about the high energy electrons within the plasma. These are the species responsible for the production of the electronically excited argon atoms and therefore the concentration of these levels depends critically on the electron energetics and concentration. Therefore, by observing the variation in concentration of a

particular level as a function of power and pressure, information is obtained about the electron concentration and energy distribution.

A brief exploration of plasma parameter space, measuring excited argon atom concentrations, has been completed in both capacitively and inductively produced plasmas. As found in Chapter 2, the inductive discharge appears to be more energetic and therefore produces a larger excited state concentration under similar conditions. The argon atom $4s[^3/_2]_1$ level concentration was found to be between 2×10^8 and 1×10^{11} atom/cm^3 and to generally increase with increasing applied power and to decrease with increasing total pressure. The temperature of the atoms was also measured in both chambers, and was found to be approximately 323 ± 17 K.

3.8 References

[1]G. E. Hall and S. W. North, *Annual Review of Physical Chemistry*, **51**, 243, (2000)
[2]K. W. Oum and G. Hancock, *J. Phys. Chem. A*, **101**, 2634, (1997)
[3]N. Sadeghi, M. Cheaib and D. W. Setser, *J. Chem. Phys.*, **90**, 219, (1989)
[4]N. Sadeghi and D. W. Setser, *J. Chem. Phys.*, **79**, 2710, (1983)
[5]V. Puech, F. Collier and P. Cottin, *J. Chem. Phys.*, **67**, 2887, (1977)
[6]P. Baltayan, J. C. Pebay-Peyroula and N. Sadeghi, *Chem. Phys.Lett.*, **104**, 168, (1984)
[7]G. R. Scheller, R. A. Gottscho, D. B. Graves and T. Intrator, *J. Appl. Phys.*, **64**, 598, (1988)
[8]N. Sadeghi and D. W. Setser, *Chem. Phys.*, **95**, 305, (1985)
[9]J. M. de Regt, R. D. Tas and J. A. M. van der Mullen, *J. Phys D: Appl. Phys.*, **29**, 2404, (1996)
[10]H. Uchida, K. Tanabe, Y. Nojiri, H. Haraguchi and K. Fuwa, *Spectrochemica Acta*, **35b**, 881, (1980)
[11]C. Fourier, G. Lemperiere and J. M. Poitevin, *Phys. Lett.*, **74A**, 313, (1979)
[12]H. Shindo and S. Imazu, *J. Quant. Spectrosc. Radiat. Transfer*, **23**, 605, (1980)
[13]P. S. Moussounda, P. Randon and J. M. Mermet, *Spectrochim. Acta*, **40B**, 641, (1985)
[14]L. P. Hart, B. W. Smith and N. Omentto, *Spectrochemica Acta*, **41B**, 1367, (1986)
[15]D. S. Baer and R. K. Hanson, *J. Quant. Spectrosc. Radiat. Transfer*, **47**, 455, (1991)
[16]J. Jonkers, M. Bakker and J. A. M. van der Mullen, *J. Phys, D: Appl. Phys.*, **30**,1928, (1997)
[17]N. Beverini, G. Cicconi, G. L. Genovesi and E. Piano *Plasma Sources Sci. Technol.*, **6**, 185, (1997)
[18]N. Sadeghi, M. van de Grift, D. Vender, G. M. W. Kroesen and F. J. de Hogg, *Appl. Phys. Lett.*, **70**, 835, (1997)
[19]F-Y. Zhang, K. Komurasaki, T. Iida and T. Fujiwara, *Applied Optics*, **38**, 1814, (1999)
[20]E. Augustyniak, S. Fillimonov and J. Borysow, *J. Appl. Phys.*, **86**, 4767, (1999)
[21]C. E. Moore, *Atomic Energy Levels as Derived from the Analysis of Optical Spectra,* U. S. Dept. of Commerce Nat. Bureau Of Standards, (1971)
[22]W. L. Wiese, J. W. Brault, K. Danzmann, V. Helbig and M. Kock, *Phys Rev. A.*, **39**, 2461, (1989)
[23]M. J. G. Borge and J. Campos, *Physica*, **119C**, 359, (1983)
[24]W. Demtröder, *Laser Specroscopy*, Springer-Verlag, (1981)
[25]A. A. Radzig and B. M. Smirnov, *Reference Data on Atoms and Molecules*, Springer-Verlag, (1985)
[26]P. W. Atkins, *Physical Chemistry*, OUP, (1978)
[27]G. C. Bjorklund, *Optics Lett.*, **5**, 15, (1980)
[28]J. A. Silver, *Applied Optics*, **31**, 707, (1992)
[29]T. C. Steimle, M. L. Costen, G. E. Hall and T. J. Sears, *Chem. Phys. Lett.*, **319**, 363, (2000)
[30]J. T. Bahns, C. C. Tsai, B. Ji, J. T. Kim, G. Zhao, W. C. Stwalley, J. C. Bloch and R. W. Field, *J. Mol. Spec.*, **186**, 222, (1997)
[31]R. L. Kronig, *J. Opt. Soc. Am.*, **12**, 547, (1926)
[32]S. W. North, X. S. Zheng, D. Fei, G. E. Hall, *J. Chem. Phys.*, **104**, 2129, (1996)
[33]W. Lenth, *Optics Lett.*, **8**, 575, (1983)
[34]W. Lenth, *IEEE J. Quant. Elect.*, **QE-20**, 1045, (1984)
[35]D. E. Cooper and J. P. Watjen, *Opt. Lett.*, **11**, 606, (1986)
[36]A. Yariv, *Quantum Electronics in Modern Communications*, OUP, (1997)
[37]PerkinElmer Instruments, Inc.

[38]P. Horowitz and W. Hill, *The Art of Electronics*, CUP, (1980)
[39]M. W. Blades and G. M. Hieftje, *Spectrochimica Acta*, **37B**, 191, (1982)
[40]B. K. Woodcock, *DPhil. Thesis*, Oxford University, (1995)
[41]S. R. Hunter, J. G. Carter and L. G. Christophorou, *J. Chem. Phys.* **90**, 4879, (1989)
[42]C. M. Ferreira and J. Loureiro, *J. Phys. D: Appl. Phys.*, **16**, 1611, (1983)
[43]W. L. Wiese, M. W. Smith and B. M. Miles, *Atomic Transition Probabilities Volume II* NSRDA, (1969)
[44]F. A. Haas and N. St. J. Braithwaite, *Plasma Sources Sci. Tecnol.*, **9**, 77, (2000)
[45]Sacher Lasertechnik

Chapter 4

Detection of the Hydroxyl Radical

4.1 Introduction

In this Chapter, four methods are described for the detection (and measurement) of the hydroxyl radical (OH). Firstly, a mechanically modulated spectroscopic method (MMS) is discussed using a frequency doubled cooled commercial diode laser. The other techniques explored are cavity ring down spectroscopy (CRDS), laser induced fluorescence (LIF) and cavity laser induced fluorescence (CLIF), all using a pulsed dye laser.

The OH radical is a highly reactive species that plays an important role in both atmospheric[1] and combustion[2] chemistry. In the troposphere (up to an altitude of approximately 10 km) it is an oxidant responsible for daytime conversion of many atmospheric trace gas pollutants (*e.g.* alkanes) to CO_2 and H_2O or less oxidised species, which are water-soluble and can be rained out. The reaction scheme for the oxidation of ethane in this region is given below as an example.

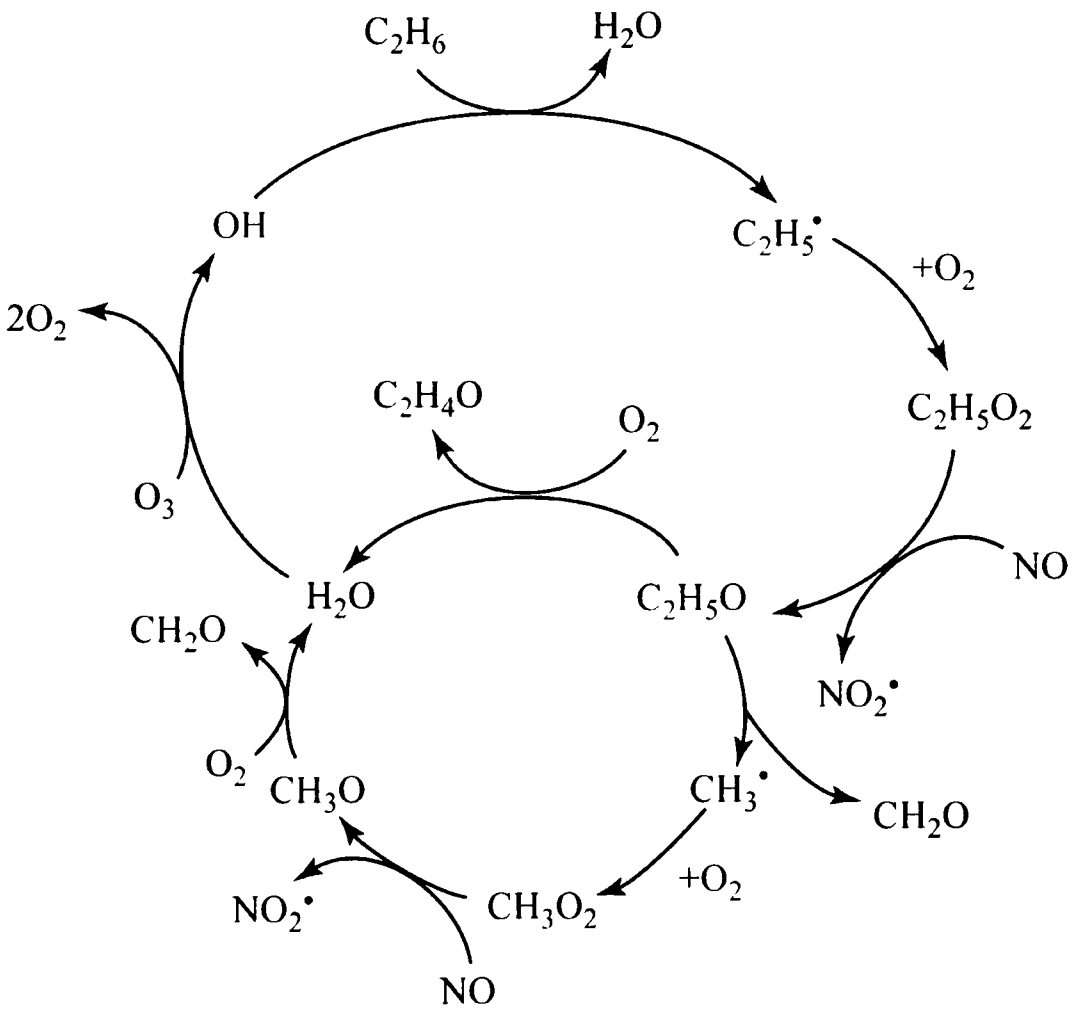

The aldehydes and ketones produced in this scheme can be photolysed or oxidised further. A general cycle for the chemistry of the troposphere is shown in Figure 4.1. From this, it is evident that the concentration of the OH radical is crucial in understanding the chemistry of this part of the atmosphere.

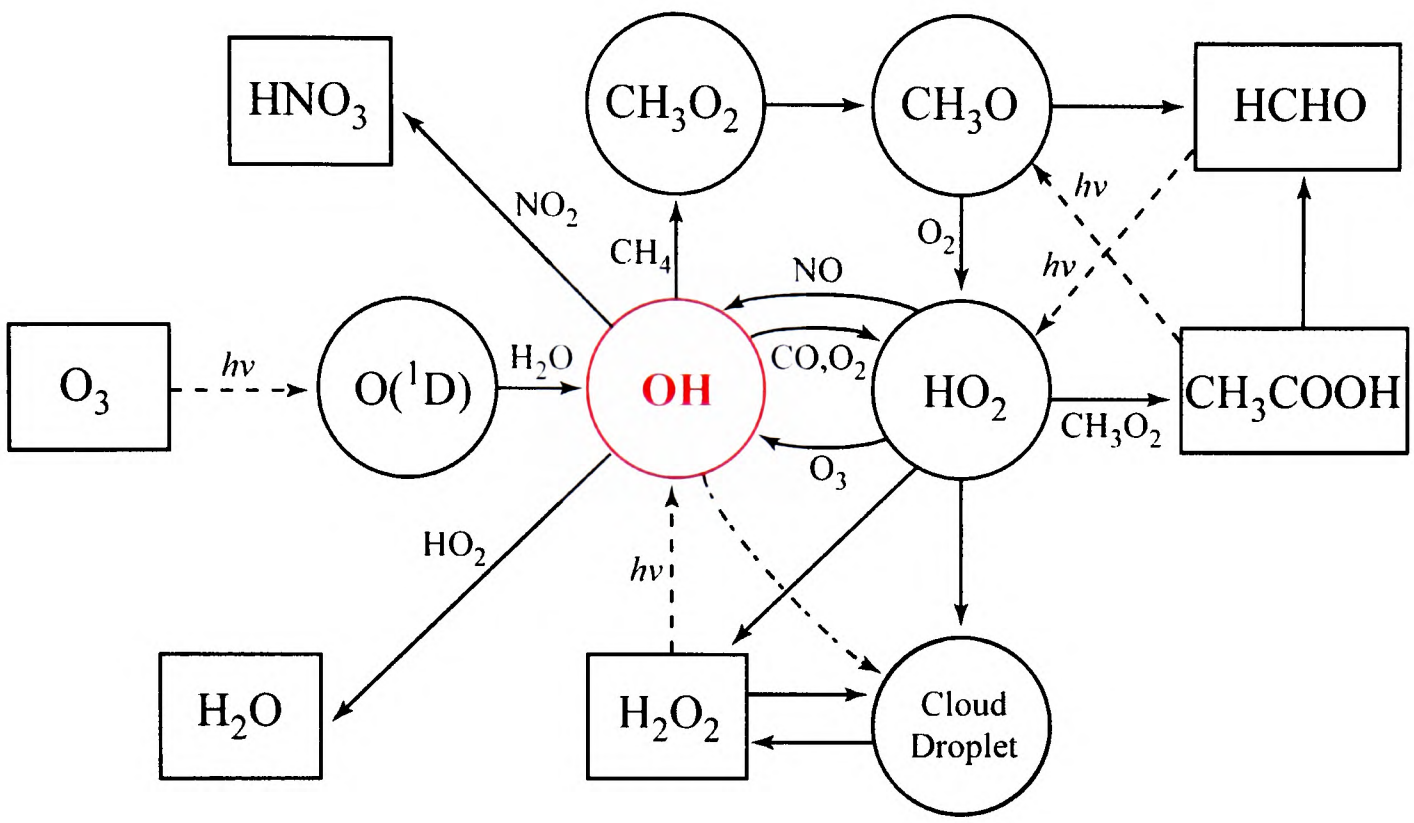

Figure 4.1 General tropospheric chemical cycle (from Wayne[1]).

In the stratosphere, the atmospheric region above the troposphere (up to approximately 50 km), the hydroxyl radical is involved in cycles that destroy ozone:

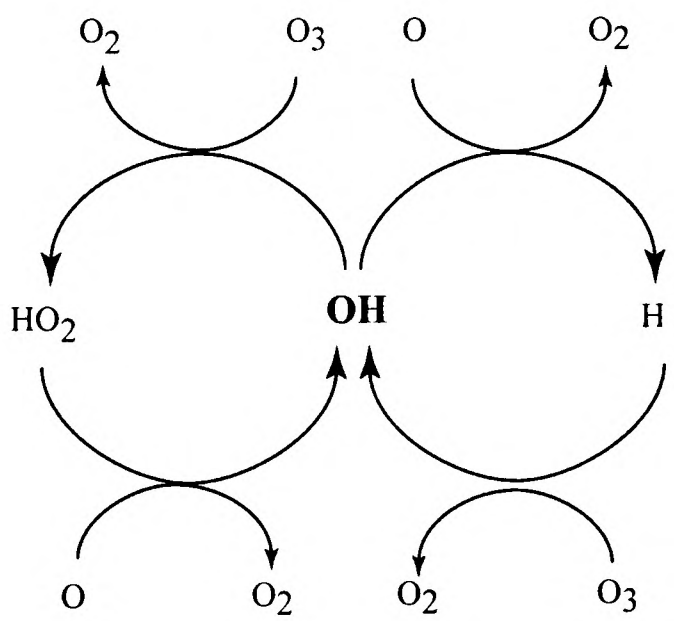

These catalytic cycles, amongst others, are responsible for the discrepancy between the measured ozone concentration and that predicted by the first atmospheric model, proposed by Chapman[3].

The importance of the OH radical in combustion can be demonstrated using the case of the explosive reaction of hydrogen and oxygen in the scheme below.

The initiation step in this reaction is $H_2 + O_2 \rightarrow HO_2^{\cdot} + H^{\cdot}$

and this is then followed by the sequence shown below, which often leads to an explosion (where M is a third body).

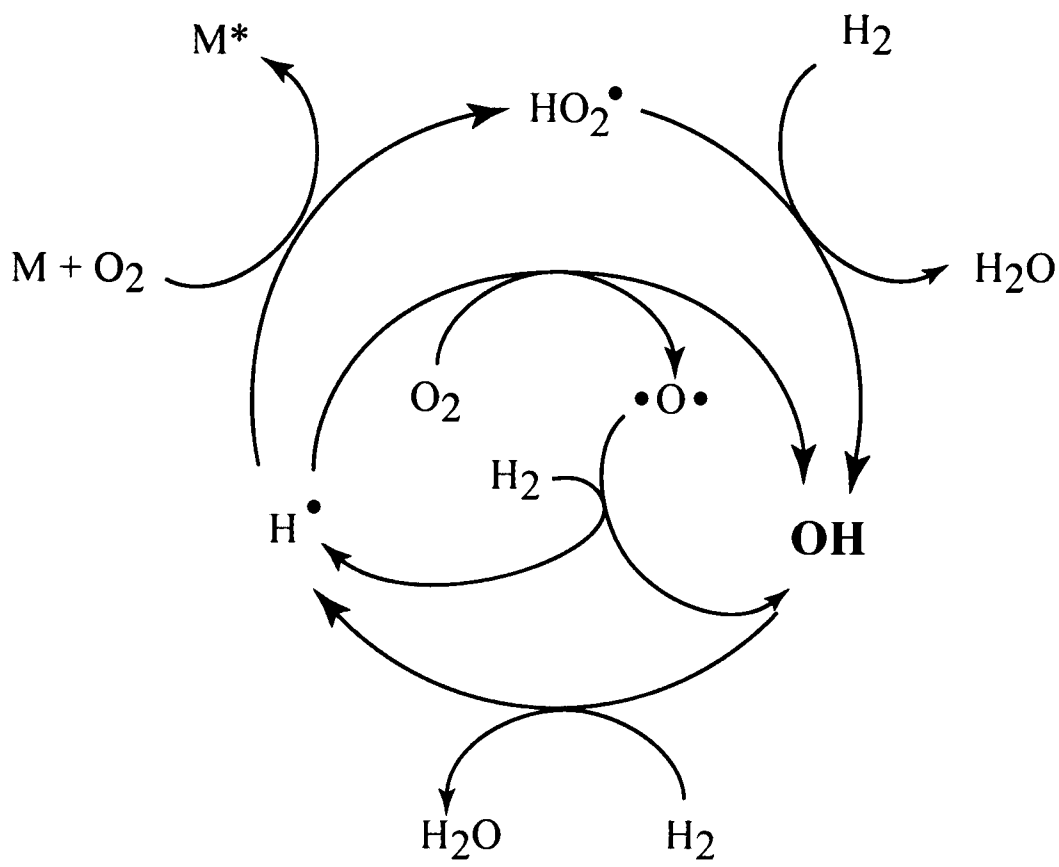

For other combustion reactions, the scheme is considerably more complex but the OH radical still plays a central role[2].

The hydroxyl radical is also one of the most commonly observed products of quantum state resolved experiments designed to measure detailed reaction dynamics[4]. This is not only because the reactions that produce the OH radical are of crucial importance in the chemical examples given above but also because it is possible to observe the species by LIF. The importance of OH in both fundamental and applied gas-phase studies is apparent and therefore new methods for its detection are of great value.

4.2 Spectroscopy of the OH Radical

In all molecules, just as in many electron atoms, the Schrödinger equation cannot be solved exactly because of the many electrostatic interactions of the electrons and nuclei, and therefore the wavefunctions and corresponding energy levels cannot be obtained exactly. Hence, approximations are required to understand the spectra of molecules. Firstly, the Born-

Oppenheimer approximation can be applied. This approximation allows the electronic energy to be obtained at fixed internuclear distances by separating the nuclear and electronic motion and simplifies the generation of a potential surface. A second approximation, that the molecular electronic orbitals can be formed from a linear combination of atomic orbitals (LCAO), further simplifies the problem. From this approximation, the electronic configuration of the ground electronic state of the hydroxyl radical is $(1s\sigma)^2(2s\sigma)^2(2p\sigma)^2(2p\pi)^3$. In this Chapter, transitions between the ground state and the first excited state of the same multiplicity are considered. This excited state configuration is $(1s\sigma)^2(2s\sigma)^2(2p\sigma)^1(2p\pi)^4$, arising from the promotion of an electron from the $2p\sigma$ orbital to one of the $2p\pi$ orbitals.

To describe the OH molecular system, several angular momentum vectors and corresponding quantum numbers are required. For all diatomic molecules, the most widely used coupling approximation is analogous to the Russell-Saunders coupling scheme for atoms[5]. The vectors and quantum numbers produced by this scheme that are required to describe the states probed in this Chapter are given in Appendix 2.

The ground state, X, of the OH radical at low N is best described by Hund's case (a). The values of the electronic quantum numbers describing this state are: $\Lambda = 1$, $S = {}^1/_2$, $\Omega = {}^3/_2$ or ${}^1/_2$. The two spin orbit manifolds, F_1 where $\Omega = {}^3/_2$ and F_2 where $\Omega = {}^1/_2$, are denoted by $^2\Pi_{3/2}$ and $^2\Pi_{1/2}$ respectively. This state is an inverted multiplet, that is the $^2\Pi_{3/2}$ manifold is lower in energy than the $^2\Pi_{1/2}$ manifold, with $A_0 \approx -139$ cm^{-1} [6]. These manifolds both exhibit Λ-doubling (see Appendix 2).

The first excited state of the same multiplicity as the ground state of the OH radical, A, is best described by Hund's case (b), because $\Lambda = 0$. The values of the electronic quantum numbers describing this state are: $\Lambda = 0$, $S = {}^1/_2$. The term symbol for this state is $^2\Sigma^+$. This excited state exhibits ρ-doubling (see Appendix 2).

A further quantum number is required to identify the vibrational levels of the electronic states. v is this vibrational quantum number of the radical, giving the vibrational energy level; for a simple harmonic oscillator, $E_{vibSHO} = h\nu(v + {}^1/_2)$. v can take the values of 0, 1, 2, ...

The single photon selection rules for the A $^2\Sigma^+$ ($v = 0$) ← X $^2\Pi$ ($v = 0$) system of the OH radical are $\Delta J = 0, \pm 1$ and $\Delta N = 0, \pm 1, \pm 2$. These selection rules allow twelve possible rotational branches, six from each of the lower state spin-orbit manifolds. These branches are labelled $\Delta J_{F'F''}$ where ΔJ is given the label P when $\Delta J = -1$, Q when $\Delta J = 0$ and R when $\Delta J = +1$. The first subscript is used to identify whether the upper state energy level is the F_1 or F_2

level and the second subscript indicates to which of the two spin orbit manifolds the lower level of the transition belongs.

Figure 4.2 is a schematic of the energy levels of the A $^2\Sigma^+$ ($v = 0$) ← X $^2\Pi$ ($v = 0$) system of the OH radical. As an example, a single transition from each of the twelve rotational branches is labelled.

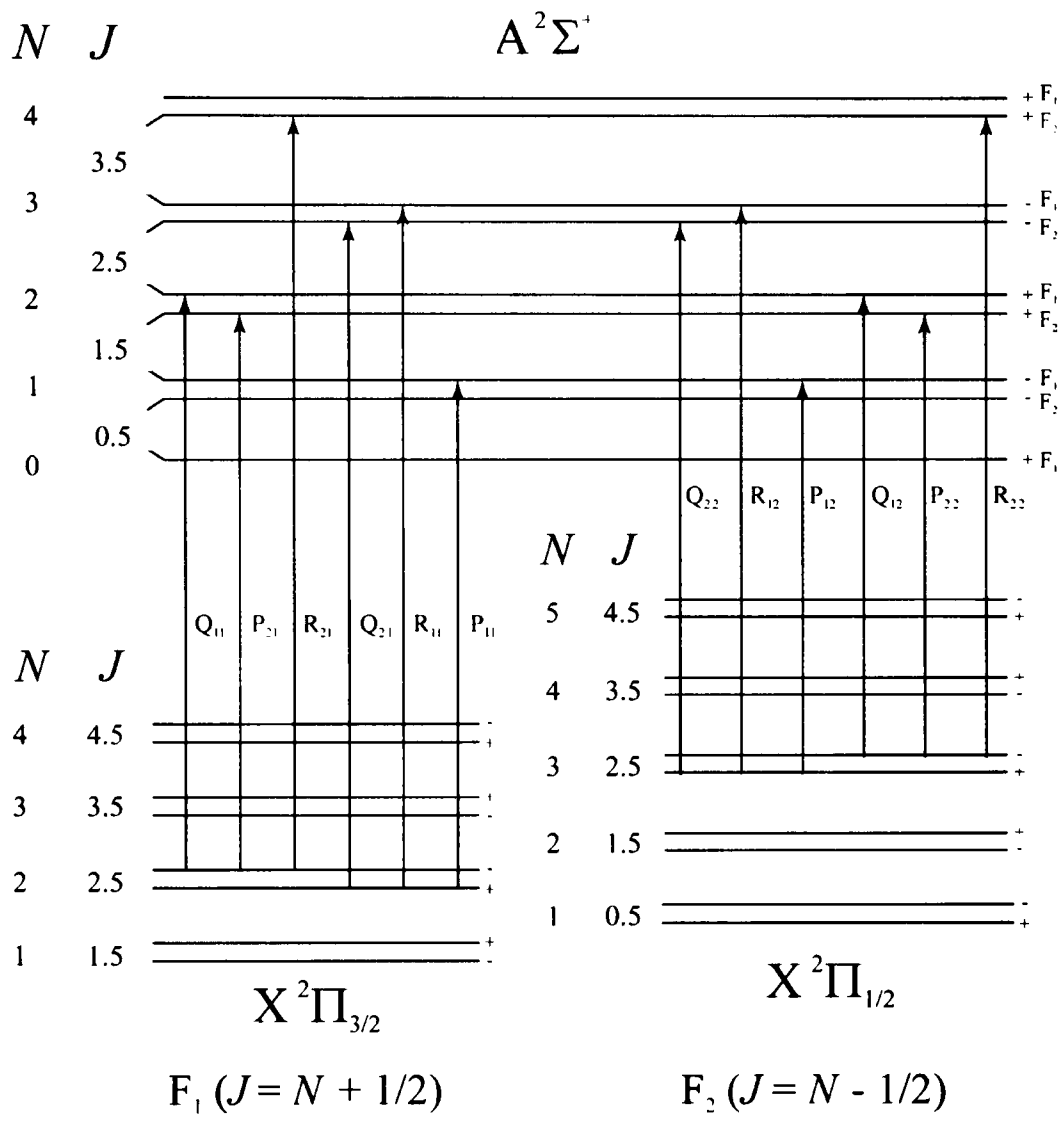

Figure 4.2 An energy level diagram of the A $^2\Sigma^+$ ($v = 0$) ← X $^2\Pi$ ($v = 0$) system of OH.

4.2.1 Detecting the OH Radical

The positions[7] and absorption cross sections[8] of the transitions within the A $^2\Sigma^+$ ($v = 0$) ← X $^2\Pi$ ($v = 0$) system in the OH radical are well documented and occur at approximately 308 nm. This is generally considered to be the most convenient band to use to detect the OH radical.

The experiments described in this Chapter use absorption on the transitions within the A $^2\Sigma^+$ ($v = 0$) ← X $^2\Pi$ ($v = 0$) system given in the table below. The table also gives the line positions, Einstein coefficients for spontaneous emission[8] (A_{ji}) and the cross sections[8] (σ_{tot}) for the transitions observed. The cross sections given are the effective cross sections for all OH

radicals; that is, the absorbance of the system at the wavelength given can be obtained from the product of this effective cross section, the path length and the total hydroxyl radical concentration, not the concentration of the radical in the specific rotational level from which the transition originates.

Transition	$\lambda_{0,air}$ / nm	A_{ji} / 10^5 s^{-1}	σ_{tot} / 10^{-16} cm^2
$Q_{11}(3)$	308.1541	5.700	7.179
$P_{21}(3)$	308.1625	1.618	1.528
$P_{11}(1)$	308.1665	8.611	5.423

4.3 Production of the OH Radical

For the experiments discussed in this Chapter, the standard microwave discharge system mentioned in Chapter 2 was used to generate the OH radical. This was achieved either directly by using a discharge where the feed gas was a wet noble gas, or indirectly *via* a chemical reaction involving a reactant produced in the discharge.

In the case of the direct production, the noble gas (either helium (Grade A BOC) or argon (Pureshield BOC)) was flowed through a fast flow glass sinter situated under approximately 10 cm of water in a glass bubbler. A proportion of the resulting gas mix was passed into the glass discharge tube through a needle valve, with the remainder vented into the atmosphere. The flow through the vent was monitored using a bubble flow meter to ensure that the pressure in the bubbler was slightly above atmospheric pressure. This maintained the pressure of water vapour carried in the noble gas to approximately that of water vapour at 1 atmosphere and 298 K, namely 18 Torr, corresponding to about 2.4 % of the gas mixture. A second inlet into the discharge was used for a flow of dry noble gas buffer to enable reduction of the water number density from this maximum value.

The indirect method utilised the bimolecular reaction

$$H + NO_2 \rightarrow OH + NO$$

which has an almost gas kinetic rate constant (1.4×10^{-10} $cm^3 molecules^{-1} s^{-1}$)[9]. The hydrogen atoms were produced in the microwave discharge from a feed gas of hydrogen (High Purity BOC) and argon (Pureshield BOC). These atoms then reacted with nitrogen dioxide (Grade

2.5 BOC) that was passed directly into the reaction vessel. The rate of flow of argon, hydrogen and nitrogen dioxide were controlled using needle valves.

For both production methods, a fast flow rate was required to ensure that both the OH radicals and the H atoms produced were not destroyed by recombination or reaction with other species or the vessel walls before entering the laser probe region. The fast flow rate was achieved by pumping the systems using a rotary pump and Roots blower combination (E2M40 and EH250) through 70 mm diameter bellows tubing. This pumping system should theoretically be able to reduce the residence time to as low as 20 ms at the pressures used (between 2 to 14 Torr measured using a capacitance manometer (Tylan General CDL-11)).

4.4 Production of 308 nm radiation

The production of radiation at around 308 nm for detection of the OH radical from a diode laser is a challenge, because diode lasers that operate in the ultra violet region are not currently available. In this section, the method of obtaining ultra violet radiation from a diode laser by Second Harmonic Generation (SHG) is discussed.

4.4.1 Second Harmonic Generation

SHG is an example of nonlinear optical phenomena, which are effects that do not depend linearly on the optical field strength. These effects depend on the properties of the material through which the radiation is passing, and normally only laser radiation is sufficiently intense for such effects to be observed. The demonstration of SHG[10] occurred the year following the demonstration of the first working laser.

To define optical non-linearity[11] it is necessary to consider the polarisation $\boldsymbol{P}(t)$, defined as the dipole moment per unit volume, of the material. This depends upon the optical field strength $\boldsymbol{E}(t)$ present in the material. For conventional linear optics, the induced polarisation depends linearly on the electric field strength

$$\boldsymbol{P}(t) = \varepsilon_0 \chi^{(1)} \boldsymbol{E}(t) \tag{4.1}$$

where the constant of proportionality, $\chi^{(1)}$, is the linear susceptibility. In a material which has a nonlinear optical response the polarisation can be expressed as a power series

$$\begin{aligned} \boldsymbol{P}(t) &= \varepsilon_0\left(\chi^{(1)}\boldsymbol{E}(t)+\chi^{(2)}\boldsymbol{E}^2(t)+\chi^{(3)}\boldsymbol{E}^3(t)+\ldots\right) \\ &\equiv \boldsymbol{P}^{(1)}(t)+\boldsymbol{P}^{(2)}(t)+\boldsymbol{P}^{(3)}(t)+\ldots \end{aligned} \tag{4.2}$$

where $\chi^{(2)}$ and $\chi^{(3)}$ are the second and third order nonlinear optical susceptibilities, respectively. The second order non-linear polarization term $\boldsymbol{P}^{(2)}(t) = \chi^{(2)}\boldsymbol{E}^2(t)$ is the term that gives rise to SHG. This term vanishes for cubic crystals but is non-zero in all anisotropic media. For an optical field described by $\boldsymbol{E} = \boldsymbol{E}_0\cos(\omega t)$, $\chi^{(2)}\boldsymbol{E}^2(t)$ describes a polarisation wave oscillating at a frequency 2ω. The solution of the coupled equations describing harmonic generation[12] in the case of an undepleted input beam results in an electric field produced at the second harmonic frequency given by

$$\boldsymbol{E}(2\omega) = \frac{\omega d_{eff}}{n_\omega c}\boldsymbol{E}^2(\omega)l\left(\frac{\sin\left(\frac{\omega(n_\omega - n_{2\omega})}{c}\right)}{\left(\frac{\omega(n_\omega - n_{2\omega})}{c}\right)}\right) \tag{4.3}$$

where l is the length of the anisotropic material with refractive indices n_ω at ω and $n_{2\omega}$ at 2ω through which the optical field $\boldsymbol{E}(\omega)$ is propagating. d_{eff} is the effective nonlinear coefficient that is dependent on the nonlinear optical properties and the orientation of the material, as are the refractive indices n_ω and $n_{2\omega}$.

The second harmonic intensity depends on the square modulus of the optical field[13] and so the maximum intensity of radiation at a frequency of 2ω results when the refractive index at the fundamental and second harmonic are the same, *i.e.* $n_\omega = n_{2\omega}$. This is called the *phase matching* condition. For the frequencies discussed in this Chapter and the crystals used, $LiIO_3$ and potassium dideuterium phosphate (KD^*P), there is only one angle for a particular frequency that the crystal is phase matched. These crystals only have one direction about which the atoms are arranged symmetrically, called the optic axis, and the materials are therefore described as uniaxial.

The square modulus of equation (4.3) implies that the maximum efficiency of SHG will occur when the fundamental beam is focused into as small an area as possible. However, this result is for plane waves, and in practice the optimum fundamental beam size in the nonlinear medium is calculated assuming that the laser is described by a Gaussian function. The theory of SHG in uniaxial crystals has been developed by Boyd and Kleinman[14], and can be used to yield the optimum beam waist within the crystal. For the maximum efficiency of SHG at 616 nm, in $LiIO_3$, it is found that the fundamental beam waist should be approximately 16 μm

(using the Sellmeier coefficients given by Dmitriev *et al.*[15]). The $LiIO_3$ crystal that was purchased for producing 308 nm radiation from a diode laser had Brewster cut faces to minimise reflection loss at the fundamental frequency. This introduces a complication in the production of the correct beam size within the crystal because of the resultant astigmatism in the beam (*i.e.* the foci in the horizontal and vertical directions are at different points along the crystal axis). Astigmatism can be compensated for by producing the focus inside the crystal by means of an off axis spherical mirror.

4.4.2 Experimental Procedure

The 616 nm output from a diode laser (described in Section 4.5) was first passed through a Thorlabs C220TM-B corrective lens followed by a 20 cm focal length quartz lens. The focus of the beam was about 10 cm prior to a reflection off an off-axis spherically concave mirror with 5 cm radius of curvature. This mirror directed the beam into the 8 mm long Brewster cut $LiIO_3$ crystal, mounted on a 3-axis rotation and translation stage. $LiIO_3$ is hydroscopic and therefore the crystal was kept at 40 °C ± 0.1 °C by resistive heating controlled by a home-built active temperature controller. The radiation exiting the crystal was collected using a 10 cm quartz lens, passed through several UG11 Schott colour glass filters and focused onto the photocathode of a photomultiplier tube (Electron Tubes Ltd 9125 QB). The output of this was maximised with respect to the crystal orientation, position and the separation of the 20 cm lens and the off-axis mirror. This SHG output was then used for the experiments described in Section 4.6.

4.5 Cooling a Commercial Diode Laser

Producing 308 nm radiation from a diode laser is a challenge, not just because frequency doubling is required, but because the shortest wavelength available from commercial diode lasers is above 630 nm, with the exception of GaN lasers that produce light at approximately 400 nm[16]. To get a commercial laser diode to produce radiation at 616 nm, it has been necessary to operate it well outside the manufacturer's recommended conditions. As mentioned in Section 1.8.6, it is possible to reduce the wavelength emitted by a diode laser by decreasing the temperature at the junction. This section describes the experimental progress in producing a reliable and convenient source of 616 nm radiation from a commercial diode laser.

4.5.1 The Initial Experiment

A dewar designed for maintaining a mercury cadmium telluride (MCT) infrared radiation detector, cooled by liquid nitrogen, was modified to mount a diode laser. This dewar was ideal for the purpose because it was manufactured with a coaxial electrical feed-through connection and an optical window in front of the brass cold block. Four further electrical feed throughs were added to the lid of the dewar. The laser diode was mounted in a brass block that also contained a Pt100 platinum resistance thermometer (R.S.). A length of coaxial resistive heating wire, with a resistance of approximately 5 Ω, was wound around the outside of the brass block to enable the temperature of the diode to be varied. The temperature of the laser was controlled by varying the power dissipated in the heating wire by means of a high power version of the controller discussed in Section 3.5.1. This stabilised the temperature with a precision of ± 1 mK over the temperature range 77 K to 290 K.

A 635 nm 5 mW diode laser (Hitachi HL 6314 MG) was slowly cooled to about 150 K, with the laser power maintained at 1 mW and its wavelength monitored using a Burleigh WA1000 wavemeter. Figure 4.3 shows the decrease of wavelength with decreasing temperature and the mode hops discussed in Section 1.8.6 are clearly apparent. The target wavelength of 616 nm was achieved at a temperature of 165 K, almost 100 K below the manufacture's lowest recommended operating temperature of 263 K.

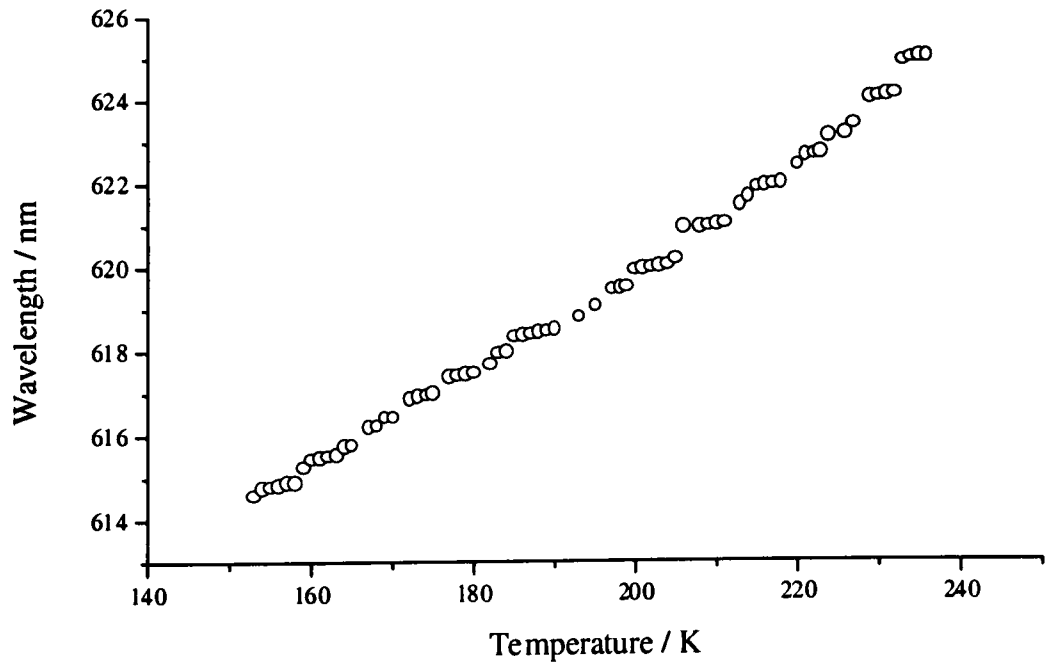

Figure 4.3 Wavelength dependence with temperature for a 635 nm Hitachi HL 6314 MG 5 mW diode laser maintained at 1 mW.

A moving coil ammeter and voltmeter, connected in series and parallel respectively with the laser diode after the protection circuit, enabled the electrical power dissipated in the diode to be calculated. From these measurements and measurements of the optical power, P_{opt}, at several

different injection currents the slope efficiency (dP_{opt}/dP_{elec}) of the laser was calculated to be 0.24, higher than the typical value of 0.18 within the manufacturer's recommended operating conditions. This is expected because at lower temperatures the free electrons in the conduction band are confined to lower energy levels, and similarly the holes in the valence band are confined to higher energies. This leads to an increased density of charge carriers and hence increased gain. This increase in gain at a particular current increases the efficiency of optical emission. A second way to observe this effect is to monitor the change in threshold current of the laser. As the gain at a particular current increases with decreasing temperature, the threshold will decrease and this is shown in Figure 4.4.

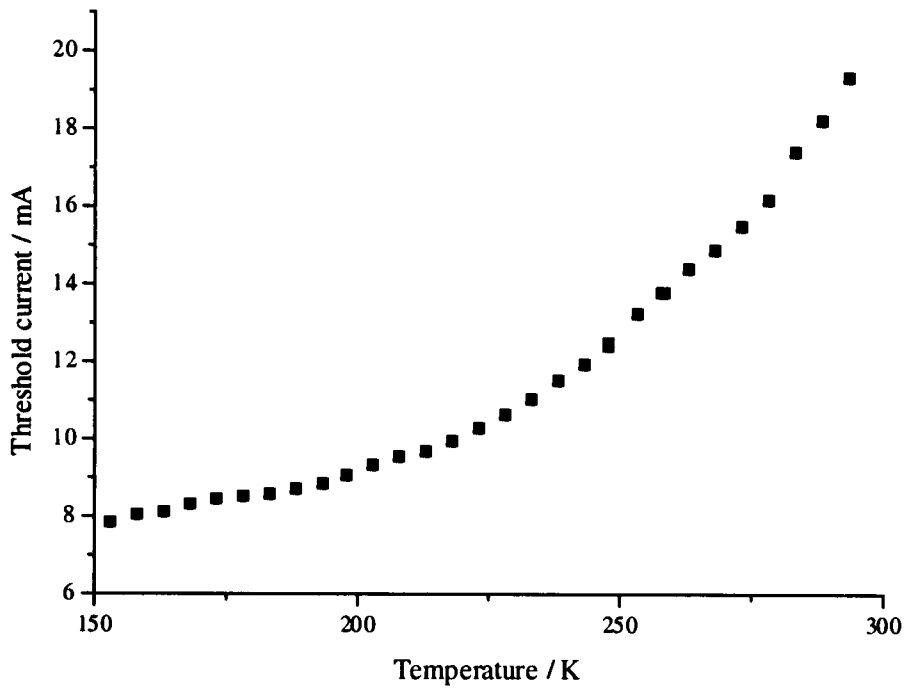

Figure 4.4 Threshold current dependence with temperature, for a 635 nm Hitachi HL 6314 MG 5 mW diode laser.

The maximum power that could be obtained from the laser diode was also measured. This involved increasing the injection current in small increments and monitoring the power over several minutes to ascertain whether any immediate damage to the laser was occurring (which would result in a decrease in the slope efficiency of the laser). Damage was found to occur above an output power of 2.5 mW, a factor of two below the maximum power within the manufacturer's recommended operating conditions. Following initial tests with this dewar, a modified system was constructed with greater liquid nitrogen capacity (the initial dewar only contained sufficient liquid nitrogen for experiments lasting less than 30 minutes) and space within the evacuated vessel to allow a corrective lens to be placed directly in front of the laser. To reduce the liquid nitrogen boil-off a Delrin spacer was placed between the liquid nitrogen vessel and the brass block containing the laser.

4.5.2 Diode Laser Lifetime

Initial experiments showed that the laser lifetime of HL 6314 MG lasers under the conditions within the dewar were limited to several hours and only one cooling cycle (cooled once to 165 K and then allowed to slowly warm to 298 K). The lifetime increased by a significant amount, in some cases by up to as much as ten cooling cycles and several days, if the front of the hermetically sealed can was removed. This suggests that some of the damage to the laser semiconductor was caused by condensation of material contained in the hermetically sealed can onto the laser surface. However, the laser diodes still had a very limited life span, many orders of magnitude shorter than the typical lifetime quoted by the manufacturer ($\approx 10^5$ hrs at 30 °C)[17] for operation within the recommended conditions. The manufacturer actually specifies that the cooler the laser, the longer the expected lifetime. Extrapolating their figures, using a logarithmic relationship[17], implies that at 165 K the median lifetime should be in excess of 10^9 hours.

To test if the cooled diode lasers had a reduced life span an experiment was designed to monitor a laser maintained at 165 K for a significant length of time. A schematic of this experiment is given in Figure 4.5.

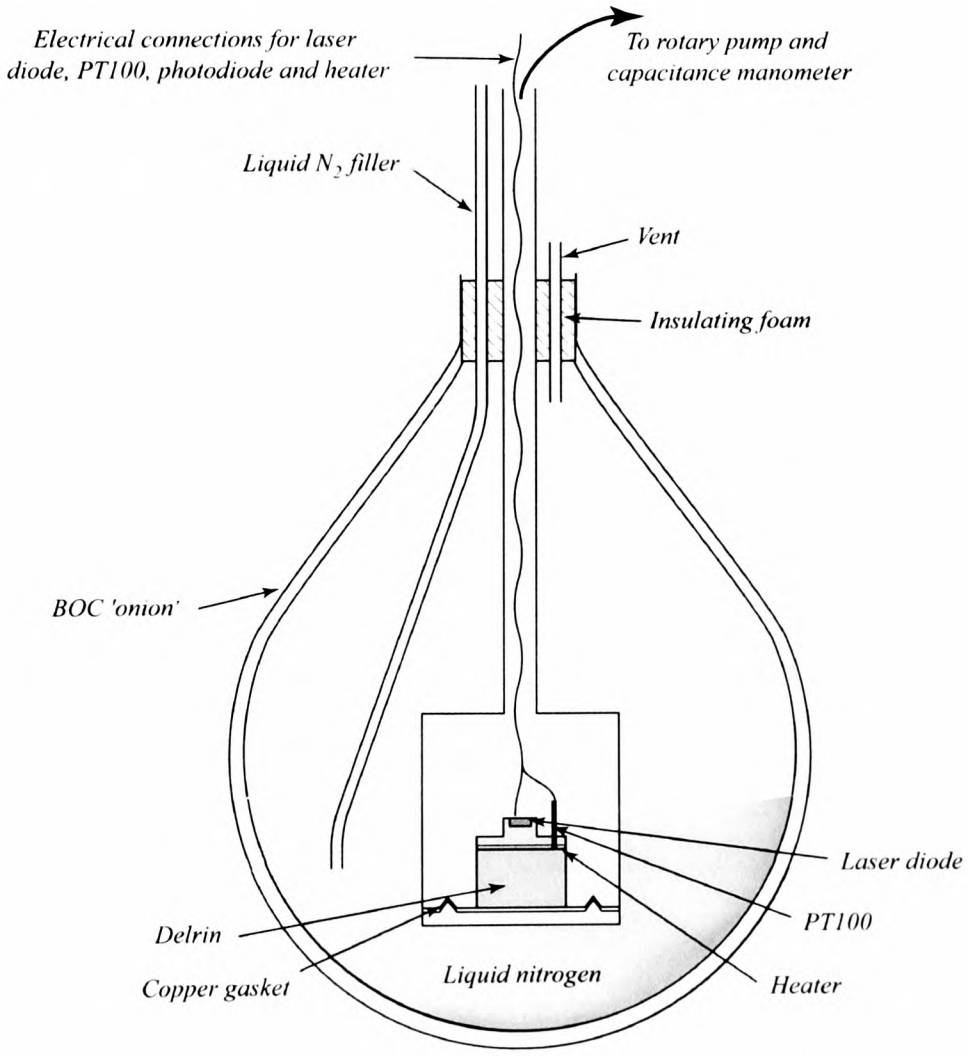

Figure 4.5 A section through the system used to evaluate the diode laser lifetime at 165 K.

The integral photodiode enabled monitoring of the laser from outside the sealed vessel. The laser was biased using a home built current source and then ramped over a range from just above zero output to 1 mW. The output from the integral photodiode was displayed on an oscilloscope and the point at which the discontinuity of the laser output occurs, corresponding to the light output at threshold, was noted. This threshold was found, as expected, to fall as liquid nitrogen was introduced into the 'onion' dewar. Once the laser block had reached 165 K, the dewar was topped up with liquid nitrogen as required (approximately every 48 hours). The laser was found to operate with a consistent threshold for in excess of 2000 hours. This result implies that the damage that destroyed the previous laser diodes occurs from repetitive heating and cooling and not from the extended use at temperatures below the manufacturer's minimum recommended operating temperature. The present strategy is to achieve the required temperature by Peltier cooling, thereby keeping the laser at 165 K without the need of a continuous supply of liquid nitrogen.

4.6 Detection of the OH Radical by Diode Laser Absorption[18]

4.6.1 Experimental Procedure

The 308 nm radiation was produced as described in Section 4.4.2. The ultraviolet radiation was separated from the fundamental output using two dichroic mirrors. The fundamental transmitted through the first of these mirrors was used to monitor the laser wavelength using a wavemeter (Burleigh WA1000). A spectrum analyser (TecOptics V4523) was used to monitor the laser's mode structure.

Three methods were used to measure the optical power of the doubled radiation. Two of these involved photon counting using a 50 Ω terminated photomultiplier tube (PMT) (Electron Tubes Ltd 9125 QB), firstly to find the mean count rate per second and secondly to find the mean time separation between photons. Both of these involved attenuating the ultraviolet radiation using calibrated filters. The third method was to terminate the signal output at 1 MΩ and then use the typical gain curve given by the manufacturer of the PMT to estimate the intensity of the radiation incident on the photocathode of the PMT. All three of these methods involved recording the power present with and without the laser radiation. These measurements all gave an output power of approximately 50 pW, about an order of magnitude lower than that

calculated for an Gaussian beam optimally focused into the crystal[14]. The loss on the crystal output face was estimated to be about 30%, and the remaining difference between the measured and optimal second-harmonic generation efficiencies may be caused by a combination of poor beam quality and absorption losses. $LiIO_3$ absorbs significantly in the region 300 – 350 nm[19] (previously RDP has been used instead to generate 317 nm[20], despite a conversion efficiency of about half that of $LiIO_3$). The poor beam quality is due to the astigmatism of the laser beam because of the large ratio of height to width of the output facet of the semiconductor and the large length of the crystal in comparison to the output aperture dimensions.

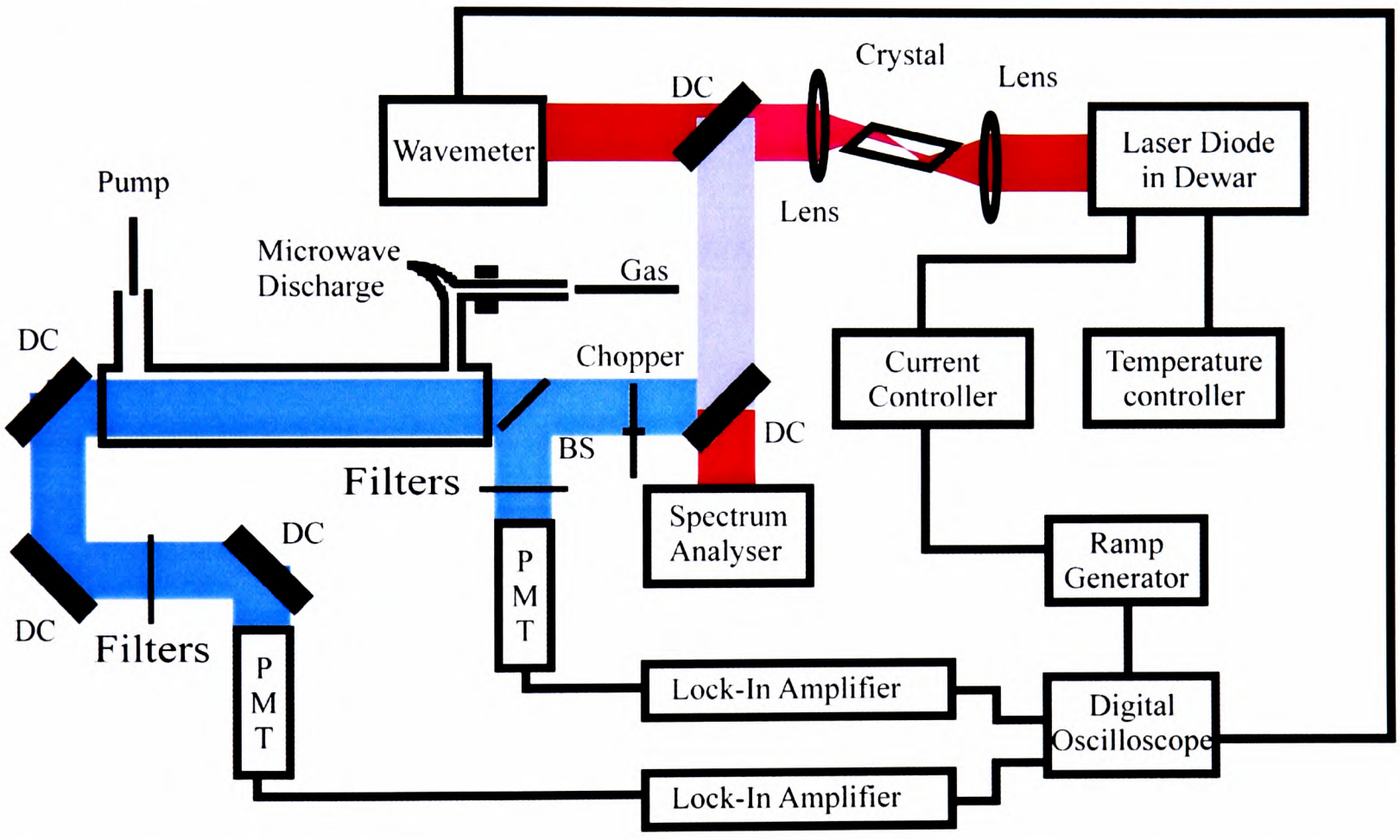

Figure 4.6 Experimental arrangement for production of 308 nm radiation and detection of the OH radical in a flow system. PMT = photomultiplier tube; DC = dichroic mirror and BS = beamsplitter.

The absorption experiment was carried out using the MMS technique described in Section 3.5.5. Figure 4.6 shows the experimental arrangement. The laser was modulated at 2 kHz with a mechanical chopper (Scitec Instruments). The radiation was then passed through an angled quartz flat, the reflection from which was focused through several Schott colour glass filters onto a PMT (Electron Tubes Ltd 9125 QB), in a radio frequency shielded housing, biased using a high voltage power supply. The reference signal produced by this PMT was amplified using a lock-in amplifier (Ortec Brookdeal 9503). The signal from this system was used to monitor changes in laser power to enable any absorption to be easily distinguished from laser intensity fluctuations.

The laser was then passed through a 75 cm long pyrex flow cell fitted with Brewster angled windows to minimise losses due to reflection. The pressure in the cell was monitored using a Penning gauge (Edwards CP 25-EK) and a capacitance manometer (Tylan General CDL 11).

The output beam was reflected from three dichroic mirrors, to reduce detection of the discharge glow, and monitored using an identical set of apparatus as used for the reference signal. The laser wavelength was varied by direct modulation of the laser current. At a given temperature, this allowed the fundamental output to be varied by typically 0.04 nm before the laser hopped onto a different longitudinal mode.

The two lock-in signals, the ramp generator signal and a voltage proportional to the wavelength from the wavemeter were recorded on a digital oscilloscope.

4.6.2 Results

The hydroxyl radical was identified (spectroscopically) by absorption on the $P_{11}(1)$, $Q_{11}(3)$ and $P_{21}(3)$ lines of the A $^2\Sigma^+$ ($v = 0$) ← X $^2\Pi$ ($v = 0$) band. Figure 4.7 shows a single scan of the lock-in amplified signals from the photomultipliers before and after the flow cell, as the doubled diode laser output was scanned from 308.153 nm to 308.164 nm. During this scan, the diode laser injection current was changed linearly with time by 2.3 mA over a period of 20 sec. The nonlinear change in the ultraviolet radiation intensity can be attributed to the lack of simultaneous tuning of the doubling crystal angle to maintain the phase-matched condition. When the scan had been corrected for background variation, the peak heights of the $Q_{11}(3)$ transition and the $P_{21}(3)$ satellite were found to be in the ratio expected from the absorption cross sections given in the table in Section 4.2.1. These transitions both originate from the same lower level, the A′ Λ–doublet of $N = 3$, $J = 3.5$ in the $^2\Pi_{3/2}$ F_1 manifold, and therefore the ratio of the absorption signals observed is only dependent on the line strengths and not the rotational distribution of the radical.

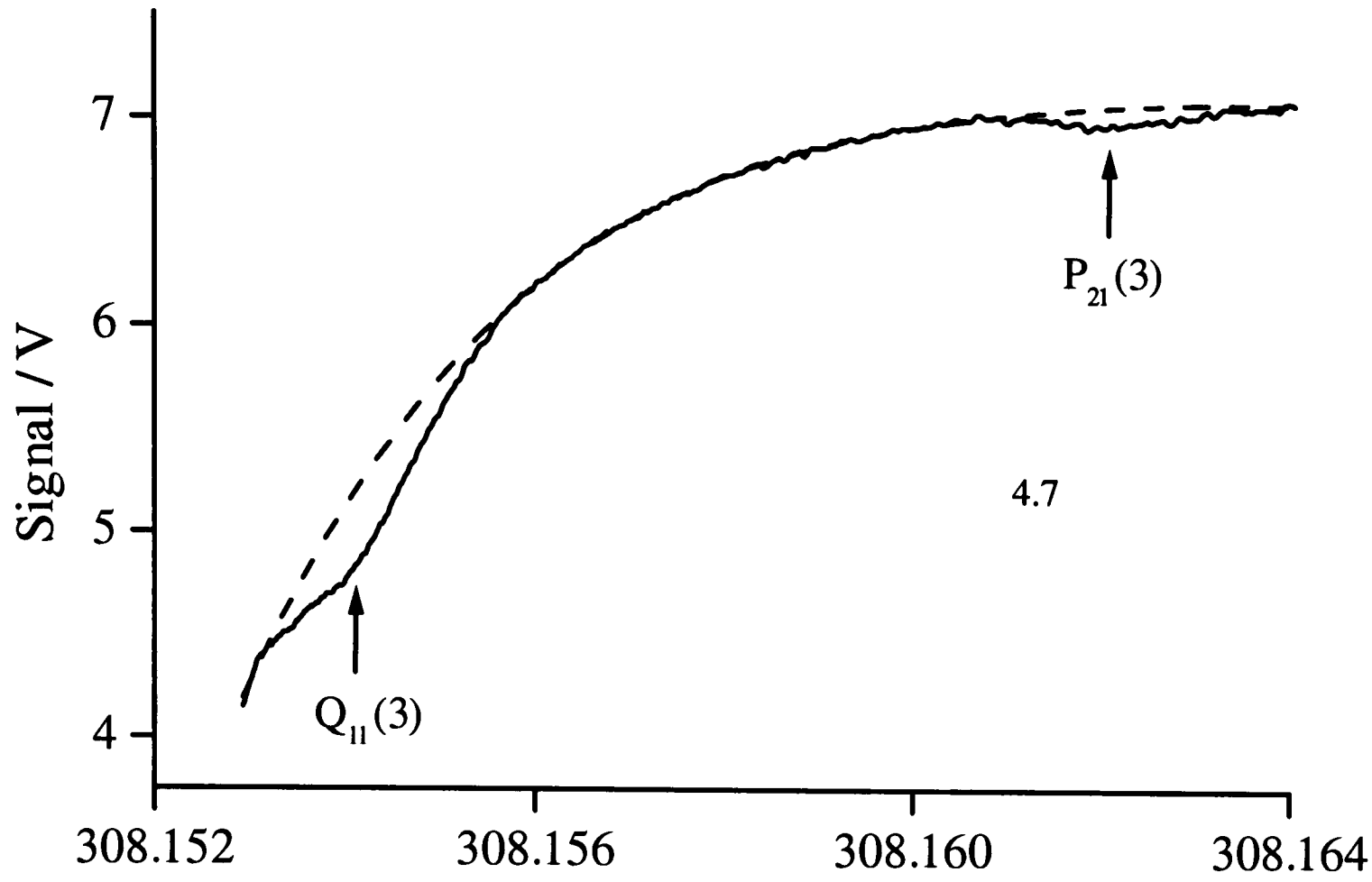

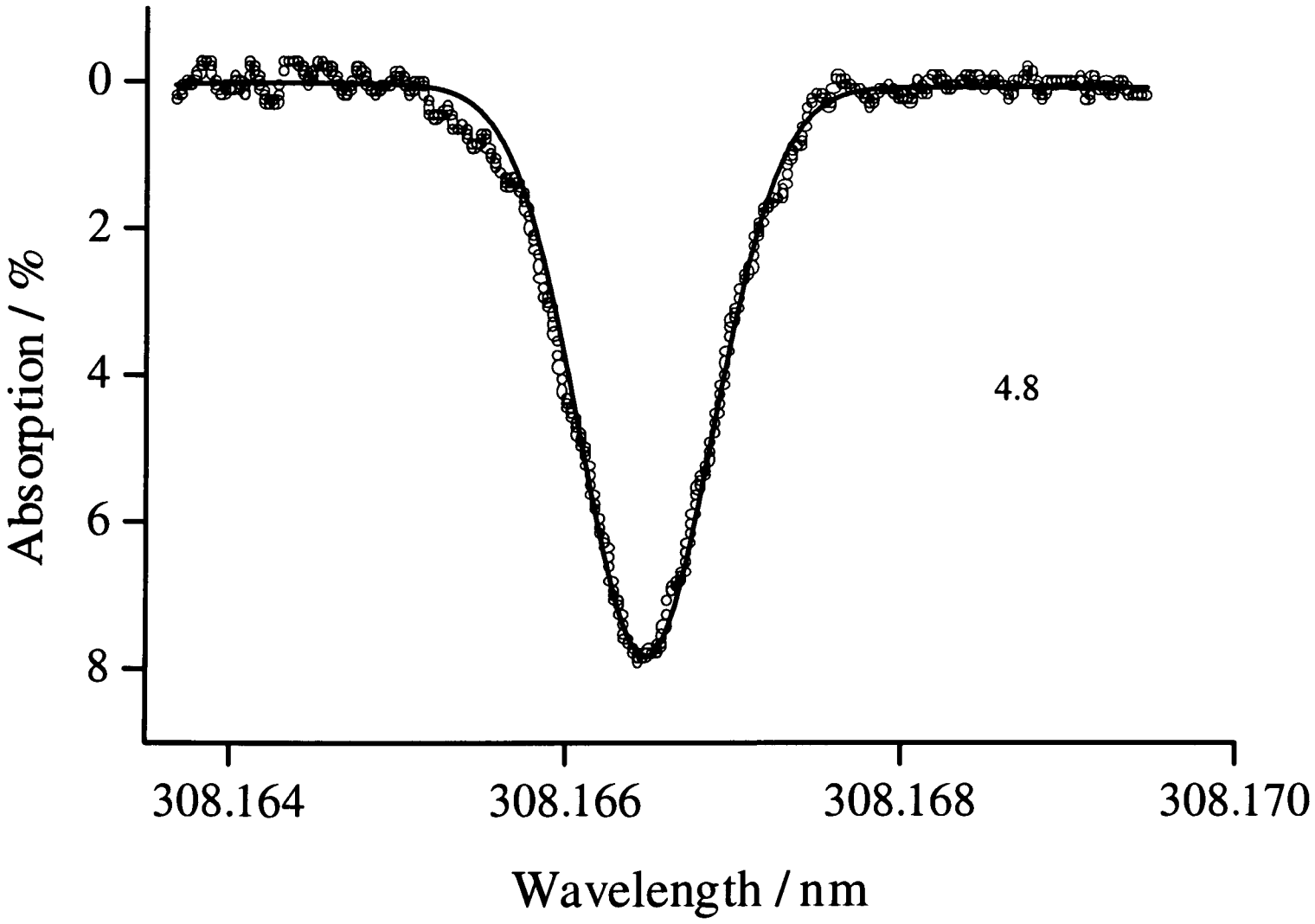

Figures 4.7 and 4.8 Absorption spectrum of the OH radical near 308.16 nm.
4.7: single scan of diode laser producing frequency doubled output between 308.153 and 308.164 nm. Traces before (dashed line) and after (solid line) passing through the flow tube showing absorption features identified as the $Q_{11}(3)$ and $P_{21}(3)$ transitions in OH.
4.8: background corrected absorption on the $P_{11}(1)$ feature at 308.1665 nm, with a simulation for absorption by a room temperature sample at 10 Torr total pressure.

Figure 4.8 shows an average of four scans at a slightly higher wavelength over the $P_{11}(1)$ transition at 308.1665 nm. An absorption of about 8 % is observed in the afterglow of a microwave discharge in 10 Torr of wet helium. An estimation of 2×10^{12} molecules cm^{-3} for the OH radical concentration, averaged along the 75 cm long flow cell, can be obtained using the Beer-Lambert Law and the fact that the total absorption cross section at the peak of this transition is 5.4×10^{-16} cm^2 at 300 K [8]. Collisional broadening at 10 Torr and 300 K cannot be neglected for OH radicals and therefore to simulate the line shape a Voigt profile is required[8]. This profile is produced from the convolution of a Gaussian (Doppler profile) and a Lorentzian (pressure broadened profile), both discussed in Section 3.3.7, and is given by[8]

$$F_v(\tilde{\nu}) = \left(1 - \frac{\omega_c}{\omega_v}\right) e^{-4(\ln 2)\Delta^2} + \left(\frac{\omega_c}{\omega_v}\right) \frac{1}{1+4\Delta^2} + 0.016\left(1 - \frac{\omega_c}{\omega_v}\right)\left(\frac{\omega_c}{\omega_v}\right)\left\{e^{-0.4\Delta^{2.25}} - \frac{10}{10+\Delta^{2.25}}\right\} \qquad (4.4)$$

where

$$\Delta = \frac{(\tilde{\nu} - \tilde{\nu}_0)}{\omega_v} \qquad (4.5)$$

and the half width of the Voigt profile, ω_v, is given by the approximation[21]

$$\omega_v \approx \frac{(\omega_C)}{2} + \sqrt{\frac{\omega_C^2}{4} + \omega_D^2} \qquad (4.6)$$

where ω_D and ω_C are the half widths of a purely Doppler and purely collision broadened profile respectively. The Doppler half width of an OH radical absorption profile at a given temperature can be calculated using[8]

$$\omega_D(T) = \omega_{D_0}\sqrt{\frac{T}{T_0}} \qquad (4.7)$$

where the Doppler width at 300 K is given by ω_{D0} = 0.93 pm or 0.098 cm^{-1} with λ_0 = 308 nm. The dependence of the collision broadened half width, ω_C, on pressure and temperature is given by[8]

$$\omega_C(T,P) = \omega_{C_0}\frac{P}{P_0}\sqrt{\frac{T_0}{T}} \qquad (4.8)$$

where ω_{C0} (= 2 pm) is the collision broadened half width measured under the reference conditions T_0 (= 300 K) and P_0 (= 101.3 kPa = 760 Torr). Figure 4.8 also shows a simulation

of the Voigt line shape for a 300 K sample at a pressure of 10 Torr. The quality of this fit is consistent with the absorbing species being the OH radical.

The main source of noise during these experiments was optical emission from the microwave discharge, two orders of magnitude more intense than the laser radiation, despite the long optical path from the discharge to the PMT, and use of a Wood's horn on the discharge arm, dichroic mirrors, filters, and small apertures. Electrical noise from the discharge also contributed a small amount to noise on the baseline.

4.6.3 The Variation of the OH Radical Concentration with Discharge Conditions

The concentration of the hydroxyl radical was measured using the system discussed above under various discharge conditions. This method of detection records an average OH radical concentration, $[OH]_{av}$, along the length of the flow cell, L, given by

$$[OH]_{av} = \frac{\int_0^L [OH]\,dx}{L} \tag{4.9}$$

If the assumption is made that the gas flow velocity, c_f, is constant along the flow cell it follows that the distance a species is from the inlet is proportional to the time it has been in the flow cell. Therefore, the average OH concentration can be found from equation (4.10).

$$[OH]_{av} = \frac{c_f \int_0^{\frac{L}{c_f}} [OH]\,dt}{L} \tag{4.10}$$

Thus, the concentration observed depends on the gas flow velocity.

4.6.3.1 Production from Water Vapour

Initially the OH radical was produced directly in the discharge from a wet noble gas. Figure 4.9 shows how the average hydroxyl radical concentration varies with total pressure in the flow cell when the carrier gas is helium. 90% of the gas flowing into the cell flowed through the bubbler and subsequently the discharge; the remaining 10 % of the flow was dry helium injected directly over the Brewster windows. This flow stopped a systematic reduction in the transmitted signal due to contamination of the windows. The figure clearly shows that the concentration of the OH radical increases with increasing pressure, as expected from the increasing number density of water molecules entering the discharge.

4.9

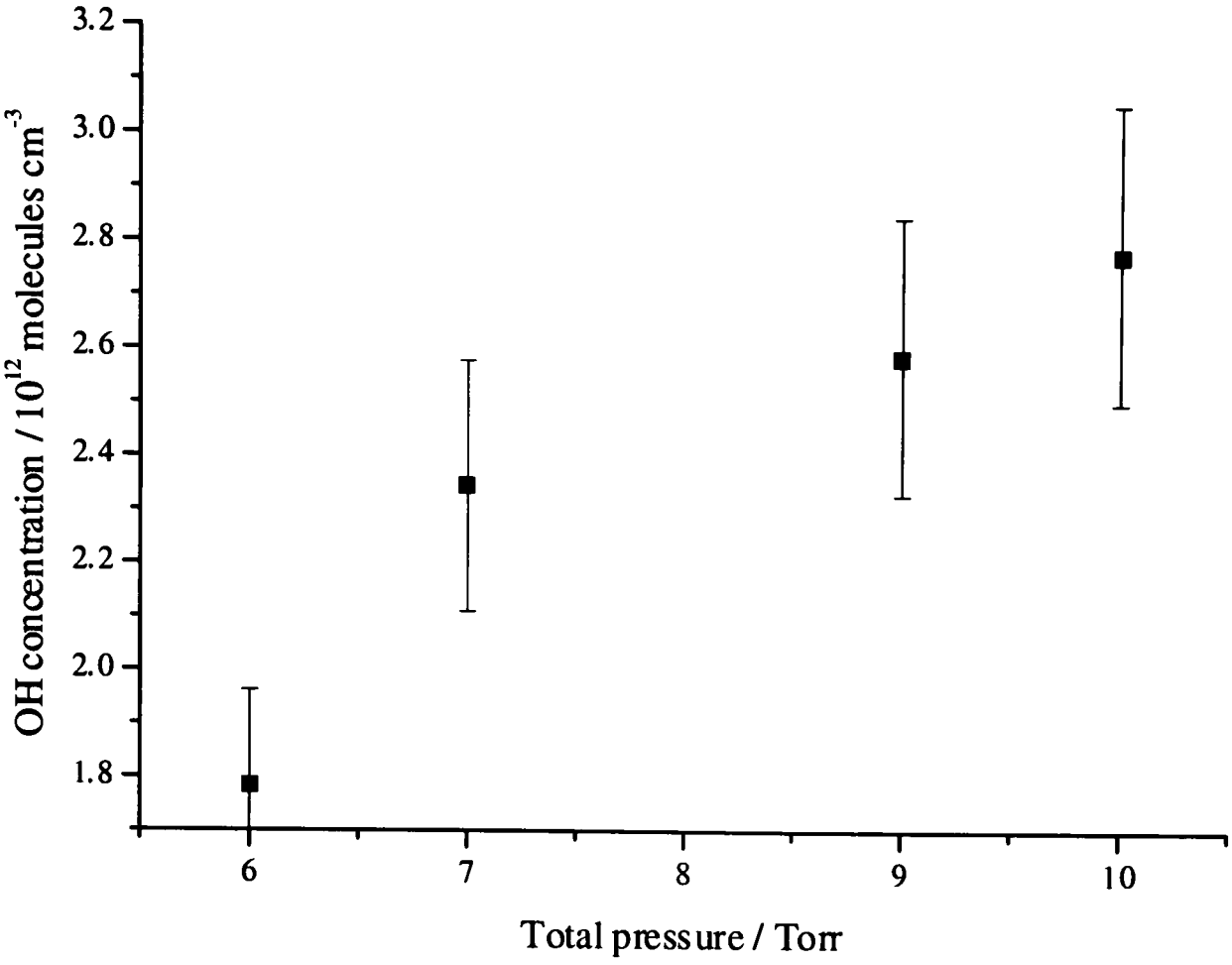

4.10

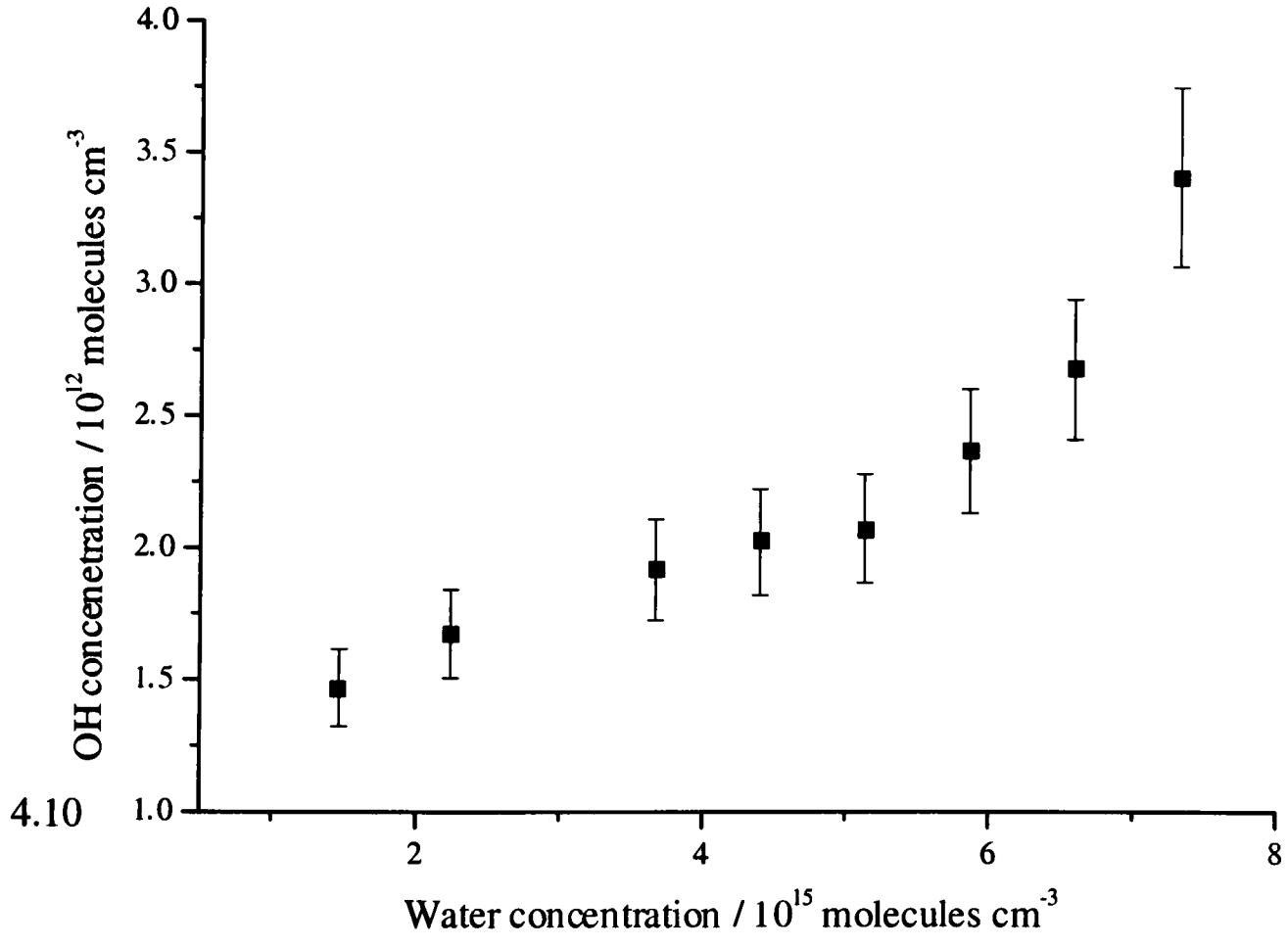

Figures 4.9 and 4.10 Absolute OH radical concentrations.
4.9: from a microwave discharge of a 9:1 ratio of wet to dry helium at various total pressures.
4.10: from a microwave discharge at a total pressure of 9.5 Torr at various water molecule number densities in helium.

The variation of the average OH radical concentration at a total pressure of 9.5 Torr with water molecule number density is shown in Figure 4.10. The concentration clearly increases with

increasing number density, but is not linear, implying that the proportion of water molecules dissociated is not constant. During the experiment, it was observed that the intensity of the optical emission produced by the discharge and the reflected power measured at the microwave generator changed considerably. These observations imply that the properties of the discharge varied considerably and therefore the dissociation efficiency would be expected to change.

A similar set of experiments were completed using argon as the carrier gas, with trends observed similar to those when helium was used. However, the main difference observed was that the average OH radical concentration was found to be about half that when helium was used, which may be explained qualitatively again by the different dissociation efficiencies of the discharge in the two gases.

4.6.3.2 Production by Chemical Reaction

For the chemical production method (see Section 4.3), the partial pressure of both nitrogen dioxide and hydrogen were varied at a total pressure of 4 Torr. The variation of the hydroxyl radical concentration with nitrogen dioxide pressure is shown in Figure 4.11; it is apparent that the average OH radical concentration falls as the amount of nitrogen dioxide is increased.

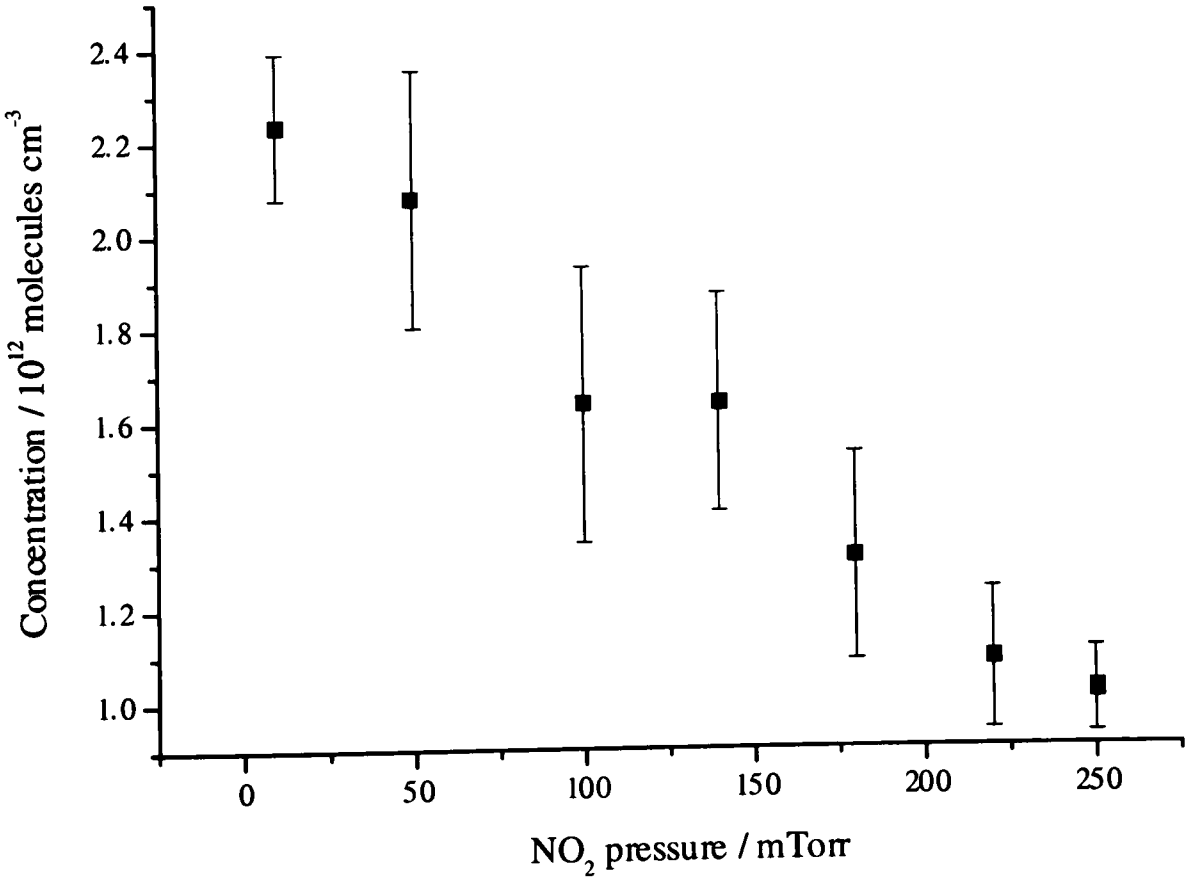

Figure 4.11 Absolute OH radical concentrations produced by the reaction, H + NO_2 → OH + NO, at a total pressure of 4 Torr at various NO_2 partial pressures and 60 mTorr of H_2. The H atoms are produced in a microwave discharge of H_2 diluted to a total pressure of 4 Torr with a noble gas.

To interpret this quantitatively it is necessary to consider the chemical kinetics of the reactions occurring in the flow cell. The OH radical was produced using the following reaction[9].

$$H + NO_2 \rightarrow OH + NO \qquad k_1 = 1.4 \times 10^{-10}\ cm^3 molecules^{-1} s^{-1}$$

This reaction was considered to be the main loss mechanism of the H atoms because the NO_2 molecules were in excess. The H atoms were continuously produced in a discharge from a known number density of hydrogen molecules, and so a continuous flow of hydrogen atoms of concentration $[H]_0$ enters the flow cell. These are removed by reaction with NO_2 and so the hydrogen atom concentration obeys the following differential equation

$$\frac{d[H]}{dt} = -k_1[H][NO_2] \tag{4.11}$$

This leads to the solution that the H atom concentration decays exponentially with time:

$$[H] = [H]_0 e^{-k_1[NO_2]t} \tag{4.12}$$

The hydroxyl radical can be removed by reactions with other species (either in the gas phase or on the walls of the cell) and by the pumping system. The pumping removal rate is accounted for by the limits of the integral in equation (4.10). Within the cell the major loss of the OH radical is *via* the third body recombination reaction with NO_2[22].

$$NO_2 + OH + M \rightarrow HNO_3 + M \qquad k_2 = 2.78 \times 10^{-13}\ cm^3 molecules^{-1} s^{-1} \text{ at 4 Torr}$$

The wall loss rate can be treated as a unimolecular process

$$OH \rightarrow \text{Products}$$

with a rate constant k_3. The only other loss rates that may be significant are the bimolecular recombination of two OH radicals to form hydrogen peroxide and the bimolecular reaction to form water and an oxygen atom. The recombination reaction rate is low at 4 Torr (7.47×10^{-14} $cm^3 molecules^{-1} s^{-1}$)[22] and can therefore be neglected. The bimolecular reaction rate is much faster under the conditions in the flow cell[22].

$$OH + OH \rightarrow H_2O + O \qquad k_4, = 1.9 \times 10^{-12}\ cm^3 molecules^{-1} s^{-1}$$

A kinetic model created using FACSIMILE[23] was used to calculate the time dependence of the OH radical concentration. An example of the trace obtained is given in Figure 4.12.

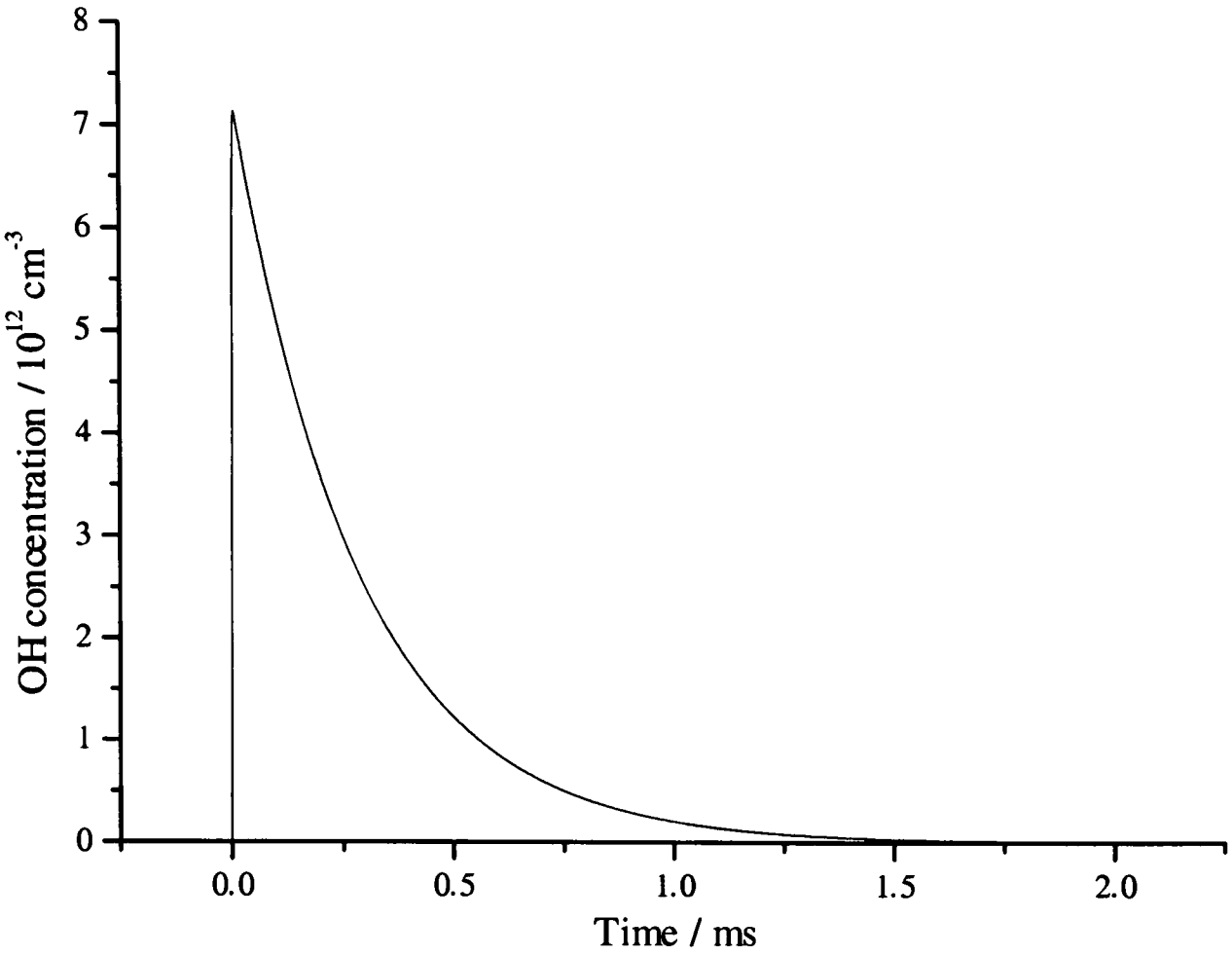

Figure 4.12 Variation of the OH radical concentration with time produced using FACSIMILE[23] and the full reaction scheme described.

The calculation was also made neglecting the OH + OH reaction ($k_4 = 0$). This increased the integral of the OH concentration by less than 1 % and therefore this reaction was neglected. The time dependence of the OH radical concentration can therefore be described by the following differential equation.

$$\frac{d[\mathrm{OH}]}{dt} = k_1[\mathrm{H}][\mathrm{NO_2}] - k_2[\mathrm{OH}][\mathrm{NO_2}] - k_3[\mathrm{OH}] \tag{4.13}$$

Substituting the hydrogen atom time dependence from equation (4.12) and solving leads to equation (4.14).

$$[\mathrm{OH}] = \frac{k_1[\mathrm{H}]_0[\mathrm{NO_2}]}{(k_2 - k_1)[\mathrm{NO_2}] + k_3}\left(e^{-k_1[\mathrm{NO_2}]t} - e^{-(k_2[\mathrm{NO_2}]+k_3)t}\right) \tag{4.14}$$

The contribution to the observed OH radical concentration can be seen from Figure 4.12 to be negligible after about 1.5 ms. For a reduction of the absorption signal by pumpout from the 75 cm cell, the gas flow velocity would have to be greater than 500 ms^{-1}, which is not possible with the pumping system used. Therefore, the upper limits of the integrals in equations (4.9) and (4.10) can be considered to have a negligible contribution in the integration. The average concentration of the OH radical is therefore given by equation (4.15).

$$[\mathrm{OH}]_{av} = \frac{c_f [\mathrm{H}]_0}{L(k_2[\mathrm{NO_2}] + k_3)} \tag{4.15}$$

Figure 4.13 shows a plot of $1/[\mathrm{OH}]_{av}$ against $[\mathrm{NO_2}]$ along with a linear fit; the experimental variation seems to agree well with this kinetic model.

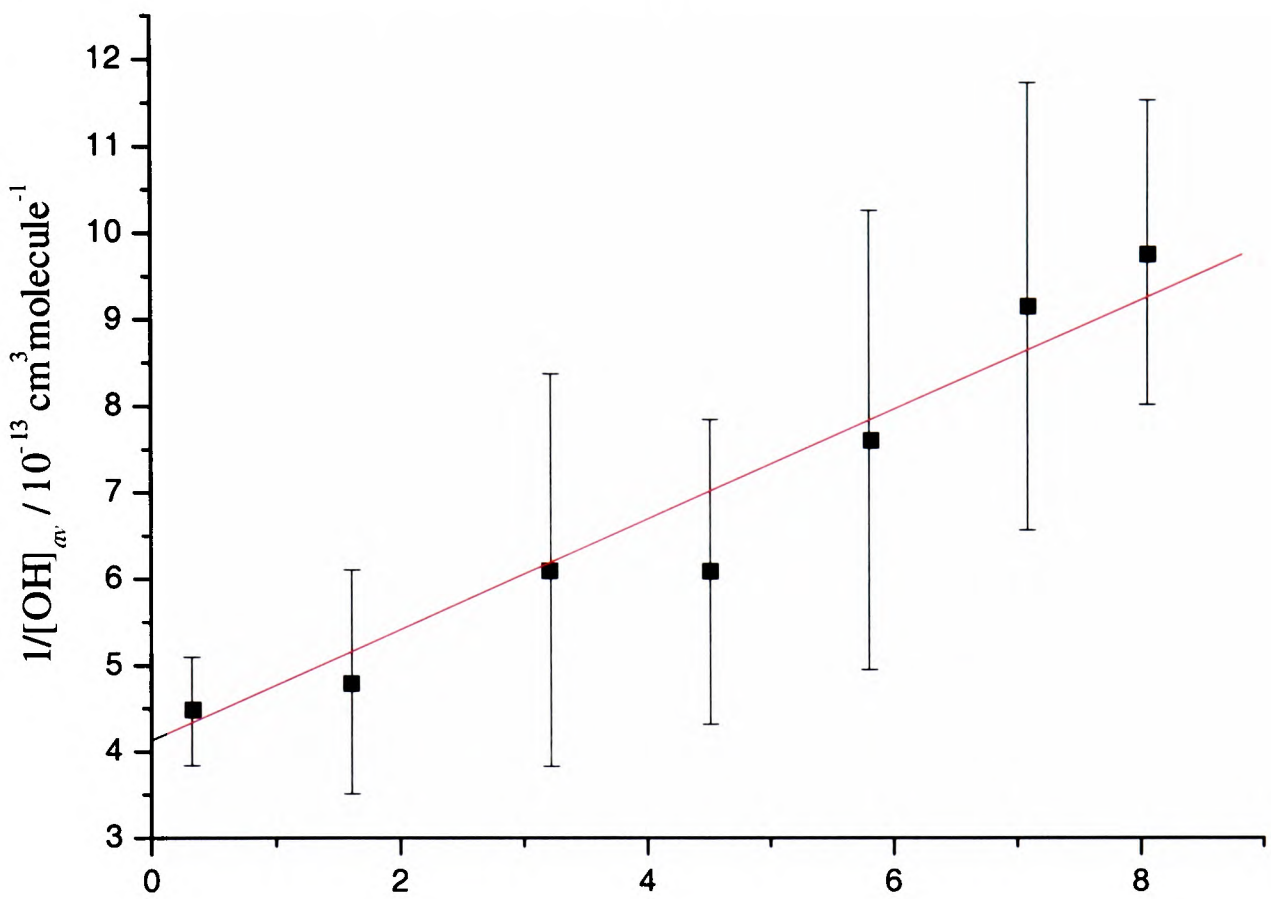

Figure 4.13 Plot of the reciprocal of the absolute OH radical concentration against NO_2 concentration compared to the linear fit expected from the kinetic model.

From the fit, k_3 is found to be 1.8×10^3 s^{-1}. The inverse of this rate constant is the lifetime of the OH radical in the cell before it is removed in a process excluding NO_2 ($\tau_{other} = 1/k_3$). The root mean square distance travelled by a species, with a diffusion coefficient D, in time t is given by the following expression in one dimension[24].

$$\sqrt{\langle x^2 \rangle} \approx \sqrt{(2Dt)} \tag{4.16}$$

From this the distance travelled in two dimensions can be calculated using Pythagoras' theorem, the third dimension is not considered because it is the flow direction and therefore the radical will not collide with the vessel wall by moving in this direction. From this calculation, it is found that during τ_{other} ($\approx$ 0.5 ms) the OH radical will on average diffuse approximately 2 mm, which is much smaller than the cell radius (25 mm). Although this calculated diffusion distance is inconsistent with the dimensions of the cell, it can be explained by the fact that the

inlet for the NO_2 molecules and the H atoms were adjacent on the flow cell and therefore the reactions which produce the OH radical occur in close proximity to the wall.

From the gradient of the plot in Figure 4.13, it is also possible to obtain a value for the product of the initial hydrogen atom concentration and the gas flow velocity, $[H]_0 c_f = 3.2 \times 10^{15}$ $cm^{-3}ms^{-1}$. An upper estimation of the flow velocity is 100 ms^{-1}, implying that approximately 1 % of the hydrogen molecules are dissociated in the discharge; this is comparable to a previously measured dissociation efficiency of a similar microwave discharge[25].

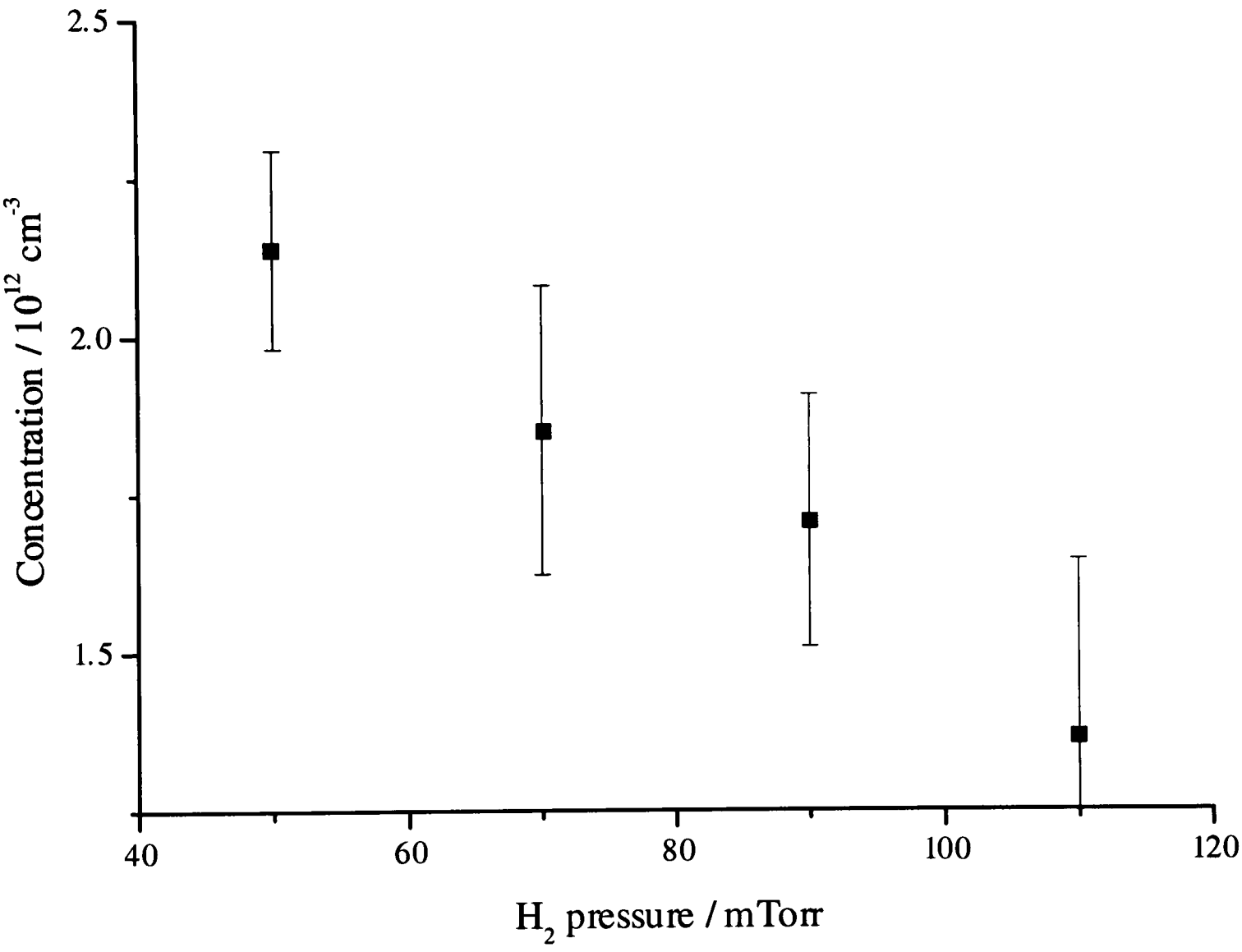

Figure 4.14 Absolute OH radical concentrations produced by the reaction, H + NO_2 → OH + NO, at a total pressure of 4 Torr at various H_2 partial pressures and 100 mTorr of NO_2. The H atoms are produced in a microwave discharge of H_2 diluted in a noble gas.

Figure 4.14 shows the variation of the OH radical concentration in the flow cell as the partial pressure of hydrogen in the discharge is increased, while the nitrogen dioxide pressure was kept constant at 100 mTorr. It is clear from the figure that the hydroxyl radical concentration falls as more hydrogen is bled into the discharge. This is not in keeping with equation (4.15) if the dissociation efficiency of the discharge was independent of the hydrogen gas pressure. This inconsistency with the kinetic model can be attributed to the discharge becoming less

efficient as the hydrogen gas pressure is increased. This explanation is supported by the observations that as the hydrogen pressure was increased, the power applied to the discharge had to be increased to maintain the same net power and that the microwave discharge would not strike with more than 110 mTorr of hydrogen present in the feed gas.

The wet noble gas method for production of OH was chosen for the experiments presented in the remainder of this Chapter. This is because although both methods produce about the same OH concentration, the chemistry involved in the afterglow of the water discharge is more predictable.

4.7 Experimental Equipment for the Pulsed Laser Experiments

To detect OH, three further techniques were examined; Cavity Ring Down Spectroscopy (CRDS), Laser Induced Fluorescence (LIF), both discussed in Chapter 1, and a novel combination of the two: Cavity Laser Induced Fluorescence (CLIF). These experiments were all completed with a pulsed laser system. However, there is the future possibility of using a more intense ultraviolet diode laser source than discussed in the previous sections, by using an enhancement cavity around the nonlinear crystal (see Chapter 5).

4.7.1 The Reaction Vessel

A stainless steel chamber with a hexagonal horizontal cross section and perpendicular optical line-of-sight paths was constructed and fitted with gimbal mirror mounts on opposite sides of the hexagon. The chamber was fitted with Brewster angle windows, gas inputs that enabled the mirrors to be kept clean by a constant flow of argon and a shaft seal mechanism onto the mirror mounts to allow movement of the mirrors. The mounts contained two concave mirrors specified with a reflectivity of 99.7 % (at 308 nm) and a radius of curvature of 1.5 m (LaserOptik), aligned to form a ring down cavity (see Appendix 1 for a discussion of optical cavities). Two stainless steel baffle arms, also equipped with Brewster angle windows, were fitted perpendicular to the ring down cavity through two opposite vertices of the hexagon. This allowed the experimental set up to be converted from that for CRDS to that for LIF experiments by the insertion of only one mirror. The experimental layout is shown in Figure 4.15.

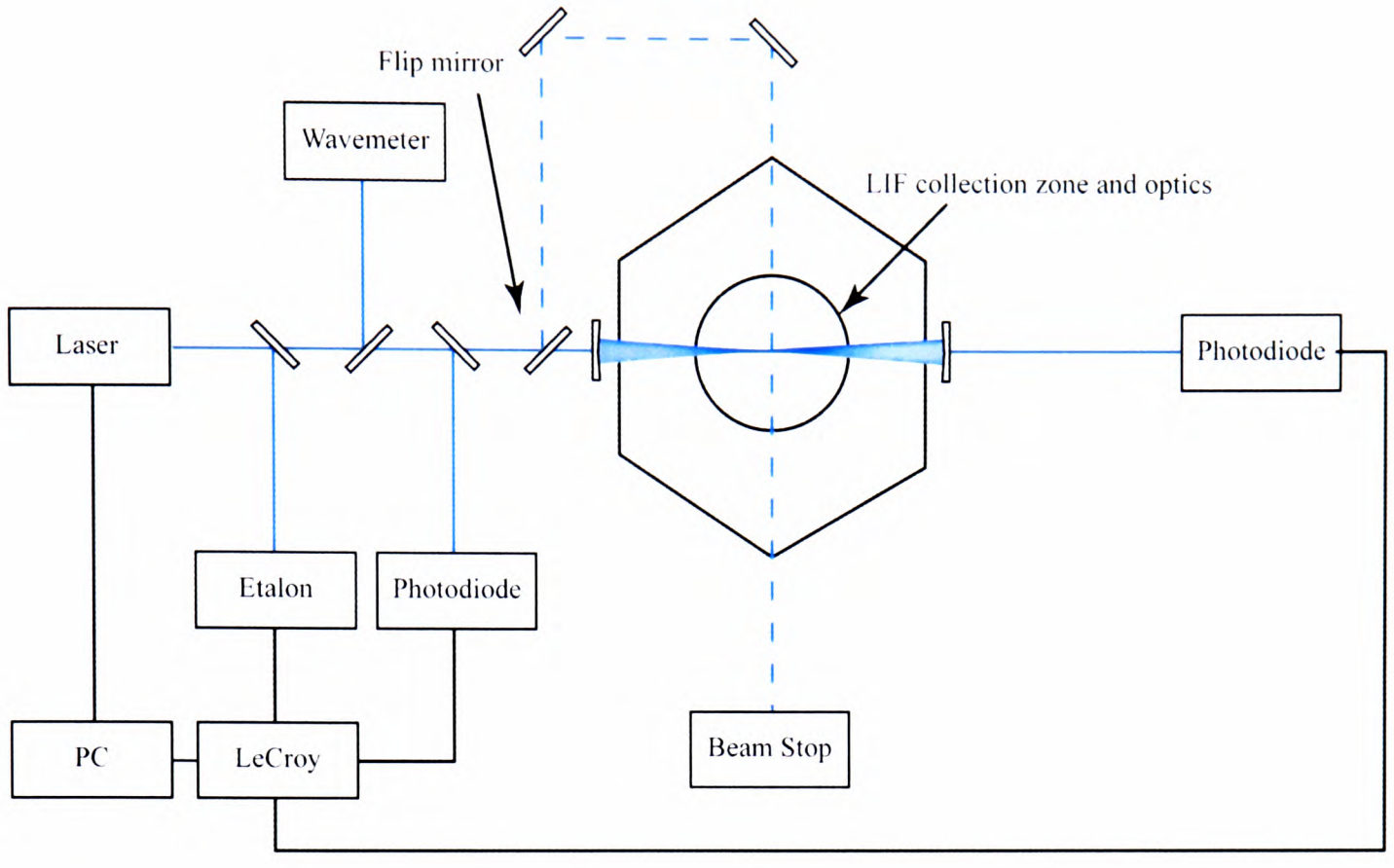

Figure 4.15 Schematic layout of combined LIF and CRDS experimental system.

The chamber was pumped through one of the remaining edges of the hexagon using the system described in Section 4.3 and the OH radical was introduced from a wet argon microwave discharge (discussed in Chapter 2) through another of the faces. In this case, because the OH radical was observed almost perpendicular to the gas flow, the average OH radical concentration observed can only be calculated from equation (4.10) by using significantly different integration limits as only a short length of time is being studied. The pressure within the chamber was monitored using a Penning gauge (Edwards CP 25-EK) and a capacitance manometer (Tylan General CDL 11) mounted on the two remaining sides.

The CRDS signal was monitored using a biased BPX 65 photodiode. The LIF and CLIF were detected through a 40 mm diameter fused silica window in the top of the chamber. The fluorescence radiation was collected by a 50 mm diameter quartz lens (focal length 145 mm). This was mounted in a translation stage that allowed the image of the laser probe zone to be focused through a small aperture and a set of interference filters, used to cut down the detection of scattered laser photons and radiation from the discharge. After being filtered, the fluorescence radiation was finally imaged onto the photocathode of a PMT (EMI 9813QKB).

4.7.2 The Laser System

The laser system consisted of a Nd:YAG pump laser (Spectron SL803-10) and an extensively modified dye laser (Spectron SL4000G). The pump laser comprised of two sections; an

oscillator and an amplifier, producing up to 800 mJ in 15 ns at 1064 nm, the output of which was then used for SHG in a temperature controlled angle tuned KD*P crystal yielding 270 mJ of 532 nm radiation.

The 532 nm laser output was used to pump the dye laser operating with DCM in methanol. The output of the oscillator of the dye laser was amplified in two longitudinally pumped amplifier cells, resulting in an output of typically 30 - 50 mJ. Frequency doubling of the dye laser was carried out in a KD*P crystal placed within an autotracker unit (SL4000 DMX) with an efficiency of ≈ 10%. The second harmonic was separated from the fundamental radiation by a colour glass filter (Schott UG11). The laser wavelength was monitored using a wavemeter (Burleigh WA4500), and during scans a photodiode observing the fringe pattern produced by a glass etalon (FSR 23.6 GHz and Finesse ≈ 16) was used to monitor precisely the relative frequency of the dye laser.

The signals obtained from the CRDS photodiode, PMT, reference photodiode and the etalon photodiode were acquired on a LeCroy 9304 (175 MHz, 100 Msamples/s) digital oscilloscope. These signals were transferred onto a personal computer (Dan 486DX33) equipped with several interface cards, which also controlled the scanning of the laser system. For the spectra taken, this PC averaged 200 shots at each point, with each shot individually normalised to the laser intensity.

4.8 Detection of OH Radical by LIF

The LIF technique is commonly used to detect the hydroxyl radical[26] in the laboratory, and has been used extensively for atmospheric measurements. It is used here so that other techniques can be compared to it and to give a direct measure of the lifetime, τ_{fl}, of the upper state of the OH radical in the experimental conditions used.

Figure 4.16 shows a time trace obtained by LIF of the OH radical pumped on the $Q_{11}(3)$ transition at 308.154 nm. The single exponential decay that was fitted to the data is also shown in the figure and in this case, at a total pressure of 3.5 Torr, the lifetime is found to be 530 ns.

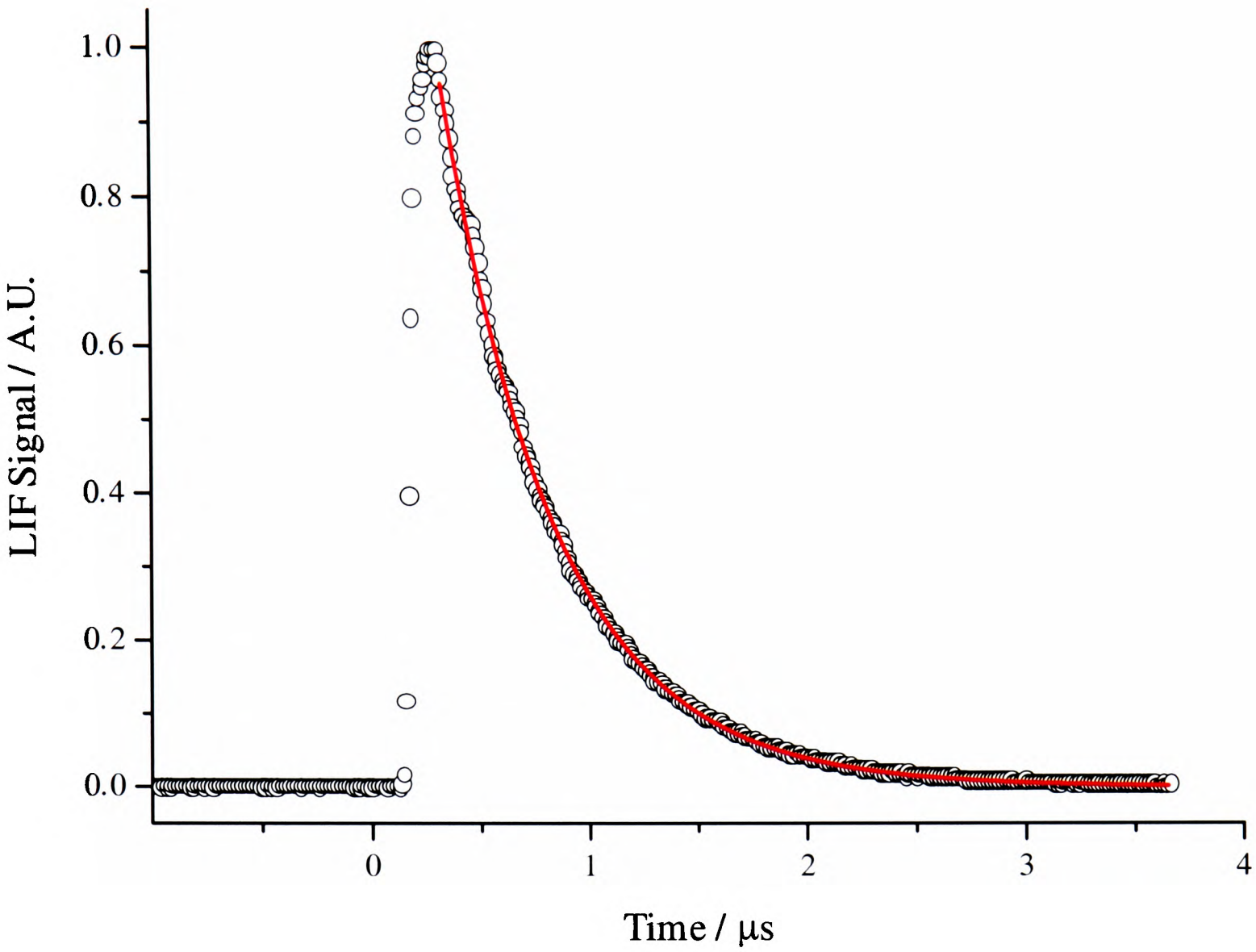

Figure 4.16 LIF time dependence of the $Q_{11}(3)$ transition from the OH radical, produced in a wet noble gas microwave discharge at a pressure of 3.5 Torr.

The lifetime of the excited level of the OH radical produced by the laser pulse not only depends on its natural radiative lifetime but also on pressure because of competing collisional deactivation. Therefore increasing the pressure, which increases the collision rate, decreases the lifetime of the excited level. This removal process also reduces the fluorescence quantum yield and hence the LIF signal, increasing the error in the measurement of the lifetime. Figure 4.17 shows how the inverse of the measured lifetime, $1/\tau_{fl}$, of the $N = 3$, $J = 3.5$ level of OH depends on the total number density. The value of the radiative lifetime ($\approx$ 700 ns) found from the intercept is in agreement with previous observervations[6] as is the argon quenching rate (10^{-11} molecules $cm^{-3}s^{-1}$)[8] found from the gradient. The expected decrease in the lifetime with increasing pressure is clearly observed.

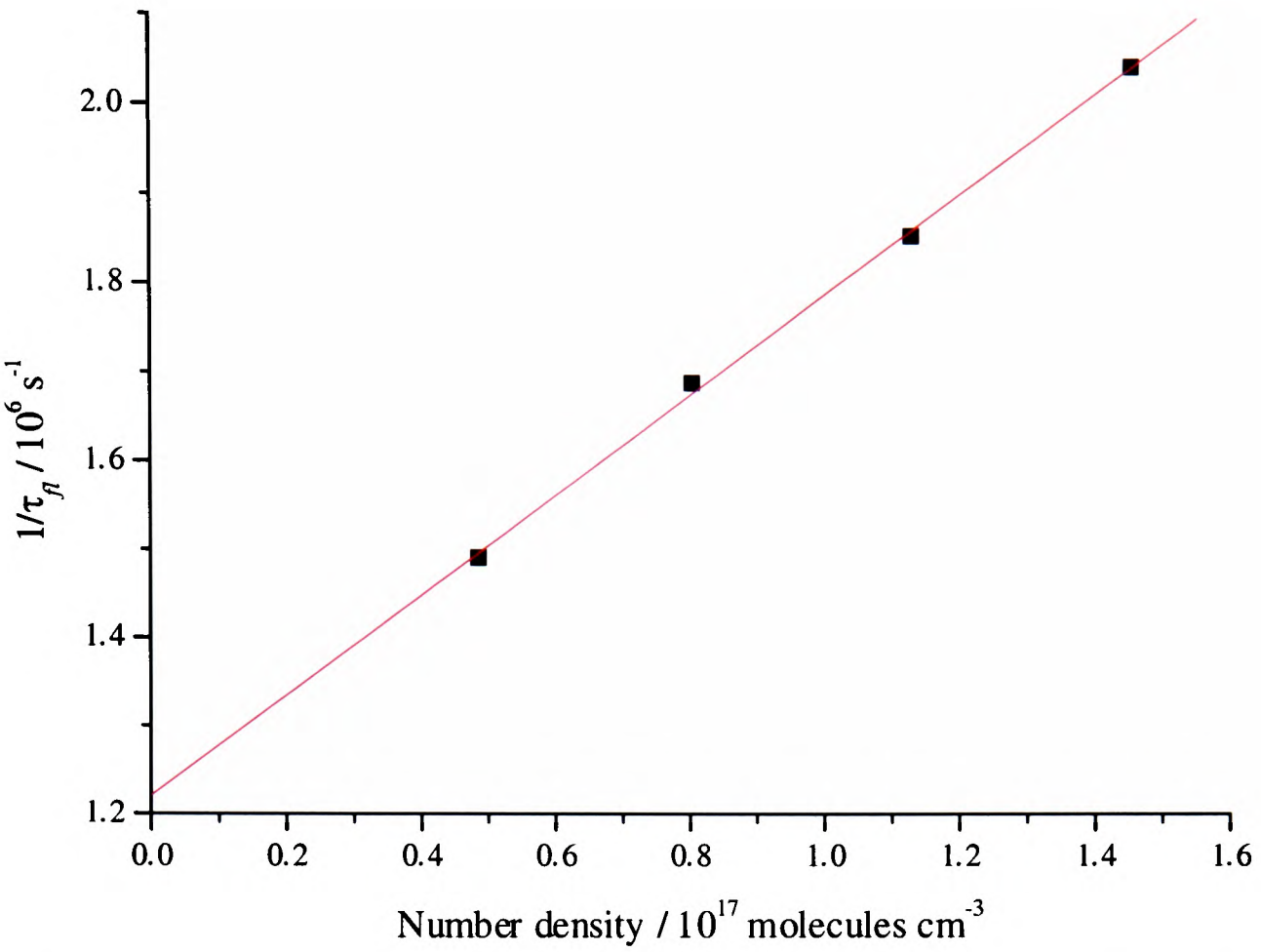

Figure 4.17 Dependence of the reciprocal of the fluorescence lifetime on pressure along with a linear fit from which the radiative lifetime was obtained.

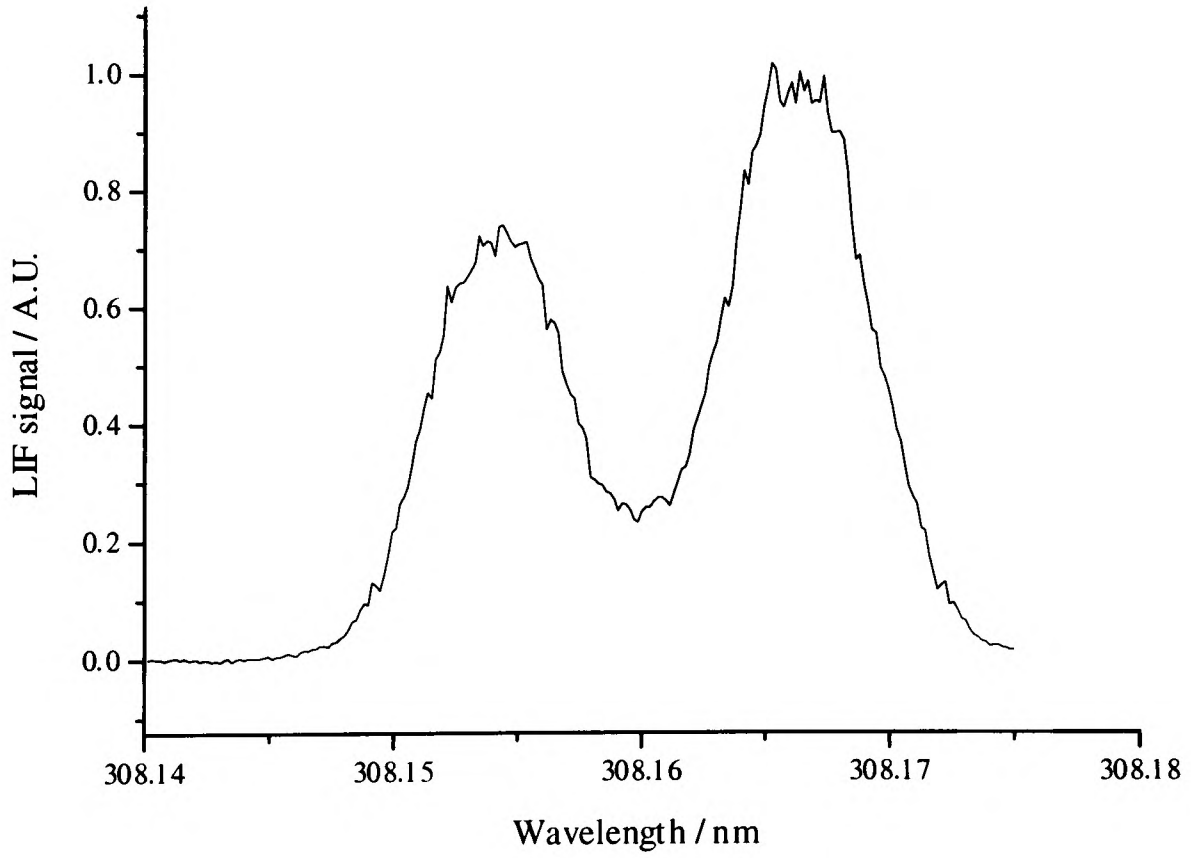

Figure 4.18 LIF spectrum of the OH radical, produced in a wet noble gas discharge, near 308.16 nm, showing the $P_{11}(1)$, $Q_{11}(3)$ and $P_{21}(3)$ features, at a pressure of 3.5 Torr.

Figure 4.18 shows a spectral scan across the $P_1(1)$, $Q_{11}(3)$ and $P_{21}(3)$ transitions obtained by integrating time traces such as Figure 4.16 at each wavelength and normalising to the laser intensity. The peaks appear much broader than in Figures 4.7 and 4.8. This broadening can be

attributed to the fact that the dye laser bandwidth (0.14 cm^{-1})[27] is much greater than the Doppler width of the transition, which in turn is much greater than the bandwidth of the diode laser used to record the scans in Figures 4.7 and 4.8. Despite broadening, the ratio of the LIF peak heights of the $P_1(1)$ and $Q_{11}(3)$ transitions is found to be approximately in the ratio expected for a thermalised sample at 300 K[8].

4.9 Detection of the OH Radical by CRDS

Pulsed CRDS has previously been used to detect OH radicals[28] in a flame. CRDS, as explained in Section 1.6.4, detects the rate of absorption rather than its magnitude and has the advantage over LIF that the absolute concentration can be measured. The time dependence of the intensity of a laser light pulse, at 308.154 nm, within the cavity, with the discharge extinguished (and a total pressure of 3.5 Torr), is shown in Figure 4.19 along with a fitted first order exponential decay, $I_0e^{-t/\tau}$. From this, it was possible to obtain a value of 230 ns for the cavity 'ringdown time', τ, a value that had little variation with the pressure in the cavity up to 5 Torr. Equation 1.20 relates mirror reflectivity to τ showing that the mirrors used were 99.64 % reflective at this wavelength. Thus, the cavity finesse is 867, which gives an effective path length of 69 m within the 25 cm ringdown cavity.

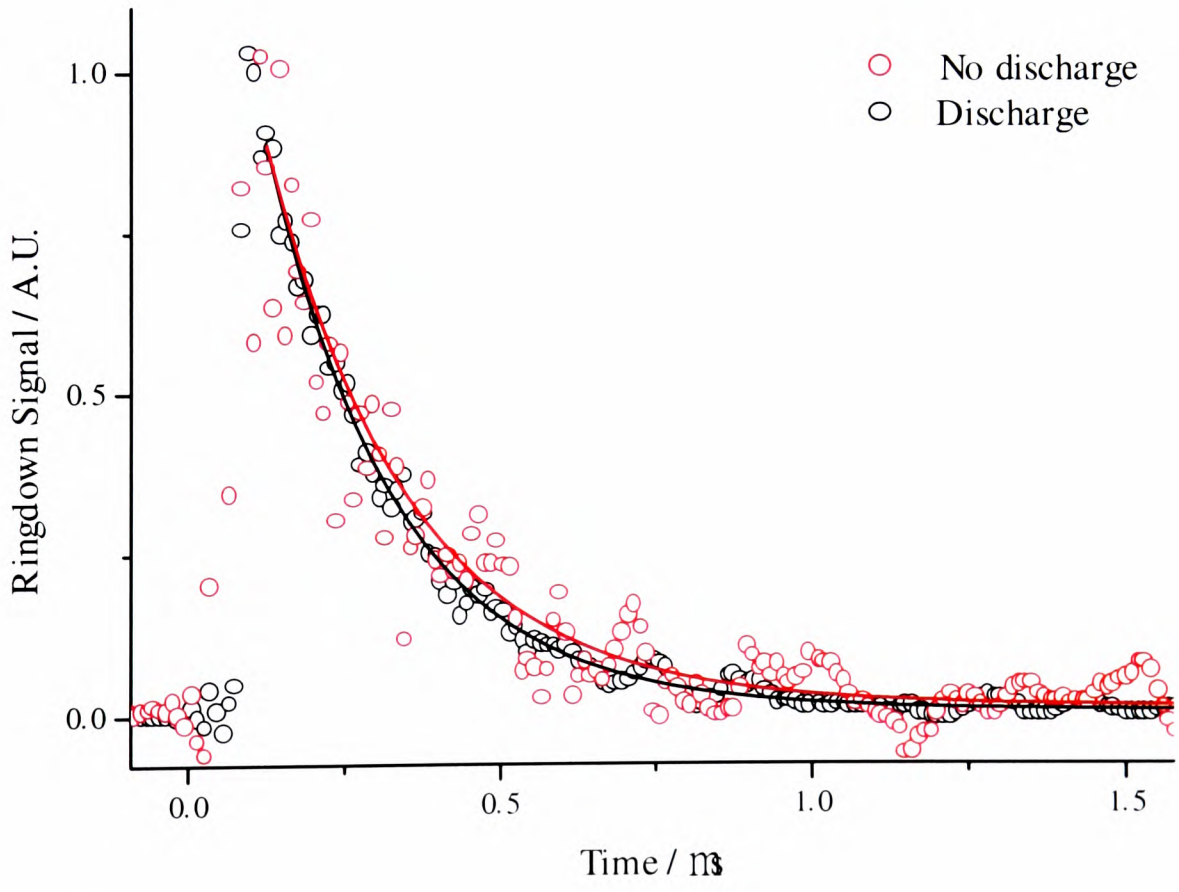

Figure 4.19 Time dependence of the intensity of a laser light pulse at 308.154 nm trapped inside the ring down cavity, with and without the discharge. Both measurements were made at a pressure of 3.5 Torr.

Figure 4.19 also shows a ringdown signal, at 308.154 nm, with the discharge struck at a total pressure of 3.5 Torr. There is a decrease in the ringdown time, τ', when the OH radical is present. From the absorption cross section, given in the table in Section 4.2.1, the concentrations of the OH radical have been calculated from:

$$\frac{N}{V} = \frac{1}{c\sigma}\left(\frac{1}{\tau'} - \frac{1}{\tau}\right) \tag{4.17}$$

(obtained from equation 1.22). The concentration at these pressures and are given in the table below for four different pressures.

Pressure / Torr	τ' / ns	$\Delta\tau$ / ns	N/V / cm^{-3}
1.5	221	8.6	7.8×10^{9}
2.5	217	13	1.2×10^{10}
3.5	205	25	2.4×10^{10}
4.5	201	29	2.8×10^{10}

The observed increase in concentration as the pressure is increased agrees well with the measurements made in Section 4.6.3.1, but the absolute concentration observed is about two orders of magnitude lower than that observed in the flow cell. The concentration observed is averaged over the 25 cm cavity. As the radical is injected into the chamber on an axis perpendicular to the cavity, and at its centre, there is probably a non uniform concentration profile along the cavity. This effect is almost certainly increased due to the flow of dry argon entering the cavity from around both mirrors. If the concentration does vary considerably within the cavity the significantly lower concentration observed in this experiment can be explained in terms of the different geometries of the experiments. The measurements in the flow cell were made along the axis of the gas flow, almost perpendicular to those made in the reaction vessel. This means that the ringdown measurement is similar to a measurement perpendicular to the gas flow in the flow cell.

The sensitivity of this ringdown experiment can be calculated from the expressions given in Section 1.6.4. The minimum detectable fractional absorption per pass, δI_{min}, is 2.7×10^{-5}, or about 1 part in 40000. Alternatively, this can be expressed as a minimum absorption coefficient $\alpha_{min} = 1.06 \times 10^{-6}$ cm^{-1} for the 25 cm long cell, corresponding to a minimum

detectable concentration of OH radicals of 1.48×10^9 cm^{-3}. The sensitivity of this and other measurements is severely limited by the reflectivity of the mirrors as high performance mirror coatings for the ultraviolet region are extremely difficult to produce and are hard to maintain. However, the results obtained in this section compare well with those of other researchers who have studied OH using pulsed CRDS[28].

The LIF spectrum shown in Figure 4.18 has a signal to noise ratio of approximately 100. Therefore, using the concentration of the OH radical determined from the CRDS experiment at a pressure of 3.5 Torr, the minimum detectable OH radical concentration, with a signal to noise ratio greater than or equal to 1, using the LIF experiment is 2.4×10^8 cm^{-3}, within the same time interval as the ringdown experiment. However, unlike the ringdown experiment in which the ultimate sensitivity is an intrinsic property of the cavity, the LIF minimum detectable concentration can be reduced by sampling for more laser shots. It should be noted that the LIF sensitivity is dependent on the collection efficiency, optical filters, PMT and electronics but this direct comparison shows that the sensitivity of the LIF technique can be much greater than the CRDS sensitivity if the experiment is conducted over a sufficiently long time period.

4.10 Detection of the OH Radical by CLIF

To combine the sensitivity of LIF and the advantages of CRDS (absolute concentration measurements and the possibility of observing time varying concentrations) a novel technique was attempted. This technique, Cavity Laser Induced Fluorescence (CLIF), involves observing the LIF produced from excitation of the species of interest by a laser pulse trapped in a high finesse cavity.

The advantage of this technique over LIF is that temporal information about the lower state concentration can be obtained in a single shot, during the ring down time. For instance in the field of reaction dynamics, a common methodology is to produce one of the reactants is produced by photodissociation of a precursor (so defining $t = 0$) and then to monitor the time dependence of the concentration of the product of a subsequent reaction to directly measure the reaction rate. To complete this type of experiment by LIF a set of experiments measuring the integrated fluorescence intensity at variable time delays between the photolysis (initiation) laser pulse and the LIF laser are required. By using CLIF this experiment can be reduced to a single shot experiment. Simulated time traces for such an experiment, generated using the

expressions discussed later in this section, have shown that kinetic information can be extracted from the data[29].

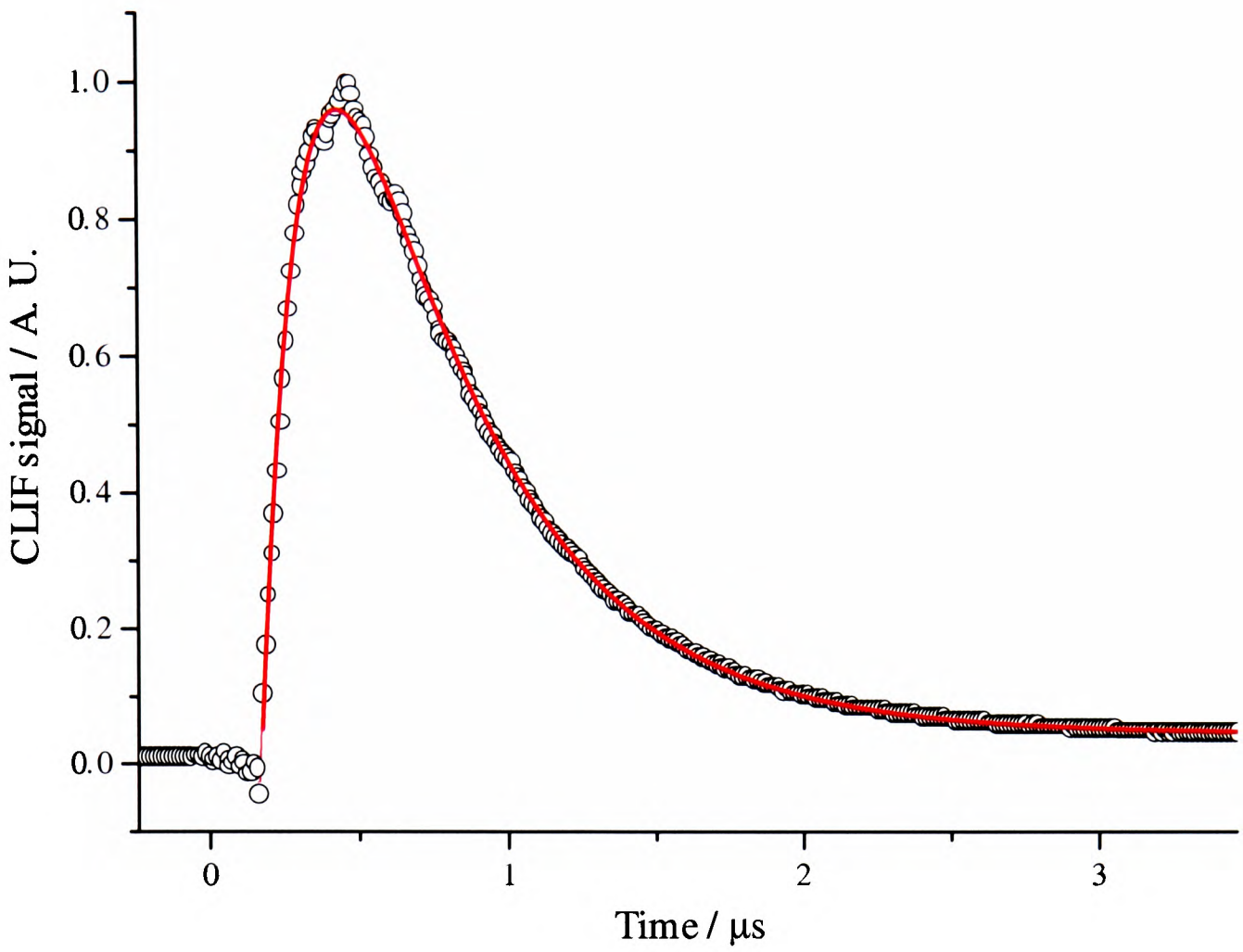

Figure 4.20 CLIF time dependence of the $Q_{11}(3)$ transition from the OH radical, produced in a wet noble gas microwave discharge at a pressure of 3.5 Torr.

Figure 4.20 shows the CLIF time trace observed, at a total pressure of 3.5 Torr, again pumping on the $Q_{11}(3)$ transition. The integrated CLIF signal was found to be about six times larger than the integrated single pass LIF signal (Figure 4.16), which is initially unexpected because the laser intensity rejected by the input mirror should be exactly compensated for by the increased interaction time between the OH radical and the radiation trapped within the cavity (this would always be the case if non-coherent radiation is used). Therefore, the time integrated photon flux that the OH radical experiences would be expected to be the same in the single pass and cavity experiments. However, this unexpected enhancement can be explained qualitatively by an interference effect. Since the pulse duration was about 15 ns, and a cavity round trip time was 1.7 ns, the laser radiation at the beginning of the pulse has circulated within the cavity several times before the pulse ends. Some of the laser radiation will be resonant with the cavity, (the laser bandwidth is about 30 times greater than the cavity FSR) and therefore the light intensity at particular wavelengths will be enhanced within the cavity,

relative to that expected from the input mirror reflectivity, leading to an increase in the observed fluorescence.

In order to interpret the time traces obtained by CLIF, it is necessary to consider how the concentration of the excited OH radical varies with time within the cavity. The excited level is produced by absorption of a proportion of the laser intensity within the cavity which can be described by the cavity ring down decay equation 1.22. The excitation rate, I_{abs}, is therefore proportional to $I_0 e^{-(1/\tau+\alpha c)t}$. The excited level is removed by fluorescence and collisional quenching, which can jointly be described by a unimolecular decay rate constant $k = 1/\tau_{fl}$ corresponding to the lifetime observed by the LIF experiments in Section 4.8. Therefore, the upper level concentration [OH*] obeys the differential equation

$$\frac{d[\mathrm{OH}^*]}{dt} = I_{abs} - k[\mathrm{OH}^*] \tag{4.18}$$

the solution of which is

$$[\mathrm{OH}^*] \propto \frac{I_0}{\frac{1}{\tau_{fl}} - \frac{1}{\tau} - \alpha c}\left(e^{-\left(\frac{1}{\tau}+\alpha c\right)t} - e^{-\frac{t}{\tau_{fl}}} \right) \tag{4.19}$$

which is of a bi-exponential form, where the first term describes the ringdown and the second the fluorescence decay rate. The time traces obtained by CLIF were fitted to a general bi-exponential function, to obtain the two time constants τ_{fl} and τ', but the quality of these fits was poor. By inclusion of a second amplitude term, R, see equation (4.20), the fitting was much more satisfactory and an example of a fit is shown in Figure 4.20.

$$[\mathrm{OH}^*]_{CLIF} = a\left(e^{-t/\tau'} - R e^{-t/\tau_{fl}}\right) \tag{4.20}$$

The table below gives the time constants that fitting to this function produced. Also included in the table are the time constants obtained at each pressure by fixing either τ_{fl} to the lifetime observed at that pressure from Section 4.8 and finding τ'_{fix}, or fixing τ' to the ringdown time (RDT) observed at that pressure in Section 4.9 and finding $\tau_{fl(fix)}$.

Pressure / Torr	LIF τ_{fl}	CLIF τ_{fl}	CLIF $\tau_{fl(fix)}$	CRDS τ'	CLIF τ'	CLIF τ'_{fix}
1.5	671 ns	613 ns	612 ns	221 ns	239 ns	220 ns
2.5	592 ns	550 ns	538 ns	217 ns	213 ns	197 ns
3.5	530 ns	448 ns	388 ns	205 ns	183 ns	158 ns
4.5	489 ns	389 ns	343 ns	201 ns	176 ns	144 ns

From the table, it is clear that there is some correlation between the time constants obtained by CLIF and those obtained by LIF and CRDS. This correlation appears to be better at low pressures when the two time constants are different. The retrieval of two similar rate constants of competing processes from a bi-exponential rate law from the fits to a given dataset has previously been reported to be exceedingly difficult[30].

The value of R ranged from about 0.4 to 0.6, whereas from equation (4.19) it would be expected to be unity. This discrepancy has proved problematic to explain. For example, saturation of the transition was considered as a possible cause for the anomaly; if the laser intensity was sufficient to reduce the fluorescence until a Boltzmann population could be re-established, it would invalidate the assumptions used to derive equation (4.19). However, the form of the CLIF time traces showed negligible variation with large changes in laser intensity, implying that saturation of the transition was not causing this discrepancy. Another and probably more significant possibility is that because the laser bandwidth is greater than the rotational linewidth, the CLIF signal is produced from a varying effective cross section across the peak. The cross section was assumed to be fixed (*i.e.* the laser bandwidth is much narrower than the linewidth) for the derivation of equation (4.19) which is clearly a poor assumption. Also, as discussed above, inherent shortcomings of the fitting procedure may also be responsible. A combination of all these possibilities may have contributed to the unexpected time dependence of the CLIF signal.

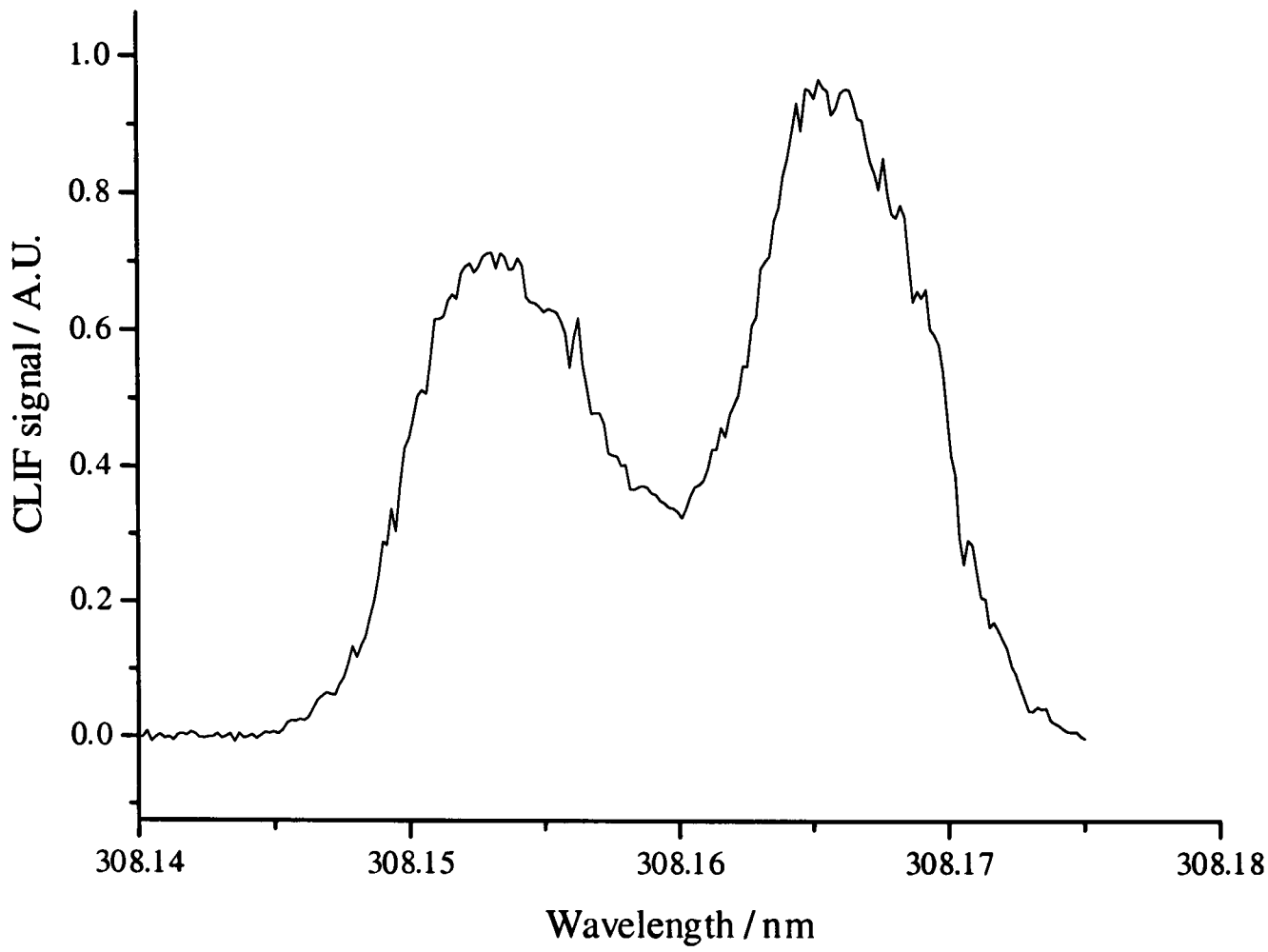

Figure 4.21 CLIF spectrum of the OH radical, produced in a wet noble gas discharge, near 308.16 nm, showing the $P_{11}(1)$, $Q_{11}(3)$ and $P_{21}(3)$ features, at a pressure of 4 Torr.

Figure 4.21 shows a spectral scan obtained by integrating the CLIF signals at each wavelength point, equivalent to that obtained by LIF (Figure 4.18). The CLIF profiles are observed to be broader than the LIF profiles. This can be explained as follows. At the peak of the profile, τ' is at a minimum and therefore the photon flux is reduced in comparison to the wings of the profile. The CLIF signal is proportional to [OH*], which in turn is proportional to the product of the frequency dependent cross section and the photon flux. Thus, the CLIF signal is greatly reduced at the peaks relative to the wings of the profile, causing an effective broadening of the profile compared to the single pass LIF profile.

4.11 Conclusions

The work in this Chapter has shown that a simple compact laser source at 308 nm can be produced from a cooled commercial diode laser. This has been used to detect the OH radical by absorption. However, for most applications (for instance atmospheric detection, combustion monitoring or reaction dynamics) absorption is insufficiently sensitive without an exceptionally long path length. For example, the first absorption measurements, of the hydroxyl radical, using absorption in the atmosphere, were completed in 1987 using a 3.2 km path length[31]. This technique suffers from problems associated with external perturbation

beyond experimental control. This can be overcome by using a White cell to achieve a long path with a relatively short distance (≈ 40 m) between the mirrors. Fundamentally, the absorption measurements are advantageous over other methods as the species is identified directly and no calibration is required. The long path length can be achieved by CRDS in a much more compact system than the White cell, but to detect atmospheric concentrations (10^6 cm^{-3})[1] of OH the CRDS technique is not viable with the mirrors that are presently available.

CLIF, on the other hand, combines the advantages of both LIF and CRDS and if used with a narrow bandwidth laser source (such as the doubled diode laser source discussed in the first half of this Chapter), absolute concentrations from a fluorescence signal could be obtained. The mirrors for the cavity should be chosen such that the ring down time is significantly different to the lifetime of the upper level so the time constants can be easily separated by the fitting procedure. Only one of the mirrors would have to be transmitting because the fluorescence signal is collected perpendicular to the laser propagation direction and therefore there is no requirement for the back mirror to transmit radiation. A metallic mirror could therefore be used, significantly increasing the finesse of the cavity.

The laser source required for CLIF would have to be more powerful than the single pass SHG cooled laser source discussed in this Chapter. A significant increase in power could be achieved by using a resonant cavity (see Section 5.4). This could enable a CLIF experiment to be completed. Unlike the 10 Hz pulsed lasers used for the CLIF experiments in this Chapter, the diode could be modulated using an acousto-optic modulator at frequencies comparable to the inverse of the lifetime of the CLIF decay. This high repetition rate could be used to greatly improve the duty cycle of a CLIF experiment, increasing the signal to noise ratio of the CLIF signal obtained in a fixed time.

Another advantage of CRDS over LIF occurs when the concentration of the species of interest varies with time on the timescale of the CRDS measurement (for instance concentration variations in a reaction); such variations could be observed in a single shot. The time variation of a concentration can be observed using LIF, but it requires a many laser shot experiment with an LIF signal recorded at each time point. Whilst CRDS allows temporal information about the concentrations of the species observed to be obtained, it is not as sensitive as LIF. By combining the two in CLIF, it may be possible to obtain the sensitivity of LIF with the advantage of CRDS in that the absolute and time varying concentrations are directly obtained, in contrast to LIF where a calibration is required.

4.12 References

[1]R. P. Wayne, *Chemistry of Atmospheres*, OUP, (1991)
[2]M. J. Pilling (Ed.), *Low Temperature Combustion and Autoignition, Comprehensive Chemical Kinetics 35*, Elsevier, (1997)
[3]S. A. Chapman, *Mem. Roy. Meteorol. Soc.*, **3**, 103, (1930)
[4]A. J. Alexander, M. Brouard, K. S. Kalogerakis and J. P. Simons, *Chem. Soc. Rev.*, **27**, 405, (1998)
[5]J. M. Hollas, *Modern Spectroscopy*, Wiley, (1987)
[6]K. P. Huber and G. Hertzberg *Molecular Spectra and Molecular Structure IV. Constants of Diatomic Molecules*, Van Nostrand Reinhold Company, (1979)
[7]G. H. Dieke and H. M. Crosswhite, *J. Quant. Spectrosc. Radiat. Transfer*, **2**, 97, (1962)
[8]H. P. Dorn, R. Neuroth and A. Hofzumahaus, *J. Geophys. Res.*, **100**, 7397, (1995)
[9]W. Tsang and J. T. Herron, *J. Phys. Chem. Ref. Data*, **20**, 609, (1991)
[10]P. A. Franken, A. E. Hill, C. W. Peters and G. Weinreich, *Phys. Rev. Lett.*, **7**, 118, (1961)
[11]R. W. Boyd, *Nonlinear Optics*, Academic Press, (1992)
[12]A. Yariv, *Quantum Electronics*, Wiley, (1989)
[13]W. Demtröder, *Laser Specroscopy*, Springer-Verlag, (1981)
[14]G. D. Boyd and D. A. Kleinman, *J. Appl. Phys.*, **39**, 8, (1968)
[15]V. G. Dmitriev, G. G. Gurzadyan and D. N. Nikogosyan, *Handbook of Nonlinear Optical Crystals*, Spinger-Verlag, (1991)
[16]S. Nakamura, *Thin Solid Films*, **344**, 345, (1999)
[17]Hitachi Optodevice Data Book, (1993)
[18]H. R. Barry, B. Bakowski, L. Corner, T. Freegarde, O. T. W. Hawkins, G. Hancock, R. M. J. Jacobs, R. Peverall and G. A. D. Ritchie, *Chem. Phys. Lett.*, **319**, 125, (2000)
[19]T. Feliksinski and J. Szewczyk, *Mat. Res. Bull.*, **16**, 1505 (1981)
[20]H. Talvitie, A. Seppänen, A. Äijälä and E. Ikonen, *Appl. Phys. B*, **66**, 397, (1998)
[21]E. E. Whiting, *J. Quant. Spectrosc. Radiat. Transfer*, **8**, 1379, (1968)
[22]W. B. DeMore, S. P. Sander, D. M. Golden, R. F. Hampson, M. J. Kurylo, C. J. Howard, A. R. Ravishankara, C. E. Kolb and M. J. Molina, *Chemical Kinetics and Photochemical Data for Use in Stratospheric Modelling*, Evaluation Number 12, JPL97-4, (1997)
[23]FACSIMILE™, process and chemical modeller, version 3.0.30, *AEA Technology plc.*, (1998)
[24]P. W. Atkins, *Physical Chemistry*, OUP, (1978)
[25]B. A. Thrush and J. P. T. Wilkinson, *Chem. Phys. Lett.*, **84**, 17, (1981)
[26]M. L. Costen, G. Hancock and G. A. D. Ritchie, *J. Phys. Chem.*, **103**, 10644, (1999)
[27]M. L. Costen, *D. Phil. Thesis*, Oxford University, (1997)
[28]G. Meijer, M. G. H. Boogaarts, R. T. Jongma, D. H. Parker, A. M. Wodtke, *Chem. Phys. Lett.*, **217**, 112, (1994)
[29]T. P. Arnold, *Part II Thesis*, Oxford University, (2000)
[30]C. Morrell, *D. Phil. Thesis*, Oxford University, (2000)
[31]D. Perner, U. Platt, M. Trainer, G. Hubler, J. W. Drummond, W. Junkermann, J. Rudolph, B. Schubert, A. Volz, D. H. Ehhalt, K. J. Rumpel and G. Helas, *J. Atmos. Chem.*, **5**, 185, (1987)

Chapter 5

Detection of the N_2^+ Ion

5.1 Introduction

Interest in studying the nitrogen molecular ion, N_2^+, has stemmed from unexplained results obtained in a previous Doppler resolved LIF study[1,2]. These experiments involved using pulsed laser Doppler resolved LIF to measure the ions' velocity components parallel and perpendicular to the sheath of the electrode in the capacitively coupled discharge system described in Chapter 2. A pulsed laser (detailed in Section 5.3.1.1), was frequency doubled to produce between 100 and 200 μJ of 330 nm radiation, in about 10 ns pulses at 20 Hz, enabling observation of the N_2^+ ion using the B $^2\Sigma_u^+ \leftarrow$ X $^2\Sigma_g^+$ detection scheme described in Section 5.2.3. The fluorescence was collected using a photomultiplier tube, from a region about 2 mm high, through a narrow-band filter centred at 458.8 ± 0.1 nm and imaging optics. The observed fluorescence signal was also temporally gated to a time period of between 100 and 200 ns about 50 ns after the laser pulse, by using a transient digitiser.

The absolute N_2^+ ion concentration was obtained by a kinetic analysis of the decay in the LIF signal in the plasma bulk after the discharge was extingished[1]. This was then used to calibrate the LIF signal obtained at various heights above the driven electrode, to obtain the concentration profile of the N_2^+ ions. The velocity distributions of the ions parallel and perpendicular to the driven electrode were then obtained. At all heights above the driven electrode the observed N_2^+ ion Doppler profiles parallel to the plane of the electrode were consistent with a thermal translational distribution at 355 K, the temperature characterising the separately measured rotational distribution. Perpendicular to the driven electrode, the acceleration of ions towards the driven electrode was clearly observed from the width of the Doppler profiles. Figure 5.1 (taken from Woodcock *et al.*[2]) shows the observed Doppler profiles. As the ions get closer to the driven electrode, both the maximum and the average ion velocity increase. However, approximately half of the ions are observed to be present in an unaccelerated distribution around zero velocity – this effect is independent of height above the electrode. Also shown in the figure are the predicted Doppler profiles obtained by Monte Carlo simulations of the behaviour of ions injected into the sheath[2] (integrated over sets of ions

matching the experimental spatial and spectral resolution). These simulations were produced by introducing ions, with random thermal velocities, into the sheath at random phases of the r.f. cycle, and calculating their progress through the sheath at 1 ns intervals[2]. The forces acting upon the ions were calculated using the analysis of Song *et al.*[3] to evaluate the time varying sheath electric field. This analysis assumes steady-state solutions at each (time-varying) sheath voltage and a collisionless form of the Child-Langmuir potential.

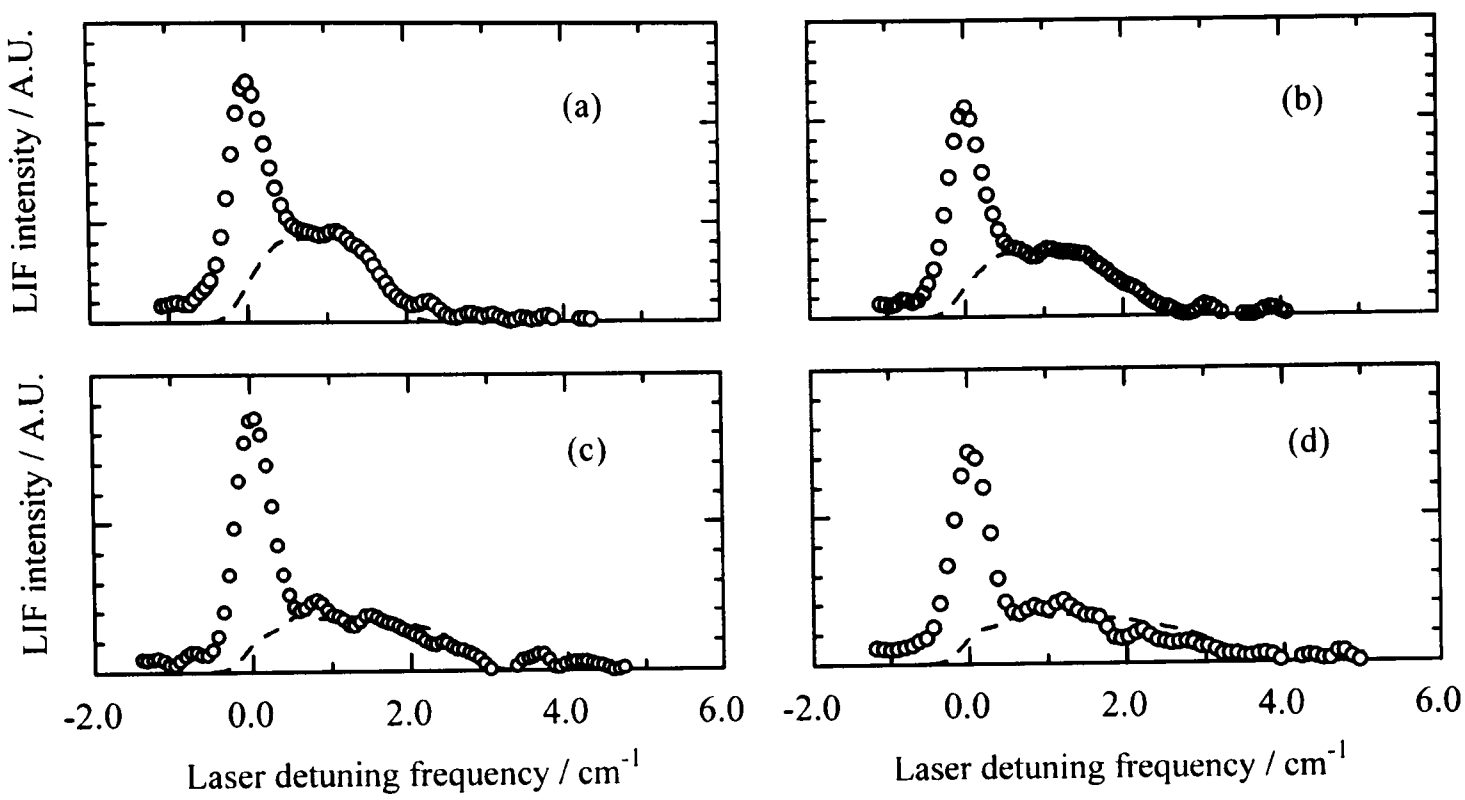

Figure 5.1 Comparison of the experimental (circles) and simulated (dashed lines) vertical Doppler profiles at four heights above the driven electrode of the CCP system described in Chapter 2 (from Woodcock[1]). The positions are (a) 9 mm, (b) 8 mm, (c) 6 mm and (d) 4 mm above the driven electrode.

From the figure, it is clear that the simulated Doppler profiles agree well with the observed profiles of the accelerated ions. However, the simulation does not predict the peak of unaccelerated ions. Many possibilities for this discrepancy have been considered; a summary is given below. These low velocity ions would not have been detected using an electrostatic probe because it has a vanishingly low detectivity for zero velocity species since it measures flux. However, the detectivity of most laser methods, including the LIF method used to produce Figure 5.1, are essentially independent of velocity.

The model included the possibility of ion formation by charge exchange. For kinetic energies below 20 eV, values for the energy dependent symmetric charge exchange and elastic scattering cross sections were extrapolated from experimentally measured values at higher kinetic energies. It was found that if the energy dependent cross sections at zero kinetic energy were increased by a factor of 200, a considerably better fit to the data, taken at 9 mm above the driven electrode, was achieved. However, it was found that the size of the simulated zero

velocity peak dropped sharply as a function of height in contrast to the almost constant behaviour observed experimentally. As a final test, the simulation was repeated with the cross sections increased by a factor of three from the previously measured values across the entire energy range. This resulted in little change in the comparative size of the zero velocity ion peak to the rest of the distribution. In the event that the slow ions are produced by symmetric charge exchange, the flux of fast neutral nitrogen molecules will be considerable and will need to be considered for a full understanding of materials processing in nitrogen plasmas (see Section 1.2 for a brief summary of the uses of nitrogen plasmas).

The assumptions used in the model to generate the electric field, including the use of a collisionless potential and a mono-energetic ion density at each point, were also considered as a possible reason for the discrepancy between the modelled and experimentally measured ion velocity distributions. However, it has been previously observed that the exact form of the potential does not significantly alter the shape of any simulated ion energy distribution[4]. Another possible flaw in the model is the assumption that the ions entering the sheath had a translational distribution that is described by a ambient temperature Boltzmann distribution. Other sheath models have used the Bohm velocity as the initial velocity (see Section 2.4.2), but as the profiles simulated are deep inside the sheath this effect is expected to be negligible[1]. In addition, since the agreement between theory and experiment for the high velocity component of the ion velocity distribution was so good, it was concluded that the physics used to model the sheath was not likely to cause the simulation to fail when describing the unaccelerated ion peak.

The next consideration, was whether the slow ions were produced as an artefact of the experimental technique. The technique uses very intense laser radiation (> 100 MWm^{-2}) and therefore, the possibility that the ions were produced by a photoionisation mechanism was considered. The many photon induced processes that could result in the ionisation of N_2 molecules (whose concentration in the sheath is about seven orders of magnitude greater than the N_2^+ ion) makes photoionisation hard to disregard. However, all such processes would require more than one 330 nm photon, *i.e.* a multi-photon process, and the experiments completed show that the size of all parts of the ion velocity distribution increase linearly with laser intensity[1], strongly suggesting that multi-photon processes can be ruled out.

A second possible experimental explanation for the observation of the slow ion peak is perhaps that, since the laser radiation passes through the bulk of the plasma before it reaches the sheath, the detection system is collecting LIF from the plasma bulk. It must also be noted that the

cylindrical glass surround of the plasma chamber will image such fluorescence back onto the same axis. Experimental tests of the imaging selectivity appear to eliminate such a mechanism[2].

The relative N_2^+ ion concentration profiles (including the slow ions) within the sheath, obtained by LIF with the laser propagating parallel and perpendicular to the electrode, appeared identical within experimental error when normalised to the value obtained in the bulk by both geometries. This profile comparison, along with the observation that the ion flux was found to remain constant with height when calculated from the profiles, is strong evidence that the slow ions do exist in the sheath.

The most plausible explanation for the zero velocity ion peak is that the slow ions are produced by impact ionisation of slow nitrogen molecules by secondary electrons produced at the electrode. These are generated by species impacting onto the electrode[5]; the perturbation of plasma processes by effects related to the electrode has been previously discussed[6,7]. Gerassimou *et al.*[6] also considered and dismissed several other effects that might reduce the lifetime of excited N_2^+ ions near the electrode surface, some of which may create a population of slow ions.

For the duration of this project, a considerable amount of time and effort has been expended in developing and testing experimental systems in an attempt to determine whether this previously observed strong zero velocity peak in the ion velocity distribution is an artefact of the experiment or a real observation. Two novel experimental methods have been proposed; these are briefly discussed in the following two sections. The preliminary experiments required to determine whether these two experimental methods could be successful are then described in the remainder of this Chapter. This involved investigating two methods of detection of the N_2^+ ion, firstly *via* the A $^2\Pi_u \leftarrow$ X $^2\Sigma_g^+$ transition by LIF and CRDS (see Section 1.6) with the ultimate aim of using CLIF (see Section 4.10) and secondly *via* the B $^2\Sigma_u^+ \leftarrow$ X $^2\Sigma_g^+$ transition by absorption using a continuous wave frequency doubled diode laser as the radiation source.

The ICP system discussed in Chapter 2 was designed to accommodate both of the experiments described below. In both cases, the region in the sheath being investigated can be changed by vertical translation of the lower electrode alone. In the previous experiments, the whole CCP system had to be translated vertically. Also, because the electrode can be biased independently

of the r.f. power applied to the inductor matching network, the velocity distributions can be obtained at different potentials with respect to the plasma.

5.1.1 Plasma Time of Flight Experiment by LIF

As discussed in Chapter 1, there is a net flux of ions moving through the sheath towards the electrode. Therefore, by exciting them with a laser propagating through the sheath at a distance d from the electrode and then observing fluorescence emitted by them at a distance d' (where $d' < d$), information about their velocity is obtained directly, see Figure 5.2. A time of flight experiment within that region is therefore proposed. Initially, this will be attempted with a laser producing pulses of about 10 ns duration. The ions in the excitation region can be assumed to be excited instantaneously at t_0, (the time the laser pulse passes through the plasma) and therefore the time dependence of the fluorescence emitted at the point of observation, relative to t_0, is the distribution of times taken by the ions to move between the excitation and observation point, a distance $d - d'$. If $d - d'$ is small, the change in velocity on moving from d to d' due to the electric field can be neglected, the velocity distribution at d can be directly obtained. If this is repeated throughout the sheath, by moving the lower electrode relative to the excitation and observation region therefore keeping $d - d'$ constant, the variation of the higher energy part of the ion velocity distribution moving towards the electrode is obtained. The complete distribution will not be observed as only ions that are still in the excited electronic state when they reach the observation region will be observed. This results in this method having the highest detection sensitivity for the highest velocity species and a vanishingly small detectivity for zero velocity species, similar to probe measurements.

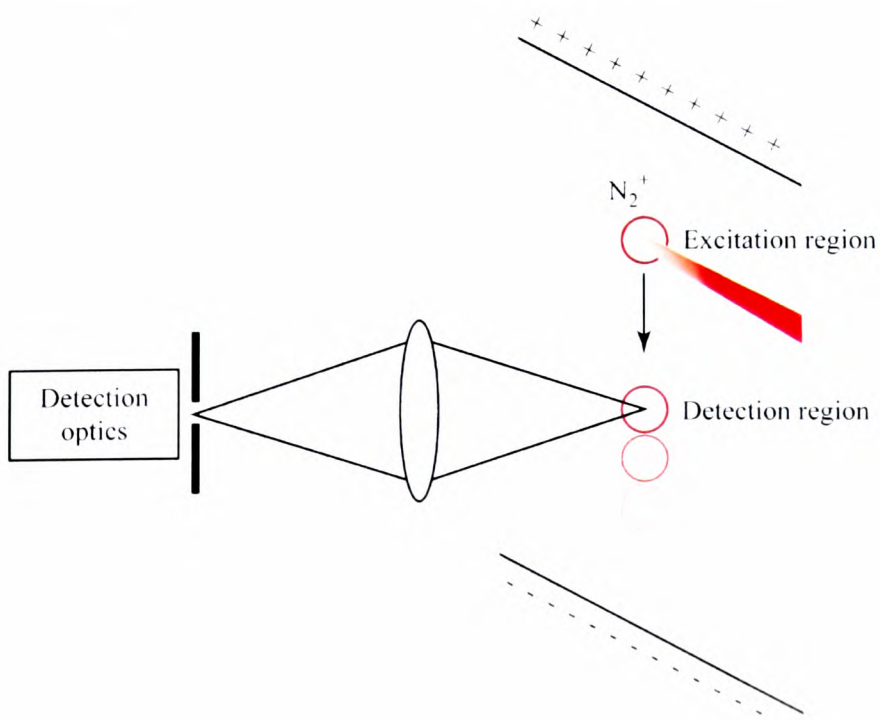

Figure 5.2 A schematic of the proposed time of flight experiment in the sheath of the plasma.

The fluorescence lifetime of the upper state must be sufficiently large so that a significant proportion of the ions passing through the observation region are still in the excited state. However, if the fluorescence lifetime of the upper state is too large, the amount of fluorescence produced will be too weak to observe (the probability that an excited state will fluoresce in the direction of the detector while in the observation region is too small). The $A\ ^2\Pi_u \leftarrow X\ ^2\Sigma_g^+$ transition in N_2^+ was chosen because the frequency of radiation required to excite it is easily produced by both pulsed and continuous wave lasers and the $A\ ^2\Pi_u$ state radiative lifetime of around 10 μs[8], which is considerably larger than that of the $B\ ^2\Sigma_u^+$ state (≈ 60 ns)[8], is sufficiently large to allow the ions to travel a measurable distance before the fluorescence becomes undetectable.

The method could eventually use a modulated continuous wave laser and phase sensitive detection (similar to the MMS discussed in Chapter 3), to obtain the velocity distribution of the ions from the observed fluorescence signal.

5.1.2 Two Dimensional Velocity Mapping by LIF

In the previous studies, the vertical and horizontal components of the ion velocity distribution were obtained independently. This does not give sufficient information to resolve the full three-dimensional velocity distribution, which is cylindrically symmetric about the field axis. To enable the full three-dimensional velocity distribution to be obtained, the following experiment is proposed.

A laser with a sub-Doppler bandwidth, propagating parallel to the electrode could be used to excite a specific component of the N_2^+ ion velocity distribution in the horizontal direction. The fluorescence produced by these ions, into a small solid angle, spectrally resolved by a tunable filter may then be observed parallel to the field (chosen to allow good resolution of the velocity components perpendicular to the electrode). This arrangement is advantageous in comparison to the previously used geometry because the laser radiation used to excite the ions does not propagate through the bulk of the plasma and therefore if the previously observed zero velocity peak is produced by LIF from the bulk it will not be observed. A schematic of this proposed experiment is given in Figure 5.3.

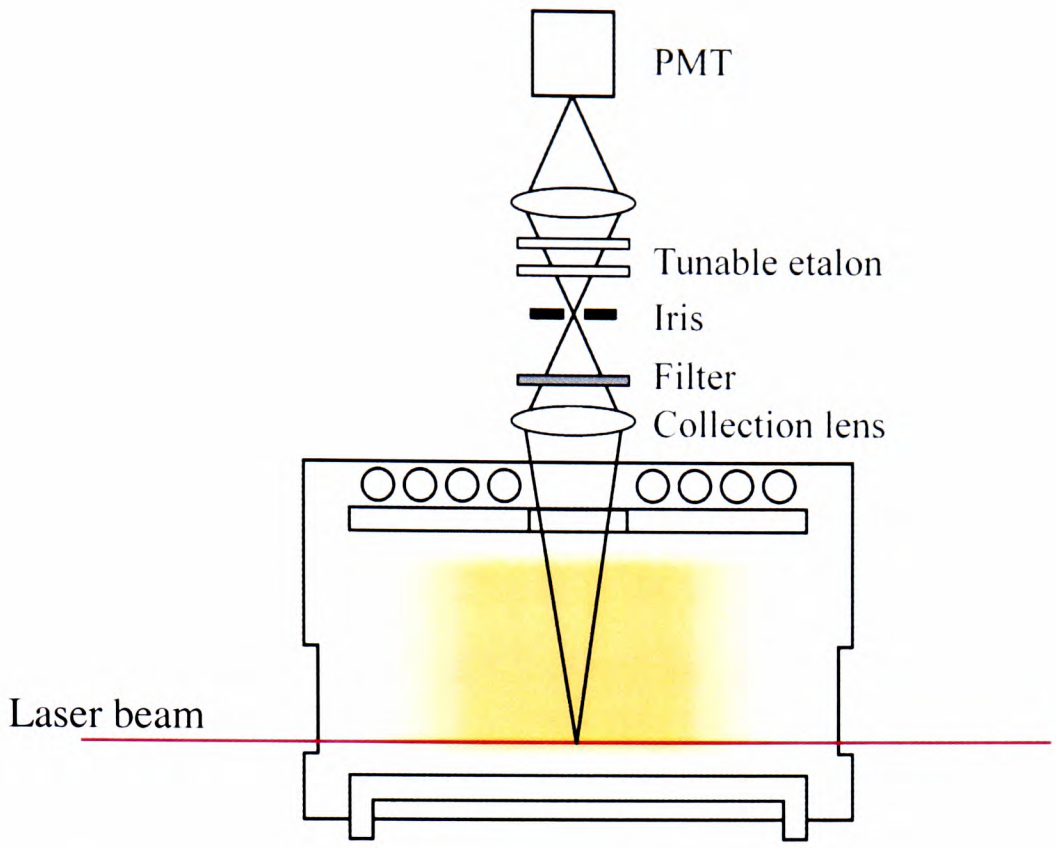

Figure 5.3 A schematic of the proposed two dimensional velocity mapping experiment.

For this experiment, the use of a continuous wave laser source has two main advantages over the pulsed source that was previously used. Firstly, continuous laser bandwidths are generally several orders of magnitude lower than those of pulsed lasers, and secondly the duty cycle of the experiment is increased by at least four orders of magnitude. This vastly increased duty cycle is generally at the expense of intensity, but calculations show that in the previous measurements the transitions interrogated were saturated[1] (*i.e.* by the end of the pulse almost half the ions in the probe region were promoted to the excited state) and therefore the laser intensity was not being efficiently used.

In this Chapter, a frequency doubled diode laser is investigated as a possible excitation source. As discussed in Section 1.8.5, the bandwidth of diode lasers is typically below 100 MHz[9]. The FWHM of a Doppler broadened single rotational transition in the B $^2\Sigma_u^+ \leftarrow$ X $^2\Sigma_g^+$ system is approximately 2.5 GHz and therefore the diode laser system should certainly have a sufficiently narrow spectral bandwidth to enable excellent resolution of the velocity distribution parallel to the electrode.

The detection filter proposed consists of a confocal (see Appendix 1) Fabry-Perot etalon[10] whose transmission curve could be shifted by moving one of the mirrors (for instance by the use of a piezo-electric transducer). The spectral resolution of such a filter can be calculated from the reflectivities of the mirrors and the cavity length. For instance, for mirrors with a reflectivity of 90 %, the cavity finesse (see Section 1.7) would be 30. If the cavity was constructed with a length of 25 mm, its free spectral range would be 3 GHz and the FWHM of

the transmission curve of the cavity would be 100 MHz, resulting in the same velocity resolution in the vertical direction as that in the horizontal plane. Ultimately, by step scanning the laser across the absorption profile in the horizontal direction and observing the spectrally resolved fluorescence, at each step of the laser by scanning the etalon, the full velocity distribution can be obtained.

5.2 Spectroscopy of the N_2^+ Ion

Figure 5.4 shows the five lowest potential energy curves of the nitrogen molecular ion[11], N_2^+. The approximations described in Section 4.2 allow the electronic configuration of the ground electronic state X of the N_2^+ ion to be given by $(1s\sigma_g)^2(1s\sigma_u^*)^2(2s\sigma_g)^2\ (2s\sigma_u^*)^2(2p\pi_u)^4(2p\sigma_g)^1$. In this Chapter, transitions between the ground state and the first and second excited states of the same multiplicity are considered. The first excited state, A, has a configuration $(1s\sigma_g)^2(1s\sigma_u^*)^2(2s\sigma_g)^2(2s\sigma_u^*)^2(2p\pi_u)^3(2p\sigma_g)^2$, arising from the promotion of an electron from one of the $2p\pi_u$ orbitals to the $2p\sigma_g$ orbital. The second excited state, B, has a configuration $(1s\sigma_g)^2(1s\sigma_u^*)^2(2s\sigma_g)^2(2s\sigma_u^*)^1(2p\pi_u)^4(2p\sigma_g)^2$, arising from the promotion of an electron from the $2s\sigma_u^*$ orbital to the $2p\sigma_g$ orbital.

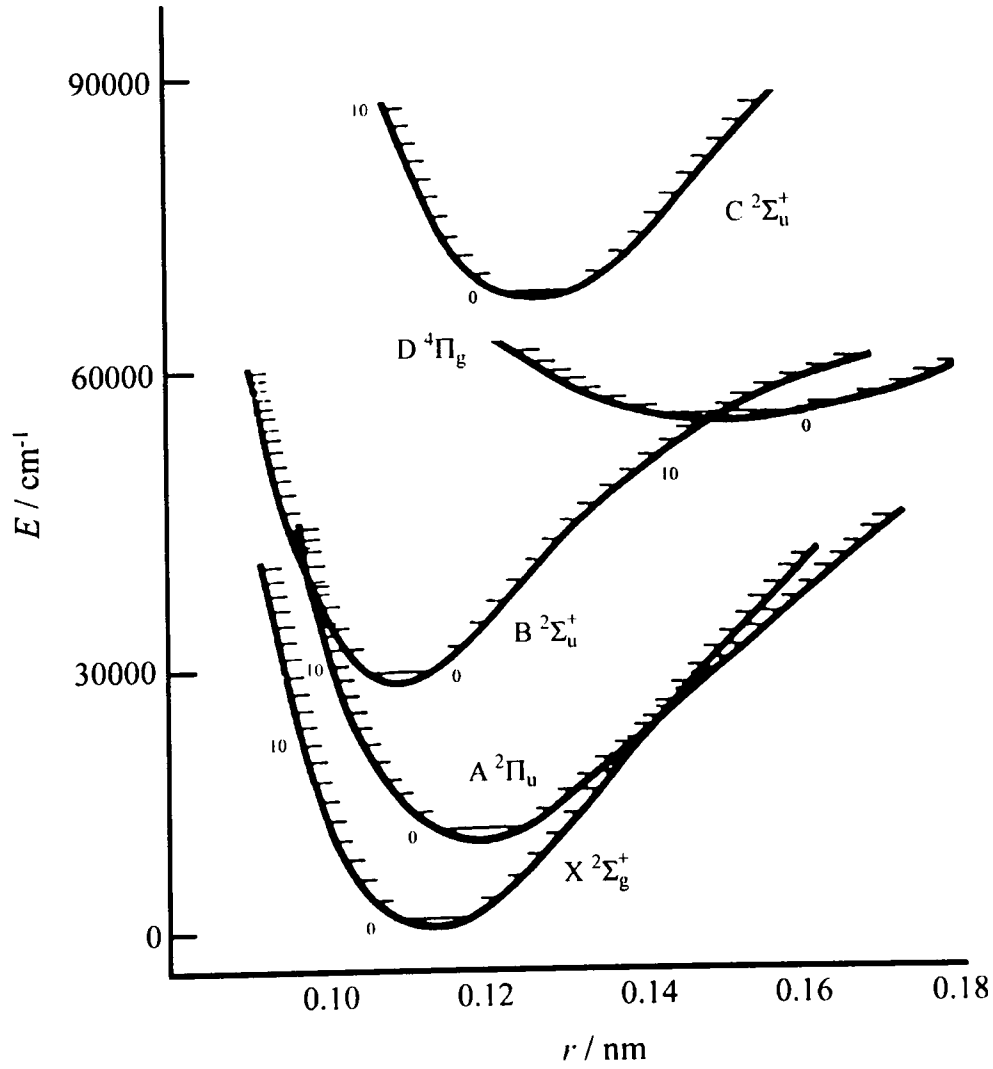

Figure 5.4 Potential energy curves for the five lowest electronic states of the nitrogen molecular ion N_2^+ (from Bensech *et al.*[11]).

As in the case of the OH radical, several angular momentum vectors and corresponding quantum numbers are required to describe the state of the N_2^+ ion. As stated previously, the most widely used coupling approximation for diatomic molecules is analogous to the Russell-Saunders coupling scheme for atoms[12]. The vectors and quantum numbers pertinent to this scheme are discussed in Appendix 2.

Again a further quantum number is required to identify the vibrational levels of the electronic states. v is this vibrational quantum number of the ion, giving the vibrational energy level (for a simple harmonic oscillator, $E_{vibSHO} = h\nu(v + {}^1/_2)$). v can take the values of 0, 1, 2, ...

The term symbol for the ground state of the N_2^+ ion, X, is $^2\Sigma_g^+$ and the coupling is best described by Hund's case (b), because $\Lambda = 0$. Analogously to the A state of the OH radical, this state exhibits ρ-doubling (see Appendix 2). The first excited state of the same multiplicity as the ground state, A, of the N_2^+ ion can again be described by Hund's case (b). The values of the electronic quantum numbers describing this state are $\Lambda = 1$, $S = {}^1/_2$. Each K level is split into two spin orbit levels, F_1 and F_2. This state is an inverted multiplet, that is the F_2 ($J = K - {}^1/_2$) level is lower in energy than the corresponding F_1 ($J = K + {}^1/_2$) level, with $A \approx -74.6$ cm^{-1} [8]. Each of the J levels exhibit Λ-doubling. The term symbol for the second excited state of the same multiplicity as the ground state of the N_2^+ ion, B, is $^2\Sigma_u^+$ and the coupling is again best described by Hund's case (b), because $\Lambda = 0$. The values of the electronic quantum numbers describing this state are $\Lambda = 0$, $\Sigma = {}^1/_2$. This state like the ground state, exhibits ρ-doubling (see Appendix 2).

The electronic selection rules, $\Delta\Lambda = 0, \pm1$, $\Delta S = 0$, $(+ \leftrightarrow +)$ or $(- \leftrightarrow -)$ and $(u \leftrightarrow g)$[12], are all obeyed for both the A $^2\Pi_u \leftarrow$ X $^2\Sigma_g^+$ and the B $^2\Sigma_u^+ \leftarrow$ X $^2\Sigma_g^+$ electronic transitions. The single photon rotational selection rules for the main branch lines of both these system of the N_2^+ ion are ΔJ and ΔK is ±1.

5.2.1 The A $^2\Pi_u \leftarrow$ X $^2\Sigma_g^+$ Detection Scheme

This energy level scheme is the inverse of the $A^2\Sigma^+ \leftarrow$ X $^2\Pi$ OH radical system, and again the rotational selection rules produce twelve possible rotational branches, six from the selection rules given above and a further six weaker sub branches (corresponding to ΔJ is ±1 and ΔK is ±2, or ΔJ is 0 and ΔK is ±1, or ΔJ is ±1 and ΔK is 0). These are labelled differently to the transitions of the $A^2\Sigma^+ \leftarrow$ X $^2\Pi$ OH radical system. By convention they are labelled $^{\Delta K}\Delta J_{F'F''}$ where ΔK and ΔJ are labelled O, P, Q, R or S when they take the values –2, –1, 0, +1 or +2 respectively. If $\Delta K = \Delta J$ then the ΔK superscript is neglected from the label. The first

subscript is used to identify whether the upper state energy level is in the F_1 or F_2 spin orbit manifolds and the second subscript indicates to which of the two spin rotation levels the lower level of the transition belongs. If $F' = F''$ then one of the subscripts is neglected.

To select the optimum LIF scheme for the time of flight experiment, it was necessary to consider several factors. As previously observed more than 90 % of the ions are in the ($v = 0$) level[1], and the best detectivity will be achieved if this state is probed by the pumping transition. This also allows a direct comparison with the previous experiments[1] as this was the level that was probed. Inspection of the Frank-Condon factors[8] shows that only the (0,0), (1,0), (2,0) and (3,0) bands merited consideration.

The (0,0) and (1,0) bands were ruled out because the wavelengths required, (around 1.1 μm and 920 nm respectively) were extremely difficult to produce from the pulsed laser system that was available. For the (2,0) system, there are three possibilities for observation of the fluorescence; firstly on the (2,0), however this was discarded immediately because it would be impossible to spectrally remove the scattered laser light, secondly (2,1) which has a larger Frank-Condon factor, and (2,4) which has the largest Frank-Condon factor. The (2,4) band occurs in the infrared where low noise, high-speed and high sensitivity detectors are not available. The (2,1) band occurs around 950 nm and appears to be the best band from which to observe the fluorescence.

If instead the (3,0) band is pumped, there are two possibilities for observation of the fluorescence; the (3,1) and the (3,5) band. The latter was neglected, again due to its long wavelength. The (3,1) band occurs at around 810 nm. To determine whether observation at 950 nm after pumping the (2,0) or observation at 810 nm after pumping the (3,0) would be more sensitive it is necessary to consider the magnitude of the plasma induced emission at these wavelengths. The two previous surveys of the plasma induced emission from a nitrogen discharge that have been completed in the CCP system[1,13] showed that the majority of the plasma emission was unsurprisingly produced by N_2 and N_2^+. The main emission from N_2 was observed to be from the 1st ($B\ ^3\Pi_g \rightarrow A\ ^3\Sigma_u^+$) and 2nd ($C\ ^3\Pi_u \rightarrow B\ ^3\Pi_g$) positive systems, while only the $B\ ^2\Sigma_u^+ \rightarrow X\ ^2\Sigma_g^+$ system of N_2^+ was observed, the $A\ ^2\Pi_u \rightarrow X\ ^2\Sigma_g^+$ system being masked by overlying N_2 emission. By inspection of the positions[8] of the band heads of the N_2 systems, it is found that at around 950 nm emission occurs on the (3,3), (8,9) and (4,4) bands of the first positive system while at around 810 nm emission on the (10,10), (11,11) and (6,5) bands of the first positive system are present. Estimating the vibrational temperature of the N_2 at the value previously measured for N_2^+ (1200K)[1], the relative population of the N_2 B state can

be calculated. With this estimate of the population and knowledge of the Frank-Condon factors it was possible to deduce that the plasma induced emission around 950 nm would be considerably more intense than that at 810 nm. For this reason, the scheme involving pumping *via* the (3,0) band and observing the fluorescence from the (3,1) band was chosen. This choice is also supported because the detectors available for 810 nm are considerably quieter than those that respond to 950 nm[14].

Figure 5.5 shows the energy levels of the A $^2\Pi_u$ ($v = 3$) ← X $^2\Sigma_g^+$ ($v = 0$) system of the N_2^+ ion involved in this detection scheme along with a sample of the transitions between them.

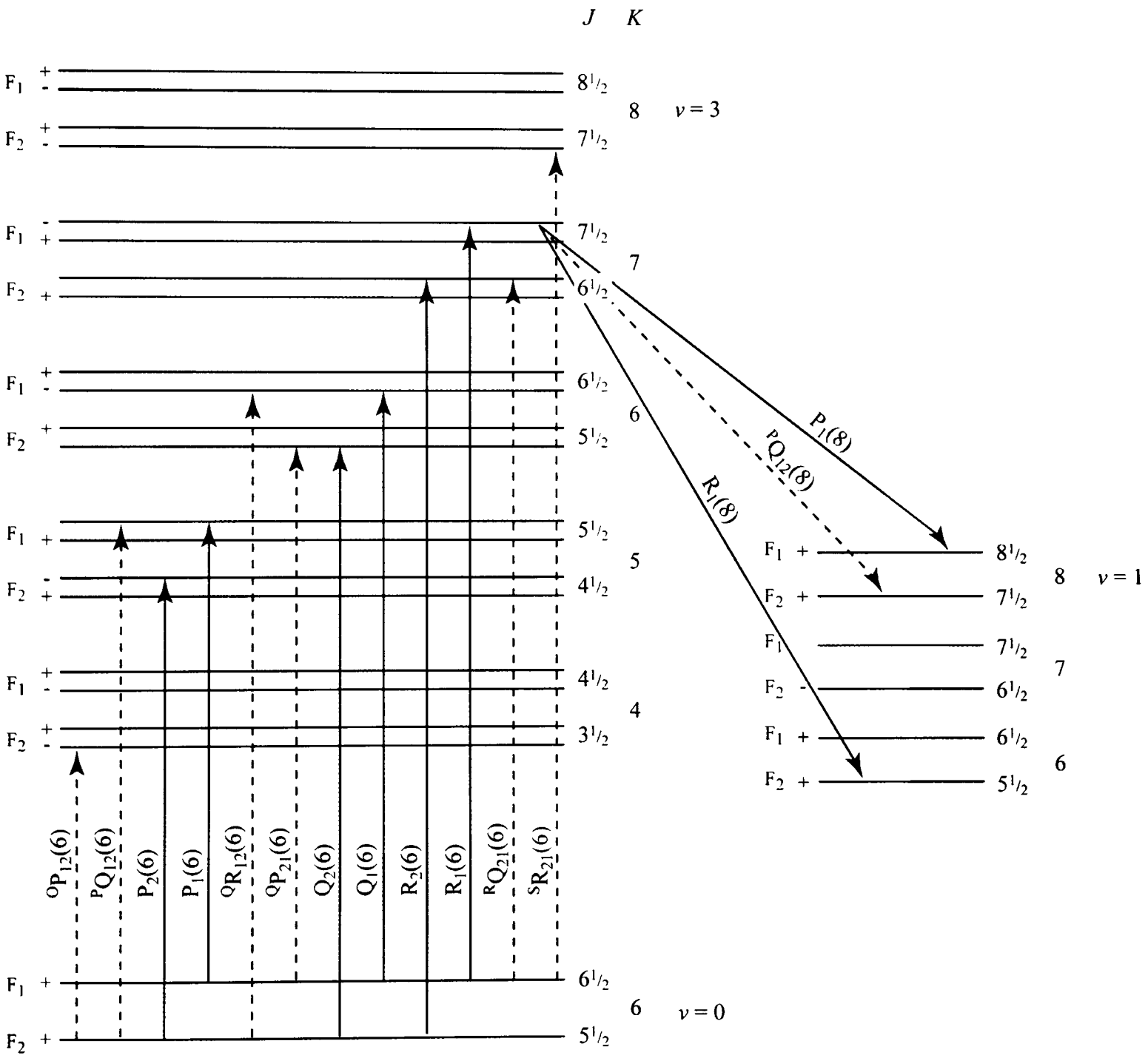

Figure 5.5 An energy level diagram of the A $^2\Pi_u$ ($v = 3$) ← X $^2\Sigma_g^+$ ($v = 0$) system of the nitrogen molecular ion N_2^+.

The absorption cross section for a transition in the A $^2\Pi_u$ ($v = 3$) ← X $^2\Sigma_g^+$ ($v = 0$) system can be estimated from the transition probability[8], $A_{12} = 1.9 \times 10^{-4}$ s^{-1}, using equation (5.1)[15].

$$\int \sigma_{12}\, d\nu = \frac{g_2}{g_1}\frac{\lambda^2 A_{12}}{8\pi} \tag{5.1}$$

This gives the cross section of a particular rotational level and it is necessary to multiply this by the fraction of molecules present in the particular rotational level of interest to calculate an effective cross section for all the N_2^+ ions. This allows the absorbance of the system at a given wavelength to be calculated from the product of the cross section, the path length and the total N_2^+ ion concentration, rather than the concentration of the ion in the specific rotational level from which the transition originates. Assuming the previously measured[1] rotational temperature of 350 K, the total cross section for the R(6) band head is found to be approximately 6×10^{-16} cm^2.

5.2.2 Simulation of the A $^2\Pi_u \leftarrow$ X $^2\Sigma_g^+$ Absorption System

The absorption spectrum of the (3,0) band (A $^2\Pi_u$ (v = 3) $\leftarrow$ X $^2\Sigma_g^+$ (v = 0)), in the region investigated in this Chapter was simulated using the line positions given by Benesh *et al.*[11] (interpolating the data to determine the positions of the few transitions not given), the linestrengths given by Zare[16] and the molecular constants for the N_2^+ ion given by Huber and Herzberg[17]. Figure 5.6 shows the spectrum obtained assuming a translational and rotational temperature of 350 K, the value estimated previously in the CCP system[1], in the situation when the linewidth is dominated by Doppler broadening.

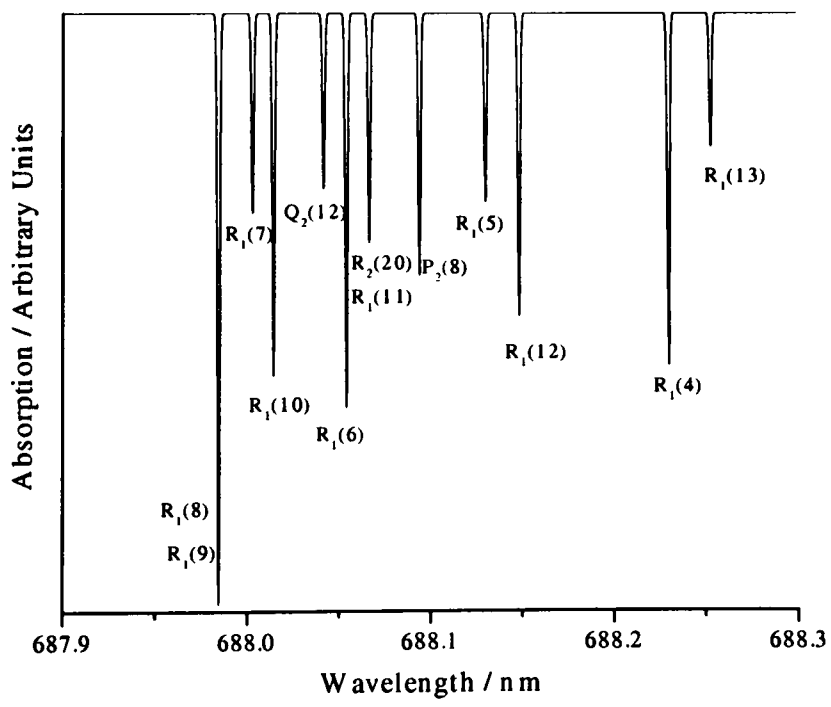

Figure 5.6 Simulation of a small region of the absorption from the A $^2\Pi_u$ (v = 3) $\leftarrow$ X $^2\Sigma_g^+$ (v = 0) system of the nitrogen molecular ion N_2^+.

5.2.3 The B $^2\Sigma_u^+ \leftarrow$ X $^2\Sigma_g^+$ Detection Scheme

The rotational selection rules given in Section 5.2 produce four main branches; while two weaker sub branches are also possible (when ΔJ is 0 and ΔK (ΔN) is ±1). These are labelled in the same way as the transitions of the A $^2\Pi_u \leftarrow$ X $^2\Sigma_g^+$ system, giving R_1, R_2, $P_1$and P_2 for the main branches and $^RQ_{21}$ and $^PQ_{12}$ for the sub branches.

Similarly to the survey of the plasma induced emission spectrum of the discharge discussed in Section 5.2.1 an investigation in the region from about 300 nm to 500 nm has previously been conducted[1]. From this, along with knowledge of the Frank-Condon factors for the possible excitation and fluorescence transitions, the optimum LIF detection scheme was determined[1] to be excitation of the R(6) transitions, *i.e.* $R_1(6)$, $R_2(6)$ and $^RQ_{21}(6)$, of the (2,0) band at 330 nm and consequent observation of the (2,4) fluorescence at 458 nm. Figure 5.7 is a schematic of the energy levels of the B $^2\Sigma_u^+$ (v = 2) ← X $^2\Sigma_g^+$ (v = 0) system of the N_2^+ ion involved in this detection scheme, along with sample transitions between them.

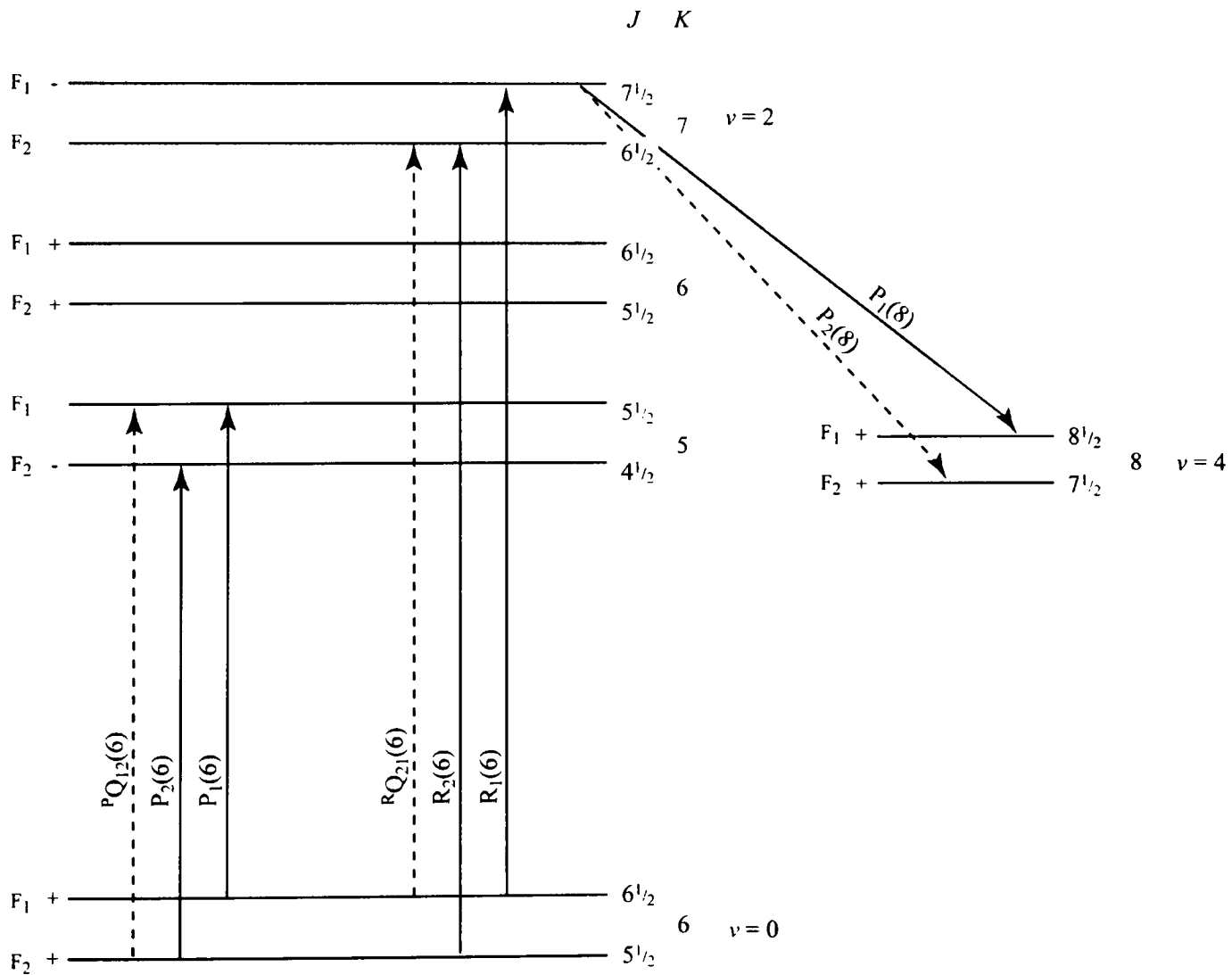

Figure 5.7 An energy level diagram of the B $^2\Sigma_u^+$ (v = 2) ← X $^2\Sigma_g^+$ (v = 0) system of the nitrogen molecular ion N_2^+.

A similar procedure to that described in Section 5.2.1 leads to a total cross section for the R(6) transitions of the B $^2\Sigma_u^+$ (v = 2) ← X $^2\Sigma_g^+$ (v = 0) system of 1.2×10^{-14} cm^2 using $A = 7.6 \times 10^5$

s^{-1} [8]. For the maximum N_2^+ ion concentration previously observed (4×10^{10} cm^{-3})[1], this corresponds to an absorption of 2 % per pass through a 40 cm discharge.

5.3 Detection *via* the A $^2\Pi_u \leftarrow$ X $^2\Sigma_g^+$ Electronic Transition

In this section, experiments involving detection of the N_2^+ ion *via* transitions to and from the A $^2\Pi_u$ state using LIF and CRDS are discussed.

5.3.1 Experimental Equipment

The N_2^+ ion was produced in both the capacitively coupled r.f. chamber and the inductively coupled chamber. For the LIF experiments, the laser entered and exited the chamber *via* Brewster angled quartz windows. The experimental layout for the LIF experiments is shown in Figure 5.8a, whilst Figure 5.8b shows the experimental layout for the CRDS experiments.

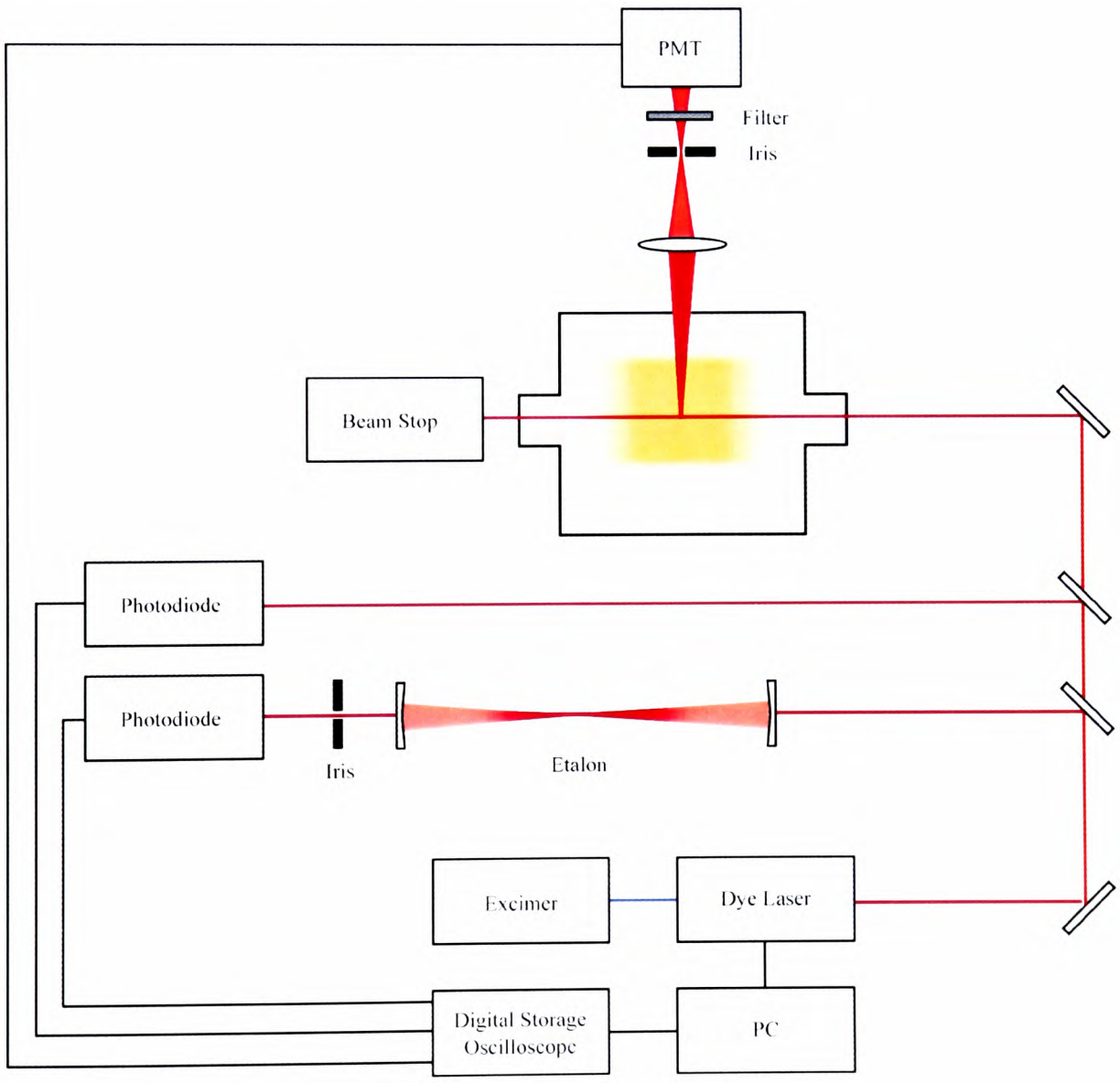

Figure 5.8a Schematic of the LIF experimental layout.

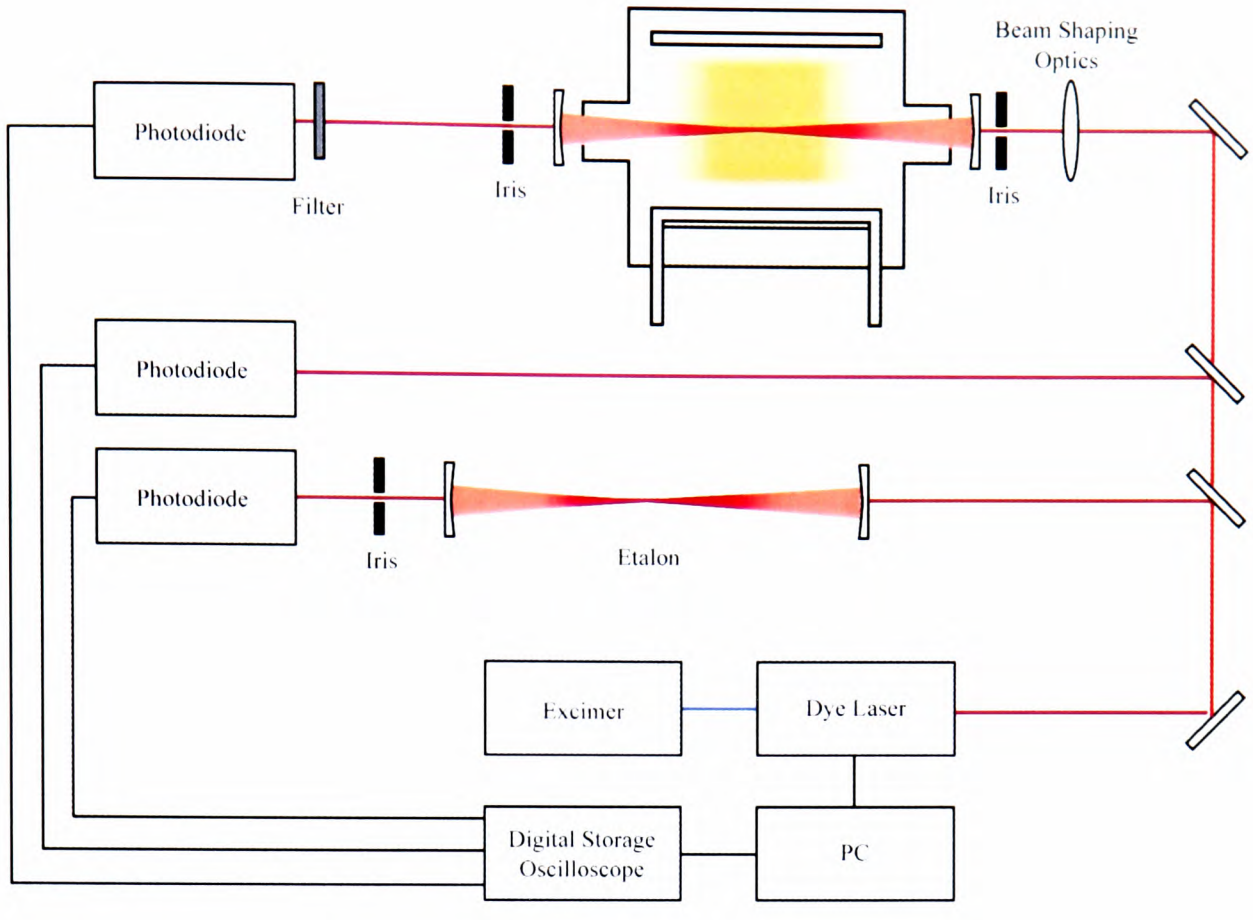

Figure 5.8b Schematic of the CRDS experimental layout.

5.3.1.1 The Laser System

An excimer pumped pulsed dye laser system was used to generate radiation at about 688 nm for excitation on the A $^2\Pi_u \leftarrow$ X $^2\Sigma_g^+$ transition of the N_2^+ ion. The excimer laser was a Lambda Physik EMG 101 MSC (XeCl mix, producing 308 nm radiation with an output pulse energy between 80 and 100 mJ), which pumped a Lambda Physik LPD3002E dye laser at a repetition rate of 10 Hz. The dyes used for the experiments were either Nile Blue 690 Perchlorate (Exciton) dissolved in methanol or Cresyl Violet 670 Perchlorate (Exciton) dissolved in ethanol. The absolute pulse energy at around 688 nm was about 1 mJ and was monitored shot to shot during experiments by a photodiode (Vartec VTB 6061UV), using a reflection from a quartz flat. The signal from this diode was also used to trigger the data acquisition system. The absolute wavelength was monitored using a Burleigh pulsed wavemeter, while the relative frequency was monitored using an etalon.

5.3.1.2 Data Acquisition and Analysis

The laser induced fluorescence produced in the CCP system was collected using a 30 cm focal length lens and then spatially filtered using a 0.5 mm horizontal slit and spectrally filtered using an interference filter (CVI F03-810.0-1.00, centre wavelength of 810 nm, a FWHM transmission of 3 nm and a peak transmission of greater than 40 %). This reduces the optical

emission from the plasma so that the red sensitive photomultiplier tube (Hamamatsu R636-10 biased using a Brandenburg 2475R high voltage power supply) used to observe the LIF was not saturated.

For the CRDS experiments, the chamber was again fitted with the gimbal mirror mounts. These mounts contained two LaserOptik mirrors specified with a reflectivity of 99.95 % (at 660 nm), one plane and the other concave with a radius of curvature of 1.5 m, forming a 50 cm long ring down cavity (see Appendix 1 for a discussion of the criteria for a stable optical cavity). The Gaussian beam dimensions of the TEM_{00} mode supported by the cavity were calculated using the ABCD matrix[10] for the cavity in MathCad 2000 Professional. The CRDS signal was monitored using a biased BPX 65 photodiode.

The signals obtained from the LIF, CRDS and laser power monitor photodiode were acquired on a LeCroy 9314 M digital oscilloscope (300 MHz 100 Msamples/s), equipped with WP02 waveform processing firmware (generally using 11 bit resolution *via* the use of the enhanced resolution function). These signals were transferred onto a Pentium PC, *via* a PCI GPIB card (National Instruments), where they were then analysed. This PC also controlled the dye laser wavelength. In the case of the CRDS experiments, the spectral scans were obtained from fitting a single exponential decay to an average of 40 enhanced resolution traces at each wavelength and then the dye laser wavelength was stepped to the next point in the scan.

5.3.2 Results of the Laser Induced Fluorescence Measurements

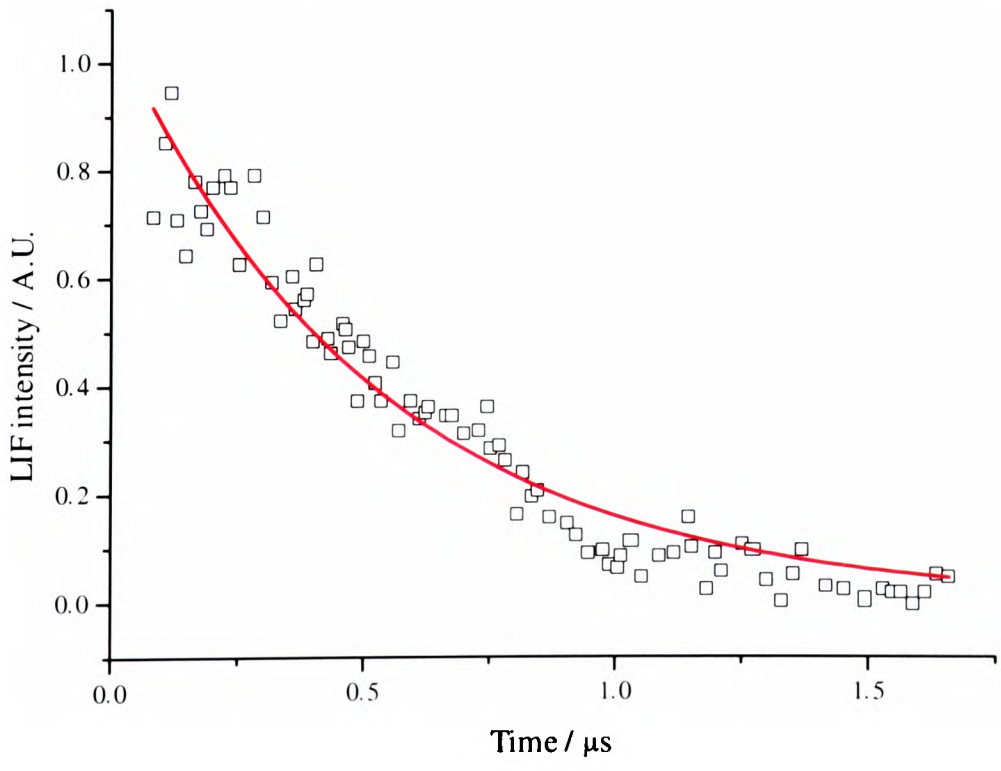

Figure 5.9 LIF signal obtained from over 100 000 laser shots from a 300 W discharge sustained in the CCP system at 100 mTorr.

To observe the LIF from the A $^2\Pi_u$ state of the N_2^+ ion, careful spatial and spectral filtering was required to remove the intense emission from the discharge. The LIF time trace observed in the CCP sustaining a 300 W 100 mTorr nitrogen plasma is given in Figure 5.9. This LIF signal was obtained from the average of in excess of 100 000 laser shots. An average of the signal produced without the plasma struck was subtracted from the signal. This procedure removes a significant amount of electrical noise produced by the excimer laser and the signal observed from scattered laser photons. However, the LIF time trace still exhibits some oscillations due to the imperfect match of the electrical noise, produced by the excimer laser, observed with and without the discharge. The signal to noise ratio is poor considering the extremely large number of laser shots that were averaged to produce the signal. A single exponential decay was fitted to the LIF signal, yielding a fluorescence lifetime of 530 ns for the $v = 3$ level of the A $^2\Pi_u$ state. This is about a factor of 20 lower than the radiative lifetime (10.7 μs)[8], and is consistent with a collisional quenching rate constant of 5.3×10^{-10} $cm^3 molecules^{-1} s^{-1}$, in agreement with the value previously estimated[1] for the $v = 0$ level of the B $^2\Sigma_u^+$ state (4.3×10^{-10} $cm^3 molecules^{-1} s^{-1}$).

5.3.3 Results of the Cavity Ring Down Measurements

The time dependence of the light intensity, within the cavity, with the discharge extinguished (and a total pressure of 100 mTorr), is shown in Figure 5.10 along with a fitted first order exponential decay, $I_0 e^{-t/\tau}$. From this, it was possible to obtain a value of 4 μs for the cavity 'ringdown time', τ. Equation 1.20 relates mirror reflectivity to τ showing that the mirrors used were 99.96 % reflective at this wavelength. Thus, the cavity finesse is approximately 7 500, which gives an effective path length of 1.25 km within the 50 cm ringdown cavity.

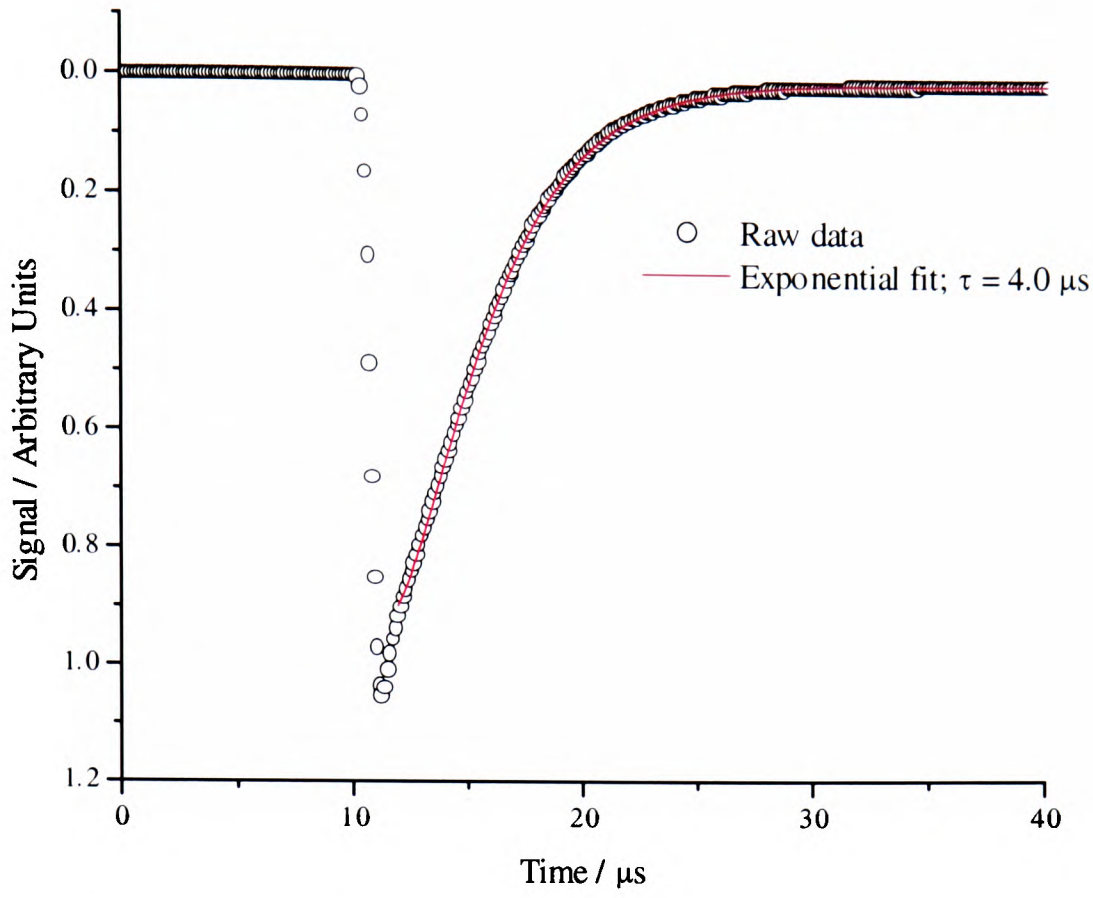

Figure 5.10 An example of a CRDS signal, along with the exponential fit. The signal rise time can be attributed to the detection electronics.

The sensitivity of this ringdown experiment can again be calculated from the expressions given in Section 1.6.4. The minimum detectable fractional absorption per pass, δI_{min}, is 3.5×10^{-7}. Alternatively, this can be expressed as a minimum absorption coefficient, $\alpha_{min} = 7 \times 10^{-9}$ cm^{-1} for the 50 cm long cell, corresponding to a theoretical minimum detectable concentration of N_2^+ ions of 1.2×10^7 cm^{-3}. This is the absolute minimum detectable concentration, however ring down times differ for different cavity longitudinal modes and so this limit is never attained, especially in the presence of the discharge optical emission and radiated noise. Thus a survey of the ring down times (RDTs) was completed at a wavelength where no absorption was expected. The results are shown as a histogram in Figure 5.11. Twice the standard deviation of the 305 measurements was found to be 320 ns. Assuming this is the minimum experimentally detectable change in the RDT, from equation 1.25, it is possible to estimate that the minimum experimental detectable fractional absorption per pass, δI_{min}, as 3.2×10^{-5}. This corresponds to an experimental minimum detectable concentration of N_2^+ ions of 1.1×10^9 cm^{-3}, which is two orders of magnitude higher than the theoretical value derived above.

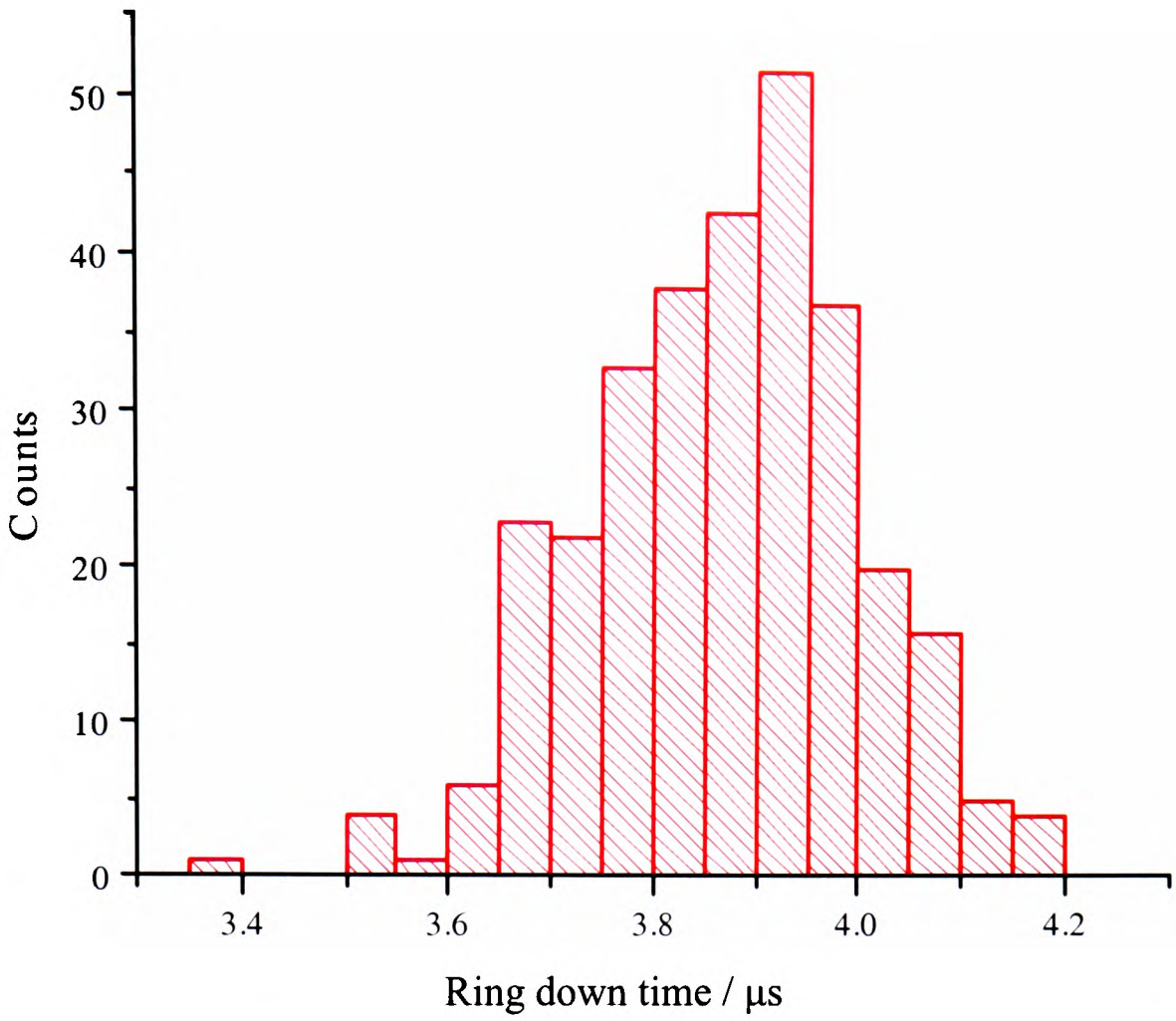

Figure 5.11 Histogram of 305 RDTs obtained, showing a distribution resembling a normal distribution with a standard deviation of 160 ns.

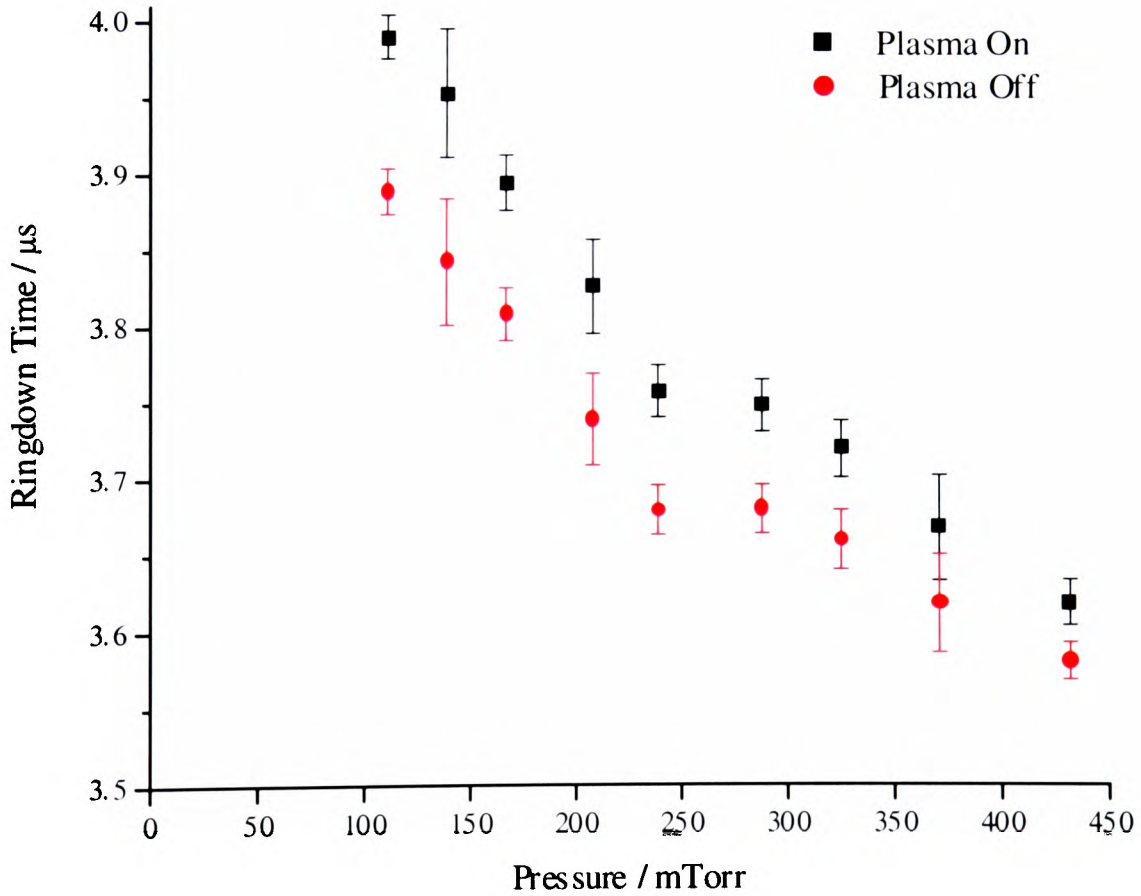

Figure 5.12 Variation in RDT with and without the discharge (100 W) at various pressures.

In addition to the effects of the plasma induced optical emission and the radiated electrical noise, the plasma also affected the ring down time by changing the reflectivity of the mirrors.

Figure 5.12 shows how the RDT varies with pressure with and without the discharge. The measurements with the discharge on were recorded after the discharge had been ignited for approximately 10 s, while those without the discharge were recorded about 10 seconds after the discharge was extinguished. From these measurements, it is clear that the RDT is significantly affected by the discharge. This type of effect has been observed previously[18] and has been overcome by operating the discharge continuously for up to several days before measurements were recorded. In previous cases, the discharge has been observed to reduce the RDT, attributed to deposition on the mirrors, not increase it as is observed here. A possible reason for the increase in the RDT observed here is that the nitrogen plasma is removing any deposit from the feedgas or back-streamed oil from the vacuum pumps.

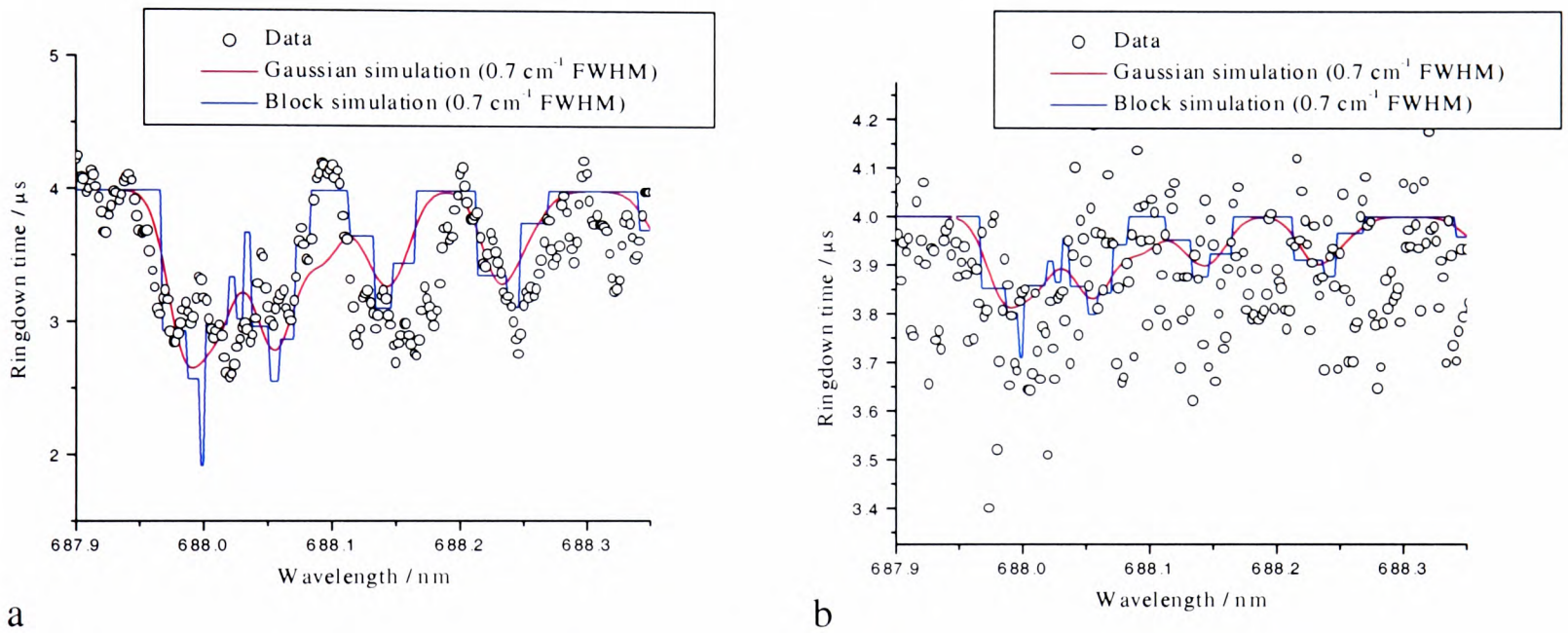

Figure 5.13 CRDS scans over a small region of the A $^2\Pi_u$ (v = 3) ← X $^2\Sigma_g^+$ (v = 0) absorption system of the nitrogen molecular ion N_2^+, (a) a 175 W plasma sustained in the CCP system at a pressure of 220 mTorr and (b) a 100 W plasma sustained in the ICP system at a pressure of 75 mTorr.

Despite the interference of the plasma on the CRDS measurements, scans over a small region of the A $^2\Pi_u$ ← X $^2\Sigma_g^+$ absorption system of the N_2^+ ion were completed in both the CCP and ICP systems. These scans result from the average of five scans, on each of which 40 RD decays at each wavelength point were recorded and averaged. From the average of these 40 decays, the RDT was obtained. Therefore, the entire data acquisition process took in excess of 10 hours. These scans, along with two different types of simulation, are shown in Figure 5.13. The Gaussian simulation assumes that the linewidth of the spectrum is dominated by the laser spectral output, assumed to be Gaussian with a FWHM of 0.7 cm^{-1}. This is the FWHM of the fundamental of the dye laser system previously measured[1] at a similar wavelength, although its spectral output was observed to be made up of many modes, each with a width of about 0.3 cm^{-1}. Therefore, the block simulation was produced assuming the laser spectral output

dominates the observed linewidth and is described by a block function of the same width as the Gaussian (the real profile is probably a structured combination of the two). It can be seen from the figure that the absorption spectrum recorded roughly coincides with the minima of the simulations, however the signal to noise ratio is exceptionally poor despite the large number of RD decays recorded at each point. A second problem is that the laser bandwidth is considerably greater than the linewidth of an individual absorption line (0.034 cm^{-1}) and therefore the assumption used to derive the expressions for CRDS, that the entire spectral output of the laser is attenuated by the same amount, is invalid. These factors mean that from the observed signals it is only possible to approximately estimate the N_2^+ ion concentrations as 5×10^9 cm^{-3} in the CCP (175 W, 220 mTorr) and 7×10^8 cm^{-3} in the ICP (100 W, 75 mTorr). The measurement in the CCP is in reasonable agreement with that previously measured at 200 W and 200 mTorr (1.5×10^{10} cm^{-3}) in this system by calibrated LIF[1], when it is considered that this is the path (of which about half is through the plasma bulk) integrated concentration and the LIF measurements were made in the middle of the bulk. The relative measurements in the two chambers agree with the observations discussed in Chapter 2.

5.3.4 Possible Future Experiments

It is clear that the LIF signal, although observable with the pulsed laser system, is not sufficient to complete the proposed time of flight experiment. In comparison to the previous measurements which used the B $^2\Sigma_u^+ \leftarrow$ X $^2\Sigma_g^+$ transition the signal is smaller, not only due to the weaker absorption but also the much lower fluorescence quantum yield (about 0.05 was observed here compared to the B $^2\Sigma_u^+$ state for which the quantum yield was previously observed[1] to always be greater than 0.5 up to 0.5 Torr in the CCP system). In addition, because the radiative lifetime is greater, a necessity for the proposed time of flight experiment, the temporal window that the LIF is observed over is greater and therefore the average intensity is lower so it is more difficult to discriminate the LIF from the plasma induced emission. Although a CRDS spectrum has been obtained in both systems, the amount of absorption due to the N_2^+ ions is very small and thus no attempt to record a CLIF signal was made, as the enhancement observed in Chapter 4 using CLIF was several orders of magnitude below what would be required for a successful time of flight experiment to be completed.

To complete the time of flight experiment a more efficient excitation method is required, such as a method using continuous wave radiation trapped inside a resonant cavity (the continuous wave equivalent to the CLIF technique discussed in Chapter 4). This cavity could be actively

held in resonance with the output of a continuous wave diode laser (see Section 5.4.2). A similar method to the MMS system described in Chapter 3 could be utilised for the detection scheme. Previously, a cavity has been held in resonance with a laser output using one component of the polarisation (for one of the locking schemes discussed in Section 5.4.2), while the other orthogonal polarisation component of the laser output is used to probe the sample[19]. This procedure could be used for the excitation scheme if the component of the polarisation used to probe the sample could be modulated using an acousto-optic modulator (AOM)[20] while the other orthogonal component bypasses the AOM and is then used to lock the cavity. This continuous wave system would increase the proportion of the experimental time that the excitation source is on by many orders of magnitude, and also enables uses of phase sensitive detection to remove noise from the plasma induced emission *via* the integration provided by a lock-in amplifier. It has been shown from the magnitude and phase of the signals produced relative to that observed in the excitation region that it is possible to obtain the velocity distribution of the ions[21], analogously to the pulsed experiment.

5.4 Detection *via* the B $^2\Sigma_u^+ \leftarrow$ X $^2\Sigma_g^+$ Electronic Transition

In this section the design, development and testing of a continuous wave laser source for detection of the N_2^+ ion *via* the B $^2\Sigma_u^+ \leftarrow$ X $^2\Sigma_g^+$ transition is discussed. This source consists of a similar frequency doubled diode laser system to that discussed in Chapter 4. However, as mentioned previously, the intensity of the second harmonic radiation produced by passing the fundamental once through the crystal is very low. This is because the conversion efficiencies are small and depend on the square of the intensity of the fundamental radiation. To detect a species in a plasma it is essential that sufficient radiation is used such that signals are not swamped by the plasma induced emission, whether the species is being detected *via* absorption or laser induced fluorescence. For the laser induced fluorescence experiment proposed in Section 5.1.2, the signal observed depends linearly on the laser power, until the intensity becomes sufficient to saturate the transition. To achieve as good a signal to noise ratio as possible, the maximum achievable amount of ultraviolet radiation must therefore be used as the excitation source. Consequently, it is necessary to enhance the fundamental intensity in the non-linear crystal. This can be achieved by containing the non-linear crystal within a resonant cavity.

5.4.1 Theory and Design

The theory of second harmonic generation (SHG) and the optimum focusing condition of a Gaussian beam is summarised in Section 4.4.1. Using this procedure developed by Boyd and Kleinman[22], the maximum efficiency of SHG at 660 nm in $LiIO_3$, is found to occur when the fundamental beam waist within the crystal is approximately 18 μm. This corresponds to a value of an efficiency, γ, of 2.7×10^{-4}. In this calculation the Sellmeier coefficients given by Dmitriev *et al.*[23] have been used. Although the SHG conversion efficiency of $LiIO_3$ is relatively high, reflection losses will still be important and will lower the finesse of the doubling cavity. Reflection losses can be minimised in two ways: using an anti-reflection coating or choosing the angle of incidence into the crystal to be the Brewster angle. It is difficult to deposit an anti-reflection coating onto a $LiIO_3$ surface; instead to minimise reflection losses at the faces of the crystal, it was purchased with Brewster cut faces. However this introduces a complication in the production of the correct beam size within the crystal because of the resultant astigmatism in the beam. This can be compensated by the reflections from spherical mirrors, of radius of curvature r, at a particular angle of incidence, α. The condition for astigmatism compensation is given by[24]

$$r \tan\alpha \sin\alpha = \frac{l\left(n^2-1\right)\sqrt{n^2+1}}{n^4} \tag{5.2}$$

where n is the refractive index of the ordinary polarisation of the fundamental radiation in the crystal, of length l. In this case, n = 1.88, l = 8.1 mm, r = 5 cm and therefore α is approximately 15°.

To utilise this correction the non-linear crystal was placed within a bowtie enhancement cavity consisting of two plane mirrors and the two spherical mirrors. A schematic of such a cavity is given in Figure 5.14. The optimum parameters u, v and θ for the cavity must be chosen such that the Gaussian waists of the TEM_{00} mode supported by the cavity is, in the centre of the crystal the same as that calculated for the maximum SHG **and** at the centre of the long arm matched to the achievable beam size produced by focusing the laser output into the bowtie cavity. To determine achievable waists in the long arm, the beam profile of several lasers were recorded after passing through different sets of lenses, by using a CCD camera interfaced to a PC running Spiricon beam profiling software.

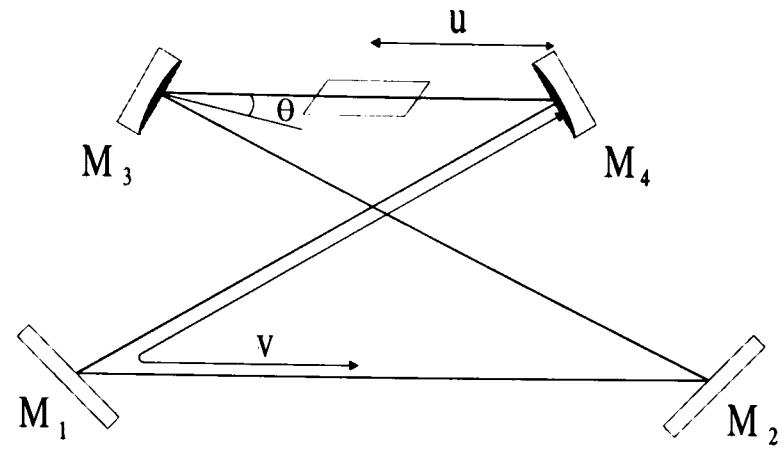

Figure 5.14 Schematic of a bowtie enhancement cavity for SHG. The defining angles and lengths are labelled.

The Gaussian beam properties around the cavity were calculated[25] using the product of the ABCD matrices[10] for all the components in the cavity (Appendix 1 contains a summary of the theory and the matrices required). The astigmatism introduced by the Brewster cut crystal faces meant that the total optical cavity matrix had to be calculated separately for the horizontal and vertical planes.

5.4.2 Experimental Equipment

The diode laser chosen was a 30 mW Blue Sky Research Circulaser PS104. Its beam profile is given in Figure 1.10b. This laser had an almost circular output and reduced astigmatism compared to other lasers, due to a correcting lens placed onto the front facet of the laser. Hardware and control equipment identical to that discussed in Section 3.5.1 was used to mount this laser and control its current and temperature.

Although the laser had an integral correction optic, it was still necessary to use a second lens to correct the divergence of the laser. The laser mount was rigidly bolted to an aluminium breadboard, onto which all the required optics for the doubling cavity were also mounted at a standard beam height of 50 mm. This small height, along with the use of large stable ½" New Focus corner mirror mounts, produced a system that was convenient and very stable. The entire system was mounted on a Melles Griot vibration control pneumatically isolated optical table to reduce vibrations which may affect the operation of the cavity.

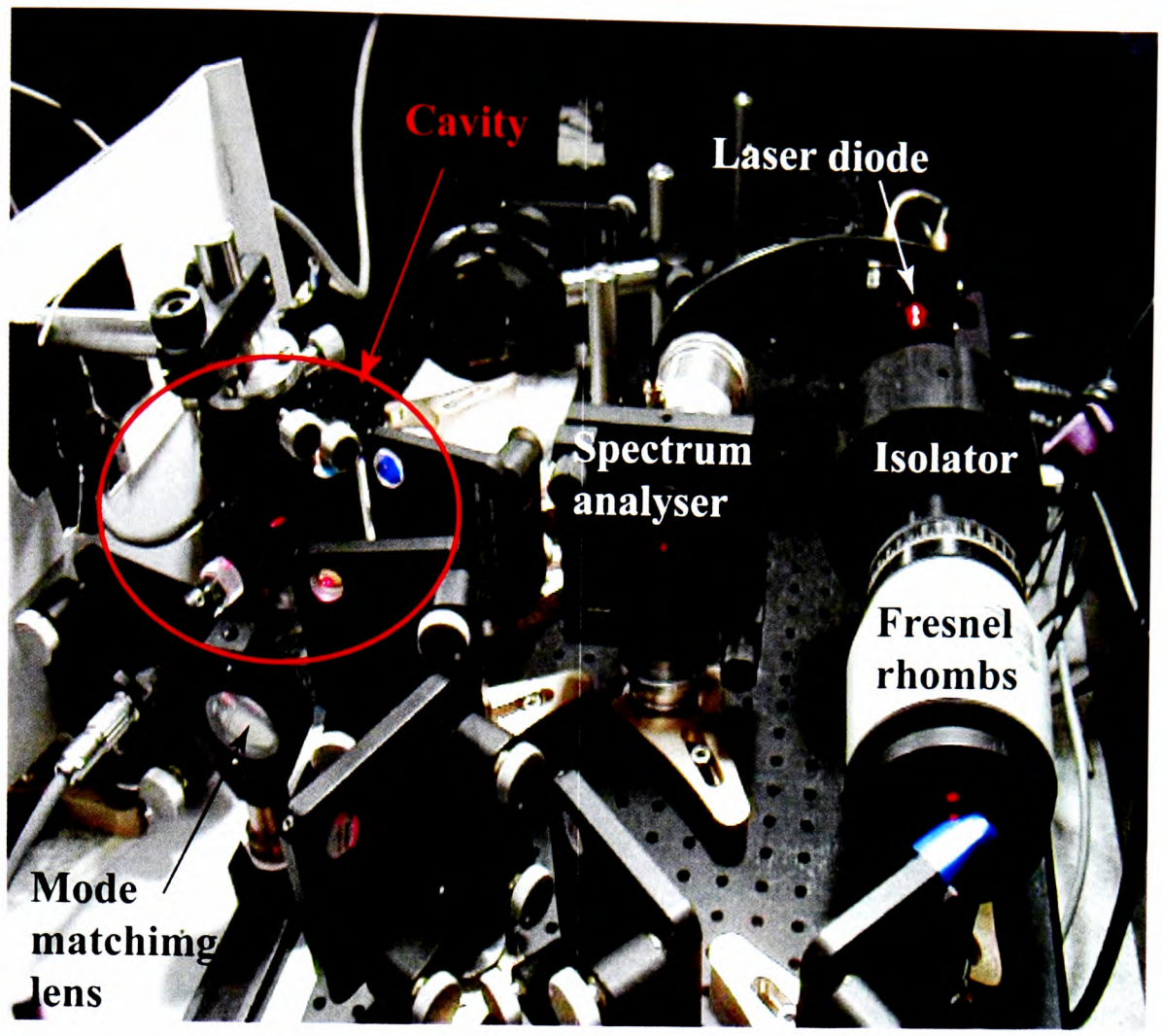

Figure 5.15 The frequency doubled diode laser system, (a) a photograph and (b) a labelled schematic.

A photograph of the laser system is given in Figure 5.15a and a schematic is given in Figure 5.15b. The diode laser is protected from optical feedback by a Faraday isolator (Leysop type FOI 5/57). A pair of Fresnel rhombs (Spectra Physics) are used to rotate the polarisation of the

laser to the correct orientation for the cavity. The next component in the optical path is the mode matching lens, mounted on an optical rail and carefully aligned so that translations of the lens along the rail did not cause the beam to change direction. A small fraction of the laser output is used to monitor the spectral output using a spectrum analyser (TecOptics V4323 spectrum analyser, with a 10 GHz Free Spectral Range and a finesse of greater than 100) and the absolute fundamental wavelength was recorded using a Burleigh wavemeter (WA1000). The cavity mirrors have specified reflectivities given in the following table.

Mirror	Reflectivity at 660 nm	Reflectivity at 330 nm
M_1	0.985	> 0.99
M_2	> 0.99	< 0.2
M_3	> 0.99	N/A
M_4	> 0.99	> 0.99

The mirrors M_2, M_3 (mounted on a piezoelectric transducer to enable the cavity length to be changed electrically) and M_4 and the $LiIO_3$ crystal (Casix) were then positioned in the geometry calculated (u = 2.8 cm, v = 15.7 cm and θ = 13.1°), while M_1 was temporarily substituted for a quartz plate of identical thickness to M_1. This allowed correct orientation of the other mirrors and, most importantly, the crystal. The correct crystal orientation and position was found by observing the light exiting the crystal after it passed through the quartz plate and a Schott UG11 filter using the CCD camera. The crystal was supported in a temperature controlled mount on a 3-axis rotation and translation stage. The $LiIO_3$ crystal needs to be heated because it is hydroscopic and therefore the crystal was kept at 40 ± 0.1 °C by resistive heating, controlled by a home-built active temperature controller. The angle and position of the crystal was altered until the maximum SHG was observed. The cavity was then completed by the installation of M_1. The CCD camera was then used to observe the fundamental loss of the cavity through M_2 without the UG11 filter. Precise cavity alignment can then be achieved by iteratively adjusting the mirrors to overlay consecutive round trips until the cavity transverse modes could be observed. Figure 5.16 shows the beam profile of some of the cavity modes.

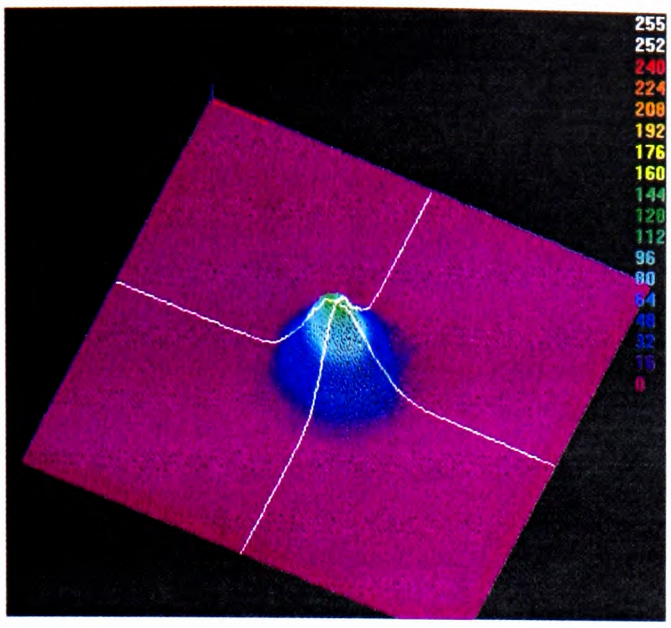

(a)

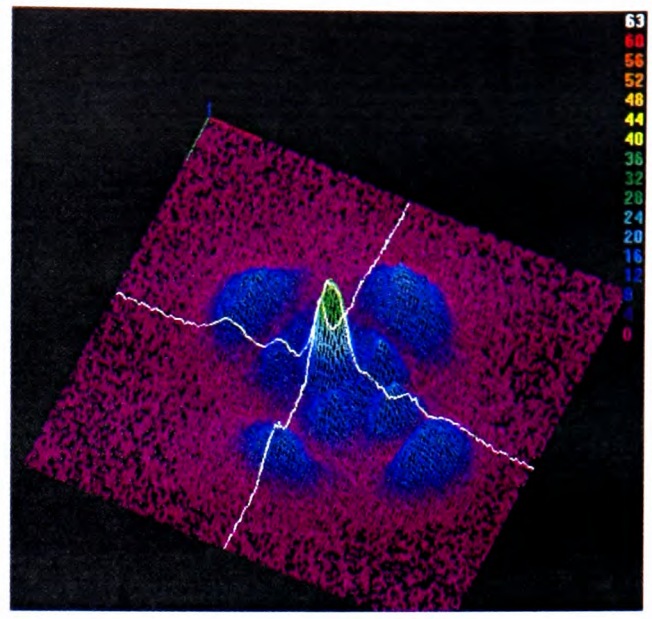

(b)

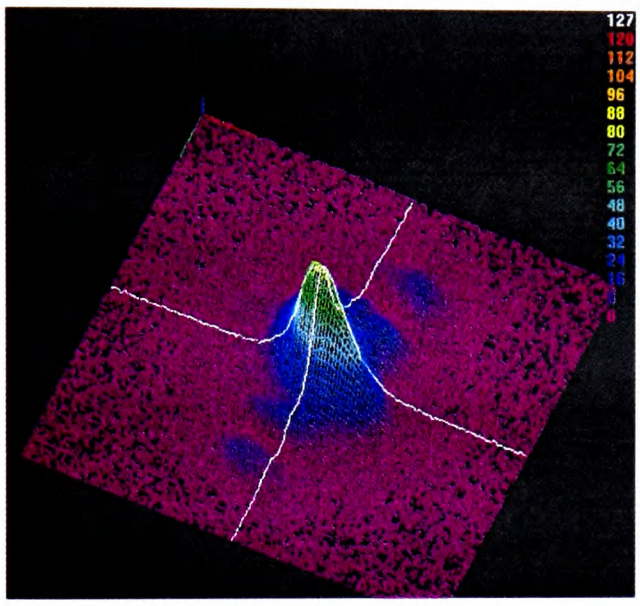

(c)

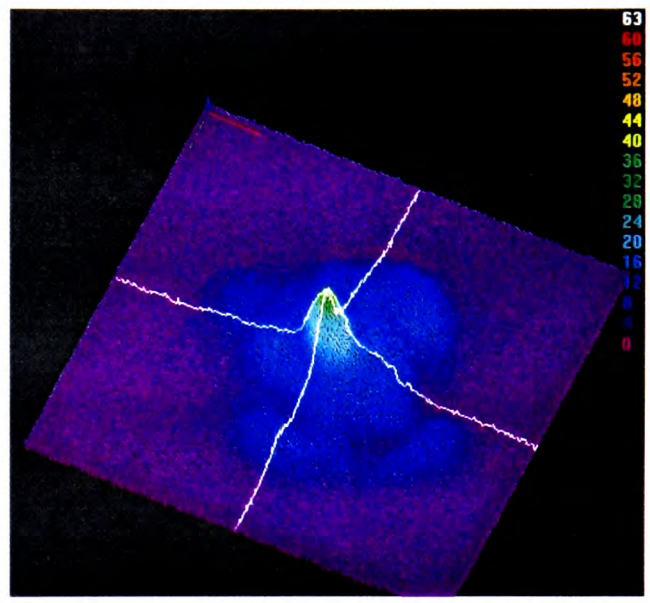

(d)

Figure 5.16 Beam profiles of the fundamental (660 nm) cavity modes of the resonant cavity of the frequency doubled diode laser system, recorded by interfacing the camera with a PC running Spiricon beam profiling software. TEM_{00} (a) and other higher order modes (b), (c) and (d) are shown.

The quality of the spatial mode matching of the laser to the cavity was observed by recording how the fundamental intensity present in the cavity varies with the position of M_3. A photodiode monitored the intensity transmitted through M_2 as the potential applied to the piezoelectric transducer on to which M_3 was varied. This allowed observation over several of the cavity free spectral ranges. The best mode matching (matching of the laser beam to the cavity TEM_{00}) was achieved by maximising the TEM_{00} peak relative to all others by iteratively adjusting the lateral positions of the cavity mirrors. Figure 5.17 shows the cavity transmission curve once mode matching had been optimised.

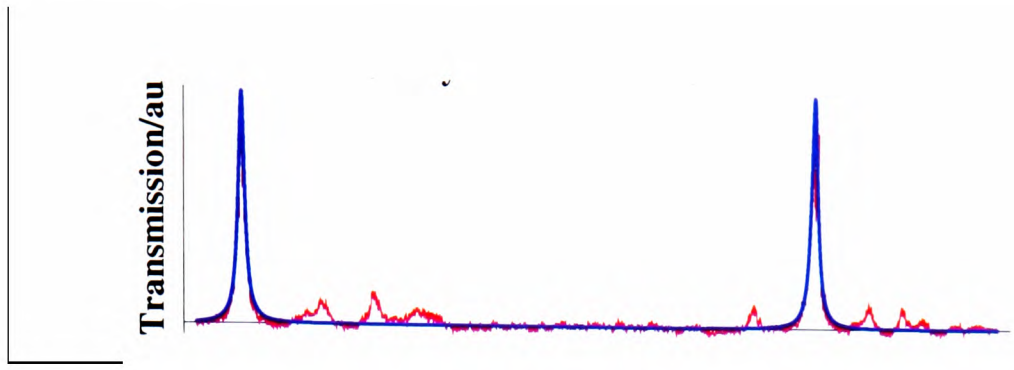

Figure 5.17 Cavity transmission spectrum (red), along with Lorentzian fits (blue) to the TEM_{00} peaks.

The relative experimental mode matching efficiency, η_{exp}, can be obtained by finding the ratio of the integrated area under the TEM_{00} peak relative to the total integrated area under the curve (which contains the contribution of all the higher order modes, which are coupled into the cavity with lower efficiency). In this case $\eta_{exp} = 0.82$. It is also possible to estimate the cavity finesse from Figure 5.17 as the ratio of the bandwidth of the TEM_{00} transmission peaks to the free spectral range. In this case, the finesse was found to be 74.

Once the cavity is optimally mode matched to the laser output, the next step is to maintain the cavity length so that the round trip distance is an integral number of wavelengths. This is described as 'locking the cavity', and is necessary because vibrations, thermal effects, air currents and noise on the laser frequency randomly change the efficiency that light is coupled into the cavity reducing the SHG efficiency. This requires an active feedback system, and the next section describes two active techniques with which a cavity can be locked to the resonance condition. Other methods such as side locking (holding the cavity on the side of the resonance peak observed in reflection) and dither locking[26] are also possible but do not continuously achieve the maximum circulating optical power in the cavity and therefore do not produce the maximum frequency doubled output, and are hence not further discussed.

5.4.3 Cavity Locking

A possible cavity locking method is that proposed by Hänsch and Couillaud[27], which involves comparison of the polarisation of the light reflected from the input coupler to that which is circulating within the cavity, observed by the fraction lost through the input coupler. It relies upon the cavity containing an element that produces a different loss for each of the two orthogonal polarisations; in this case, the $LiIO_3$ crystal with Brewster cut faces. The polarisation of the light incident on the cavity is adjusted by the Fresnel rhombs, so that it contains not only the linear polarisation component the cavity is designed for but also a small proportion of the orthogonal component that is reflected by the crystal faces. The reflected

light is then observed through a $^{\lambda}/_{4}$ retarder, which for the initial case converts the linearly polarised light into circularly polarised light[9], and a linear polarisation beam splitter by a pair of photodiodes. The intensities incident on the photodiodes should be equal when no light is propagating around the cavity. Once a combination of the light that has been in the cavity and the light directly reflected from the input coupler is observed a difference in intensities will result. However, if the cavity is resonant then the radiation exiting the cavity will be in phase with that reflected from the input coupler. The difference between the two photodiode signals is called the error signal, and at resonance has a null point. A Hänsch and Couillaud error signal for the doubling system discussed here is given in Figure 5.18.

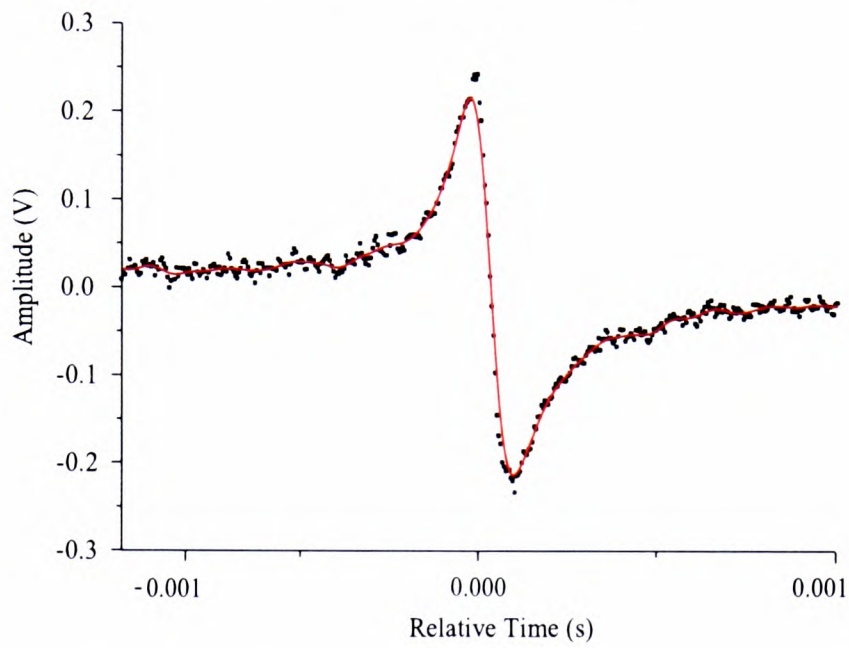

Figure 5.18 An example of the raw error signal obtained using the Hänsch and Couillaud locking signal, along with the signal observed after the low pass filtering electronics.

This error signal is then used as an input for a filtered proportional and integral servo amplifier system, which actively maintains the resonance condition either by changing the cavity length with the piezoelectric transducer, varying the laser frequency, or both simultaneously in different frequency regimes.

A second locking method is the Pound-Drever-Hall method[28], which is effectively a high frequency version of dither locking. The error signal for this procedure is obtained identically to the FMS signals observed in Chapter 3, except that rather than observing an atomic absorption line the absorption due to the cavity is used. The modulation frequency is chosen so that it is comparable with the width of the Lorentzian cavity resonance, therefore a differential type of signal is observed (see Section 3.4.1). In this case this error signal was obtained using the oscillator, demodulator and amplifier described in Chapter 3, and again the modulation frequency was chosen to be 195 MHz, because at this frequency the maximum signal is observed (due to the specific frequency response of the electronic components used). An

example of an error signal obtained by this method is given in Figure 5.19. This error signal was used as the input to the same servo system as the Hänsch-Couillaud error signal.

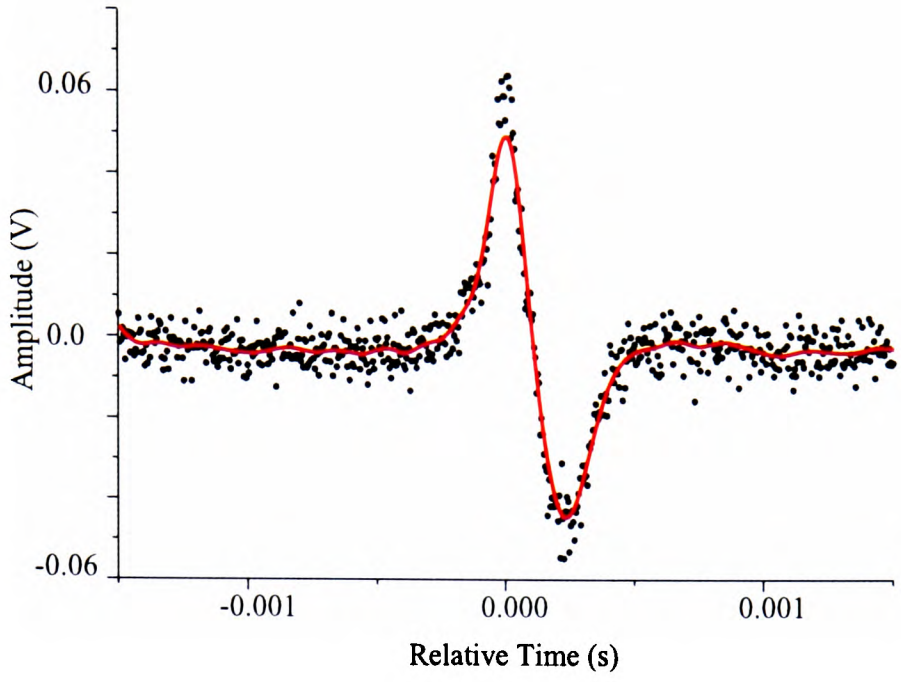

Figure 5.19 An example of the raw error signal obtained using the Pound-Drever-Hall locking signal, along with the signal observed after the low pass filtering electronics.

It was found that the Pound-Drever-Hall method provided a much more robust lock than the Hänsch-Couillaud method, which appeared to be more susceptible to other noise sources around the laboratory, *e.g.* that produced by the plasma systems and their vacuum pumps. This is probably because the commercial (Minicircuits) electronics used to produce the Pound-Drever-Hall error signal were affected less than the home-built system used for the Hänsch-Couillaud method. Generally, the Hänsch-Couillaud method would be advantageous for a cavity of this type because it is a passive method unlike the Pound-Drever-Hall method that involves modulating the laser. The stability of the laser output using both locking schemes was significantly improved by excluding air currents from within the cavity. This was achieved by enclosing the cavity in a small box and then enclosing the whole laser system in a larger box. This larger box was coated in aluminium foil to form a Faraday cage around the laser system, reducing the discharge systems' effect on the stability of the output.

5.4.4 Cavity Diagnostics

Using a Newport continuous wave power meter the ultraviolet output power was measured to be above 450 nW, for a period of 10 seconds while the cavity was locked using the Pound-Drever-Hall method. However, it was found that in the short term the ultraviolet power output varied apparently randomly between its maximum value and 80 % of this value. To test the long term stability, a digital oscilloscope was set to trigger if the frequency doubled output fell

below half of its initial value. For in excess of 36 hours no trigger was observed, implying that the system is certainly sufficiently stable for use in experiments lasting several hours. To test whether the electronics successfully maintained the resonance condition as the laser frequency was varied a ramp signal was put onto the laser injection current. The laser cavity was observed to remain in resonance during the ramp provided the ramp rate did not exceed about 0.5 mA/min, although the lock was lost at the turning points of the ramp. Generally, the electronics rapidly relocked the cavity although not always to the TEM_{00} mode, significantly reducing the frequency doubled output.

From the measured finesse (74) it is possible to calculate a number of parameters relating to the cavity enhancement. For example, T_{eff}, the round trip losses in the cavity can be found from equation (5.3) and $T_{eff} = (1 - R^2) = 0.081$.

$$F = \frac{\pi\sqrt{R}}{1-R} \tag{5.3}$$

The intracavity losses, l, due to all components in the cavity with the exception of the input coupler, are given by $T_{eff} - T_1$ where T_1 is the transmission of the input coupler. In this case l = 6.6 %; this is attributed to less than 100 % reflectivity of M_2, M_3 and M_4, to absorption and scattering in the crystal and to the conversion of the fundamental power into second harmonic power.

A second parameter that can be directly measured is the resonant reflectivity of the cavity, R_R. This is the ratio of power reflected from M_1 during a cavity resonance to that when it is out of resonance. In this case, a photodiode was used to observe the maximum fall in reflectivity as the cavity is swept, using the piezoelectric transducer, across several free spectral ranges. If the cavity is exactly impedance and mode matched, R_R is zero. Impedance matching is the condition when the transmission of the input coupler, T_1, is equal to the intracavity losses. This condition results in the largest enhancement factor, ε, of the cavity, given by[29]

$$\varepsilon = \frac{1-R_1}{\left(1-\sqrt{R_1(1-l)}\right)^2} \approx \frac{4T_1}{(T_1+l)^2} \tag{5.4}$$

(the approximation is only valid when T_1, $l \ll 1$). In the cavity described here, there is a considerable impedance mismatch; R_R was found to be 0.55 and as mentioned in Section 5.4.2 the mode matching efficiency had been measured to be 82 %. The residual reflectivity due to the impedance mismatch is R_c (= $(T_{eff} - 2T_1)^2 / T_{eff}^2$)) and is found to be 0.4. The difference between R_c and the observed reflectivity, R_R, gives an indication of the quality of mode

matching, characterised with the parameter $\eta = 1 - (R_R - R_c)$ which is found to be 0.85, in good agreement with the experimentally measured value of 0.82.

Measurements of the parameters describing the cavity enable an estimate of the expected ultraviolet output power to be made. The power circulating in the cavity, P_c, can be found from $\eta\varepsilon P_{in}$, where P_{in} is the incident fundamental power on M_1 (20 mW). The second harmonic power is given by $P_{sh} = \gamma P_c^2$, where γ is the doubling efficiency calculated in Section 5.4.1. If estimations are made for the loses associated with absorption and scattering within the crystal and reflection at its output face ($\approx$ 30 %), reflection from M_4 and M_1 (< 5 %) and transmission through M_2 ($\approx$ 20 %), then the expected output power is 3.2 μW. This implies the doubling efficiency is approximately an order of magnitude lower than the theoretical value. This can be explained by a number of factors, including the possible failure to exactly achieve the optimum beam profile within the crystal, required for maximum SHG, and inaccuracies in the calculation of the doubling efficiency. It has been previously noted that it is extremely difficult to experimentally achieve theoretically calculated conversion efficiencies[24,27].

The quality of the enhancement produced in the cavity depends on both the mode matching which in this case is reasonable and the impedance matching, which in this case is poor. To increase the intensity of the ultraviolet radiation produced by this cavity it would therefore be necessary to improve the impedance matching.

5.4.5 Results

Despite the low laser power, absorption experiments to detect N_2^+ *via* the $B\ ^2\Sigma_u^+ \leftarrow X\ ^2\Sigma_g^+$ transition, were attempted in the ICP chamber described in Chapter 2. These are discussed below.

The divergence of the ultraviolet radiation emerging from the cavity was partially corrected using three quartz lenses, after which a proportion of the beam ($\approx$ 20 %) was reflected from a quartz flat, while the remainder was steered through the plasma chamber using dielectric coated turning mirrors. By the exit of the plasma chamber, its power had been attenuated by approximately an order of magnitude due to reflection losses on the mirrors, lenses and plasma chamber windows and some loss at an iris placed after the chamber to spatially select the laser beam. The intensities of the reference reflection and the beam passing through the plasma chamber were observed using a pair of identical photomultiplier tubes (PMT) (Electron Tubes Ltd 9125 QB) fitted with UG11 filters to remove the fundamental radiation. The time response of the signals produced were varied using a matched pair of incrementally variable terminators.

Absorption will be observed as a reduction in the ratio of the signal from the PMT after the chamber to the signal from the PMT before the chamber. This method should enable direct compensation for the variations in the laser intensity. The absorption signal would be observed as the difference in the ratio at a wavelength on resonance with a transition in the B $^2\Sigma_u^+ \leftarrow$ X $^2\Sigma_g^+$ system compared to the ratio off resonance.

Without the discharge present, a continuous laser intensity was clearly observed by both the PMTs. However, once the discharge was struck the plasma induced emission, many orders of magnitude more intense than the laser, made it impossible to observe the laser signal on the PMT. To reduce the plasma emission a narrow bandwidth interference filter, centred at 330 nm (CVI F10-330.0-4-0.5 FWHM 10 nm peak transmittance 30 %), was placed in front of the PMT. Although this significantly reduced the plasma induced emission, it was still found to be several orders of magnitude more intense than the laser. To reduce the plasma induced emission further a monochromator (Edinburgh instruments 121 S15 *f*4.0, dispersion 5.3 nm/mm, slit width 200 μm) with a resolution of 1.1 nm FWHM was used in addition to the interference filter. The beam shaping optics before the chamber were then used to change the spatial properties of the beam so that it was focused onto the entrance slit of the monochromator, after the chamber. The best resolution from the monochromator was, therefore, not attained, as this is achieved when the collecting optics have the same *f* number as the monochromator resulting in full illumination of the grating[15]. However, the loss in spectral resolution is more than compensated by the reduction in the observed plasma induced emission. This is because no lens was required after the chamber and so only the plasma induced emission incident on the entrance slit was collected rather than the entire emission incident on the lens being focused through the slit. Use of the monochromator reduced the signal due to plasma induced emission to about three orders of magnitude greater than that due to the laser.

A further reduction of about order of magnitude in the observed plasma induced emission was achieved by placing the entire observation system (PMT, filter and monochromator) about 3 m away from the chamber and resetting the beam shaping optics to the entrance slit of the monochromator.

To remove some of the signal observed due to plasma induced emission, the MMS technique was applied. This involved mechanically modulating the laser beam using an optical chopper (Scitec Instruments), and using two identical lock-in amplifiers (Brookdeal 401A) to detect the signal due to the laser on the two PMTs (whose time response was adjusted so their time

constant was significantly shorter than the inverse of the modulation frequency). Despite the use of 10-second lock-in time constants the random noise on the ratio of the PMT signals due to the plasma induced emission was still more than an order of magnitude larger than the expected change due to absorption by the N_2^+ ion.

With the PMTs terminated into 50 Ω, photon counting techniques were applied after the radiation was attenuated sufficiently that the count rate was significantly below 1 MHz, corresponding to the limit of the pulse counting PC interface card used. Again, the variation in the signal due to plasma induced emission was considerably larger then the expected absorption, and comparable to that observed using the lock-in method. It was therefore concluded that the amount of absorption must be increased if it were to be observed.

To increase the amount of absorption observed due to the N_2^+ ions, an attempt to extend the path length within the plasma was made. Initially, this involved the use of two 3" diameter UV enhanced aluminium mirrors, to obtain up to five passes through the discharge. This was the maximum number of passes possible because the laser beam's spatial properties changed so significantly with distance, that significant proportions of the beam struck the edges of the slots, even for 5 passes, reducing the intensity. Furthermore, the increased path length was over compensated for by the reduction in laser power due to the reflection losses on the chamber windows, losses due to the beam not passing cleanly through the slots and the non-unity reflectivity of the aluminium mirrors used. Therefore, no improvement was observed.

A final attempt to increase the signal was made. An optical cavity was constructed around the plasma, consisting of two mirrors specified with a reflectivity of 99.5 % at 308 nm, with radius of curvature of 1.5 m, mounted in the mirror boxes described previously. This removes the problem of reflection losses from the chamber windows, but the effects of the plasma on the mirror reflectivity observed in Section 5.3.3 will cause changes in the effective path length of the radiation in the cavity. The beam was focused into the centre of the cavity using the beam shaping optics to achieve a beam waist as close as possible to that calculated for the cavity TEM_{00} mode.

The cavity was aligned so that the maximum transmission was observed, while one mirror was ramped rapidly by the piezoelectric transducer. The transmission profile of the cavity was then recorded using a slower ramp. The cavity transmission was found to be independent of mirror position. This may be explained qualitatively by the low intensity and therefore very small optical field present in the 'cavity' – the front mirror acts independently of the rear mirror and

radiation incident upon the 'cavity' enters with an efficiency dependent upon the front mirror reflectivity alone. Preliminary experiments completed on other cavities in an attempt to measure a 'threshold' intensity for resonant cavity behaviour have as yet provided inconclusive results. As no resonant cavity behaviour was observed, it is impossible to apply CRDS or related techniques such as a cavity enhanced absorption experiment[30]. Effectively, this cavity only increases the path length of radiation through the plasma, at the expense of the intensity reflected from the front mirror.

The increase in effective path length provided by this cavity was estimated by measuring the ratio of transmitted power with the back mirror aligned along the cavity axis (approximately equal to $P_{in}(1 - R)/2$ as half the light transmitted through the front mirror will be lost through the back mirror, if the cavity shows no resonance behaviour) to that with it misaligned (approximately equal to $P_{in}(1 - R)^2$ as each mirror will transmit the proportion $1 - R$ of the light incident on it). This ratio was found to be about 8, implying the path length through the plasma was increased by a factor of approximately 16. From this, the reflectivity of the mirrors at 330 nm is estimated to be 94 %, and unsurprisingly is considerably lower than the specified reflectivity at 308 nm.

This increased path length was gained at the expense of spatial filtering in the imaging system because a lens was required to focus the cavity output through the entrance slot of the monochromator. This increased the observed plasma induced emission by considerably more than an order of magnitude. Coupled with the reduction in the observed laser intensity due to the reflectivity of the front mirror this made observation of an absorption signal unfeasible.

5.4.6 Possible Future Experiments

The fundamental problem with the present system is that the laser system produces insufficient power to attempt the proposed experiments. This could be changed by both using a more powerful laser diode, improving the mode matching of the laser to the cavity and changing the cavity input coupler to improve the impedance matching. An alternative to a more powerful single diode laser is to use either a master diode laser seeding an amplifier diode[31] or a diode pumping a tapered amplifier[32]. These types of systems could even be used consecutively as the source for SHG.

To improve the mode matching a more complex system of optics could be used, rather than the single mode matching lens. This may enable better adjustment of the spatial output of the laser to the cavity TEM_{00} mode.

It is difficult to know, in advance, which input coupler reflectivity will give the best impedance matching, meaning that it is probably necessary to have a collection of input couplers with a range of reflectivitities, and to test them experimentally to achieve the best cavity performance[24]. However, this is expensive. An alternative strategy is to use a beam splitter, in the long arm of the bowtie cavity, to couple the laser output into the cavity. This is advantageous compared to a finite set of input couplers because the transmission into the cavity can be smoothly altered by rotating the beam splitter around its vertical axis[33].

5.5 Conclusions

LIF and CRDS signals have been observed using the A $^2\Pi_u \leftarrow$ X $^2\Sigma_g^+$ transition of the N_2^+ ion. The lifetime of the A $^2\Pi_u$ state in the discharge was found to be sufficiently long for a time of flight experiment to be completed (an ion with a velocity of 10 kms^{-1} on average would travel 5 mm before radiating). Although the preliminary tests for the time of flight experiment have shown that this method is not feasible with a pulsed laser, the basic cavity locking procedures required for an analogous continuous wave experiment have been successfully demonstrated.

The source constructed and characterised to be used to detect N_2^+ *via* the B $^2\Sigma_u^+ \leftarrow$ X $^2\Sigma_g^+$ electronic transition was found to be insufficiently intense for the proposed two dimensional velocity mapping experiment. However, several strategies to improve its performance have been suggested.

5.6 References

[1]B. K. Woodcock, *D. Phil. Thesis*, Oxford University, (1995)
[2]B. K. Woodcock, J. R. Busby, T. G. M. Freegarde and G. Hancock, *J. Appl. Phys.*, **81**, 5945, (1997)
[3]Y. P. Song, D. Field and D. F. Klemperer, *J. Phys. D*, **23**, 673, (1990)
[4]P. W. May, *PhD. Thesis*, Bristol University, (1994)
[5]M. J. Goeckner, R. P. Fetherston, W. N. G. Hitchon, N. C. Horswill, H. R. Keiter, M. M. Shamim, R. A. Breun, J. R. Conrad and T. E. Sheridan, *Phys. Rev. E*, **51**, 3760, (1995)
[6]D. E. Gerassimou, S. Cavadias, D. Mataras and D. E. Rapakoulias, *J. Appl. Phys.*, **67**, 146, (1990)
[7]J. K. Olthoff, R. J. Van Brunt and S. B. Radovanov, *Appl. Phys. Lett.*, **67**, 473, (1995)
[8]A. Lofus and P. Krupenie, *J. Phys. Chem. Ref. Data*, **6**, 113, (1977)
[9]A. Yariv, *Quantum Electronics in modern Communications*, OUP, (1997)
[10]O. Svelto, *Principles of Lasers 4thEdition*, Plenum Press, (1998)
[11]W. Bensech, D. Rivers and J. Moore, *J. Opt. Soc. Am.*, **70**, 792, (1980)
[12]J. M. Hollas, *Modern Spectroscopy*, Wiley, (1987)
[13]S. Main, *Part II Thesis*, Oxford University, (1998)
[14]Hamamatsu, Product Catalogue, (1997)
[15]W. Demtröder, *Laser Spectroscopy*, Springer-Verlag, (1981)
[16]R. N. Zare, *Angular Momentum*, Wiley, (1988)
[17]K. P. Huber and G. Hertzberg, *Molecular Spectra and Molecular Structure IV. Constants of Diatomic Molecules*, Van Nostrand Reinhold Company, (1979)
[18]F. Grangeon, C. Monard, J-L Dorier, A. A. Howling, Ch. Hollenstein, D. Romanini and N. Sadeghi, *Plasma Sources Sci. Technol.*, **8** , 448, (1999)
[19]B. A. Paldus, C. C. Harb, T. G. Spence, B. Wilke, J. Xie, J. S. Harris and R. N. Zare, *J. Appl. Phys.*, **83**, 3991, (1998)
[20]www.a-a.fr
[21]T. G. M. Freegarde, *Private Communication*, (2000)
[22]G. D. Boyd and D. A. Kleinman, *J. Appl Phys.*, **39**, 8, (1968)
[23]V. G. Dmitriev, G. G. Gurzadyan and D. N. Nikogosyan, *Handbook of Nonlinear Optical Crystals*, Spinger-Verlag, (1991)
[24]T. Kaing and M. Houssin,*Opt. Comm.*, **38**, 423, (1998)
[25]T. P. Arnold, *Part II Thesis*, Oxford University, (2000)
[26]C. E. Hamilton, *Opt. Lett.*, **17**, 728, (1992)
[27]T. W. Hänsch and B. Couillaud, *Opt. Comm.*, **35**, 3, (1988)
[28]R. W. P. Drever, J. L. Hall, F. V. Kowalski, J. Hough, G. M. Ford, A. J. Munley and H. Ward, *Appl. Phys. B*, **31**, 97, (1983)
[29]J. C. Bergquist, H. Hemmati and W. M. Itano, *Opt.Comm.*, **43**, 437, (1982)
[30]R. Engeln, G. Berden, P. Peeters and G. Meijer, *Sci. Instrum.*, **69**, 3763, (1998)
[31]M. de Angelis, G. M. Tino, P. De Natale, C. Fort, G. Modugno, M. Prevedelli and C. Zimmerman, *Appl. Phys. B*, **62**, 333, (1996)
[32]A. K. Goyal, P. Gavrilovic and H. Po, *Appl. Phys. Lett.*, **71**, 1296, (1997)
[33]K. R. Lykke, *Opt. Comm.*, **157**, 88, (1998)

Chapter 6

Summary and Concluding Remarks

The use of plasmas is very widespread, with one of the most commonly observed examples being the fluorescent lamp. Plasmas are also very important in industrial processing systems, and have found uses in the aerospace, automotive, steel, biomedical, toxic waste management and, most significantly, the electronics industries. The first Chapter of this Thesis included a concise introduction to plasmas and a summary of some of these applications. Also contained within Chapter 1 was a brief discussion of a selection of the parameters used to describe a plasma. Measurement of these intrinsic properties of processing plasmas is critically important in understanding discharges, so that the optimum processing conditions can be achieved. A description of a selection of the techniques that have previously been used to study gas discharge systems was given.

A significant proportion of previous studies of plasmas have involved the use of lasers to investigate the properties of the discharge whilst minimising the disturbance to it. A relatively recent technological development has been the production of reliable diode lasers (presently almost exclusively produced by plasma processing). These lasers were used for a significant proportion of the experiments described within this Thesis and hence a description of their operation and properties was given at the end of Chapter 1.

The experiments described within this Thesis were carried out in three discharge systems, two of which used radio frequency to produce the discharge; the other was a commercial flow system. The two radio frequency systems were discussed in detail in Chapter 2. These were an extensively modified capacitively coupled commercial system, and an inductively coupled system (a research system specifically designed and constructed for the type of experiments described within this Thesis).

The remainder of this Thesis described the development and testing of several different diagnostic methods. In Chapter 2, the radio frequency discharges were studied using a planar probe. This enabled measurement of the ion flux and electron temperature in both inductively coupled and capacitively coupled plasmas at various pressures and applied powers. In both

plasma systems, the ion flux was found to increase with increasing power and decrease with increasing pressure, effects which can be understood in terms of simple theory. The electron temperature measurements relied on the assumption that the electron energy distribution is Maxwellian and these were found to be considerably less precise than the ion flux measurements. Plasmas struck in different gases were also compared, the results being explained in terms of the ionisation potentials of the gases. From the measurements made it was possible to compare the ion densities produced in the inductively coupled and capacitively coupled plasma systems. At the same pressure and applied power, the ion density was found to be about five times greater in the capacitively coupled system. This can be explained in terms of the power dissipated into the discharge per unit volume, the conditions under which the systems were operating and the probe position. The ion density at low pressures and high powers in the inductively coupled plasma system, in which a capacitive to inductive transition was observed (although around this point no obvious hysteresis was observed), is expected to be greater than those achievable in the capacitively coupled plasma systems.

Chapter 3 described the first application of Frequency Modulation Spectroscopy (FMS) as a plasma diagnostic. A thorough description of the technique was given along with an explanation of the analysis required to obtain reliable quantitative information from it. This diagnostic was shown to be very effective, giving a significantly increased S/N ratio compared to both single pass absorption and low frequency mechanical modulation techniques. It was used to measure excited argon atom concentrations in both capacitively and inductively produced plasmas. The argon atom $4s[^3/_2]_1$ level concentration was found to be between 2×10^8 and 1×10^{11} atoms/cm^3 and to generally increase with increasing applied power and to decrease with increasing total pressure, in agreement with a simple discharge model. The temperature of the atoms was also measured and was found to be approximately 323 ± 17 K.

Chapter 4 described how a simple compact laser source at 308 nm was produced from a frequency doubled cooled commercial diode laser. It also described how this was used to detect the OH radical, by absorption, within the afterglow of a microwave discharge, produced either directly or chemically. Kinetic models provided explanations of the variations in OH concentration with discharge conditions.

Also in Chapter 4 a novel method, cavity laser induced fluorescence (CLIF), that combines the advantages of both laser induced fluorescence (LIF) and cavity ring down spectroscopy CRDS, was shown to increase the sensitivity of a diagnostic system compared to absorption. This method could be used to follow concentration variations of a reaction in a single laser shot.

Although such variation can be observed using LIF, it requires calibration and a many laser shot experiment, with a signal recorded at each time point. Whilst CRDS allows temporal information about the absolute concentrations of the species observed to be obtained, it is not as sensitive as LIF. By combining the two in CLIF, it may be possible to retain the sensitivity of LIF with the advantage of CRDS, so that absolute and time varying concentrations can be obtained in a single pulsed laser shot.

Previous measurements of the velocity distribution of the N_2^+ ion by LIF, within the sheath of the discharge observed a large proportion of the ions in a non-accelerated distribution. These zero velocity ions cannot be easily explained by theoretical modelling and thus further experiments are required to determine whether the signal implying these ions are present is real or just an experimental artefact. In Chapter 5, two such experiments are proposed; firstly a plasma time of flight experiment and secondly a two-dimensional mapping experiment. The design and initial testing of the systems required for these experiments was given in Chapter 5.

LIF and CRDS signals were observed using the A $^2\Pi_u \leftarrow$ X $^2\Sigma_g^+$ transition of the N_2^+ ion. The lifetime of the A $^2\Pi_u$ state in the discharge was found to be sufficiently long for a time of flight experiment to be contemplated (an ion with a velocity of 10 kms^{-1} on average would travel 5 mm before radiating). Although the preliminary tests for the time of flight experiment showed that this method is not feasible with a pulsed laser, the basic cavity locking procedures required for an analogous continuous wave experiment were successfully demonstrated.

A frequency doubled diode laser source was constructed and tested, with the eventual aim of detecting N_2^+ *via* the B $^2\Sigma_u^+ \leftarrow$ X $^2\Sigma_g^+$ electronic transition. This was found to be insufficiently intense to be used for a proposed two-dimensional velocity mapping experiment, but several strategies to improve its performance were suggested.

This Thesis described the development and testing of several novel plasma diagnostics, along with a newly constructed plasma system. Several of the techniques were shown to be advantageous compared to methods previously used, although in other cases a considerable amount of further investigation is required to assess their success.

Appendix 1

Optical Cavities

This Appendix contains a summary of the necessary mathematics of ray and Gaussian optics. Also given is a brief discussion of a procedure that can be used to determine whether an optical cavity is stable.

A1.1 Ray Optics

A beam of light can be considered as a collection of rays; each individual ray can be described as propagating at an angle, θ, to and at a distance, r, from an axis of propagation. By convention the axis of propagation is chosen to be the optic axis of the optical elements the beam passes through (*e.g.* the line that passes through the two centres of curvature of a lens). It is possible to calculate the properties of a ray at one point on the optic axis (r′, θ') by taking the product of a vector describing the ray at a previous point on the optic axis (r, θ) and a 2 × 2 matrix describing the properties of the optical elements (for example lenses and mirrors) the ray has passed through[1], as shown in equation (A1.1).

$$\begin{bmatrix} r' \\ \theta' \end{bmatrix} = \begin{bmatrix} A & B \\ C & D \end{bmatrix} \begin{bmatrix} r \\ \theta \end{bmatrix} \tag{A1.1}$$

The 2 × 2 matrix, which is generally known as the ABCD matrix, can be found from the product of the matrices describing each of the individual optical elements the ray passes through (see below), in propagating from (r, θ) to (r', θ').

A1.2 Specific Transformation Matrices

The following table contains a list of ABCD matrices for the specific optical elements that are generally used in the construction of an optical cavity.

Optical element	Matrix
Propagation of a ray in free space ($n = 1$) through a distance d.	$\begin{bmatrix} 1 & d \\ 0 & 1 \end{bmatrix}$
Propagation of a ray through a thin lens of focal length f.	$\begin{bmatrix} 1 & 0 \\ -1/f & 1 \end{bmatrix}$
Propagation of a ray through a dielectric interface with refractive indices n_1 and n_2.	$\begin{bmatrix} 1 & 0 \\ 0 & n_1/n_2 \end{bmatrix}$
Propagation of a ray through a spherical dielectric interface of radius R, with refractive indices n_1 and n_2.	$\begin{bmatrix} 1 & 0 \\ \left((n_2-n_1)/n_2\right)(1/R) & n_1/n_2 \end{bmatrix}$
Reflection of a ray by a spherical mirror with radius of curvature R.	$\begin{bmatrix} 1 & 0 \\ -2/R & 1 \end{bmatrix}$

A1.3 Gaussian Optics

Laser beams generally have a Gaussian transverse intensity profile, which is completely characterised by its beam waist, w, and the radius of curvature its wavefront, R. The minimum beam waist, w_0, occurs at a point in space where the wavefront radius of curvature is infinite, corresponding to a planar wavefront. If this point is defined as $z = 0$ on the axis of propagation of a Gaussian beam, consisting of monochromatic radiation of wavelength λ ($=\lambda_0/n$ where λ_0 is the wavelength of the radiation in a vacuum and n is the refractive index of the material through which the radiation is propagating), the beam waist at any point on the axis of propagation is given by[1]

$$w(z) = w_0 \sqrt{1 + \left(\frac{\lambda z}{\pi w_0^2} \right)^2} \tag{A1.2}$$

The beam wavefront curvature $R(z)$, at any point on the axis of propagation is given by[1]

$$R(z) = z \left(1 + \left(\frac{\pi w_0^2}{\lambda z} \right)^2 \right) \tag{A1.3}$$

These parameters that define the properties of a Gaussian beam are shown in Figure A1.1.

By defining the Rayleigh range, z_R, the depth of focus of the Gaussian beam (an alternative parameter used is the confocal parameter $b = 2z_R$),

$$z_R = \frac{\pi w_0^2}{\lambda} \tag{A1.4}$$

it is possible to rewrite equations (A1.2) and (A1.3) in the following form.

$$w(z) = w_0 \sqrt{1 + \left(\frac{z}{z_R}\right)^2} \tag{A1.5}$$

$$R(z) = z\left(1 + \left(\frac{z_R}{z}\right)^2\right) \tag{A1.6}$$

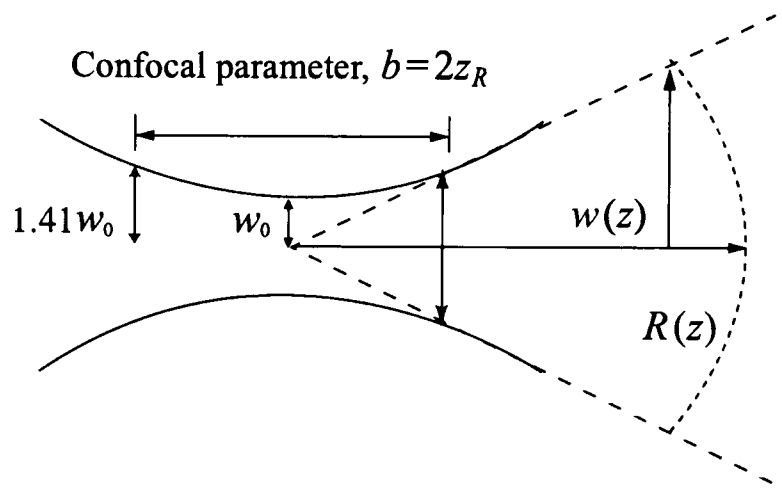

Figure A1.1 Gaussian beam parameters associated with angular divergence.

If a beam at one point in space has a Gaussian transverse intensity profile then as it propagates through any optical element its waist size and radius of curvature will change, but its intensity profile will still be a Gaussian function. This arises from the result that the Fourier transform of a Gaussian function is simply another Gaussian function.

The resultant Gaussian beam waist and radius of curvature on propagation through optical a series of elements can be predicted using equation (A1.8) and the ABCD matrices, described in the previous section, by employing the complex beam parameter, q

$$\frac{1}{q} = \frac{1}{R(z)} - i\left(\frac{\lambda}{\pi(w(z))^2}\right) \tag{A1.7}$$

$$q' = \frac{Aq + B}{Cq + D} \tag{A1.8}$$

Here q is the complex beam parameter at one point in space where the Gaussian beam properties are known and q' is the predicted complex beam parameter at a point in space after the optic elements described by the ABCD matrix.

A1.4 Cavity Stability

A stable optical cavity is one in which the mirrors that constitute the cavity have the same radius of curvature as the Gaussian beam wavefront predicted at their point in the cavity. As described in the previous section, it is possible to describe the properties of a propagating Gaussian beam using the ABCD matrix analysis, and therefore this method can be used to obtain the criteria for a stable optical cavity. The cavity is stable if there is a solution to equation (A1.8) with $q = q$' using the ABCD matrix that describes all the optical elements a beam encounters in one round trip of the cavity. Thus the beam profile is invariant after a single trip around the cavity. The parameter q then describes the TEM_{00} mode (the lowest order mode) that the cavity 'supports'.

It is possible to use the ray optics introduced in Section A1.1 to determine whether a cavity is stable. For a cavity to be stable, the rays must be re-entrant (that is, after a finite number of passes in the cavity it will retrace its previous path). The condition for re-entrance is

$$\begin{bmatrix} r' \\ \theta' \end{bmatrix} = \kappa \begin{bmatrix} r \\ \theta \end{bmatrix} \tag{A1.9}$$

where κ is a constant less than unity. If it were greater than unity, the ray will move progressively away from the optic axis until it is lost from the cavity (and hence the cavity will be unstable). Equation (A1.9) can be directly compared to equation (A1.1) where the ABCD matrix describes all the optical elements the ray encounters in one round trip of the cavity. For a cavity consisting of a mirror of radius of curvature R_1 separated by a distance d from a second mirror of radius of curvature R_2 equation (A1.1) can be written as follows[1]:

$$\begin{bmatrix} r' \\ \theta' \end{bmatrix} = \begin{bmatrix} 1-\dfrac{2d}{R_2} & d\left(2-\dfrac{2d}{R_2}\right) \\ -\left(\dfrac{2}{R_1}+\dfrac{2}{R_2}\left(1-\dfrac{2d}{R_1}\right)\right) & -\left(\dfrac{2d}{R_1}-\left(1-\dfrac{2d}{R_1}\right)\left(1-\dfrac{2d}{R_2}\right)\right) \end{bmatrix} \begin{bmatrix} r \\ \theta \end{bmatrix} \tag{A1.10}$$

Almost all optical cavities can be reduced to this description, although in some cases the effective radius of curvature of the effective mirrors may be different in two orthogonal planes (for instance if there is a crystal whose faces are not normal to the axis of propagation of radiation around the cavity (see Section 5.4.1)).

By equating equations (A1.9) and (A1.10) an eigenvalue equation is generated whose solutions can be used to obtain the following requirement for stability[1].

$$0 < \left(1-\frac{d}{R_1}\right)\left(1-\frac{d}{R_2}\right) < 1 \tag{A1.11}$$

Therefore, only certain combinations of mirror separation and radii of curvature result in a stable cavity. This condition for stability can be simplified to $0 < g_1 g_2 < 1$, by introducing the parameters g_1 and g_2 ($g_1 = 1 - d/R_1$ and $g_2 = 1 - d/R_2$). Symmetric resonators (consisting of two identical mirrors) have $g_1 = g_2$ because $R_1 = R_2$. These regions of stability are shown in Figure A1.2.

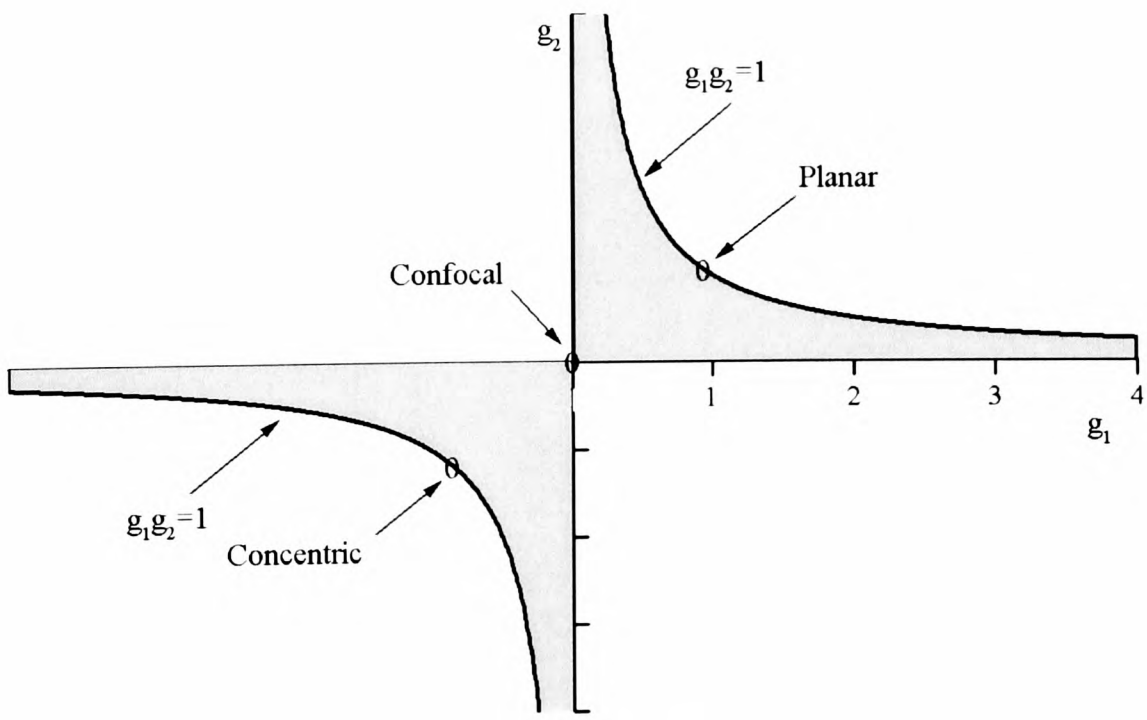

Figure A1.2: The Fox-Li Stability Diagram (the lines are labelled by the *g* parameters).

From equation (A1.11) it is found that plane-parallel cavities ($R_1 = R_2 = \infty$), confocal cavities ($R_1 = R_2 = d$) and concentric cavities ($R_1 = R_2 = d/2$) are all on the edge of stability and therefore lie on the lines between the high and low loss regions in Figure A1.2.

A1.5 Reference

[1]O. Svelto, *Principles of Lasers 4th Edition*, Plenum, (1998)

Appendix 2

Molecular Angular Momenta

In this Appendix the vectors and quantum numbers required to describe the states of some diatomic molecules are given, along with a brief discussion of the coupling between them. Also included is the nomenclature used to describe a particular molecular electronic energy state.

A2.1 Vectors and Quantum Numbers

$\boldsymbol{L}$ is the total orbital angular momentum vector of all the electrons in the molecule. L is the quantum number denoting the magnitude of $\boldsymbol{L}$.

$\boldsymbol{S}$ is the total electronic spin angular momentum of all the electrons in the molecule. S is the quantum number denoting the magnitude of **S**.

Λ is an orbital angular momentum quantum number that arises from Hund's coupling case (a). In this situation, spin-orbit coupling between $\boldsymbol{L}$ and $\boldsymbol{S}$ is sufficiently weak (analogous to Russell-Saunders coupling in atoms) that $\boldsymbol{L}$ strongly couples to the nuclear electrostatic field, and precesses about the internuclear axis. The magnitude of $\boldsymbol{L}$ is undefined and consequently L is not a good quantum number; only the component of $\boldsymbol{L}$ along the internuclear axis, $\Lambda\hbar$, is defined. Λ can take the values 0, ±1, ±2, ±3..., and results in a doubly degenerate electronic state if $\Lambda > 0$.

Σ is the spin quantum number analogous to Λ. $\boldsymbol{S}$ is coupled to the internuclear axis by the magnetic field caused by the orbital motion of the electrons. This spin-orbit coupling results in the component of $\boldsymbol{S}$ along the axis being $\Sigma\hbar$. Σ can take the values $S, S-1,\ldots,-S$, similar to m_s in atoms.

Ω is the total electronic angular momentum quantum number given by the sum of orbital angular momentum and spin angular momentum, with values of $\Omega = |\Lambda + \Sigma|$. The spin-orbit interaction splits the levels with different values of Λ and Σ. The energy level shift is given by $A\Lambda\Sigma$, where A is the spin orbit coupling constant.

N is the angular momentum quantum number of the nuclei in the molecule, which quantifies the rotational energy of the molecule. The rotational energy, E_{rot}, neglecting any centrifugal distortion, is given by $BN(N + 1)$, where B is the rotational constant of the molecule.

The resultant of the coupling of the electronic and nuclear angular momenta ($\boldsymbol{N}$ and $\boldsymbol{\Omega}$), resulting from the breakdown of the Born-Oppenheimer approximation, is $\boldsymbol{J}$. The quantum number J is the total angular momentum quantum number of the molecule.

K is an angular momentum quantum number that arises from a situation described as Hund's case (b). In this situation, $\boldsymbol{S}$ is not coupled to the internuclear axis and therefore Σ is not defined. $\boldsymbol{N}$ and $\boldsymbol{\Lambda}$ couple to give $\boldsymbol{K}$, which then couples with $\boldsymbol{S}$ to give $\boldsymbol{J}$.

A2.2 Λ-doubling

When the angular momentum coupling within the molecule is best described by Hund's case (a) the total angular momentum, $\boldsymbol{J}$, can have its projection either parallel or anti-parallel to the internuclear axis. Consider the ground electronic state of OH; if the radical is not rotating, these two levels are degenerate because they correspond to the opposite directions of rotation of the unpaired pπ electron about the internuclear axis. However, once the molecule is rotating ($N > 0$), this degeneracy is lifted – this phenomenon is known as Λ-doubling. This effect increases in magnitude with increasing molecular angular velocity because the electron does not follow the nuclear motion precisely (a phenomenon know as electron slip). In the high J limit the pπ electron lies either in the plane of nuclear rotation (resulting in an electronic wavefunction that is symmetric with respect to reflection in the plane of nuclear rotation), or perpendicular to it (resulting in an electronic wavefunction that is anti-symmetric with respect to reflection in the plane of nuclear rotation). These states are labelled the $\Pi(A')$ Λ–doublet and the $\Pi(A'')$ Λ–doublet respectively.

A2.3 ρ-doubling

When the molecule possesses no orbital angular momentum ($\Lambda = 0$), to a first approximation all rotational levels with $N > 0$ are doubly degenerate, because $\boldsymbol{\Sigma}$ can be projected in two ways onto the internuclear axis; either parallel or anti-parallel. However, if $\boldsymbol{\Sigma}$ couples with the molecular rotation ρ-doubling occurs. This results in two values of J for each value of K; $K + {}^1/_2$ belonging to the F_1 manifold and $K - {}^1/_2$ belonging to the F_2 manifold. The parity of these states is given by $(-1)^N$.

A2.4 Molecular Term Symbols and Symmetry

The terminology (term symbol) for describing a state is ${}^{2S+1}\Lambda_{\Omega}$ where Λ is represented by Σ, Π, Δ, Φ, Γ... for $\Lambda = 0, 1, 2, 3, 4...$ respectively. The value of Ω is only given if Λ and S are non zero. For Σ states the electronic wavefunction can be symmetric or antisymmetric with respect to reflection in a plane containing the internuclear axis, and are labelled with the superscript symbol + or – respectively (giving a term symbol ${}^{2S+1}\Sigma^{+/-}$).

For homonuclear diatomic molecules a further symmetry label is used to denote the electronic states. If the electronic state is symmetric with respect to inversion through the centre of mass of the molecule it is given the subscript label *g* (from the German for even, *gerade*) and if it is antisymmetric it is labelled with the subscript *u* (from the German for uneven, *ungerade*). This results in the term symbol ${}^{2S+1}\Lambda_{g/u}$ for homonuclear diatomic molecules.